

TABLE OF CONTENTS

<u>Section</u>		<u>Page</u>	
1	SUMMARY AND INTRODUCTION	1	1/A9
2	FDI STRUCTURE	2	1/B3
	2.1 Introduction	9	1/B3
	2.2 Redundancy Trigger	9	1/B3
	2.3 The Sequential Probability Ratio Test	10	1/B4
	2.4 Time Trigger	12	1/B6
	2.5 Failure Identification by the Outer Loop	13	1/B7
3	ANALYTIC REDUNDANCY SPRT's	15	1/B9
	3.1 Introduction	15	1/B9
	3.2 Translational Kinematics	16	1/B10
	3.3 Translational Dynamics	21	1/C1
	3.4 Rotational Kinematics	24	1/C4
	3.5 Altitude Kinematics	28	1/C8
4	CALCULATION OF FDI SYSTEM PARAMETERS	33	1/C13
	4.1 Introduction	33	1/C13
	4.2 Rate Gyros	33	1/C13
	4.3 Attitude Gyros	37	1/D3
	4.4 Accelerometers	43	1/D9
	4.5 Altimeters	50	1/E2
	4.6 Alpha Vanes and Mach Meters	52	1/E4
	4.7 Additional Tests	55	1/E7
	4.8 Summary	60	1/E12
5	QUALITY SPRT's	63	1/F1
6	OUTER LOOP LOGIC	69	1/F7
	6.1 Introduction	69	1/F7
	6.2 Failure Identification - Redundancy Trigger ...	69	1/F7
	6.3 Failure Identification - Time Trigger	71	1/F9
	6.4 Additional Outer Loop Tasks	71	1/F9

<u>Section</u>		<u>Page</u>	
7	SIMULATION RESULTS	73	1/F11
	7.1 Introduction	73	1/F11
	7.2 Time Trigger Performance	73	1/F11
	7.3 Redundancy Trigger Performance	84	1/G8
	7.4 Hard Failure Identification	89	1/G13
8	APPLICATION TO FLIGHT TEST DATA	91	2/A6
	8.1 Introduction	91	2/A6
	8.2 Discussion of Flight Data	91	2/A6
	8.3 Calculation of FDI System Parameters	95	2/A10
	8.4 FDI Algorithm Modifications	102	2/B3
	8.5 Injected Failure Identification	105	2/B6
	8.6 Summary	114	2/C1
9	CONCLUSIONS AND RECOMMENDATIONS	159	2/F4
<u>Appendix</u>			
A	TURBULENCE ESTIMATOR	163	2/F8
B	AERODYNAMIC COEFFICIENT APPROXIMATION	167	2/F12
C	SCALE FACTOR FAILURES	171	2/G2
D	SIMULTANEOUS ψ AND θ FAILURES	175	2/G6
E	DESIGN AND PERFORMANCE OF AN ALTITUDE KINEMATICS FILTER	179	2/G10
	E.1 Introduction	179	2/G10
	E.2 AK Filter Design	179	2/G10
	E.3 Acceleration Bias Estimation	182	2/G13
	E.4 Performance Results	184	3/A6
F	COMPENSATION OF TURN ERROR IN DIRECTIONAL GYROS	189	3/A11
	F.1 Introduction	189	3/A11
	F.2 Derivation of Turn Error Expression	190	3/A12
	F.3 Results of Turn Error Compensation of Flight Data	196	3/B4
	F.4 Summary and Conclusions	199	3/B7
	LIST OF REFERENCES	208	3/C2

LIST OF ILLUSTRATIONS

Figure		Page	
4-1	Low Turbulence Wind Profile	46	1/D12
7-1	Rate Gyro Time Trigger Performance	75	1/F13
7-2	Accelerometer Time Trigger Performance	80	1/G4
7-3	Mach Meter and Alpha Vane Time Trigger Performance .	82	1/G6
7-4	Rate Gyro Direct Redundancy Trigger Performance	85	1/G9
7-5	Accelerometer Direct Redundancy Trigger Performance	86	1/G10
7-6	Alpha Vane Direct Redundancy Trigger Performance ...	88	1/G12
8-1	Segment 1	117	2/C4
8-2	Segment 1 (cont.)	118	2/C5
8-3	Segment 2	119	2/C6
8-4	Segment 2 (cont.)	120	2/C7
8-5	Segment 3	121	2/C8
8-6	Segment 3 (cont.)	122	2/C9
8-7	Segment 4A	123	2/C10
8-8	Segment 4A (cont.)	124	2/C11
8-9	Segment 4B	125	2/C12
8-10	Segment 4B (cont.)	126	2/C13
8-11	Segment 4C	127	2/C14
8-12	Segment 4C (cont.)	128	2/D1
8-13	Segment 4D	129	2/D2
8-14	Segment 4D (cont.)	130	2/D3
8-15	Segment 5	131	2/D4
8-16	Segment 5 (cont.)	132	2/D5
8-17	Segment 6	133	2/D6
8-18	Segment 6 (cont.)	134	2/D7
8-19	Segment 4C, Roll Rate Gyro 1 +BFM Bias at T=29,RK ..	135	2/D8
8-20	Segment 4A, Roll Rate Gyro 2 +BFM Bias at T=0,RK ...	136	2/D9
8-21	Segment 3, Roll Rate Gyro 2 Fail to Zero at T=0,RK .	137	2/D10
8-22	Segment 4C, Pitch Rate Gyro 1 -BFM Bias at T=29,RK.	138	2/D11
8-23	Segment 4A, Pitch Rate Gyro 2 +BFM Bias at T=0,RK...	139	2/D12
8-24	Segment 3, Pitch Rate Gyro 2 Fail to Zero,RK.....	140	2/D13
8-25	Segment 4C, Yaw Rate Gyro 2 -BFM Bias at T=29,RK....	141	2/D14

List of Illustrations (cont.)

Figure		Page	
8-26	Segment 4A, Yaw Rate Gyro 1 +BFM Bias at T=0,RK.....	142	2/E1
8-27	Segment 3, Yaw Rate Gyro 1 Fail to Zero at T=0,RK....	143	2/E2
8-28	Segment 2, Roll Attitude Gryo 1 -BFM Bias at T=37,RK.	144	2/E3
8-29	Segment 2, Pitch Attitude Gyro 1 +BFM Bias at T=37,RK	145	2/E4
8-30	Segment 4B, Mach Meter 1 -BFM Bias at T=130,TK.....	146	2/E5
8-31	Segment 4B, Mach Meter 1 +BFM Bias at T=160,TK.....	147	2/E6
8-32	Segment 4A, Mach Meter 2 +BFM Bias at T=8,TK.....	148	2/E7
8-33	Segment 4B, Alpha Vane 1 +BFM Bias at T=130,TD.....	149	2/E8
8-34	Segment 4C, Alpha Vane 1 +BFM Bias at T=36,TD.....	150	2/E9
8-35	Segment 4B, Longitudinal Accelerometer 2 +BFM Bias at T=80,TK.....	151	2/E10
8-36	Segment 4A, Longitudinal Accelerometer 1 Fail to Zero at T=0,TK.....	152	2/E11
8-37	Segment 4A, Lateral Accelerometer 2 -BFM Bias at T=12,TD.....	153	2/E12
8-38	Segment 4C, Lateral Accelerometer 2 +BFM Bias at T=36,TD.....	154	2/E13
8-39	Segment 4B, Normal Accelerometer 2 -BFM Bias at T=90,AK.....	155	2/E14
8-40	Segment 4B, Normal Accelerometer 2 -BFM Bias at T=125,AK.....	156	2/F1
8-41	Segment 4B, Normal Accelerometer 2 -BFM Bias at T=140,AK.....	157	2/F2
8-42	Segment 4C, Normal Accelerometer 1 +BFM Bias at T=10,AK.....	158	2/F3
A-1	Continuous Velocity Estimator	163	2/F8
A-2	Residual Processing	164	2/F9
E-1	Segment 2, AK Filter Performance Without Additive Acceleration Bias	186	3/A8
E-2	Segment 2, AK Filter Performance with and without Additive Acceleration Bias	187	3/A9
F-1	Elements of Error Geometry for a Directional Gyro...	191	3/A13
F-2	Turn Error Due to Non-horizontal Floor Plane	194	3/B2
F-3	Spherical Geometry for Non-horizontal Spin Axis	194	3/B2
F-4	Turn Error Due to Non-horizontal Spin Axis	196	3/B4
F-5	Attitude History for Segments 2, 3, 4A and 4C	201	3/B9
F-5	(cont.)	202	3/B10
F-6	Segment 4A, Turn Error Compensation Assuming Horizontal Spin Axes	203	3/B11
F-7	Segment 4A, Turn Error Compensation Assuming Non-horizontal Spin Axes	204	3/B12

List of Illustrations (cont.)

Figure		Page	
F-8	Segment 2, Turn Error Compensation Assuming Non-Horizontal Spin Axes	205	3/B13
F-9	Segment 3, Turn Error Compensation Assuming Non-horizontal Spin Axes	206	3/B14
F-10	Segment 4C, Turn Error Compensation Assuming Non-horizontal Spin Axes	207	3/C1

LIST OF TABLES

Table		Page	
I	Sensor Information	16	1/B10
II	Summary of FDI System Parameters	61	1/E13
III	Attitude Gyro and Altimeter Simulation Results	89	1/G13
IV	Hard Failure Simulation Results	90	1/G14
V	Flight Data Segment Times	91	2/A6
VI	Minimum BFM and Standard Deviation Data	97	2/A12
VII	New BFM Levels	101	2/B2
VIII	Self-Test Thresholds	104	2/B5
IX	AP-101 Execution Times	161	2/F6
B.1	Worst-Case Acceleration Error due to Polynomial Approximation	170	2/G1

MAR 8 1978

NAS1.26, 2944

NASA Contractor Report 2944

COMPLETED
ORIGINAL

**Reliable Dual-Redundant
Sensor Failure Detection
and Identification for
the NASA F-8 DFBW Aircraft**

James C. Deckert, Mukund N. Desai,
John J. Deyst, Jr., and Alan S. Willsky

CONTRACT NAS1-13914
FEBRUARY 1978

NASA

217

NASA Contractor Report 2944

**Reliable Dual-Redundant
Sensor Failure Detection
and Identification for
the NASA F-8 DFBW Aircraft**

James C. Deckert, Mukund N. Desai,
and John J. Deyst, Jr.

The Charles Stark Draper Laboratory, Inc.
Cambridge, Massachusetts

Alan S. Willsky

Massachusetts Institute of Technology
Cambridge, Massachusetts

Prepared for
Langley Research Center
under Contract NAS1-13914

3024 28030



National Aeronautics
and Space Administration

**Scientific and Technical
Information Office**

1978

BLANK PAGE

BLANK PAGE

RELIABLE DUAL-REDUNDANT SENSOR FAILURE DETECTION AND
IDENTIFICATION FOR THE NASA F-8 DFBW AIRCRAFT

James C. Deckert*, Mukund N. Desai*, John J. Deyst, Jr.*
and Alan S. Willsky†

SECTION 1

SUMMARY

A technique is developed which provides reliable failure detection and identification for a dual-redundant subset of the flight control sensors aboard the NASA F-8 digital fly-by-wire aircraft. The technique is successfully applied to simulated sensor failures on the NASA Langley Research Center real-time F-8 digital simulator and to sensor failures injected on telemetry data from a test flight.

INTRODUCTION

With the introduction of flight critical fly-by-wire systems into operational aircraft and the proposed use of direct sideforce and lift devices in future generation aircraft, attention has been focusing on the development of highly reliable, fault tolerant flight control systems. Because of the difficulty in developing the required reliability in single sensors, current practice for fault tolerant sensor operation involves the use of voting among three or more sensors of the same type. Such a voting scheme with three sensors provides operational capability in the presence of a single failure. However

* Staff Engineer, the Charles Stark Draper Laboratory, Inc., Cambridge, Mass.

† Associate Professor, Department of Electrical Engineering and Computer Science, Massachusetts Institute of Technology, Cambridge, Mass.

in such a triplex voting system, the two sensors which remain following the identification of the failure of the third sensor provide no identification capability for the subsequent failure of one of the remaining pair. Thus the third sensor in a triplex system is in essence being used only to vote, and provides little appreciable benefit in terms of performance under no-fail conditions. The attendant costs in both initial acquisition and subsequent maintenance of this third sensor of each type have motivated the study described in this report.

In this study we have developed the methodology for a highly reliable single fault tolerant sensor system in which only dual redundancy is present, i.e., in which only two sensors of each type are present*. The technique in essence involves voting, but the third "vote" is provided by the analytic redundancy which exists in the functional or kinematic relationships between the variable being measured by the suspect sensor type and the variables being measured by the other sensors on the aircraft. Although sophisticated techniques using analytic redundancy have been developed previously (for example, Refs. 1-3), it is fair to say that these methods are all at a relatively early stage of development, and most may be criticized for computational complexity greatly exceeding the constraints imposed by any foreseeable onboard flight computer.[†]

We have developed our analytic redundancy sensor failure detection and identification (FDI) technique specifically for the dual redundant sensors on the NASA F-8 digital fly-by-wire (DFBW) aircraft, although its application to another aircraft with a different sensor complement is straightforward. Throughout the study we have tried to emphasize both computational simplicity and reliability. The important features of the technique are the following:

- 1) We limit ourselves to looking for bias failures since
 - a) Although descriptions of actual failure modes are not currently available, it is felt that biases are likely.
 - b) Techniques looking for bias failures can find most other types of failures.

* This technique, used in conjunction with a triplex system, can provide operational capability following the nonsimultaneous failure of two sensors of the same type.

[†] See Ref. 10 for a survey of failure identification techniques.

- 2) We use direct comparison between the dual sensor outputs to detect failures, and use analytic redundancy for identifying which instrument has failed. In this way, the analytic redundancy tests can be made more robust.
- 3) In addition, we periodically initiate the analytic redundancy tests to identify changes which affect like instruments in the same way (e.g., thermal effects on sensors mounted in the same part of the aircraft).
- 4) All reasonable functional and kinematic relationships between a given instrument type and the other types are developed in order to extract the maximal amount of information available.

The organization of the report is as follows: In Section 2, we describe the FDI structure consisting of time trigger or direct redundancy trigger followed by analytic redundancy tests. We also discuss the analytic decision statistic, the sequential probability ratio test (SPRT). In Section 3 we develop in detail the four kinds of analytic redundancy used in this study: translational kinematics, translational dynamics, rotational kinematics and altitude kinematics. In Section 4 we choose a consistent set of parameters for the sensor FDI system. These parameters include the instrument biases which each analytic redundancy test is designed to identify and the time limits for those tests. In Section 5 we develop the quality sequential probability ratio test (QSPRT), which is a form of SPRT which allows us to account for the worst-case effects of unmodeled errors in the analytic redundancy tests. In Section 6, we discuss the outer loop logic, the main function of which is combining the QSPRT and SPRT outputs from all the analytic redundancy tests in order to identify a failed sensor. In Section 7 we present some representative results obtained using the NASA Langley Research Center real-time F-8 simulator. These results demonstrate the capability of the algorithm at the design flight condition in the presence of high turbulence and biases on unfailed instruments. In Section 8 we present the results of a study in which the analytic redundancy FDI algorithm is applied to telemetry data obtained during a test flight of the F-8 DFBW aircraft. The importance of this section is twofold: First it indicates the ease with which the algorithm can be tailored to new sensor information, and second it demonstrates the capability of the algorithm to identify injected failures at several flight conditions and during maneuvers. In Section 9 we make some concluding remarks and recommendations for the form of the algorithm to be coded in the onboard computer for flight test.

LIST OF ABBREVIATIONS

AK	Altitude kinematics, residual in meters
BFM	Bias failure magnitude
DFBW	Digital fly-by-wire
DG	Directional gyro, measuring azimuth angle
DR	Direct redundancy
ETL	Elapsed time limit
FDI	Failure detection and identification
QSPRT	Quality sequential probability ratio test
RK	Rotational kinematics, residual in radians
RSS	Root of the sum of the squares
SPRT	Sequential probability ratio test
TD	Translational dynamics, residual in m/s^2
TK	Translational kinematics, residual in m/s
VG	Vertical gyro, measuring roll angle and pitch angle
WCF	Worst-case expectation of SPRT for failed instrument
WCU	Worst-case expectation of SPRT for unfailed instrument

LIST OF SYMBOLS

\underline{A}	Vector of ideal accelerometer outputs
$\underline{A'}$	Vector of ideal accelerometer outputs compensated for lever-arm effects
a	Acceleration (m/s^2)
a_b	Measured acceleration bias (m/s^2)
a_v	Vertical acceleration (m/s^2)
B	Instrument failure bias assumed by an individual SPRT
b	Test error, bias
c	Directional gyro turn error
$\underline{C_m}$	Measured unit vector coefficient for gravity in aircraft axes
C_n	QSPRT decision quantity at time t_n
D	Aerodynamic drag
E	Expectation operator
e_h	Error in the estimate of altitude (m)
e_v	Error in the estimate of altitude rate (m/s)
\underline{F}	Vector of aerodynamic forces on aircraft
F_e	Engine thrust
f, G	Translational kinematics SPRT gain factor
g	Acceleration of gravity ($9.81 m/s^2$)
h	Altitude (m)
k	Filter gain
L	Aerodynamic lift
M	Test error
M	Mach number

List of Symbols (cont.)

m	Aircraft mass
m_k	Hypothesized mean in y_k due to sensor failure
N	Number of samples in residual window
N_p	Number of passes allowed through identification logic
p	Roll rate, defined about aircraft longitudinal axis(rad/s)
q	Pitch rate, defined about aircraft lateral axis(rad/s)
\bar{q}	Dynamic pressure
r	Yaw rate, defined about aircraft normal axis(rad/s)
S	Aircraft wing area, also wind shear
s	Laplace variable
T	Sample period
t	Time, independent plot variable (sec)
T_c	Time to cross negative threshold for B failure
T_m	Time to cross negative threshold for $3/\sqrt{2}$ failure
T_o	Time at which TK gain is clipped
\underline{V}	Velocity of aircraft with respect to the air mass in body axes
v	Vertical velocity (m/s)
V_s	Velocity of sound
x, y, z	Orthogonal axis system
Y	Aerodynamic sideforce
α	Angle of attack(rad)
β	Sideslip angle(rad)
y	Filter residual, also input to SPRF
δ	Directional gyro spin axis tilt
δ_a	Aileron position(deg)
δ_e	Elevator position(deg)
δ_r	Rudder position(deg)
c	Direct redundancy threshold parameter
ϵ_h, ϵ_v	Altimeter filter residual variables
ζ	Dummy variable

List of Symbols (cont.)

λ	Log likelihood ratio
v	Sensor variance
θ	Euler pitch angle (rad)
$\underline{\xi}$	Inertial acceleration of air mass
ρ	Tilt angle of aircraft floor plane
σ^2	Variance of the observation of γ
τ	Normal accelerometer bias estimator time constant
τ_f	Altitude filter time constant
τ_m	Mean detection time
ϕ	Euler roll angle (rad)
ψ	Euler azimuth angle (rad)
ψ_g	Actual azimuth angle (rad)
ψ_i	Indicated azimuth angle (rad)
Ω	Skew-symmetric cross-product matrix
ω	Filter natural frequency

Superscripts

\cdot	Time derivative
\wedge	Estimated quantity
$-$	Averaged quantity

Subscripts

b	Bias quantity
e	Error term
m	Measured quantity
$1,2$	Relative to instrument 1 or 2 of a given type, also denoting altitude and altitude rate filter gains
$1,2,3$	Orthogonal body axis system x,y,z
$-$	Vector quantity

Subscripts (cont.)

O	Initial condition
B	Body axis
GIM	Gimbal axis
I	Inertial axis
k	Variable at time t_k
x	Longitudinal body axis
y	Lateral body axis
z	Normal body axis

SECTION 2

FDI STRUCTURE

2.1 Introduction

The FDI for a dual redundant instrument type is normally accomplished in two steps. First, the failure of one instrument of the pair is detected by examining only the dual instrument readings. Then upon detection of the failure by the redundancy trigger, several SPRT's are initiated utilizing the direct redundancy and all possible analytic redundancy among the failed instrument type and the other instrument types. Additionally, the analytic redundancy SPRT's for each instrument are initiated periodically by a time trigger in order to identify generic instrument failures. The identification of a failed instrument is accomplished via logical processing of the various SPRT outputs as discussed in Section 6.

2.2 Redundancy Trigger

A direct redundancy detector, called a redundancy trigger, operates on the moving window average of the output of instrument 1 minus the output of instrument 2 for each instrument type. A bias failure magnitude (BFM) is defined for each instrument type based on both the a priori sensor statistics and the capabilities of the various analytic redundancy failure identification techniques in the presence of allowable errors on unfailed instruments. A threshold magnitude and window size are chosen for each instrument type to give reasonable false alarm and missed alarm probabilities, where a false alarm is the indication of a bias when in fact a bias of half the defined magnitude or larger is not present, and a missed alarm is the failure to detect the presence of a bias of magnitude larger than the defined BFM. If the redundancy trigger detects a significant mean in the moving window average of the output of instrument 1 minus the output of instrument 2, it follows that if the sign of this mean is positive (negative) either instrument 1 has a positive (negative) bias or instrument 2 has a negative (positive) bias.

2.3 The Sequential Probability Ratio Test

As implemented in this study, the SPRT makes sequential observations of the process \underline{y} , which represents a comparison between the suspect instrument and other unfailed instrument types*. The sample from the process \underline{y} at time t_k is called \underline{y}_k . The SPRT gathers enough information to choose between the two hypotheses:

H_1 : At time t_k , the process \underline{y} is Gaussian with mean \underline{m}_k and covariance P .

H_2 : At time t_k , the process \underline{y} is Gaussian with mean $\underline{0}$ and covariance P .

where H_1 is the failure hypothesis and H_2 is the no-failure hypothesis. The log likelihood ratio λ for the k^{th} sample is defined as

$$\lambda_k = - \ln \frac{p(\underline{y}_k | H_1)}{p(\underline{y}_k | H_2)}$$

and after n samples have been taken (assuming the independence of the \underline{y} 's), the log likelihood ratio of the n samples is given by

$$u_n = - \ln \frac{p(\underline{y}_1, \dots, \underline{y}_n | H_1)}{p(\underline{y}_1, \dots, \underline{y}_n | H_2)} = \sum_{k=1}^n \lambda_k \quad (2.1)$$

For the case of the two hypotheses given above, the form of λ_k is given by

$$\lambda_k = \left(\frac{\underline{m}_k}{2} - \underline{y}_k \right)^T P^{-1} \underline{m}_k$$

and the log likelihood ratio for n samples given by Eq. (2.1) becomes

$$u_n = \sum_{k=1}^n \left(\frac{\underline{m}_k}{2} - \underline{y}_k \right)^T P^{-1} \underline{m}_k \quad (2.2)$$

Assuming that either H_1 or H_2 is true, the stipulation of incorrect classification probabilities directly yields the thresholds $a < 0$ and $b > 0$ and the following decision rule:^{4,5}

* The details of this process for the various instruments on the F-8 are presented in Section 3.

$$\begin{aligned}
u_n &\leq a && \text{accept } H_1 \\
a &< u_n < b && \text{take another sample} \\
b &\leq u_n && \text{accept } H_2
\end{aligned}
\tag{2.3}$$

If the log likelihood ratio is between the thresholds, a choice of hypotheses cannot yet be made which meets the specified incorrect classification probabilities, and another sample must be taken.

One attractive property of the SPRT is that it minimizes the average number of observations necessary to meet these probabilities. In addition, the SPRT is independent of the a priori probabilities of the two hypotheses. It is because of these properties of the SPRT and because of its inherent simplicity as shown in Eq. (2.2) and (2.3) that the SPRT was chosen as the basic identification tool for this study. A further simplification follows since all of the observed processes in this work are chosen to be scalar or the sum of scalars. The scalar form of Eq. (2.2) is given by

$$u_n = \sum_{k=1}^n \frac{m_k}{\sigma^2} \left(\frac{m_k}{2} - \gamma_k \right) \tag{2.4}$$

where σ^2 is the variance of the scalar process γ . Observe that if the mean m_k is present in γ_k , the expected value of u_n is

$$E[u_n] = \frac{1}{2\sigma^2} \sum_{k=1}^n (-m_k^2) \tag{2.5}$$

In fact any mean of γ_k with the sign of m_k and greater in magnitude than $|m_k|/2$ will drive u_n toward the negative threshold, which by our definition indicates an instrument failure. Thus an individual SPRT may make a false identification unless the mean m_k is chosen such that biases in instruments operating within tolerance have magnitude less than $|m_k|/2$.

In response to a redundancy or time trigger, several SPRT's are begun. In the case of initiation by the redundancy trigger, one direct redundancy SPRT observes the difference between instrument 1 and instrument 2 of the detected failure type, the same process observed by the redundancy trigger. The mean which constitutes the failure hypothesis, m_k , has magnitude equal to the pre-defined sensor

BFM and has the sign of the moving window average computed by the trigger. This SPRT serves to corroborate the trigger concerning the presence of a bias between the two instruments. Additionally, one SPRT for each instrument of the failed type is begun for every kind of analytic redundancy available. Detailed descriptions of these tests are given in the next section. The underlying basis for the analytic redundancy SPRT's is the comparison of the measurement of a variable obtained using the suspect instrument and another measurement of the same variable obtained using other instrument types. The difference in these measurements forms the residual γ_k which is the input to the SPRT. The mean for each SPRT, m_k , is calculated to be consistent with the predefined sensor BFM and the failure sign information from the redundancy trigger.

2.4 Time Trigger

On initiation by the time trigger for a particular instrument type, one SPRT for each sensor is begun for every kind of analytic redundancy for which the mean m_k (the failure signature) is observable following the failure. Thus there are some instrument types, e.g., the yaw attitude gyro, for which time triggers are not possible*.

Since there is no direct comparison of instruments for a time trigger, failure sign information is not available in this case, and a failure of either sign is possible for each instrument. A failure of either sign is identified by a single SPRT for an individual instrument as follows: Eq. (2.4) is rewritten as

$$u_n = \frac{1}{\sigma^2} \left[\sum_{k=1}^n \frac{m_k^2}{2} - \sum_{k=1}^n m_k \gamma_k \right] \quad (2.6)$$

The mean m_k is chosen to be consistent with a positive instrument failure with magnitude equal to the BFM. Then the SPRT output is defined to be

$$\tilde{u}_n = \frac{1}{\sigma^2} \left[\sum_{k=1}^n \frac{m_k^2}{2} - \left| \sum_{k=1}^n m_k \gamma_k \right| \right] \quad (2.7)$$

*The reasons for this are clarified in Section 3.

If \tilde{u}_n crosses the negative threshold, a failure is indicated, and the sign of the failure is the sign of the sum whose absolute value is used in Eq. (2.7).

2.5 Failure Identification by the Outer Loop

Because most instrument types have more than one form of analytic redundancy available for use in FDI, it is not practical for the failure identification process to be performed by the individual SPRT's via Eq. (2.3) for the different forms of analytic redundancy. Instead an outer loop observes the outputs u_n (or \tilde{u}_n for a time trigger) from all of the SPRT's running for the triggered instrument type. Since the different forms of analytic redundancy have different error sources, many of them dependent upon flight condition and maneuver activity, it is necessary that the outer loop have some measure of the goodness or quality of each form of analytic redundancy test at each point in time. This measure is provided by a quality SPRT (QSPRT) for each form of analytic redundancy associated with the suspect instrument type. Thus in response to a time or redundancy trigger for a particular instrument type, a QSPRT for each form of analytic redundancy is calculated in addition to the SPRT's for the individual instruments. The outputs of these QSPRT's and the outputs of the SPRT's associated with individual instruments are then combined by the outer loop to perform failure identification. The details of the outer loop are given in Section 6, while the details of the QSPRT's are given in Section 5.

BLANK PAGE

BLANK PAGE

SECTION 3

ANALYTIC REDUNDANCY SPRT's

3.1 Introduction

The dual redundant instrument types which are available on the F-8-DFBW aircraft are the following: longitudinal accelerometer, lateral accelerometer, normal accelerometer, roll rate gyro, pitch rate gyro, yaw rate gyro, vertical gyro, directional gyro, altimeter, Mach meter and alpha vane. In addition, a nonredundant beta vane is available. Each vertical gyro gives an indication of pitch angle θ and roll angle ϕ . Table I indicates the white noise and quantization levels assumed in this study for the various sensors. Also shown are the RSS bias magnitudes for unfailed sensors, where known. In this report only the failures of the dual redundant instrument types are addressed, and failures of the indication of θ and ϕ for each vertical gyro are considered to be independent. The consideration of simultaneous failures of both of these measurements is discussed in Appendix D.

Four types of analytic redundancy are utilized in this study: Translational kinematics redundancy exists between the integrated output of the accelerometers, vertical gyros and rate gyros and the outputs of the air data sensors, i.e., the Mach meter, altimeter and alpha and beta vanes. Translational dynamics redundancy relates the aerodynamic forces on the aircraft measured by the accelerometers and the calculated aerodynamic forces based on the air data sensors through stored aerodynamic coefficients. Rotational kinematics redundancy relates the integrated outputs of the rate gyros and the outputs of the vertical and directional gyros. Altitude kinematics redundancy exists between the altitude given by the altimeter outputs and the altitude computed as the double-integral of the accelerometer and vertical gyro outputs.

In the following subsections, these four types of analytic redundancy and the SPRT's exploiting them will be discussed in detail.

* Although triple redundancy exists for the accelerometers and rate gyros, this added redundancy will not be assumed here.

Table I Sensor Information

SENSOR TYPE	SIGMA	QUANTIZATION	RSS UNFAILED BIASES
Mach	.01	.0056	—
α (rad)	.01	.00017	—
a_x (m/s ²)	.3	.011	.46
a_y (m/s ²)	.3	.011	.46
a_z (m/s ²)	.3	.054	.46
p (rad/s)	.0024	.0024	.01
q (rad/s)	.0007	.0007	.003
r (rad/s)	.0007	.0007	.003
ϕ (rad)	.01	.0015	—
θ (rad)	.01	.0015	—
ψ (rad)	.01	.0015	—
β (rad)	.01	.00017	—
h (m)	3.05	3.4	—

The SPRT's will be formulated assuming initiation by the direct redundancy trigger. Modifications of these tests in the case of initiation by the time trigger are straightforward, and follow the discussion in Section 2.

3.2 Translational Kinematics

The translational kinematics SPRT's utilize the redundant information concerning the translational motion of the aircraft. The body mounted linear accelerometers measure the body axis components of the non-gravitational contribution to the acceleration of the aircraft with respect to inertial space. The measured velocity, \underline{v}_m , is the noisy measurement of the velocity \underline{v} of the aircraft with respect to the air mass expressed in body axes. This air-relative velocity vector is a function of Mach number M , angle of attack α , sideslip angle β , and the speed of sound V_s , which is itself a function of the altitude h :

$$\underline{V} = \begin{bmatrix} \cos \beta \cos \alpha \\ \sin \beta \\ \cos \beta \sin \alpha \end{bmatrix} V_s(h) \quad (3.1)$$

The differential equation for the air-relative velocity in body coordinates is given by

$$\dot{\underline{V}} = \frac{1}{m} \underline{F} + \underline{g} - \underline{\Omega} \underline{V} - \underline{\xi} \quad (3.2)$$

where m is the aircraft mass, \underline{F} is the aerodynamic force on the aircraft and \underline{g} is the gravity vector. The matrix $\underline{\Omega}$ is the skew-symmetric cross-product matrix:

$$\underline{\Omega} = \begin{bmatrix} 0 & -r & q \\ r & 0 & -p \\ -q & p & 0 \end{bmatrix} \quad (3.3)$$

where p , q , and r are the roll rate, pitch rate and yaw rate respectively. The vector $\underline{\xi}$ is the acceleration of the air mass with respect to inertial space. Assuming that the accelerometers are located at the same position \underline{R} relative to the center of mass, the vector \underline{A} composed of the outputs of ideal x , y and z accelerometers is related to the aerodynamic force via

$$\underline{A} = \frac{1}{m} \underline{F} + [\underline{\Omega}^2 + \dot{\underline{\Omega}}] \underline{R} \quad (3.4)$$

The compensated ideal accelerometer output vector \underline{A}' is defined as

$$\underline{A}' = \underline{A} - [\underline{\Omega}^2 + \dot{\underline{\Omega}}] \underline{R} \quad (3.5)$$

Equations (3.2), (3.4) and (3.5) yield

$$\dot{\underline{V}} = \underline{A}' + \underline{g} - \underline{\Omega} \underline{V} - \underline{\xi} \quad (3.6)$$

The translational kinematics SPRT's utilize the following discrete approximation to Eq. (3.6) to propagate the air-relative velocity estimate \underline{V} ahead one time step, where $T = (t_n - t_{n-1})$:

$$\hat{\underline{V}}'(t_n) = \hat{\underline{V}}(t_{n-1}) + (\bar{\underline{A}}'_m + \bar{\underline{C}}_m \underline{g} - \bar{\underline{\Omega}}_m \bar{\underline{V}}_m) T \quad (3.7)$$

The measured air-relative velocity is incorporated into the estimate via

$$\hat{\underline{V}}(t_n) = \hat{\underline{V}}'(t_n) + k \underline{Y}(t_n) \quad (3.8)$$

where

$$\underline{Y}(t_n) = \underline{V}_m(t_n) - \hat{\underline{V}}'(t_n) \quad (3.9)$$

The inputs to the translational kinematics SPRT's are the components of the measurement residual vector $\underline{Y}(t_n)$. In Eq. (3.7) a bar over a variable indicates that it is averaged over the interval (t_{n-1}, t_n) , an m subscript indicates a measured quantity, and the prime on $\hat{\underline{V}}'(t_n)$ indicates that it is the propagated estimate not including the present measurement. The vector $\bar{\underline{A}}'_m$ indicates the average of the compensated accelerometer outputs at t_n and t_{n-1} . The compensation equation given by Eq. (3.5) is utilized, with the $\dot{\Omega}$ terms obtained as the differences of the respective rate gyro outputs at times t_n and t_{n-1} divided by the time step, and the Ω terms being the averages of those rate gyro outputs. The local vertical vector $\bar{\underline{C}}_m$ is obtained using the average of the vertical gyro measurements of ϕ and θ over the interval:

$$\bar{\underline{C}}_m = \begin{bmatrix} -\sin \bar{\theta}_m \\ \cos \bar{\theta}_m \sin \bar{\phi}_m \\ \cos \bar{\theta}_m \cos \bar{\phi}_m \end{bmatrix} \quad (3.10)$$

The matrix $\bar{\Omega}_m$ uses the averages of the rate gyro outputs. It is also used in the accelerometer compensation equations. The vector $\bar{\underline{V}}_m$ in Eq. (3.7) likewise denotes the measured air-relative velocity based on the average of the air data sensor outputs at time t_n and t_{n-1} .

There are three important aspects of the form of Eq. (3.7):

1. The term in braces indicates an estimate of the air-relative acceleration of the aircraft at the midpoint of the propagation interval, and the resulting integration rule is good to approximately second order. This second order integration rule is used to ensure accurate filter performance during high rotation rate or acceleration maneuvers.

2. The average measured velocity is used in the right hand side of Eq. (3.7). Although the standard form of the extended Kalman filter for this system⁶ would employ the estimate $\hat{\underline{V}}$, we have chosen to use the average measured velocity derived from air data to decouple the three components of $\hat{\underline{V}}$. This decoupling allows the use of scalar SPRT's which will be discussed presently.
3. There is no term in Eq. (3.7) corresponding to the acceleration of the air mass, $\underline{\xi}$. Since the effect of a constant value of $\underline{\xi}$, i.e., wind shear, is indistinguishable from the effect of an accelerometer bias on the residual process \underline{y} , our interpretation of a nonzero component of \underline{y} must account for the possibility of wind shear. This idea will be expanded upon shortly.

Assuming that we are interested in identifying bias errors in the sensors, it is clear from Eq. (3.7) that at least three types of sensor biases will appear as acceleration errors in the propagation equation for $\dot{\underline{V}}$:

1. Accelerometer biases through $\underline{\bar{A}}'_m$
2. Vertical gyro biases through $\underline{\bar{C}}_m$
3. Rate gyro biases through $\Omega_m \underline{\bar{V}}_m$

Thus translational kinematics SPRT's are started when the failure of an accelerometer, vertical gyro or rate gyro is detected by the trigger. In order to avoid the transient effects of air data sensor noise, one set of Eq. (3.7) through (3.9) is always running to provide the initial velocity estimates for the SPRT's.* The structures of the SPRT's for all of these instrument types are analogous. Two versions of the filter given by Eq. (3.7) through (3.9) are implemented, one version using the output of the number 1 instrument of the detected failure type, plus all the necessary measurements from the other instrument types, and the other version using the same information with the exception that it uses the output of the number 2 instrument of the detected failure type. The residual process \underline{y} from the filter using a particular instrument is the input process sampled

* Good results have been obtained with k chosen to give a discrete approximation to a continuous filter with a 1/2 second time constant.

by the SPRT looking for the effect of a bias in the same instrument. The expected error in acceleration used in the SPRT varies at each sample and is obtained from Eq. (3.7) using the predefined sensor bias size and the sign of the difference between instruments 1 and 2 as given by the redundancy trigger.

In order to decrease identification times and minimize computational complexity, the translational kinematics SPRT's use a zero value for the gain k in Eq. (3.8). Thus the time-varying mean \underline{m}_k for each SPRT is simply incremented at each sample by the expected velocity error using the assumed sensor bias failure via Eq. (3.7). For the case of a constant vehicle state and a sensor bias error, the means for the two SPRT's are of opposite sign and grow in magnitude linearly with time. We note that for an accelerometer bias, the resulting velocity error shows up only in the corresponding residual component, allowing the implementation of scalar SPRT's. For rate gyro failures, the corresponding acceleration bias, arising from the $\Omega \underline{V}$ term, leads to a velocity error essentially in one component. This is exact when α and β are zero, and the unidirectional assumption is justified for reasonable angles of attack and sideslip. Hence we can also implement scalar SPRT's in this case.

Examination of Eq. (3.7) is instructive for determining the sizes of biases in the various instruments which can be identified with this technique. Recall that it is highly unlikely that a mean will be indicated by the SPRT if the actual mean present in the process is less than half the mean of the test. Thus, the sum of the acceleration errors due to the acceptable biases in all other instruments used in Eq. (3.7) must be less than half the SPRT mean for the instrument type being checked, or a false identification may be made. By carefully setting the BFM's for the various instruments in all SPRT's in a consistent manner, the problem of false identification from undetected sensor biases can be minimized. This selection process is detailed in Section 4.

The remaining factor which can contribute to false identification in the translational kinematics SPRT's is wind shear. Simulations at Mach 0.6 at 6100 m altitude with a modified Dryden wind model⁸ using a 99% sigma value of 5.5 m/sec and a correlation length of 533 m have produced wind shears of 3 m/sec² which persist for as long as 6 seconds. A simple approach to removing the effect of this

wind shear in turbulence involves limiting the SPRT gain (formerly m_k/σ^2). The parameters of the SPRT gain can be made a function of the turbulence level as reflected by the variance of the residuals in the continuously running initialization filter. In this way, the slower response due to SPRT modification can be avoided in the absence of turbulence. The implementation of this clipped SPRT gain is discussed in Section 4, while the turbulence estimator is discussed in Appendix A.

3.3 Translational Dynamics

The translational dynamics SPRT's utilize the redundant information related to the aerodynamic forces on the aircraft. The accelerometers measure these aerodynamic forces together with the lever arm forces arising from the fact that the instruments are not located at the vehicle center of mass. In particular \underline{A}' , the vector of ideal x, y, and z accelerometer outputs corrected for lever arm effects, is related to the vector of aerodynamic forces on the vehicle, \underline{F} , via

$$\underline{A}' = \frac{1}{m} \underline{F} \quad (3.11)$$

\underline{F} may be written as

$$\underline{F} = \begin{bmatrix} F_e - D \cos \alpha + L \sin \alpha \\ Y \\ - D \sin \alpha - L \cos \alpha \end{bmatrix} \quad (3.12)$$

with L the lift, D the drag, Y the sideforce and F_e the engine thrust.

If the aircraft has no flap, leading edge or speedbrake extensions, the lift, drag and sideforce are given by

$$\begin{aligned} L &= C_L \bar{q} S \\ D &= (C_D + C_{D\delta e}) \bar{q} S \\ Y &= (C_{Y\beta} \beta + C_{Y\delta r} \delta r + C_{Y\delta a} \delta a) \bar{q} S \end{aligned} \quad (3.13)$$

where the sideforce equation neglects small terms due to roll and yaw rates. In Eq. (3.13), S is the wing area, \bar{q} the dynamic pressure; and δ_r , δ_a , δ_e are the rudder, aileron and elevator positions respectively. The aerodynamic coefficients in Eq. (3.13) have been determined experimentally

and are tabulated as functions of Mach, angle of attack and elevator position. In addition, thrust has been tabulated as a function of air-relative velocity, altitude and throttle position. By utilizing these tables, or functional approximations to these tables, expected accelerometer outputs can be calculated based on the air data sensors, providing analytic redundancy.

The translational dynamics SPRT's are used to identify failures in the accelerometers, alpha vanes and Mach meters*. After detection by the redundancy trigger of an accelerometer failure the calculation of two SPRT's is begun, one for each of the accelerometers of the detected failure type. The input to each SPRT is the respective compensated accelerometer output minus the expected accelerometer output based on the air data measurements. As in the case of the translational kinematics SPRT's these calculations are made for the midpoint of the sample interval using average sensor outputs. Each SPRT mean is calculated using the predefined accelerometer BFM and the sign information from the redundancy trigger. These mean calculations are performed only when the SPRT's are started and are held constant thereafter.

For the case of an alpha vane or Mach meter detected failure, the procedure is analagous to that outlined above though somewhat more complicated. Two SPRT's are calculated, each using identical air data output, except for the detected failure type, to compute the expected lift and drag on the vehicle. Each of the two SPRT's uses a different member of the pair of instruments for which a failure has been detected to make these calculations. The expected compensated x and z accelerometer output using these two sets of air data sensors are then computed using Eq. (3.11) through (3.13). These two sets of expected compensated x and z accelerometer outputs are then used to calculate the x and z acceleration gradients with respect to the detected failure type. Then the x and z means for the two SPRT's are calculated using the computed gradients, the predefined alpha or Mach bias and the sign information from the redundancy trigger. The input to each SPRT consists of a two-dimensional vector of the expected minus the actual x and z accelerometer output. The noises in the two components of this vector are assumed to be uncorrelated with equal

* Recall, since we have only a single β -vane, we have not considered FDI for this instrument.

variance σ^2 to facilitate computation. To be specific, assume that an alpha vane failure has been detected by the redundancy trigger. Using alpha vane 1 and the other air data sensor types, expected compensated x and z accelerometer outputs $a_{x,1}$ and $a_{z,1}$ are calculated via Eq. (3.11) through (3.13), with expected outputs $a_{x,2}$ and $a_{z,2}$ calculated using alpha vane 2 and the same set of other air data. Assuming that the predefined alpha vane BFM is b_α and the sign of $(\alpha_1 - \alpha_2)$ is s_α from the redundancy trigger, the means for the SPRT using alpha vane 1 are

$$m_{x,1} = \frac{a_{x,1} - a_{x,2}}{\alpha_1 - \alpha_2} b_\alpha s_\alpha \quad (3.14)$$

$$m_{z,1} = \frac{a_{z,1} - a_{z,2}}{\alpha_1 - \alpha_2} b_\alpha s_\alpha$$

while the means for the SPRT using alpha vane 2 are

$$m_{x,2} = -m_{x,1} \quad (3.15)$$

$$m_{z,2} = -m_{z,1}$$

With the actual compensated accelerometer outputs given by A'_x and A'_z , the SPRT variable u for alpha vane 1 is incremented by

$$\Delta u_1 = \left[\left(\frac{m_{x,1}}{2} - a_{x,1} + A'_x \right) m_{x,1} + \left(\frac{m_{z,1}}{2} - a_{z,1} + A'_z \right) m_{z,1} \right] / \sigma^2$$

while the increment for the SPRT using alpha vane 2 is

$$\Delta u_2 = \left[\left(\frac{m_{x,2}}{2} - a_{x,2} + A'_x \right) m_{x,2} + \left(\frac{m_{z,2}}{2} - a_{z,2} + A'_z \right) m_{z,2} \right] / \sigma^2$$

The means given by Eq. (3.14) and (3.15) are calculated at each sample using sensor outputs averaged over the interval.

The two major sources of error in the translational dynamics SPRT's involve the aerodynamic coefficients in Eq. (3.13). One error is the difference between the functional approximations to the coefficients, used in the flight computer, and the tabulated values of the coefficients. The impact of this error source is minimized by the proper choice of fitting functions and by forcing the best fits

in the most common flight regimes. When the aircraft is flying outside the region of good fit, appropriate increases are made in the worst case bias error used to calculate the QSPRT for translational dynamics. The fitting functions for the aerodynamic coefficients, and the attendant worst-case errors, are discussed in Appendix B.

The second error source is the difference between the tabulated aerodynamic coefficients, which reflect our a priori knowledge, and the true coefficients for the aircraft. It is felt that the tabulated coefficients have the correct shape, but may be biased due to external stores, geometry differences from nominal for an individual aircraft, etc. The magnitude of any such biases and their effects on the translational dynamics SPRT's await analysis of flight test data.

3.4 Rotational Kinematics

3.4.1 Introduction

In this section, we consider failure identification for the angular sensors, the rate gyros and attitude gyros, using the kinematic relationship between the angular rate and the attitude of the aircraft.

The body mounted rate gyros provide noisy measurements p_m, q_m, r_m of the rigid body rates p, q, r about the longitudinal, lateral and normal body axes, respectively. The attitude sensors, directional and vertical gyros, provide the measurements ψ_m, θ_m, ϕ_m of the Euler angles ψ, θ, ϕ which define the orientation of the body axes with respect to the navigation frame. The order of the three rotations involved in going from the navigation frame to the body frame is yaw (ψ), pitch (θ), and roll (ϕ).

The rigid body rates p, q and r are related to the Euler angles and their rates via the relationships⁷

$$\begin{aligned} p &= \dot{\phi} - \dot{\psi} \sin \theta \\ q &= \dot{\theta} \cos \phi + \dot{\psi} \cos \theta \sin \phi \\ r &= -\dot{\theta} \sin \phi + \dot{\psi} \cos \theta \cos \phi \end{aligned} \tag{3.16}$$

The inverse relationships expressing the Euler angle rates in terms of the rigid body rates can be obtained from the above equations to yield:

$$\begin{aligned}
\dot{\phi} &= p + q \sin \phi \tan \theta + r \cos \phi \tan \theta \\
\dot{\theta} &= q \cos \phi - r \sin \phi \\
\dot{\psi} &= q \sin \phi \sec \theta + r \cos \phi \sec \theta
\end{aligned}
\tag{3.17}$$

Equations (3.17) are not convenient to use to obtain the Euler angle rates from the rigid body rates because of the singularities at $\theta = \pm \pi/2$. Alternate approaches which avoid this singularity involve the differential relationships between elements of the direction cosine matrix or attitude quaternion and the rigid body rotation rates. However, the attendant computational complexity of these approaches may be avoided for the purpose of failure identification by the following set of equations (easily derived from Eq. (3.16) and (3.17)) which also avoids the singularity:

$$\begin{aligned}
\dot{\phi} &= p + \dot{\psi} \sin \theta \\
\dot{\theta} &= q \cos \phi - r \sin \phi \\
\dot{\psi} &= (\dot{\phi} - p) \sin \theta + (q \sin \phi + r \cos \phi) \cos \theta
\end{aligned}
\tag{3.18}$$

The form of kinematic relations (3.16) and (3.18) is well suited to failure identification of the rate gyros and the attitude gyros in that the derivative of a variable is not written as a function of the variable itself.

3.4.2 Attitude Sensor Failures

Utilization of the rotational kinematics for failure identification of the attitude sensors is illustrated here by a detailed consideration of the roll attitude sensor. The other sensors can be considered in a similar fashion.

The predicted change in the roll angle over a time interval (t_{n-1}, t_n) can be obtained using a discrete approximation of Eq. (3.18)

$$\hat{\phi}'(t_n) = \hat{\phi}(t_{n-1}) + \bar{p}_m T + [\psi_m(t_n) - \psi_m(t_{n-1})] \sin \bar{\theta}_m \tag{3.19}$$

where average measurements are used as before to minimize filter errors. The comparison of the measured roll angle and the predicted roll angle $\hat{\phi}'$ yields the residual

$$\gamma_{\phi}(t_n) = \phi_m(t_n) - \hat{\phi}'(t_n) \quad (3.20)$$

The residual γ_{ϕ} is used to update the estimate $\hat{\phi}$ via

$$\hat{\phi}(t_n) = \hat{\phi}'(t_n) + k \gamma_{\phi}(t_n) \quad (3.21)$$

where k represents a suitably chosen filter gain.

Equations (3.19) through (3.21) represent the roll filter. The pitch and yaw filter equations may be similarly obtained using Eq. (3.18). As in the translational kinematics filters, these rotational filters have been simplified in form to minimize computational complexity and to limit each failure signature to a single channel. This decoupling of the roll, pitch and yaw channels is accomplished by using measurements, rather than estimates, of the Euler angles and body rates in the propagation equations (e.g., Eq. (3.19)).

As in the translational kinematics case, a conflict exists between the desire for noise suppression in normal operation and the desire for large, observable failure signatures. The conflict was resolved in that case by using a single filter with appropriate nonzero gain k to initialize, after failure detection by the trigger, the two $k=0$ filters used by the SPRT's for failure identification. A similar implementation of Eq. (3.19) through (3.21) for failure identification of the attitude sensors will now be presented.

A nonzero value of k is chosen in Eq. (3.21) to give good filter performance in the absence of failures by minimizing the effects of allowable noise on unfailed instruments*. Two versions of the equations are implemented, each using a different roll attitude sensor to give ϕ_m . Each filter stores the last N residuals γ_{ϕ} from Eq. (3.20). The signature of an attitude sensor bias in the residual decays exponentially at a rate proportional to the gain k , making it difficult to identify in the presence of noise. However, if the gain k is zero, the sensor bias failure signature is a step in the residual. This step persists in time, enhancing its identification. Therefore, at the time a roll attitude gyro failure is detected, calculations are made which effectively set $k=0$ for the two filters commencing N samples prior to the detection time. This is accomplished by using

* The same value of k as for the translational kinematics filters has given good results.

the stored $k \neq 0$ residuals via the relation

$$\gamma_{k=0}(t_n) = \gamma_{k \neq 0}(t_n) + k \sum_{\tau=t_d-N}^{t_{n-1}} \gamma_{k \neq 0}(\tau)$$

where t_d denotes the failure detection time. The $k=0$ residuals for each filter are the input to an SPRT looking for a bias in the filter's roll attitude gyro, where each SPRT mean has the predefined roll BFM and sign consistent with the output of the redundancy trigger*.

Pairs of uncoupled filters similar to Eq. (3.19) through (3.21) are implemented for the pitch and yaw attitude sensors, and failure detection and identification for these sensors are accomplished in a manner identical to that described above for the roll attitude sensors.

The primary error sources in the $k=0$ residuals given by Eq. (3.19) through (3.21) are the acceptable biases on unfailed rate gyros and the uncertainty in the orientation of the axes about which the body rates and Euler angle rates are measured. This axis uncertainty can arise from such factors as mounting errors, structural bending and attitude sensor errors. The effects of these error sources are accounted for explicitly in the QSPRT's for the rotational kinematics tests for attitude gyros.

3.4.3 Attitude Rate Sensor Failures

As was done for attitude sensor failures, failure identification for the attitude rate sensors will be illustrated by considering only one instrument, the roll rate gyro. Analogous procedures are followed for the pitch and yaw rate gyros.

The predicted roll rate $p'(t_n)$ at the midpoint of the interval (t_{n-1}, t_n) is related to the attitude sensor measurements by the discrete approximation to the first relation of Eq. (3.16):

$$p'(t_n) T = [\phi_m(t_n) - \phi_m(t_{n-1})] - [\psi_m(t_n) - \psi_m(t_{n-1})] \sin \bar{\theta}_m \quad (3.22)$$

* Note that if there are significantly more than N samples between the onset of the attitude sensor bias and its detection by the redundancy trigger, the failed instrument cannot be identified by this test. Thus it is impractical to use rotational dynamics tests following a time trigger for an attitude instrument.

and the residual between the measured motion and the predicted motion is given by

$$\tilde{\gamma}_p(t_n) = [\bar{p}_m - p'(t_n)]T \quad (3.23)$$

where again the overbar indicates a quantity averaged over the time interval. In order to minimize the effects of attitude measurement noise in the effective differentiation in Eq. (3.22), the residual γ_p is defined as

$$\gamma_p(t_n) = \sum_{\tau=t_d}^{t_n} \tilde{\gamma}_p(\tau) \quad (3.24)$$

where t_d is the time of roll rate gyro failure detection by the redundancy trigger. Since the summation operation in Eq. (3.24) follows the differencing in Eq. (3.22), the use of γ_p for failure identification removes the undesirable noise correlation in successive samples of $\tilde{\gamma}_p$. Two residual processes γ_p are formed after roll rate gyro failure detection, each one using a different roll rate gyro measurement. Each process γ_p constitutes the input to an SPRT looking for the effect of a bias failure in the corresponding roll rate gyro. The mean of each SPRT starts at zero and is incremented at each sample by a quantity whose magnitude is the predefined roll rate gyro BFM multiplied by the time step and whose sign is consistent with the output of the redundancy trigger.

The primary error source in failure identification for the attitude rate gyros via Eq. (3.22) through (3.24) and their analogues for the pitch and yaw rate gyros is Euler angle bias. This bias can arise from the acceptable biases on unfailed instruments or from axis misalignment, and its effect, which is proportional to vehicle maneuver rate, is accounted for in the appropriate QSPRT.

3.5 Altitude Kinematics

The altitude kinematics SPRT utilizes the differential relationship

$$\ddot{h} = a_v$$

where h is the altitude and a_v the inertial vertical acceleration of the aircraft. The vertical acceleration can be estimated using the relationship

$$\begin{aligned} a_{v,m} = & a_{x,m} \sin \theta_m - a_{y,m} \sin \phi_m \cos \theta_m \\ & - a_{z,m} \cos \phi_m \cos \theta_m - g \end{aligned} \quad (3.25)$$

where $a_{x,m}$, $a_{y,m}$ and $a_{z,m}$ represent the lever arm compensated outputs of the body mounted accelerometers and ϕ_m and θ_m are the outputs of the roll and pitch attitude gyros, respectively.

From Eq. (3.25), it may be noted that the error in the derived acceleration, $a_{v,m}$, due to a bias in one of the accelerometers depends upon the orientation of the accelerometer input axis with respect to the vertical, whereas the effect of a bias in the pitch or roll attitude gyros depends upon the orientation of the vehicle as well as the magnitude of the vehicle acceleration components. Thus, the altitude kinematics relationship is normally suited for FDI for the altimeter and normal accelerometer. The relationship is unsuitable for FDI for the remaining instruments, x and y accelerometers and the roll and pitch attitude gyros, except during maneuvers involving large attitude excursions and accelerations.

As in the case of other kinematic SPRT's considered earlier, the modes of processing the altimeter outputs and the derived vertical acceleration are different during the times of normal operation and when the fault isolation of one of the failed instruments is needed.

During the normal operation, the measurements are processed by two non-zero gain ($k \neq 0$) filters for the estimates \hat{h}^i and \hat{v}^i , $i=1,2$, as follows:

$$\hat{h}^i(t_{n+1}) = \hat{h}^i(t_n) + \hat{v}^i(t_n)T + \bar{a}_{v,m} T^2/2 + k_1 \gamma^i(t_{n+1}) \quad (3.26)$$

$$\hat{v}^i(t_{n+1}) = \hat{v}^i(t_n) + \bar{a}_{v,m} T + k_2 \gamma^i(t_{n+1}) \quad (3.27)$$

where the residual $\gamma^i(t_{n+1})$ and the average vertical acceleration $\bar{a}_{v,m}$ are defined as

$$\gamma^i(t_{n+1}) = h_m^i(t_{n+1}) - (\hat{h}^i(t_n) + \hat{v}^i(t_n)T + \bar{a}_{v,m}T^2/2) \quad (3.28)$$

$$\bar{a}_{v,m} = \frac{1}{4} \sum_{i=1}^2 \{a_{v,m}^i(t_n) + a_{v,m}^i(t_{n+1})\} \quad (3.29)$$

In Eq. (3.28) and (3.29), h_m^i represents the i^{th} altimeter output, and $a_{v,m}^i$ represents the vertical acceleration derived using the i^{th} set of accelerometers and the attitude gyros. The gain k_1 is selected to be equal to $\sqrt{2k_2T}$, based on the optimal Kalman filter for a double integral plant with T the sample period*. The selection of the value of the other gain k_2 , which determines the bandwidth of the filter, is based on considerations discussed in detail in Appendix E.

At the time of failure detection, the effect of the failure on the filter residuals is enhanced effectively by starting two zero-gain ($k=0$) filters (one for each instrument) with initialization being provided by the $k \neq 0$ filters. The considerations in the mechanics of initialization are different in the case of altimeters versus the accelerometers and the attitude gyros, as discussed below.

In the case of altimeters, the two $k=0$ filters are started N samples prior to the time of failure detection for reasons similar to those for attitude sensor failure isolation using the rotational kinematics SPRT. This is effectively accomplished by storing the last N samples of the $k \neq 0$ filter residuals and calculating the residuals for the two $k=0$ filters as follows:

$$\gamma_{k=0}^i(t_{n+1}) = \gamma_{k \neq 0}^i(t_{n+1}) + \epsilon_h^i(t_n) + \epsilon_v^i(t_n)T \quad (3.30)$$

$$\epsilon_h^i(t_{n+1}) = \epsilon_h^i(t_n) + \epsilon_v^i(t_n)T + k_1 \gamma_{k \neq 0}^i(t_{n+1}) \quad (3.31)$$

$$\epsilon_v^i(t_{n+1}) = \epsilon_v^i(t_n) + k_2 \gamma_{k \neq 0}^i(t_{n+1}) \quad (3.32)$$

where $i=1,2$. In Eq. (3.30) through (3.32), ϵ_h^i and ϵ_v^i represent respectively the differences between the i^{th} $k \neq 0$ and $k=0$ filter altitude and velocity estimates. The computations of $\gamma_{k=0}^i$ residuals are started at t_{d-N} , N samples prior to the detection of a failure at time t_d with initial conditions

* This value of gain for the optimal filter gives a filter damping ratio of .707

$$\varepsilon_h^i(t_{d-N}) = \varepsilon_v^i(t_{d-N}) = 0 \quad (3.33)$$

In the case of accelerometers and attitude gyros, the two $k=0$ filters are started at the time of failure detection. The filter equations are as follows

$$\hat{h}_{k=0}^i(t_{n+1}) = \hat{h}_{k=0}^i(t_n) + \hat{v}_{k=0}^i(t_n)T + \{\bar{a}_{v,m}^i(t_{n+1}) + \bar{a}_{v,m}^i(t_n)\}T^2/4 \quad (3.34)$$

$$\hat{v}_{k=0}^i(t_{n+1}) = \hat{v}_{k=0}^i(t_n) + \frac{1}{2} \{\bar{a}_{v,m}^i(t_{n+1}) + \bar{a}_{v,m}^i(t_n)\}T \quad (3.35)$$

$$\hat{v}_{k=0}^i(t_{n+1}) = \frac{1}{2} \{\hat{h}_m^1(t_{n+1}) + \hat{h}_m^2(t_{n+1})\} - \hat{h}_{k=0}^i(t_{n+1}) \quad (3.36)$$

with initial conditions given by

$$\hat{h}_{k=0}^i(t_d) = \frac{1}{2} \sum_{j=1}^2 \hat{h}^j(t_d) \quad (3.37)$$

$$\hat{v}_{k=0}^i(t_d) = \frac{1}{2} \sum_{j=1}^2 \hat{v}^j(t_d) \quad (3.38)$$

In Eq. (3.35), $\bar{a}_{v,m}^i$ represents the derived vertical acceleration using the i^{th} sensor of the failed pair of instruments and the average of the pairs of unfailed instruments.

The $k=0$ residuals for each filter are input to an SPRT looking for the effects of a bias failure in the particular sensor of the failed pair used in the filter. The SPRT mean is defined as the signature in the residual of a sensor bias with magnitude equal to the predefined value and sign consistent with the output of the redundancy trigger.

The primary noise sources in the $k=0$ filter residuals are

1. The error in the initialization of the velocity estimate of the filter (see Eq. (3.38)).
2. The presence of acceptable biases on the unfailed instruments used in the filter.

Choice of an appropriate bandwidth for the $k \neq 0$ filters is required to keep small the effect of the altimeter noise and the instrument

bias on the initial velocity estimates. For example, decreasing the bandwidth of the filter (i.e., smaller gains) leads to reduced errors in the velocity estimate due to altimeter noise but leads to increased errors due to the effect of biases in the accelerometers and the attitude gyros. The trade-off choice of the filter gains can be based on the knowledge of the altimeter noise statistics and the magnitude of the allowable biases in the unfailed instruments. Thus far, a choice of k_2 numerically equal to the gain used in the translational and rotational kinematics filters has worked well.

SECTION 4

CALCULATION OF FDI SYSTEM PARAMETERS

4.1 Introduction

As we have seen, each instrument type enters into the calculations for several SPRT's, either as the suspect instrument being examined for possible failure or as one of the other instruments being used in the SPRT (or QSPRT) calculations. Thus, the BFM's for the various instruments are all interrelated, and their calculations must be considered together. Additionally, although the theory indicates that the various SPRT's will eventually reach a decision by crossing a threshold, it is clearly undesirable to allow the running time of these tests to be unbounded, and each analytic redundancy SPRT must have associated with it an elapsed time limit (ETL). In this section we describe a methodology whereby a consistent set of BFM's and ETL's are calculated for the various dual-redundant sensors aboard the aircraft. This methodology is conservative, as we have chosen to design the system to work under "worst-case" conditions. We will consider the various instrument types one or two at a time, indicating the various worst-case assumptions and any tradeoffs that may arise. The underlying philosophy of our approach will become clear to the reader as he examines these calculations. We note here that when the BFM and ETL calculations depend upon the aircraft state, trim conditions at Mach=0.6 and h=6100 m are used. The full state-dependent terms are used in the calculation of the QSPRT's, however, as discussed in Section 5.

4.2 Rate Gyros

4.2.1 Roll, p

Recall the defining equations for the roll rate gyro translational kinematics SPRT given by Eq. (3.22) through (3.24), where we set

$$T \equiv (t_n - t_{n-1}) = .0625 \text{ sec}$$

and for simplicity we define the detection time to be zero.

Examining these equations, we make the following observations:

1. If a bias failure of magnitude B develops in p_m , the effect on the residual $\gamma_p(t_j)$ is BjT . Thus, it follows from Eq. (2.4) that if the BFM of p is B, the SPRT output is of the form

$$u_n = \sum_{j=0}^n \frac{BjT}{\sigma^2} \left[\frac{BjT}{2} - \gamma_p(t_j) \right] \quad (4.1)$$

2. To determine σ , we note that $\gamma_p(t_n)$ is essentially

$$\int_0^{t_n} p_m(t) dt = \phi_m(t_n) + \phi_m(0) + \int_0^{t_n} \dot{\phi}_m(t) \sin \bar{\theta}_m(t) dt$$

Physical constraints limit the size of $\dot{\phi}$, and thus the dominant noise in this residual comes from the measurements of ϕ . Thus we set σ^2 equal to twice the variance in our measurement of ϕ , or from Table I

$$\sigma^2 = 0.0002 \text{ rad}^2$$

3. We now want to take into account any unmodeled effects that might cause difficulties in the test. Examining the form of γ , we see that we can regard $\phi(0)$ as an initialization for the integration of p to yield the present value of ϕ . Thus, any initialization error in $\phi(0)$ will bias the test, and we assume a worst case bias on γ of twice the standard deviation of the measurement of ϕ

$$b = 0.02 \text{ rad}$$

4. We choose a value for the BFM equal to twice the RSS unfailed bias in the roll rate gyro

$$B = 0.02 \text{ rad/sec}$$

5. We now note that conditioned on the presence of a failure of BFM size and of a worst case initialization bias in the direction opposite to the failure (making the failure more difficult to identify), we have

$$E[u_n] = \sum_{j=0}^n \frac{BjT}{\sigma^2} \left[-\frac{BjT}{2} + b \right] = -\frac{B^2 t_n^3}{6\sigma^2 T} + \frac{Bbt_n^2}{2\sigma^2 T} \quad (4.2)$$

where we have approximated the summations by integrals. We note that as a function of t_n , $E[u_n]$ is first driven in the positive direction by the initialization bias (leading to the possibility of a missed detection) but that subsequently the failure term dominates, driving the expectation toward the negative threshold. Using thresholds of magnitude 9.2, corresponding to false alarm and missed alarm probabilities of 0.0001^5 , we have the following equation for the time T_c at which the negative threshold is crossed by $E[u_n]$

$$\frac{B^2 T_c^3}{6\sigma^2 T} - \frac{BbT_c^2}{2\sigma^2 T} - 9.2 = 0$$

Using the parameters given earlier, we find

$$T_c = 3.2 \text{ sec}$$

6. From the form of the SPRT in Eq. (4.1), we see that for any failure of size larger than $B/2$, $E[u_n]$ will eventually go negative. As we have seen, we need about 3.2 seconds to detect a failure of size $B=0.02$, and clearly this time will increase as we decrease the size of the actual failure. On the other hand, the size of the failure we can detect for p will impact our ability to detect ϕ failures, since we must use the p sensors in the SPRT for ϕ . We have adopted the following philosophy: in all SPRT's, the measured values for all variables other than the suspect instrument

type will be obtained by averaging the values from the two instruments of the given type. In computing the design parameters for this test we will assume an undetected bias in the measured values for the unfailed instruments to be $1/2$ the corresponding BFM. Considering this undetected bias to be the RSS of the biases in the two instruments being averaged, we see that we need to be able to detect a bias on the order of $\text{BFM}/\sqrt{2}$.

Returning to Eq. (4.1), let us assume that γ includes the effect of a $B/\sqrt{2}$ failure (note that the SPRT is still "looking" for a size B failure). Then, assuming a worst case initialization error, we find that

$$E[u_n] = - \frac{(\sqrt{2} - 1)B^2 t_n^3}{6\sigma^2 T} + \frac{Bbt_n^2}{2\sigma^2 T}$$

Let us define T_m to be the time at which this quantity crosses the failure threshold. Then equating the above expression to -9.2 yields

$$\frac{(\sqrt{2} - 1)B^2 T_m^3}{6\sigma^2 T} - \frac{Bb T_m^2}{2\sigma^2 T} - 9.2 = 0 \quad (4.3)$$

and solving gives

$$T_m = 7.3 \text{ sec}$$

If we adopt the philosophy of setting the ETL for any test at $1.5 T_m$, we then have

$$\text{ETL} = 11 \text{ sec}$$

4.2.2 Pitch, q, and Yaw, r

Since the analyses for these two instruments are identical, we shall limit the details of the discussion to q. We use the relationship from Eq. (3.16)

$$q = \dot{\theta} \cos \phi + \dot{\psi} \cos \theta \sin \phi$$

We note that the residual for the SPRT for q is essentially the difference between the integrals of the left- and right-hand sides

of the above equation. Thus we again get a ramp in the residual for a bias failure in q , and Eq. (4.1) describes the form of the SPRT output. As in the case of p , we disregard the effect of $\dot{\psi}$ in determining sources of uncertainty in the residual, and, again following the argument for p , we set σ^2 equal to twice the variance in the measurement of θ

$$\sigma^2 = 0.0002 \text{ rad}^2$$

The worst case initialization bias for the test is again taken as twice the standard deviation of the angle measurement, in this case θ :

$$b = .02 \text{ rad}$$

Finally, we choose a value for BFM of twice the RSS unfailed bias in the yaw rate gyro

$$B = .006 \text{ rad/sec}$$

Now we note that Eq. (4.2) and (4.3) hold for this analysis, and, substituting the above numbers we obtain

$$\begin{aligned} T_c &= 10.2 \text{ sec} \\ T_m &= 24.2 \text{ sec} \\ \text{ETL} &= 36 \text{ sec} \end{aligned}$$

Again, we note that these numbers also apply to the yaw rate gyro.

4.3 Attitude Gyros

4.3.1 Introduction

Recall our method for identifying attitude gyro failures using rotational kinematics. We utilize Eq. (3.18) to design two filters to estimate each of the angles ϕ , θ , and ψ . For prediction update, we utilize Eq. (3.18) with all terms on the right-hand side computed using the average of the two sensor outputs of each type (illustrated in Eq. (3.19) only for ϕ for convenience). At measurements we update our estimate via Eq. (3.20) and (3.21). In Eq. (3.20) we utilize the two suspect ϕ sensors separately — one for each of the two filters — in order to isolate the effect of the failed instrument in one and only one or the two filter residuals.

Recall that we store a window of the most recent residuals, and when a failure is detected by the redundancy trigger we manipulate the stored residuals to determine the corresponding residuals for the $k=0$ filter. These residuals, which arise as the difference between ϕ_m and straight integration of the right-hand sides of Eq. (3.18) from the initial estimate at the beginning of the window, are the inputs to the attitude gyro rotational kinematics SPRT's. Let us make several general observations:

1. The effect on the corresponding residual of an attitude gyro bias failure is a bias of the same magnitude. Thus the form of all of the attitude gyro rotational kinematics SPRT outputs is

$$u_n = \sum_{j=0}^n \frac{B}{\sigma^2} \left[\frac{B}{2} - \gamma(t_j) \right] \quad (4.4)$$

2. The value of σ^2 is taken as the variance of the sensor noise in the corresponding attitude gyro. In our case these variances are all the same:

$$\sigma^2 = 0.0001 \text{ rad}^2$$

3. One important error source is initialization errors in starting the $k=0$ filters. These enter the residuals in a manner identical to the failure, and effectively decrease the failure which we see. There are two sources for this initialization error: an angle bias due to a BFM/2 bias in the measured value of rate, and a noise component. Since we use the $k \neq 0$ filter for initialization, the angle noise on this estimate is smaller than the raw measurement noise. In particular, we assume that the gain k and the measurement noise variance are given and we postulate a process noise variance which makes the gain optimal. Thus at steady state, the variance of the estimate is equal to the gain times the variance of the raw angle measurements. For our choice of gain, $k = \frac{1}{8}$, it follows that σ_0 , the standard deviation of the initial estimate, is given by

$$\sigma_0 = .0036 \text{ rad}$$

The bias in the initial angle estimate due to a bias in rate measurement of b is given by

$$b_o = \frac{bT}{k}$$

Since the gain is chosen to be

$$k = \frac{T}{\tau}$$

the initial estimate bias becomes

$$b_o = b\tau$$

where τ is the stipulated time constant of the filter. Now, we assume measured rate biases of BFM/2, and for our choice of a 0.5 sec filter time constant, we have

$$b_o = \text{BFM}/4$$

where the BFM is for the appropriate rate instrument. Assuming the worst case effect to be the sum of this bias plus twice the filter estimate standard deviation, we obtain worst case initialization errors of

$$M_\phi = 0.012 \text{ rad} \tag{4.5}$$

$$M_\theta = M_\psi = 0.008 \text{ rad}$$

As an aside, we note from Eq. (4.5) that the choice of angle initialization errors of 0.02 rad for the calculation of the rate gyro ETL's is overly conservative, resulting in somewhat larger rate gyro ETL's than necessary.

4. A second fundamental unmodeled effect that can create difficulties in the test arises from the integration of the right-hand sides of Eq. (3.18). Biases in p_m , q_m , or r_m , will produce ramps in the corresponding residuals. We note here that this correspondence holds precisely only in the $\theta=\phi=0$ case. Since these calculations are to determine parameter values we will assume this case for simplicity. During on-line operation variations in θ and ϕ will be

taken into account by the QSPRT. Also, as discussed in Section 4.2.1, we will assume that the worst-case measured rate biases are half the corresponding BFM's.

To compute the effect of the ramp on the SPRT, we must specify the SPRT somewhat more precisely. We assume the following structure: given the mean time τ_m for the trigger to detect a failure of size BFM (we discuss the calculation of τ_m below), we take the residual window to be of length $4\tau_m/3$. Also, we start the SPRT calculations τ_m into the window. Thus the effect of a rate gyro bias of size b on the residual j time steps following initiation of the SPRT is

$$b[jT + \tau_m/3]$$

where the $\tau_m/3$ term is due to the effect of the ramp over the first quarter of the window.

5. Given these worst-case effects and assuming a bias failure of size B , we can compute from Eq. (4.4)

$$\begin{aligned} E[u_n] &= \sum_{j=1}^n \frac{B}{\sigma^2} \left[\frac{B}{2} - B + M + bjT + b\tau_m/3 \right] \\ &\approx - \frac{B(B-2M)t_n}{2\sigma^2 T} + \frac{Bbt_n^2}{2\sigma^2 T} + \frac{Bb\tau_m t_n}{3\sigma^2 T} \end{aligned} \quad (4.6)$$

6. In order to calculate τ_m , we must be more explicit about the direct redundancy trigger. Each instrument type has associated with it a moving window of instrument output differences N samples long, where N may be different for each instrument type. A failure is detected if the average of these N instrument output differences exceeds a threshold of

$$\frac{BFM}{2} + \epsilon$$

The sample variance of the moving window average, σ_s^2 , is given by

$$\sigma_s^2 = \frac{2v}{N}$$

assuming uncorrelated noise on the individual sensor outputs of variance v . In order to define ϵ , we stipulate equal miss alarm and false alarm* probabilities of 10^{-4} . This requires that

$$\epsilon = 3.65 \sigma_s = \frac{BFM}{4} \quad (4.7)$$

with a resulting threshold of .75 BFM. This results in a mean time to detect of .75 NT, which using the above equations may be written

$$\tau_m = \frac{320 v}{B^2} T \quad (4.8)$$

7. With this expression for τ_m and the given values for σ^2 and T , we obtain the following equation for the time at which $E[u_n]$ crosses the failure threshold

$$(8 \times 10^4) b B T_c^2 + \left[\frac{107b}{B} - (8 \times 10^4) B(B-2M) \right] T_c + 9.2 = 0 \quad (4.9)$$

We note that this is a quadratic and hence has two solutions. Examining Eq. (4.6) we see that for a short time the first term dominates, driving $E[u_n]$ negative, but eventually the quadratic term dominates, making the expectation positive. This is not surprising, since initially we expect the step failure to be larger than the ramp due to possible rate gyro biases, but eventually the ramp will dominate. Consequently, we expect there to be a minimum size of B for which $E[u_n]$ will reach the negative threshold, and that for any $B > B_{min}$ there will be two values of T_c - the smaller corresponding to the time at which $E[u_n]$ first reaches the negative threshold, and the larger corresponding to the time it crosses the threshold as it approaches the positive threshold. Thus, we will want to choose ETL somewhere between these two

*Recall from Section 2.2 that a false alarm is the detection of the presence of any bias smaller in magnitude than $BFM/2$.

numbers. Examining Eq. (4.9), we see that B_{\min} can be calculated by determining the value of B for which the two solutions are identical.

4.3.2 Bank Angle, ϕ

In this case, we use the fact that the BFM for p is .02 rad/sec to set

$$b = .01 \text{ rad/sec}$$

From Eq. (4.5) we have

$$M = 0.012 \text{ rad}$$

Examination of Eq. (4.9) with these parameter values indicates a minimum value of B between 0.04 and 0.05 rad. We choose the roll attitude gyro BFM of

$$B = 0.06 \text{ rad}$$

Substituting this value into Eq. (4.9) gives

$$T_c = 0.05, 3.93 \text{ sec}$$

Since ETL must be between these two values of T_c , we choose

$$ETL = 2 \text{ sec}$$

Substitution of the BFM size into Eq. (4.7) gives a mean detection time of

$$\tau_m = .56 \text{ sec}$$

4.3.3 Pitch Angle, θ , and Yaw Angle, ψ

Since the BFM's for q and r are 0.006, we set

$$b = 0.003 \text{ rad/sec}$$

From Eq. (4.5) we have

$$M = 0.008 \text{ rad}$$

Examination of Eq. (4.9) with these parameter values indicates a minimum value of B between 0.025 and 0.03 rad. We choose pitch and yaw attitude gyro BFM's of

$$B = 0.055 \text{ rad}$$

Substituting this BFM value into Eq. (4.9) gives

$$T_c = 0.06, 12.5 \text{ sec}$$

and we choose the elapsed time limit as

$$ETL = 3 \text{ sec}$$

Substitution of the BFM size into Eq. (4.8) gives a mean detection time of

$$\tau_m = 0.66 \text{ sec}$$

4.4 Accelerometers

4.4.1 Introduction

In this section, we determine the accelerometer biases and ETL's to be used by the translational kinematics SPRT's. In a later section, we will discuss the additional analytic redundancy tests which may be used for the accelerometers, and the corresponding biases and ETL's for these tests. In general, the biases being looked for in these various tests will be different, reflecting the different capabilities of the tests. For the purpose of calculating unmodeled effects in SPRT's for other instrument types due to biases in the accelerometers, we will use $\text{BFM}/2$ as the undetected accelerometer bias, where BFM is the smallest of the biases being looked for by the SPRT's for the accelerometers.

Recall that the basic equation for the translational kinematics SPRT's is Eq. (3.6). For each accelerometer the residual used in the SPRT consists of the measured velocity component in the corresponding direction minus the integrated velocity component as computed from Eq. (3.6).

We make the following observations:

1. The effect on the residual of an accelerometer bias is a ramp. This suggests an SPRT structure of the form

$$u_n = \sum_{j=1}^n \frac{B_j T}{\sigma^2} \left(\frac{B_j T}{2} - v(t_j) \right) \quad (4.10)$$

2. The first important unmodeled effect is due to bias in the measured values of q and r^* . Let us assume we are flying at Mach=.6 at 6.1 km and that the velocity is essentially along the x direction. Then rate gyro biases cause no errors in the V_x channel, the r bias causes a ramp error in the V_y residual, while a q bias leads to a ramp in the V_z residual. For worst case analysis we assume possible r and q biases of BFM/2, corresponding to an acceleration bias of 0.55 m/sec in the y and z channels.
3. One important error source in the translational kinematics tests is the wind term $\underline{\xi}$. There are two aspects to this problem. First, we can encounter different levels of turbulence and must use appropriate values of σ^2 in the SPRT's. Second, the wind acceleration may have low frequency components, i.e., wind shears, that mimic the effects of accelerometer failures in the residuals for several seconds. In order to avoid false identification due to this last effect, we slow the translational kinematics SPRT's down substantially, thus filtering out this low frequency effect. This will be discussed in detail shortly.
4. We may have errors in the initial velocity estimates due to two sources: biases in the accelerometers and rate gyros and white estimation error. Since the filter gains in this

* p enters into the Coriolis term in a small way and is neglected in this analysis.

case are identical to the gains for the rotational kinematics filters, the same analysis holds as in Section 4.3.1, i.e., the bias in initial velocity is half the total acceleration bias, and the variance in the estimate is one-eighth the variance in measured velocity. We assume BFM values of 1.5 m/sec^2 for the longitudinal and normal accelerometers and 2 m/sec^2 for the lateral accelerometers. By using the RSS of the effects of the accelerometer biases and rate gyro biases, we obtain initial velocity estimate biases of 0.37 m/sec in V_x , 0.67 m/sec in V_y and 0.59 m/sec in V_z . Now, noise in the estimate of V_x is essentially due to Mach meter noise with a variance of $9.3 \text{ m}^2/\text{sec}^2$, giving a standard deviation of the estimate of V_x of 1.1 m/sec . The noises in V_y and V_z are due to the noises in the beta and alpha vanes respectively, with variances of $3.3 \text{ m}^2/\text{sec}^2$. Thus the standard deviations of the estimates of V_y and V_z are 0.64 m/sec . Assuming the worst case error in the initial velocity estimate to be the sum of the bias and twice the standard deviation, we have the following initial velocity estimation errors*:

$$\begin{aligned} M_x &= 2.6 \text{ m/sec} \\ M_y &= 2.0 \text{ m/sec} \\ M_z &= 1.9 \text{ m/sec} \end{aligned} \tag{4.11}$$

Given this background, we will develop the translational kinematics SPRT's for the individual accelerometer types.

4.4.2 Longitudinal Accelerometer, A_x

As described in Appendix A, we have designed a turbulence estimator to make a binary decision: "low turbulence" or "high turbulence". Let us assume first that we are in the low turbulence case. In this case, σ^2 is dominated by Mach meter errors and we take

* Note that biases in the air data sensors do not concern us, since the initial velocity estimate will follow these biases, and this bias will drop out in the difference between the velocity calculated using air data and the velocity calculated as the integral of the accelerometer output plus the initial estimate.

$$\sigma^2 = 9.3 \text{ m}^2/\text{sec}^2$$

In addition, as our model of a worst-case low turbulence shear, we have chosen a velocity profile given by

$$S(t) = \begin{cases} (1.5 t) \text{ m/sec} & , 0 \leq t \leq 6 \text{ sec} \\ (9 - 1.5(t-6)) \text{ m/sec} & , 6 \text{ sec} \leq t \leq 12 \text{ sec} \\ 0 & t > 12 \text{ sec} \end{cases} \quad (4.12)$$

The shape of the wind velocity due to this shear is shown in Figure 4-1.

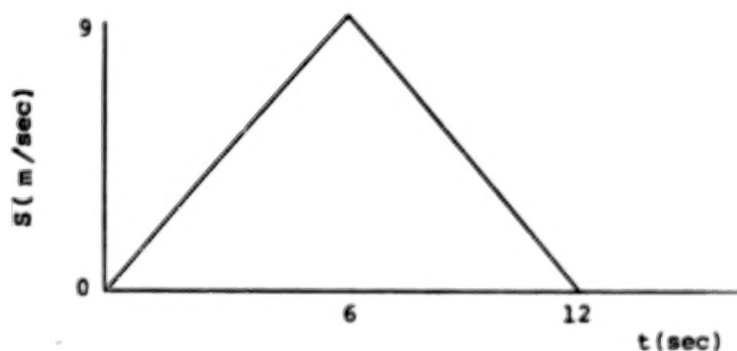


Figure 4-1 Low Turbulence Wind Profile

Finally, examining the proposed SPRT as given by Eq. (4.10), we see that the gain grows linearly with time. In some initial tests we observed that this gain became sufficiently large so that a shear such as that given by Eq. (4.12) could lead to the identification of the wrong accelerometer as failed. Thus, we have modified the SPRT by clipping the gain:

$$u_n = \sum_{j=1}^n \frac{Bf(t_j)}{\sigma^2} \left(\frac{B_j T}{2} - \gamma(t_j) \right) \quad (4.13)$$

where

$$f(t_j) = \min(t_j, T_0)$$

and the time T_0 is to be determined so that in the worst-case shear with no other error sources the expectation of $u(t_n)$ will just touch (but not exceed) the failure threshold when there is no failure.

From Eq. (4.13) we calculate

$$\begin{aligned} E[u_n] &= \sum_{j=1}^n \frac{Bf(t_j)}{\sigma^2} \left(\frac{BjT}{2} - S(t_j) \right) \\ &\approx \int_0^{t_n} \left[\frac{B^2 f(t)t}{2\sigma^2 T} - \frac{Bf(t)S(t)}{\sigma^2 T} \right] dt \end{aligned} \quad (4.14)$$

We now set

$$B = 1.5 \text{ m/sec}^2$$

for a_x and note that the maximum value of $E[u_n]$ occurs when

$$\frac{BT^*}{2} = S(T^*)$$

Solving, we find

$$T^* = 8.1 \text{ sec}$$

Using the parameter values established so far, we choose T_0 so that

$$E[u^*] = -9.2$$

This leads to

$$T_0 = 0.2 \text{ sec}$$

Now, we assume a $B/\sqrt{2}$ failure, worst-case low turbulence shear, and worst-case velocity initialization error. The expected value of the SPRT output in that case is given by

$$E[u_n] = \int_0^{t_n} \left[-\frac{(\sqrt{2}-1)B^2 f(t)t}{2\sigma^2 T} + \frac{Bf(t)S(t)}{\sigma^2 T} + \frac{MBf(t)}{\sigma^2 T} \right] dt \quad (4.15)$$

Substituting our parameter values into Eq. (4.15) and solving gives

$$T_m = 33.3 \text{ sec}$$

and therefore we choose

$$ETL = 50 \text{ sec}$$

Now let us consider the high turbulence case. In this case the worst-case shear is taken to be twice the shear given in Eq. (4.12), and we wish to modify the SPRT to accommodate this shear. Specifically, we wish to leave T_0 fixed at 0.2 sec and increase σ^2 so that the most negative value of $E[u_n]$ is exactly -9.2. In this case, the most negative value of $E[u_n]$ occurs at \tilde{T} , where

$$\frac{BT}{2} = 2S(\tilde{T})$$

Solving, we find

$$\tilde{T} = 9.68 \text{ sec}$$

and the new value of σ^2 is

$$\sigma^2 = 33 \text{ m}^2/\text{sec}^2$$

Now, again assuming an accelerometer bias of $B/\sqrt{2}$, worst-case high turbulence shear and worst case initial velocity error, we solve Eq. (4.15) with the new parameters to obtain

$$T_m = 44.5 \text{ sec}$$

and we choose for this high turbulence case

$$ETL = 67 \text{ sec}$$

4.4.3 Lateral and Normal Accelerometers, A_y and A_z

For these cases, we must consider the unmodeled effects due to possible rate gyro biases. This bias can cause ramp effects in the residuals of the form bt , with $b=0.55 \text{ m/sec}^2$. We proceed in the analysis as follows.

First, because of this rate gyro bias effect, we must look for larger bias failures. Specifically, we choose

$$B = 2 \text{ m/sec}^2$$

Again, we must clip the SPRT gain and we follow an analogous approach to that used in the a_x case. That is, we assume no failure and a worst case shear, but no gyro bias effect (since when RSS'd with the shear the contribution of such a bias is quite small). Given these conditions, we want $E[u_n]$ to touch but not exceed the failure threshold. Thus, we can use Eq. (4.14), and evaluate T^* , the point at which the expectation reaches a minimum. Again, this occurs when

$$\frac{BT^*}{2} = S(T^*)$$

and using $B=2 \text{ m/sec}^2$ we obtain

$$T^* = 7.3 \text{ sec}$$

and solving for the time T_0 at which the gain is clipped we find again

$$T_0 = 0.2 \text{ sec}$$

Now with $\sigma^2=9.3$, we calculate the time to cross the failure threshold assuming a failure of size B , worst-case shear in low turbulence, worst-case initialization error and worst-case gyro bias. The expectation becomes

$$E[u_n] = \int_0^{t_n} \left[\frac{-B^2 f(t)t}{2\sigma^2 T} + \frac{Bf(t)S(t)}{\sigma^2 T} + \frac{MBf(t)}{\sigma^2 T} + \frac{Bbf(t)t}{\sigma^2 T} \right] dt$$

Using $M=2.4$ from Eq. (4.11) and the other relevant parameters, we find

$$T_c = 24.4 \text{ sec}$$

We note that because of the worst-case rate gyro bias, we cannot identify a failure of $B/\sqrt{2}$. Thus, we limit ourselves to identifying failures of size B and choose

$$ETL = 37 \text{ sec}$$

Finally, we consider the high turbulence case. Following the same approach as in the longitudinal accelerometer, we increase σ^2 to $47 \text{ m}^2/\text{sec}^2$ and obtain

$$T_c = 35.1 \text{ sec}$$

$$ETL = 53 \text{ sec}$$

4.5 Altimeters

For the altimeters we have only one form of analytic redundancy, altitude kinematics, based on the relationship

$$\ddot{h} = a_x \sin \theta - a_y \sin \phi \cos \theta - a_z \cos \phi \cos \theta - g \quad (4.16)$$

We implement one filter based on Eq. (4.16) for each altimeter measurement and store a window of residuals. Once the redundancy trigger detects a failure, we use these residuals to determine the residuals for a $k=0$ filter (straight integration of Eq. (4.16), starting at the beginning of the window). These residuals form the input to the SPRT's. We note the following:

1. The effect of an altimeter bias failure on these residuals is a bias of the same size, assuming the failure occurs in the window.
2. In the same way we performed the calculation for the attitude gyros, we determine a relationship between the mean time τ_m for trigger detection and the BFM size B :

$$\tau_m = \frac{320\sigma^2}{B^2} T$$

where σ^2 is the altimeter noise variance. As in the attitude gyro case, we set the window size at $4\tau_m/3$ and start the SPRT calculations τ_m into the window.

3. The major unmodeled effects are in the open loop integration of Eq. (4.16). Any error in our initial condition on \dot{h} will lead to a ramp in the residual, while (assuming level flight) any undetected normal accelerometer measurement bias b (up to $B/2$) will lead to an error in the residual quadratic with time. For our choice of gains, this velocity error will be numerically equal to the normal acceleration

bias. We define the total velocity error, due to accelerometer bias and measurement noise, e , to be

$$e = 1.37 \text{ m/sec}^*$$

4. Initial altitude error is dominated by the altimeter quantization size, and we define this initial altitude error, M , to be one quantum size

$$M = 3.4 \text{ m}$$

Now, assuming a failure of size B and the worst-case unmodeled effect, the expected value of the SPRT output is given by

$$E[u_n] = \sum_{j=1}^n \frac{B}{\sigma^2} \left[M - \frac{B}{2} + eT(j+q) + \frac{bT^2}{2} (j+q)^2 \right]$$

where

$$q = \frac{107 \sigma^2}{B^2}$$

The above expression may be approximated by the integral

$$E[u_n] \approx \frac{B}{T\sigma^2} \int_0^t \left[M - \frac{B}{2} + \frac{b(qT)^2}{2} + eqT + (e+bqT)t + \frac{bt^2}{2} \right] dt \quad (4.17)$$

Using the values of e and M given above, and the additional values

$$\sigma^2 = 9.3 \text{ m}^2$$

$$B = 30 \text{ m}$$

$$b = .75 \text{ m/sec}^2$$

Eq. (4.17) gives the following times at which $E[u_n]$ crosses the failure threshold

$$T_c = .016, 2.65 \text{ sec}$$

As in the case of rotational kinematics for the attitude gyros, the expectation crosses the threshold twice, first when the altitude bias term dominates and later as the velocity and acceleration biases

* See Appendix E for a discussion of the altitude filters

dominate, driving the expectation positive. Based on the above calculations, we choose for the altimeter

$$B = 30 \text{ m}$$

$$ETL = 2 \text{ sec}$$

4.6 Alpha Vanes and Mach Meters

Recall that bias failures in these instruments are identified using the translational dynamics SPRT, in which we compare accelerations as measured by the accelerometers with those computed from α , Mach, δ_e , etc., using approximate equations for the relationships between these variables and lift and drag. Recall also that both α and Mach affect accelerations in both the x- and z-directions and thus the SPRT uses a two-dimensional residual vector.

In order to determine parameters (BFM's, ETL's) for α and Mach sensor failures, we must use a linearized model for the effect of failures on the computed forces. Specifically, let F_1 denote the the computed acceleration in the x-direction, and let F_3 denote that in the z-direction. Let

$$\lambda_{i\alpha} = \left. \frac{\partial F_i}{\partial \alpha} \right|_{\text{Trim}, i=1,3}$$

$$\lambda_{iM} = \left. \frac{\partial F_i}{\partial M} \right|_{\text{Trim}, i=1,3}$$

We have used the following values for these quantities, evaluated at trim at Mach=0.6, h=6.1 km

$$\lambda_{1\alpha} = 2.6 \text{ m/sec}^2 \text{ rad}$$

$$\lambda_{3\alpha} = 183 \text{ m/sec}^2 \text{ rad}$$

$$\lambda_{1M} = 2.3 \text{ m/sec}^2 \text{ Mach}$$

$$\lambda_{3M} = 21.7 \text{ m/sec}^2 \text{ Mach}$$

Given these values, the first order effect of a bias failure of size B_α in α is a bias of

$$\lambda_{1\alpha} B_\alpha$$

in the x-acceleration calculation, and

$$\lambda_{3\alpha} B_\alpha$$

in the z-acceleration calculation. Similar calculations hold in the case of β , and from now on we will drop the subscripts "x" or "z" since the analyses in the two cases are identical form.

There are three major unmodeled effects: undetected biases in the a_x or a_z accelerometers, a bias in the measured value of the other air-data sensor, and biases in the approximate expressions for F_1 and F_3 . These biases are due both to inaccuracies in our knowledge of the precise functional relationships and also to errors in the approximate forms for the aerodynamic coefficients used on-line. These approximations are used in order to reduce the storage requirements, which are extremely high if tables are used (see Appendix B).

Given these assumptions, an approximation to the expectation of the SPRT is

$$E[u_n] = \sum_{j=1}^n \frac{1}{\sigma^2} \left[\left(-\frac{\lambda_1 B}{2} + b_1 + \Delta F_1 + \eta_1 \right) \lambda_1 B + \left(-\frac{\lambda_3 B}{2} + b_3 + \Delta F_3 + \eta_3 \right) \lambda_3 B \right] \quad (4.18)$$

where

$$b_1 = b_3 = \text{undetected x,z bias} = .73 \text{ m/sec}^2$$

$$\Delta F_1, \Delta F_3 = \text{x-,z-direction table error}$$

$$\eta_1, \eta_3 = \text{x-,z-direction error due to bias in other air-data sensor}$$

For our purposes Eq. (4.18) is extremely conservative since $b_1, \Delta F_1, \eta_1, b_3, \Delta F_3, \eta_3$ are all at their maximum values and all are in the worst directions. On probabilistic grounds, one can argue that they should be replaced by an RSS of all four effects. This yields

$$E[u_n] = \sum_{j=1}^n \frac{B}{\sigma^2} \left[- \frac{(\lambda_1^2 + \lambda_3^2)B}{2} + \bar{B} \right] \quad (4.19)$$

where

$$\bar{B} = \sqrt{\lambda_1^2 (b_1^2 + \Delta F_1^2 + \eta_1^2) + \lambda_3^2 (b_3^2 + \Delta F_3^2 + \eta_3^2)}$$

$$\sigma^2 = 9.3 \text{ m}^2/\text{sec}^4$$

Note that from Eq. (4.19) it is clear that in order to detect the failure we must have

$$B > \frac{2\bar{B}}{(\lambda_1^2 + \lambda_3^2)} \equiv B_{\min} \quad (4.20)$$

For given values of ΔF_1 and ΔF_3 , and B satisfying Eq. (4.20), the time to cross the failure threshold can be calculated from Eq. (4.19). In particular, for the alpha vane, we choose

$$\begin{aligned} \Delta F_1 &= \Delta F_3 = .56 \text{ m/sec}^2 \\ \eta_1 &= .12 \text{ m/sec}^2 \\ \eta_3 &= 1.1 \text{ m/sec}^2 \end{aligned}$$

which yields

$$B_{\min} = .016 \text{ rad}$$

We choose the bias for alpha to be

$$B = .0175 \text{ rad}$$

which yields

$$T_c = 9.5 \text{ sec}$$

and we choose

$$ETL = 16 \text{ sec}$$

With the identical choice for ΔF_1 and ΔF_3 for the Mach meter and

$$\begin{aligned} \eta_1 &= .032 \text{ m/sec}^2 \\ \eta_3 &= 2.25 \text{ m/sec}^2 \end{aligned}$$

we obtain

$$B_{\min} = .22 \text{ Mach}$$

We choose B for the Mach meter to be

$$B = .23 \text{ Mach}$$

which yields

$$T_c = 13.2 \text{ sec}$$

and we choose

$$ETL = 18 \text{ sec}$$

4.7 Additional Tests

4.7.1 Introduction

We note that failures in some instruments may be found using more than one form of analytic redundancy*. Up to this point, we have only determined biases and ETL's for each instrument type for one form of analytic redundancy SPRT. We now examine the remaining possibilities, calculating biases and ETL's for each. Note that this means that a given instrument may have different biases and ETL's in the SPRT's for different forms of analytic redundancy.

4.7.2 Pitch and Yaw Rate Gyros

It is possible to use translational kinematics to identify bias failures in these instruments through the Coriolis term in the acceleration equation. The analysis in Section 4.4.3 holds (and is identical for q and r), except we reverse the roles of accelerometer and gyro biases. That is we must consider a BFM/2 undetected measurement bias in a_y or a_z . Also, assuming a nominal velocity of 183 m/sec, the error in Coriolis acceleration due to a B bias in q or r is $(183 B) \text{ m/sec}^2$ (here B is measured in rad/sec). Assuming equal acceleration measurement errors in the y and z directions of 1 m/sec^2 , we obtain for the low turbulence case

$$B = 0.015 \text{ rad/sec}$$

$$ETL = 38 \text{ sec}$$

*Sensors with no additional tests include p, ψ and h.

and for the high turbulence case

$$B = 0.015 \text{ rad/sec}$$

$$ETL = 55 \text{ sec}$$

The translational kinematics SPRT's in these cases use the same clipped gains as those derived in Section 4.4.3.

4.7.3 Roll and Pitch Attitude Gyros

It is possible that either translational kinematics or altitude kinematics could be used to detect ϕ or θ bias failures when the aircraft attitude is within certain regions. Since such tests are very much flight trajectory dependent, it is impossible to determine universal detection parameters, and it seems most appropriate to design several trajectories that the pilot could fly to allow us to detect such failures. This issue has not been considered in detail and awaits future investigation.

4.7.4 Longitudinal Accelerometer

It is possible that altitude kinematics could be used to identify a_x sensor failures, but again this is trajectory dependent and needs further study. We can, however, consider the use of translational dynamics to pick up a_x bias failures. In analogy with Section 4.6, we can write down a linearized expected value for the likelihood ratio

$$E[u_n] = \sum_{j=1}^n \frac{B}{\sigma^2} \left[-\frac{B}{2} + b \right] \quad (4.21)$$

where in this case

$$b = \sqrt{\lambda_{1a}^2 b_a^2 + \lambda_{1H}^2 b_H^2 + \Delta F_1^2} \quad (4.22)$$

and b_a , b_H are taken as $\text{BFM}/\sqrt{2}$ and $\text{BFM}/2$ respectively*. Assuming

$$B = 2.4 \text{ m/sec}^2$$

$$\Delta F_1 = .59 \text{ m/sec}^2$$

$$\sigma^2 = 9.3 \text{ m}^2/\text{sec}^4$$

*The BFM for Mach is 0.1 and is derived in Section 4.7.7.

we use the parameters given in Section 4.6 and compute

$$ETL = 45 \text{ sec}$$

4.7.5 Lateral Accelerometer

Again in this case we might be able to use altitude kinematics, but we leave this trajectory-dependent analysis to the future. Although we have not implemented a translational dynamics SPRT for β (since we have only one β vane), we can use such an SPRT to identify a_y bias failures. Again, the form of the expectation of the likelihood ratio is given by Eq. (4.21) where b models table errors and the effects of biases in the β vane. We have used a value of 0.3 m/sec^2 for b . We then choose

$$\begin{aligned} B &= 2 \text{ m/sec}^2 \\ \sigma^2 &= 7.6 \text{ m}^2/\text{sec}^4 \end{aligned}$$

and calculate the time to identify a $BFM/\sqrt{2}$ failure as

$$T_m = .9 \text{ sec}$$

and choose

$$ETL = 11 \text{ sec}$$

4.7.6 Normal Accelerometer

We first examine the use of translational dynamics. We can utilize Eq. (4.21) and modify Eq. (4.22) by changing the "1" subscript to a "3". We choose

$$\begin{aligned} B &= 5.5 \text{ m/sec}^2 \\ \Delta F_3 &= .59 \text{ m/sec}^2 \\ \sigma^2 &= 9.3 \text{ m}^2/\text{sec}^4 \end{aligned}$$

and calculate

$$ETL = 8 \text{ sec}$$

We now note that a_z failures can also be identified using altitude kinematics. We will assume level flight, and in this case an a_z bias enters quadratically in the residual. Thus for a bias B the expectation of the SPRT output is

$$E[u_n] = \sum_{j=1}^n \frac{B_j^2 T^2}{2\sigma^2} \left[\frac{B_j^2 T^2}{4} - \gamma(t_j) \right]$$

where $\sigma^2 = 9.3$, the variance of the altimeter measurement noise. Assuming worst case initialization errors in altitude and altitude rate of M and e respectively, the expected SPRT output for a failure of $B/\sqrt{2}$ becomes

$$E[u_n] = \sum_{j=1}^n \frac{B_j^2 T^2}{2\sigma^2} \left(\frac{B_j^2 T^2}{4} (1 - \sqrt{2}) + ejT + M \right)$$

which can be approximated as

$$E[u_n] = \frac{1}{T\sigma^2} \left[\frac{B^2 t^5}{40} (1 - \sqrt{2}) + \frac{Bet^4}{8} + \frac{BMt^3}{6} \right] \quad (4.23)$$

Solving for T_m , with $B = 1.5 \text{ m/sec}^2$, $e = 1.37 \text{ m/sec}$, $M = 3.4 \text{ m}$ gives

$$T_m = 14 \text{ sec}$$

and we choose

$$ETL = 21 \text{ sec}$$

4.7.7 Mach Meters

Because a bias in the α vane does not produce an appreciable bias in V_z , translational kinematics cannot be used to identify step failures in this instrument of less than about 0.2 rad, and thus is of little use for this instrument. However, translational kinematics is useful for identifying step failures in the Mach meters. The development closely parallels the use of rotational kinematics to identify step failures in the attitude gyros. Thus we have two first-order uncoupled velocity estimators, each using a different Mach meter as the measurement, and we store a window of residuals for each.

We design the test to look for a Mach bias B and calculate the two times T_m that the expectation of the SPRT output crosses the failure threshold for a B failure. We assume an x velocity initialization error of M , an x acceleration bias b due to the RSS of BFM/2 acceleration measurement bias and wind shear, and a Mach variance v to obtain

$$E[u_n] = \sum_{j=1}^n \frac{V_s B}{\sigma^2} \left[-\frac{V_s B}{2} + M + b \left(jT + \frac{107 v T}{B^2} \right) \right]$$

Approximating the above equation by an integral and setting it to the failure threshold gives

$$\frac{V_s B b}{2\sigma^2 T} T_m^2 + \frac{V_s B}{\sigma^2 T} \left[-\frac{V_s B}{2} + M + \frac{107 b v T}{B^2} \right] T_c + 9.2 = 0 \quad (4.24)$$

Now, the initialization velocity error from Eq. (4.11) is

$$M = 2.6 \text{ m/sec}$$

The speed of sound at 6.1 km is

$$V_s = 316 \text{ m/sec}$$

The variance of the Mach meter is

$$v = 10^{-4}$$

and we choose

$$B = .1$$

In low turbulence, the variance of the translational kinematics residuals is given by

$$\sigma^2 = 9.3 \text{ m}^2/\text{sec}^2$$

and the value of b , the RSS of wind shear and BFM/2 acceleration measurement bias, is given by

$$b = 1.69 \text{ m/sec}^2$$

From Eq. (4.24), we calculate

$$T_c = .013, 15.2 \text{ sec}$$

and choose

$$ETL = 7 \text{ sec}$$

In high turbulence, we have

$$\sigma^2 = 33 \text{ m}^2/\text{sec}^2$$

$$b = 3.14 \text{ m/sec}^2$$

and we calculate

$$T_c = .05, 8 \text{ sec}$$

and we choose

$$ETL = 4 \text{ sec}$$

4.8 Summary

In this section we have derived a consistent set of biases and ETL's to be used by the various analytic redundancy SPRT's for the different instruments. The minimum value of the biases used by the applicable SPRT's for each instrument type is defined to be the BFM for that type, and it is this bias level which the redundancy trigger is designed to detect. For the accelerometers attitude and rate gyros, at least one form of analytic redundancy test can identify failures of size $\text{BFM}/\sqrt{2}$, and thus the worst-case biases on these measurements entering other tests is assumed to be $\text{BFM}/2$. For the alpha vanes, Mach meters, attitude gyros and altimeters, the worst case measurement errors are assumed to be $\text{BFM}/\sqrt{2}$. Table II presents a summary of the results presented in this section, with question marks indicating possible tests which have not been fully investigated.

Table II Summary of FDI System Parameters

Sensor Type	Translational		Kinematics		Rotational Kinematics	Altitude Kinematics	Translational Dynamics		BFM
	Low Turbulence		High Turbulence				B	ETL	
	B	ETL	B	ETL					
a_x (m/sec ²)	1.5	, 50	1.5	, 67		?	2.4	, 18	1.5
a_y (m/sec ²)	2	, 37	2	, 53		?	2	, 11	2
a_z (m/sec ²)	2	, 37	2	, 53		1.5 , 21	5.5	, 8	1.5
Mach	0.1	, 7	0.1	, 4			0.23	, 18	0.1
α (rad)							0.0175	, 16	0.0175
p (rad/sec)					0.02	, 11			0.02
q, r (rad/sec)	0.015	, 38	0.015	, 55	0.006	, 36			0.006
ϕ (rad)	?		?		0.06	, 2	?		0.06
θ (rad)	?		?		0.055	, 3	?		0.055
ψ (rad)					0.055	, 3			0.055
h (m)							30	, 2	30

BLANK PAGE

BLANK PAGE

SECTION 5

QUALITY SPRT's

As we have discussed, the various SPRT's have been designed to be somewhat conservative, i.e., we have chosen design parameters (BFM, ETL) and SPRT structure (e.g., the use of a clipped gain in the translational kinematics SPRT) to hedge against possible unmodeled effects. In order to judge the value of any given test, however, one must take into account such possibilities as the effect of maneuvers, flight condition, and the size of the failure as indicated by the difference between the two identical instruments following a redundancy trigger. Since such effects must be determined on-line, we were led to the conclusion that we need to calculate on-line some statistic that tells us the quality of each SPRT. Specifically, our goal was to determine a statistic such that we could be sure a given SPRT was good if the statistic said it was. This philosophy led to the development of the quality SPRT (QSPRT).

Basically, for each analytic redundancy test the QSPRT computation involves the calculation of the worst-case expected values of the likelihood ratios of the failed and unfailed instruments of the given type. That is, given all relevant flight information (sensor outputs, maneuver or turbulence indications, etc.) we compute the worst-case unmodeled effects. These are then used to determine the worst-case expectation of the SPRT output for the unfailed instrument. For the failed instrument we combine the worst case expectation with an expected failure size to determine a worst case expectation for the SPRT for the failed instrument. In the case of a redundancy trigger, the expected failure size is determined using the difference between the two suspect sensor outputs. For a time trigger, we simply assume a B-sized failure. In some sense, the QSPRT is a direct measure of signal strength versus noise strength and thus provides an excellent statistic for determining the quality of the test.

The general form for the QSPRT can be derived as follows. For a redundancy trigger, the SPRT output for each instrument is of the form

$$u_n = \frac{1}{2} \sum_{j=1}^n G(t_j) M(t_j) - \sum_{j=1}^n G(t_j) \gamma(t_j) \quad (5.1)$$

while for a time trigger, generalizing Eq. (2.7), the SPRT output for each instrument is of the form

$$u_n = \frac{1}{2} \sum_{j=1}^n G(t_j) M(t_j) - \left| \sum_{j=1}^n G(t_j) \gamma(t_j) \right| \quad (5.2)$$

In the above equations, $M(t_j)$ is the expected mean in the residual $\gamma(t_j)$ caused by a B-sized failure and $G(t_j)$ is the SPRT gain, which is $M(t_j)/\sigma^2$ in all tests but translational kinematics. We note that $G(t_j)$ and $M(t_j)$ are of the same sign, and both are assumed positive for this analysis.

Now, define $m(t_j)$ to be the magnitude of the bias in $\gamma(t_j)$ which we expect to see. For a time trigger $m(t_j)$ is clearly equal to $M(t_j)$, since we must assume the existence of a B-sized failure. For a redundancy trigger, $m(t_j)$ is calculated from the difference in the sensor outputs. Let $b(t_j)$ be the magnitude of the worst-case unmodeled error in $\gamma(t_j)$ due to all sources of error in the analytic redundancy test. Then, the worst-case expectation for the SPRT for the failed instrument is

$$WCF_n = \sum_{j=1}^n G(t_j) \left[\frac{M(t_j)}{2} + b(t_j) - m(t_j) \right] \quad (5.3)$$

and the worst-case for the unfailed instrument is

$$WCU_n = \sum_{j=1}^n G(t_j) \left[\frac{M(t_j)}{2} - b(t_j) \right] \quad (5.4)$$

Note that in Eq. (5.3) $b(t_j)$ drives WCF positive, decreasing the probability of correct identification, while in Eq. (5.4) it drives WCU negative, increasing the probability of declaring the wrong instrument as failed. Clearly, we should not be willing to believe the test unless

$$C_n \equiv WCF_n - WCU_n = \sum_{j=1}^n G(t_j) [2b(t_j) - m(t_j)] < 0 \quad (5.5)$$

Let us enumerate the conditions under which Eq. (5.5) may hold. The first is when

$$WCF_n < 0, \quad WCU_n > 0 \quad (5.6)$$

Clearly this is the best conceivable case. The next possibility is

$$WCF_n < 0, \quad WCU_n < 0 \quad (5.7)$$

In this case the unfailed instrument may appear to have failed, i.e., its SPRT may be negative, but the SPRT of the failed instrument is even more negative (by Eq. (5.5)). The final case is

$$WCF_n > 0, \quad WCU_n > 0 \quad (5.8)$$

and in this case the failed instrument may appear unfailed, but the unfailed instrument looks even more so (by Eq. (5.5)). Finally, note that for a time trigger with $m(t_j) = M(t_j)$ we have

$$WCF_n = -WCU_n \quad (5.9)$$

Thus, Eq. (5.5) holds if and only if $WCF_n < 0$.

Based on these observations, we have devised the following rule for defining the QSPRT:

1. If we are on a time trigger

$$QSPRT_n = WCF_n$$

2. If we are on a redundancy trigger

- a) If $C_n < 0$

$$QSPRT_n = WCF_n$$

- b) If $C_n \geq 0$

$$QSPRT_n = +9.2$$

In the outer loop logic (see Section 6) the QSPRT's are used to determine which tests should be believed. A test is believed only if $QSPRT_n < 0$, with increasing confidence being given as it becomes more

negative. Thus, we can determine the effect of the above definition of QSPRT. For time triggers, there is no difficulty, since we believe the test only if $WCF_n < 0$. In the case of redundancy triggers, we must have $C_n < 0$ and $WCF_n < 0$ to believe the test. Referring to Eq. (5.6) through (5.8), we see that there are two cases in which this will hold. In the first of these, Eq. (5.6), we see that the test has a sufficiently high signal-to-noise ratio to determine which instrument has failed and which has not ($WCF_n < 0$, $WCU_n > 0$).

Consider the case of Eq. (5.7), where we also assume that Eq. (5.5) holds. In this case, the unmodeled bias is sufficiently large so that it could make the unfailed instrument appear failed. However, the actual failure size, as measured by $m(t_j)$, is even larger; and thus the SPRT for the failed instrument is even more negative. Hence, we use a negative value for the QSPRT, indicating that we can decide which instrument has failed. One might think that if Eq. (5.7) holds, we might want $C_n < -L$ for some positive number L to guarantee that the actual SPRT of the failed instrument is truly less than that of the unfailed instrument. However recall that in calculating the two SPRT's, identical information is used except for the suspect sensors. Hence, the difference between the actual SPRT's is due solely to the differences in suspect sensor outputs, and this is precisely what C_n measures, where C_n is even more conservative in that it takes into account the possibility of a worst-case bias. Thus if $C_n < 0$, we can be sure that the failed instrument has a smaller SPRT than the unfailed one.

Examining Eq. (5.8), we see that if $C_n < 0$ but $WCF_n > 0$, we are setting $QSPRT_n = WCF_n > 0$. This means the following: If Eq. (5.5) and (5.8) hold we know that the unfailed instrument will have a more positive SPRT. However, in our design we have chosen to be conservative. That is, in this case, we will not declare the least positive of the SPRT's to be that of the failed instrument. Rather, we require that the SPRT be able to positively identify the failed instrument (i.e., $WCF_n < 0$) before we will make a decision. A decision rule under the conditions of Eq. (5.8) could easily be derived, but we have chosen not to do so in this study.

The error sources contributing to $b(t_j)$ for the various forms of analytic redundancy for each instrument type include all those sources enumerated in Section 4, including initialization errors, wind shear for translational kinematics and table errors for

translational dynamics. In addition the QSPRT includes all state-dependent error sources, evaluated not at trim as in Section 4, but at the measured vehicle state.

All sources of error for the various types of analytic redundancy are indicated below. The time-varying coefficients of these sources are added after the beginning of the test to allow cancellation for oscillatory maneuvers. The worst-case contributions of these individual error sources are then added at each sample time except for translational dynamics, in which case the effects are RSS'd. For a particular suspect instrument type using a particular analytic redundancy test, all error sources but that of the suspect type are used in the QSPRT calculation. The redundancy types and associated error sources are as follows:

1. Translational Kinematics
 - a) V initialization error
 - b) Pitch and yaw rate measurement biases
 - c) Acceleration measurement biases
 - d) Wind shear
 - e) Pitch and yaw attitude measurement biases
2. Rotational Kinematics
 - a) Angle initialization error
 - b) Attitude rate measurement bias
 - c) Attitude measurement bias
 - d) Axis misalignment
 - e) Rate gyro scale factor error
3. Altitude Kinematics
 - a) Initialization error in h and \dot{h}
 - b) Acceleration measurement biases
 - c) Pitch and roll attitude measurement biases
4. Translational Dynamics
 - a) Table errors
 - b) Acceleration measurement biases
 - c) Air-data measurement biases

BLANK PAGE

BLANK PAGE

SECTION 6

OUTER LOOP LOGIC

6.1 Introduction

In Section 4 we discussed the selection of a consistent set of B's and ETL's for the various analytic redundancy tests for the different instrument types. The BFM for each instrument type was then defined to be the smallest B for the various applicable analytic redundancy tests. In these calculations, all maneuver-dependent error sources were evaluated at trim at Mach 0.6 at 6.1 km altitude. The ETL for each test for a given sensor type was defined to be 1.5 times the time required, at trim, for the expectation of the SPRT output for the failed sensor to cross the failure threshold. In Section 5, we discussed the QSPRT, which is a measure of the signal-to-noise ratio of its associated analytic redundancy test. The QSPRT calculates worst-case effects of all relevant error sources, using the measured aircraft state to evaluate maneuver-dependent terms. In this section, we discuss the outer loop failure identification logic, which uses the SPRT and QSPRT outputs of all the analytic redundancy tests for a particular instrument type in order to identify a failed instrument. We also discuss some other functions of the outer loop, such as time trigger initiation.

6.2 Failure Identification - Redundancy Trigger

Following a direct redundancy trigger, all SPRT's and QSPRT's associated with the suspect instrument type are begun, including the direct redundancy SPRT. Also, all SPRT and QSPRT calculations associated with any currently running time trigger are terminated, to be reinitiated following resolution of the direct redundancy trigger. This resolution may be accomplished in three ways: indication of a false alarm, identification of the failed instrument, or indication of an unidentifiable failure. A false alarm counter for the suspect instrument type is incremented if after a nominal period of time,

currently 0.5 seconds, the output of the direct redundancy SPRT becomes positive. This false alarm indication causes all calculations initiated by the direct redundancy trigger to stop, and the direct redundancy trigger calculations are restarted.

The task of failure identification is made quite simple by the QSPRT. We are currently using the following logic for failure identification, but many variations are possible, and some may prove more effective following extensive system tests.

Recall from Section 5 that we have chosen a conservative approach to failure identification in that we will only fail an instrument on the indication that the instrument has failed and not on the indication that its counterpart has not failed. Consequently we are using WCF as the QSPRT output (or $+9.2$ when $C_n \geq 0$). At each sample time t_n , we make a failure identification check using each form of analytic redundancy. We make this check only for the instrument with the smallest SPRT, call it instrument j . Then at time t_n before ETL for the particular test, we declare instrument j failed if

$$QSPRT_n \leq -9.2 \quad \text{and} \quad SPRT_n^j \leq -9.2$$

At time t_n at or beyond ETL for the test, we declare instrument j failed if

$$QSPRT_n < 0 \quad \text{and} \quad SPRT_n^j \leq -9.2$$

or

$$QSPRT_n \leq -9.2 \quad \text{and} \quad SPRT_n^j < 0$$

If at any sample time any test declares an instrument failed, the status of that instrument is changed to failed and the direct redundancy trigger has been resolved. Subsequently, the failed instrument is not used in any control or FDI calculations, and dual redundancy no longer exists for that instrument type.

If the longest ETL for all analytic redundancy tests is reached without resolution of the redundancy trigger, a pass counter is incremented. If the value of the pass counter is no larger than N_p , the QSPRT's and SPRT's are restarted, and the failure identification

checks continue. In the unlikely event that the value of the pass counter exceeds N_p^* , an unidentifiable failure flag is set for the suspect instrument type. At this point the pilot may maneuver (or stop maneuvering) the aircraft in order to enhance the identifiability of the failure.

During the failure identification check using any form of analytic redundancy, the instrument with the lowest SPRT is provisionally failed if

$$QSPRT_n < 0 \text{ and } SPRT_n^j < 0$$

The provisionally failed instrument is removed from all control calculations, but the failure identification tests continue until resolution of the trigger. Only one instrument of a given type is ever provisionally failed, and a provisional failure during the current test overrides any previous provisional failure. Also, the provisional failure status of an instrument is removed if its counterpart is identified as failed. This capability of the dual-redundant system to make provisional failures tends to minimize the time required to remove a failed sensor from the system without a corresponding increase in false identifications.

6.3 Failure Identification - Time Trigger

Following initiation by the time trigger, all applicable analytic redundancy QSPRT and SPRT calculations are begun. No decision is made until the longest applicable ETL is reached. At that time an instrument is declared provisionally failed if for some form of analytic redundancy the SPRT associated with the instrument is less than the QSPRT and the QSPRT is less than -9.2. The instrument is declared only provisionally failed to allow its use following the identification, via a redundancy trigger, of the hard failure of the other instrument.

6.4 Additional Outer Loop Tasks

In addition to its primary task of failure identification, the outer loop performs some "bookkeeping" tasks which we enumerate below.

The outer loop schedules the time triggers for those instrument types whose failures are observable in at least one analytic redundancy test at any time subsequent to the failure. As we saw in Section 4,

*Currently we use $N_p = 3$ for all instruments but the yaw attitude gyros and altimeters, for which $N_p = 1$.

all instruments except the yaw attitude gyros and altimeters are in this category. However, since the observability of ϕ and θ failures in the altitude kinematics tests is so maneuver-dependent, we also exclude those instruments from the time triggers. Thus in the absence of a direct redundancy trigger, the outer loop cycles through a list containing the rate gyros, accelerometers, Mach and alpha sensors, calculating QSPRT's and SPRT's for one instrument type at a time. If no failure is identified within the longest ETL for a particular instrument type, the calculations for that type are terminated and the calculations for the next instrument type in the list are begun. When the calculations for the last type in the list are terminated, the calculations for the first type in the list are begun. If a direct redundancy trigger occurs, all calculations being performed for the time trigger are terminated, and these calculations are not restarted until after resolution of the direct redundancy trigger.

As discussed in Appendix D, a possibility exists for the simultaneous failure of the indications of ϕ and θ from a vertical gyro, and a methodology is presented there for the identification of the failed unit. The logic involved in that decision process would be performed by the outer loop.

Although not currently implemented, the outer loop could schedule analytic redundancy failure checks in previously failed instruments in order to take advantage of possible instrument "healing".

SECTION 7

SIMULATION RESULTS

7.1 Introduction

In this section we present some representative results obtained using the analytic redundancy FDI algorithm described in the previous sections in conjunction with the nonlinear six degree of freedom real-time F-8 digital simulator at the NASA Langley Research Center. For these results, the simulated aircraft was at the design flight condition of Mach 0.6 at 6.1 km altitude. The control surfaces were trimmed for horizontal flight, and the simulated sensor outputs were corrupted by white noise and quantization as characterized by the parameters indicated in Table I. It is important to note that all variables are truncated at the upper and lower ordinate values given in the figures.

7.2 Time Trigger Performance

As indicated in Section 6, the outer loop is designed to monitor the status of the rate gyros, accelerometers, Mach meters and alpha vanes via cyclical time trigger initiation. This procedure was tested at two levels of turbulence: zero turbulence and thunderstorm turbulence with rms winds of 6.4 m/sec^{*}. For the case in which all instruments have zero bias values, the FDI algorithm performs as expected following time trigger initiation for both turbulence levels, i.e., each instrument of every type is correctly indicated as unfailed. Thus no false alarms occurred in the simulations with zero bias.

Additional time trigger simulations were performed in which the number 2 instrument of every type contains a bias of +0.4 BFM. This bias is within the allowable tolerances for unfailed instruments, but its level approaches the limits of these tolerances. The results of these simulations at the two turbulence levels will be discussed in detail below for the various instrument types.

* Note that this figure is 16% higher than the Dryden wind model used to derive the high turbulence "worst case" shear in Section 4.4.2.

7.2.1 Rate Gyros

Figure 7-1 shows the results for the rate gyros. The left side indicates the behavior during no turbulence while the right side indicates behavior during thunderstorm turbulence. On each side, results are shown successively for the roll (p), pitch (q), and yaw (r) rate gyros. Ten variables are plotted; they are in order from the top:

- 1) Rotational kinematics (RK) QSPRT
- 2) RK residual for instrument 1
- 3) RK residual for instrument 2
- 4) RK SPRT for instrument 1
- 5) RK SPRT for instrument 2
- 6) Translational kinematics (TK) QSPRT
- 7) TK residual for instrument 1
- 8) TK residual for instrument 2
- 9) TK SPRT for instrument 1
- 10) TK SPRT for instrument 2

As indicated in Section 4.7.2, the relatively small value of the angle of attack precludes the use of TK for identifying roll rate gyro failures. Thus, variables 6-10 are not applicable to the roll rate gyro. As mentioned before, all variables are truncated in the figure at the upper and lower limits indicated.

Consider the case of no turbulence, shown on the left in the figure. At $t=0$ the roll rate gyro time trigger is given, and the calculations of the RK QSPRT and the SPRT's for the two instruments are begun. Note that the RK residual for instrument 2 contains a ramp due to its bias, while the ramp is absent in the residual for unbiased instrument 1. The RK QSPRT initially is positive, reflecting the worst-case assumption for ϕ initialization error. It becomes negative after about 3 seconds, due to the dominating effect of the assumed BFM failure in the roll rate gyro. The RK SPRT's for instruments 1 and 2 cross the no failure boundary after about 2 seconds. These SPRT's reflect the absence of a ramp with a slope of magnitude BFM in the residuals for either of the two instruments.

After 11 seconds the RK ETL for the roll rate gyro is reached. As mentioned in Section 6.3, no decision is made on a time trigger until the longest applicable ETL is reached. Thus, because only the RK test is available for the roll rate gyros, the RK QSPRT and SPRT's for the two instruments are examined at this time. The QSPRT is below

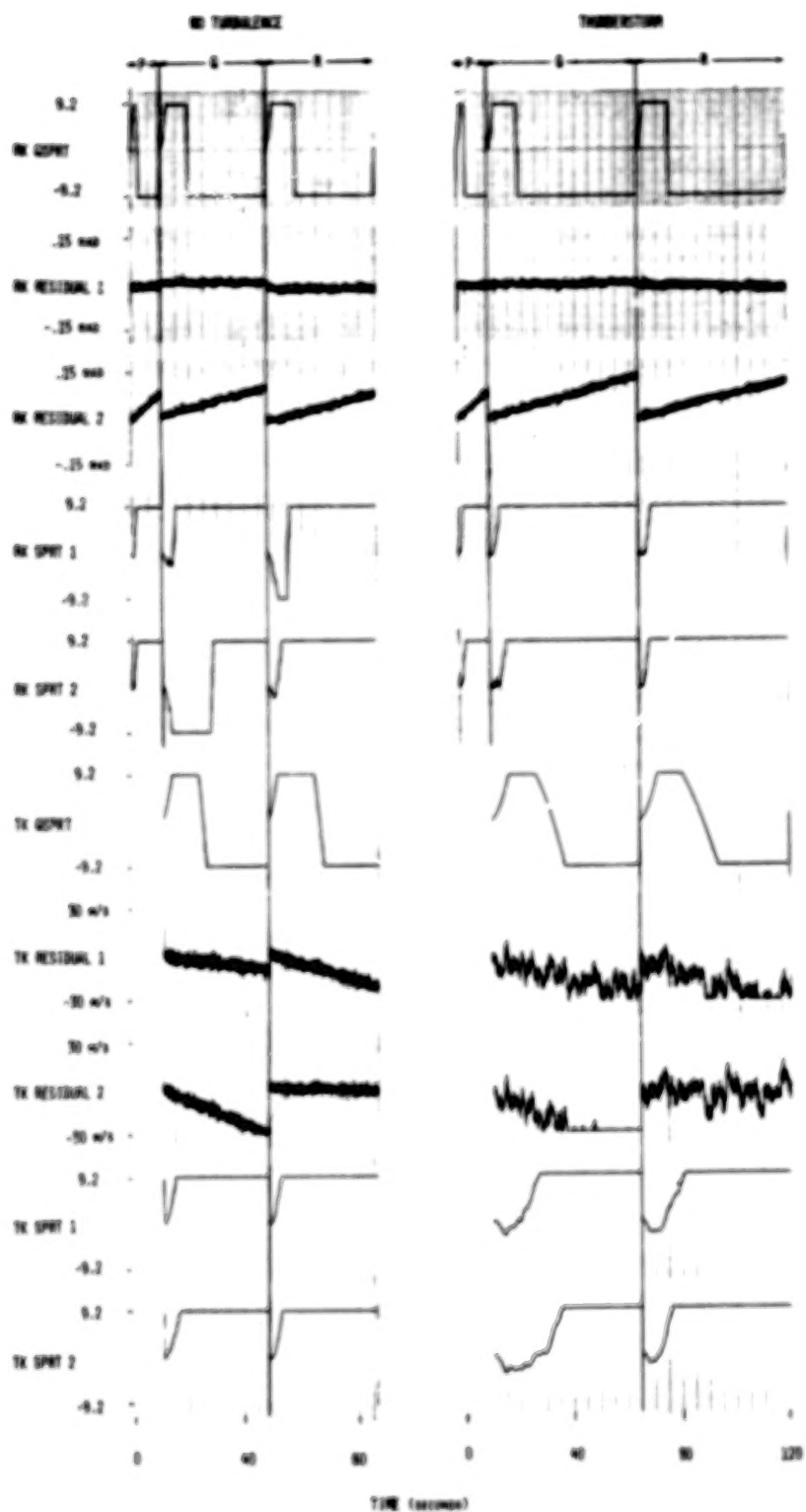


Figure 7-1 Rate Gyro Time Trigger Performance

the failure threshold indicating that the RK test is good, and the SPRT's for both instruments are positive. Thus no failure is indicated. We note that the truncation in the figure hides the extreme magnitudes of the SPRT's, which in this case reach approximately 700.

Following the outer loop decision on the unfailed status of the roll rate gyros, the time trigger for the pitch rate gyro is given, and the RK and TK QSPRT and SPRT calculations are initiated. As in the case of the roll rate gyro, the figure indicates that the RK residuals for pitch rate gyro 1 contain no ramping term, while the residuals for pitch rate gyro 2 contain a ramp due to the bias present in that instrument. Note that the slope of the RK residual ramp for pitch rate gyro 2 is smaller than that for roll rate gyro 2, reflecting the smaller BFM for the pitch rate gyros. Variables 6-10 in the figure indicate quantities associated with TK analytic redundancy which are unavailable for the roll rate gyros but are available for the pitch and yaw rate gyros. We note that there are ramps in the TK residuals for both pitch rate gyros. These residuals are the normal component of the air-relative velocity as computed from air data minus the open loop estimate obtained from Eq. (3.7). Thus the ramp in the TK residuals for pitch rate gyro 1 is due to the effect of the bias in normal accelerometer 2, which is being averaged with normal accelerometer 1 for use in Eq. (3.7). The ramp in the residual for pitch rate gyro 2 has a larger magnitude slope than that for instrument 1 because the sign of the effect of its bias in the Coriolis term in Eq. (3.7) is the same as the sign of the bias in normal accelerometer 2.

After the TK ETL for the pitch rate gyros of 38 seconds, the outer loop makes a decision concerning the status of the pitch rate gyros. The RK and TK QSPRT's are both below -9.2, indicating that both tests are good. Also, the TK and RK SPRT's for both instruments are positive, and thus no failure is indicated.

It is instructive to note that at the time the RK QSPRT crosses below the -9.2 threshold, the RK SPRT for pitch rate gyro 2 is also below -9.2. If the decision logic used following a redundancy trigger, given in Section 6.2, were applied at this time, pitch rate gyro 2 would be incorrectly identified as failed. This problem arises because the QSPRT has no direct redundancy information available following the time trigger and assumes the presence of a failure of size BFM in its calculation. In particular, if the QSPRT had correctly assumed a

0.4 BFM bias in its calculations, it would not have crossed the -9.2 boundary before the SPRT for pitch rate gyro 2 had crossed the +9.2 boundary. In order to avoid the identification of a moderately biased instrument as failed on a time trigger, the logic of Section 6.3 is adopted. This logic extends the identification time and exploits the fact that the QSPRT is the WCF for a BFM-sized failure and therefore should be greater than the SPRT calculated using the failed sensor.

Following the outer loop decision on the unfailed status of the pitch rate gyros, the time trigger for the yaw rate gyros is given. The RK residuals for the yaw rate gyros are similar to those for the pitch rate gyros, with those for instrument 2 having an obvious ramp component. However, there is a notable difference in the TK residuals, which for the yaw rate gyros consist of the difference between the lateral component of the air-relative velocity as computed from air data minus the open loop estimate. In particular the TK residuals for biased instrument 2 have no observable ramp component. The reason for this is that the effect of the bias in yaw rate gyro 2 essentially cancels the effect of the bias in lateral accelerometer 2. The ramp in the residuals for yaw rate gyro 1 is due to the additive effects of the biases in roll attitude gyro 2 and lateral accelerometer 2. When the TK ETL of 38 seconds is reached, the RK and TK QSPRT's and SPRT's are examined by the outer loop. Both the RK and TK QSPRT's are below -9.2, indicating that both tests are good. Since the RK and TK SPRT's for both instruments are positive, no failure is indicated.

The simulation of the rate gyro time triggers in thunderstorm turbulence is shown on the right side of Figure 7-1. Again, the order of the time triggers is roll, pitch and then yaw. The roll rate gyro time trigger runs for 11 seconds, the RK ETL, and then a failure status decision is made for those instruments. Following this decision, the pitch rate gyro time trigger is initiated. Because the turbulence estimator described in Appendix A correctly indicates a high turbulence level, the smaller TK SPRT gains are used together with the high turbulence ETL of 55 seconds. Thus a failure decision is made for the pitch rate gyro at $t=66$ sec, after which the time trigger for the yaw gyros is initiated. Again the smaller TK SPRT gains and larger TK ETL are used, and a failure status decision for the yaw rate gyros is made at $t=121$ sec.

Examination of the figure indicates the RK QSPRT, residuals and SPRT's for the roll rate gyros are virtually identical to those obtained in the absence of turbulence. At t=11 sec, the outer loop examines the RK QSPRT and SPRT's. Although the RK QSPRT is negative indicating a good test, the RK SPRT's for both instruments are positive, and therefore no failure indication is given for the roll rate gyros.

At t=11 sec, the time trigger for the pitch rate gyros is initiated. As in the case of no turbulence, the RK residuals for instrument 1 have no appreciable bias, while the RK residuals for instrument 2 have a bias of slope 0.4 BFM. The RK SPRT's become positive more quickly than in the no turbulence case due to some "beneficial" maneuver-dependent errors introduced by the turbulence. The TK QSPRT goes initially positive at a slower rate than before due to the smaller, high turbulence gain. The TK QSPRT remains positive longer than before because of the assumption of twice the wind shear profile assumed for low turbulence. The TK residuals for the two instruments have, on the average, slopes similar to the no turbulence case, but with the addition of high amplitude low frequency noise due to the thunderstorm turbulence. Beyond t=40 sec, the turbulence keeps the residual for instrument 2 below the truncation level of -30 m/sec. The TK SPRT's for the two instruments remain negative for several seconds due to the low frequency wind shears. However because the shears are not sustained, both SPRT's eventually cross the no-fail threshold. At t=66 sec, the outer loop makes a decision on the failure status of the pitch rate gyros, and since both the TK and RK SPRT's for both instruments are positive, no failure indication is given.

At t=66 sec, the time trigger for the yaw rate gyros is initiated. Again, the RK variables are quite similar to those obtained in the absence of turbulence, while the TK residuals and SPRT's reflect the presence of low frequency wind shears in the turbulence. After reaching the TK ETL of 55 seconds at t=121 sec, the outer loop examines the yaw rate gyro QSPRT's and SPRT's. Because both the TK and RK SPRT's for both instruments are positive, no failure indication is given.

7.2.2 Accelerometers

Time triggers were run for the accelerometers and air data sensors in the same two turbulence environments used for the rate gyro simulations. Again, +0.4 BFM biases were present on the number 2 instrument of every type. As in the case of the rate gyros the

simulations without turbulence presented no surprises, and those results will not be discussed here.

Results of simulation of time triggers for the accelerometers in thunderstorm turbulence are presented in Figure 7-2. Only the most powerful form of analytic redundancy for each particular instrument type is presented, i.e., translational kinematics for longitudinal accelerometers (x), translational dynamics (TD) for lateral accelerometers (y) and altitude kinematics (AK) for normal accelerometers (z). The present outer loop logic uses only these principal tests for provisional failure identification following accelerometer time triggers. However, the time waited until a decision is made is the longest ETL of the three analytic redundancy types, which is the high turbulence TK ETL for each of the accelerometers: 67 seconds for x and 53 seconds for y and z.

The left column in Figure 7-2 gives the time trigger results using translational kinematics for the longitudinal accelerometers. The TK QSPRT exhibits the same behavior as the high turbulence pitch and yaw rate gyro results shown in Figure 7-1. The TK residuals for instrument 1 are essentially zero mean with low frequency noise due to turbulence, while the residuals for instrument 2 contain a ramp of slope 0.4 BFM. The SPRT for instrument 1 crosses the no-fail boundary at $t=20$ sec and remains above the boundary for the duration of the time trigger. The combined effects of the high turbulence and the bias on the number 2 accelerometer cause its SPRT to remain negative, but above the failure threshold of -9.2, for nearly the entire run. At the TK ETL of 67 seconds, the SPRT's for both instruments are above the failure threshold, and no failure is indicated by the outer loop.

The center column of Figure 7-2 gives the time trigger results using translational dynamics for the lateral accelerometers. The TD QSPRT crosses the negative threshold at $t=1$ sec and remains below the threshold for the rest of the simulation. This indicates that the effect of table error is less than the effect of a lateral accelerometer BFM failure throughout the simulation. The two lateral TD residuals are shaped nearly the same, reflecting the high turbulence present. However, the residuals for instrument 2 have a positive bias of about 1 m/sec^2 due to the bias on that instrument. The TD SPRT for instrument 1 crosses the no-fail threshold at $t=1$ sec and remains above that level, while the TD SPRT for instrument 2 oscillates

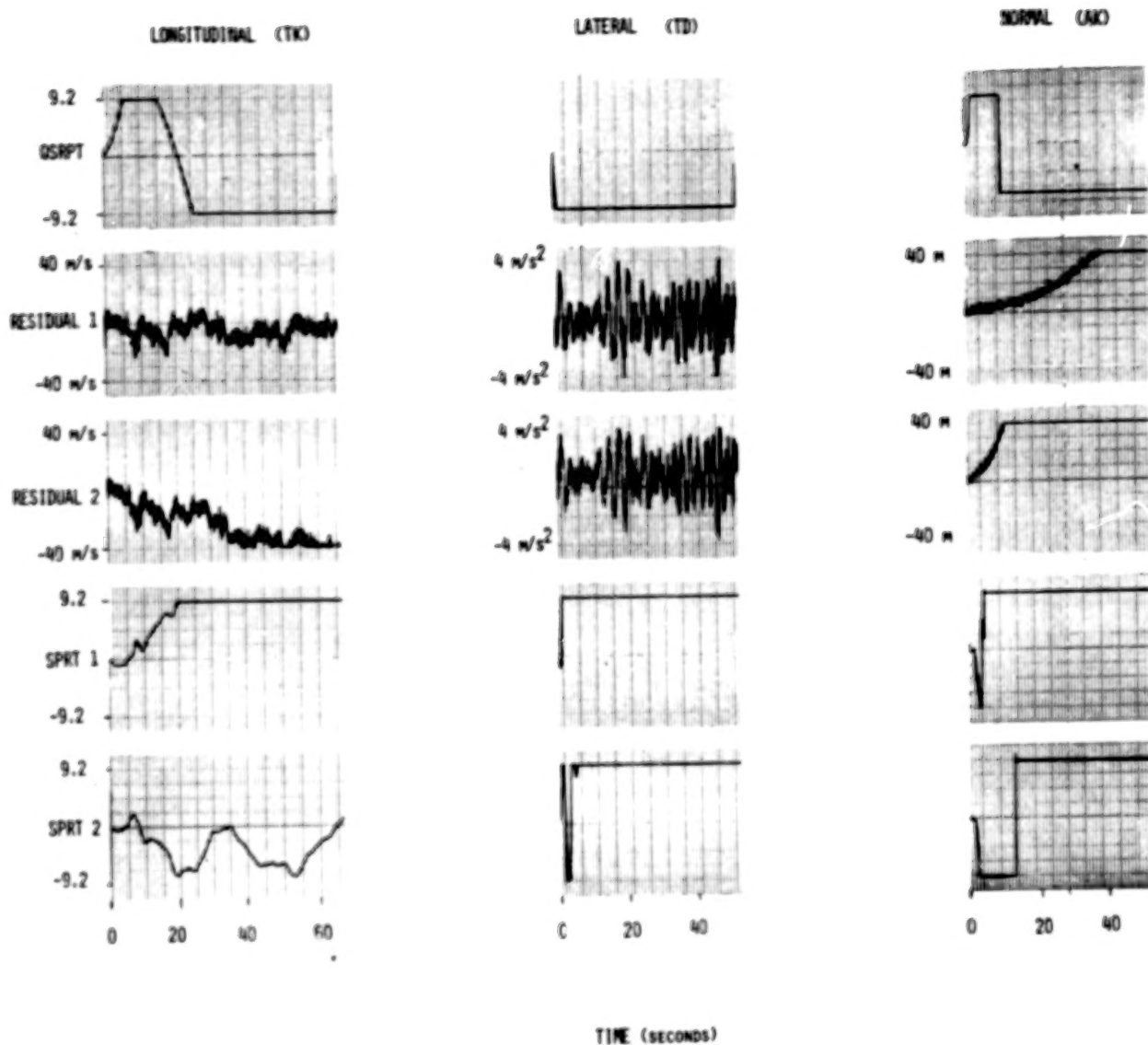


Figure 7-2 Accelerometer Time Trigger Performance

initially but remains above the no-fail threshold following $t=5$ sec. At the lateral accelerometer TK ETL of 53 seconds, the outer loop examines the TD QSPRT and SPRT's and indicates no failure is present.

The right column of Figure 7-2 gives the time trigger results using altitude kinematics for the normal accelerometers. The AK QSPRT starts off positive due to worst case initialization errors in estimated altitude and altitude rate. However, the quadratic effect of the assumed accelerometer BFM failure soon dominates, and the QSPRT crosses the failure threshold after about 9 seconds and remains below that level to the end of the run. The AK residual for instrument 1 grows quadratically due to the combined effects on the open loop altitude estimate of the biases in the number 2 lateral and longitudinal accelerometers*. The AK residuals for instrument 2 also grow quadratically, but much faster due to the bias present in that instrument. The AK SPRT's reflect this residual behavior, with the SPRT for instrument 1 remaining below the no-fail threshold until $t=5$ sec and the SPRT for instrument 2 remaining below the no-fail threshold until $t=13$ sec. At the normal accelerometer TK ETL of 53 seconds, the outer loop examines the AK QSPRT and SPRT's and determines that no failure is present.

7.2.3 Mach Meters and Alpha Vanes

Results of simulation in thunderstorm turbulence of time triggers for the Mach meters and alpha vanes are presented in Figure 7-3. Because only the residuals for translational dynamics are observable for all time following a bias failure, the outer loop uses only the TD QSPRT and SPRT in its failure decisions for these instruments. The left column of Figure 7-3 shows the time trigger results for the Mach meters, while the right column gives these results for the alpha vanes. As described in Section 4.6 there are two residuals for each instrument, one in the longitudinal direction and one in the normal direction. These residuals are the second through the fifth variables shown in Figure 7-3.

Observing the Mach meter results in the left column, the TD QSPRT crosses the negative threshold in 1 second and remains below that

* Note that the aircraft is no longer at zero bank angle because of the effects of turbulence.

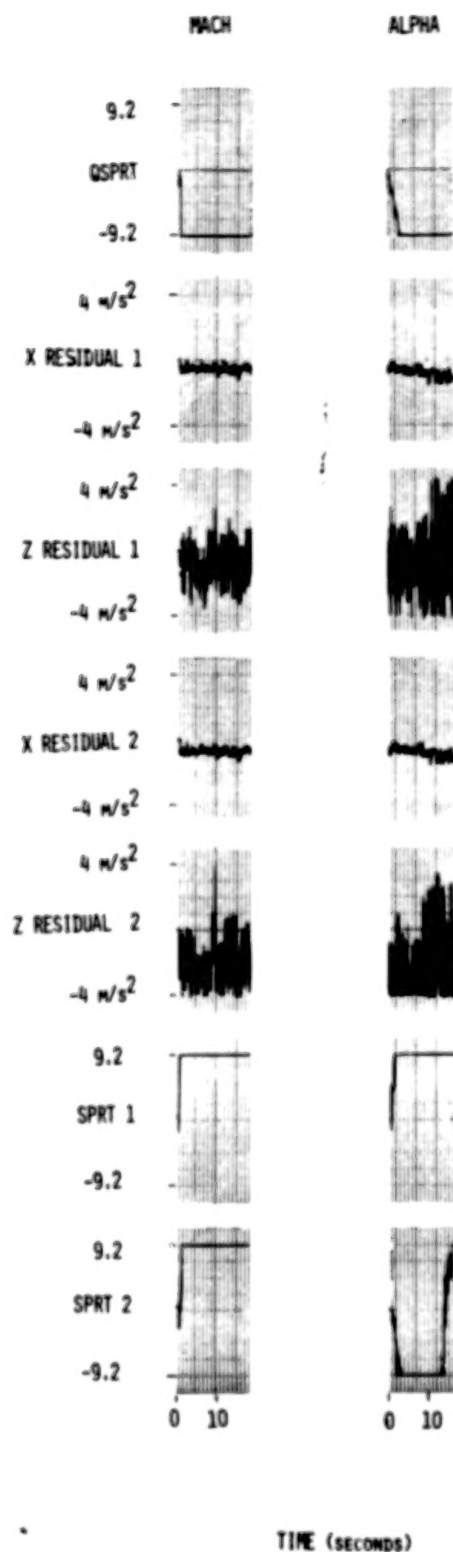


Figure 7-3 Mach Meter and Alpha Vane Time Trigger Performance

level for the rest of the run. The x and z residuals for instrument 1 are quite noisy, reflecting the high turbulence level. In addition, both residuals are biased due to the combined effects of the biases on the number 2 accelerometers and alpha vane. The residuals for the number 2 Mach meter are similar in shape to those of instrument 1 but biased even more due to the presence of the 0.4 BFM bias on Mach meter 2. These biases are much smaller than expected by the SPRT's, however, since they are looking for the effects of a Mach bias of 0.23. Thus, both SPRT's cross the no-fail threshold within 2 seconds, and remain above that level to the end of the run. After the Mach meter TD ETL of 18 seconds, the outer loop examines the TD QSPRT and SPRT's and determines that no failure has occurred.

The results for the alpha vanes are shown in the right column of Figure 7-3. The TD QSPRT crosses the negative threshold after 3 seconds, and remains below that level. The x residuals for instrument 1 and 2 are essentially identical, indicating the insensitivity of this channel to alpha vane bias. There is a low frequency drift in the alpha vane x residuals not present in the Mach meter residuals due to a different turbulence sequence in the alpha vane simulation. The low frequency shape of the z residuals are similar for alpha vanes 1 and 2, reflecting the effects of turbulence, but the residual bias for instrument 2 is of higher magnitude than that for instrument 1 due to the bias on alpha vane 2. Note that the magnitude of the high frequency noise on the alpha vane z residuals is larger than that of the Mach meter z residuals due to the fact that the average of the two alpha vanes is used to compute the residuals for the Mach meters. The converse effect on the x residuals is much less obvious due to the scaling of the plots. The TD SPRT for alpha vane 1 crosses the no-fail threshold at 2 seconds and remains above that level. However, the TD SPRT for alpha vane 2, following the effect of the instrument bias and the low frequency wind shear, crosses the failure threshold at t=3 sec and remains below that level until t=14 sec. It then crosses the no-fail threshold two seconds later. At the alpha vane TD ETL of 16 seconds, the outer loop examines the TD QSPRT and SPRT's and determines that no failure has occurred. However, the large amount of time during which the SPRT for alpha vane 2 remains below the failure threshold does indicate a high probability of provisionally failing, after a time trigger, an alpha vane with a bias of smaller magnitude

than half the present BFM. If this were to create a problem in an operational environment, it could be alleviated by raising the alpha vane BFM, since the problem stems from the relative effects of an alpha BFM failure versus the error in the TD test due to other instrument biases and table errors. An increase in the alpha vane BFM will not require increasing the BFM's of any other instrument since alpha does not have a first order effect in the primary tests of the other instruments.

7.3 Redundancy Trigger Performance

The direct redundancy trigger and subsequent identification logic for each instrument type was tested in a moderate turbulence environment with rms winds of 1.2 m/s. In each case, the number 2 instrument of every type contained a bias of +0.4 BFM, while the number 1 instrument of every type other than the one being tested contained no bias. The test for each instrument type was initiated by inserting a failure bias of size -BFM on the number 1 instrument.

7.3.1 Rate Gyros

The results for the rate gyros are shown in Figure 7-4. Only the direct redundancy (DR) SPRT and the RK QSPRT, RK residuals and RK SPRT are given since DR and RK are the primary tests for these instruments. The left column gives the results for the roll rate gyros, the center column the results for the pitch rate gyros, and the right column the results for the yaw rate gyros. The time at which detection occurs can be seen as the time at which the DR SPRT changes from zero. These detection times are .25 seconds for roll and .19 seconds for pitch and yaw. For all three instrument types the DR SPRT immediately confirms the presence of a failure. Correct identification occurs when the RK QSPRT crosses the failure threshold, since by that time the RK SPRT for instrument 1 is both below the failure threshold and below the RK SPRT for instrument 2. These failure identification times are 2.3 seconds after the failure for the roll rate gyros, 7.3 seconds for the pitch rate gyros and 8.1 seconds for the yaw rate gyros.

7.3.2 Accelerometers

The results for the accelerometers are given in Figure 7-5. As in Figure 7-2, only the quantities associated with the primary test for each accelerometer type are given: TK for the longitudinal accelerometers, TD for the lateral accelerometers and AK for the

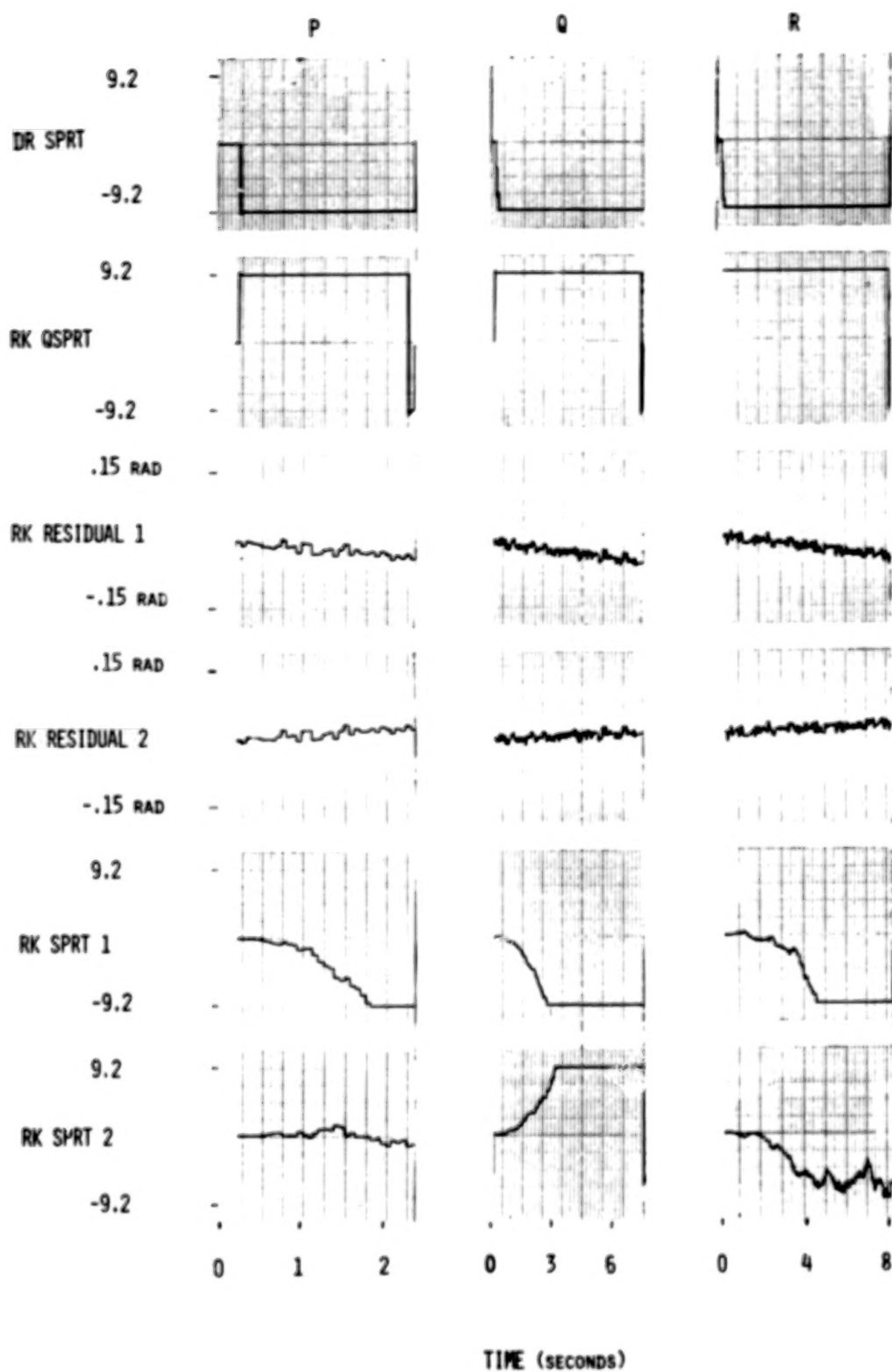


Figure 7-4 Rate Gyro Direct Redundancy Trigger Performance

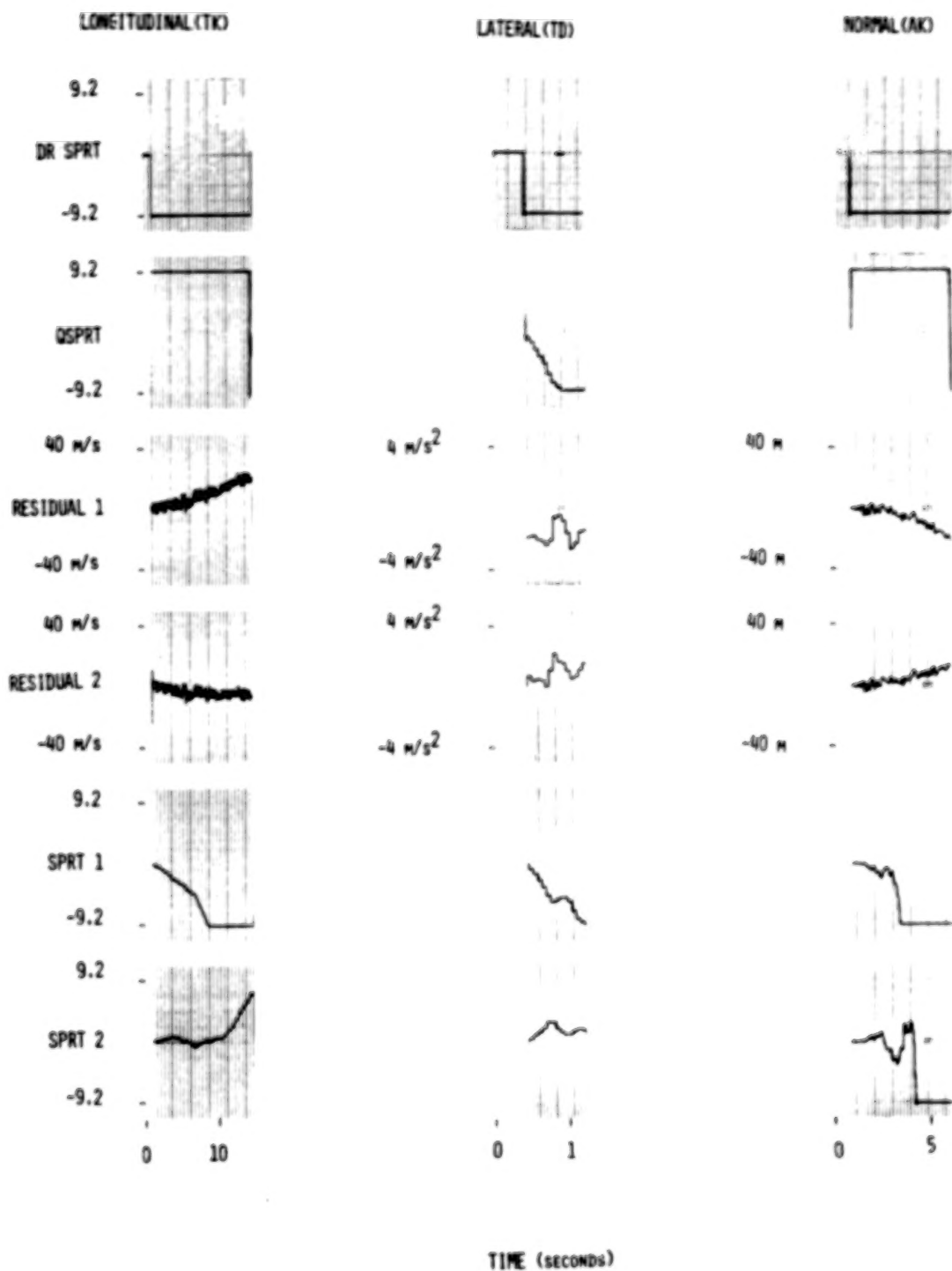


Figure 7-5 Accelerometer Direct Redundancy Trigger Performance

normal accelerometers. In addition the DR SPRT's for the three accelerometer types are also given as the first quantity plotted for each instrument. The times at which the BFM-sized failures are detected are 1 second for the longitudinal accelerometers, 0.38 seconds for the lateral accelerometers and 0.69 seconds for the normal accelerometers. The times at which the number 1 instrument of each type are correctly identified as failed are 14.5 seconds for longitudinal accelerometer 1, 1.25 seconds for lateral accelerometer 1 and 6.38 seconds for normal accelerometer 1. Identification for the longitudinal and normal accelerometers occurs when the QSPRT crosses the failure threshold, since by that time the SPRT for instrument 1 is both below the SPRT for instrument 2 and below the failure threshold. Because of a particularly bad sequence of beta vane noise the TD SPRT for lateral accelerometer 1 crosses the failure threshold after the TD QSPRT. Thus correct identification of lateral accelerometer 1 is delayed until its TD SPRT crosses the failure threshold approximately 0.38 seconds after the TD QSPRT crossing.

7.3.3 Mach Meters and Alpha Vanes

Simulations of -BFM failures on the number 1 Mach meter and alpha vane were made, and the results for the alpha vanes are given in Figure 7-6. Before discussing this figure, we will summarize the results for the Mach meters. No figure is given for the Mach meters because failure identification is made at the time of failure detection, using the window of stored TK residuals as described in Section 4.7.7. Correct identification of the failure of Mach meter 1 occurs 0.25 seconds after failure injection.*

In the alpha vane results shown in Figure 7-6, the same quantities are plotted as in Figure 7-3, with the addition of the alpha vane DR SPRT. The failure of an alpha vane is detected at 1.2 seconds, the DR SPRT immediately confirms the presence of the failure, and the failure of alpha vane 1 is correctly identified at 2.3 seconds. In this case the TD SPRT for instrument 1 crosses the failure threshold after the TD QSPRT because of the additive effects of the actual Mach bias and table errors, which are RSS'd in calculating the QSPRT. Modification of the QSPRT calculations so that all error effects are summed will remove this possibly troublesome situation.

* This number represents CSDL simulation only, since time constraints prevented including the Mach meter TK SPRT's in the Langley simulation.

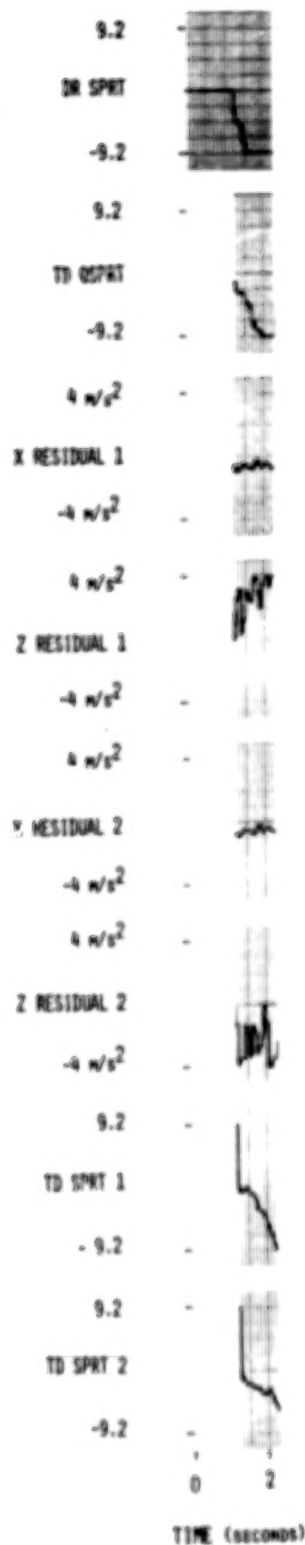


Figure 7-6 Alpha Vane Direct Redundancy Trigger Performance

7.3.4 Attitude Gyros, Altimeters

As with the Mach meters, failure identification for the attitude gyros and altimeters is accomplished by first using as inputs to the SPRT's the window of stored residuals. If there is not enough information in this window of residuals to make an identification, additional residuals are processed sequentially after failure detection. Because in these simulations at most three additional samples after detection were required for identification, the strip chart recordings are quite short and difficult to read. Therefore no figure will be presented for the attitude gyros. The results are summarized in Table III.

Table III Attitude Gyro and Altimeter Simulation Results

Instrument Type	Detection Time (sec)	Identification Time (sec)
ϕ	1.5	1.5
θ	1.375	1.5625
ψ	1.375	1.5
h	1.125	1.1875

7.4 Hard Failure Identification

In addition to the BFM failure simulations described above, larger bias failures were simulated for the rate gyros and accelerometers. The simulation included thunderstorm turbulence and +0.4 BFM biases on instrument 2 of every type. The inserted biases were $-\frac{1}{2}g$ on the number 1 accelerometers and -0.1 rad/sec on the number 1 rate gyros. The results are summarized in Table IV. In all cases the number 1 instrument was correctly identified as failed. The times given in the table are the time from failure injection to the given event.

We note that the failed normal accelerometer is not provisionally failed or identified as failed for three seconds. Because the instrument outputs are being averaged for use in the autopilot, this means that an erroneous 1/4g acceleration signal will be fed to the autopilot. It is important to note that the thunderstorm turbulence subjects the aircraft to 1/3g normal accelerations for as long as ten seconds. Thus,

Table IV Hard Failure Simulation Results

Instrument	Detection (sec)	Provisional Failure (sec)	Failure Identification (sec)
a_x	0.25	—	0.9375
a_y	0.1875	0.1875	0.3125
a_z	0.1875	—	3.0
p	0.125	0.625	0.875
q	0.0625	0.4375	1.125
r	0.125	0.625	1.1875

the erroneous $1/4g$ signal for 3 seconds should not adversely affect a control system designed to perform well in thunderstorm turbulence. In the absence of high turbulence, the translational dynamics test will quickly provisionally fail the bad accelerometer, removing it from autopilot calculations.

TABLE OF CONTENTS

<u>Section</u>		<u>Page</u>	
1	SUMMARY AND INTRODUCTION	1	1/A9
2	FDI STRUCTURE	9	1/B3
	2.1 Introduction	9	1/B3
	2.2 Redundancy Trigger	9	1/B3
	2.3 The Sequential Probability Ratio Test	10	1/B4
	2.4 Time Trigger	12	1/B6
	2.5 Failure Identification by the Outer Loop	13	1/B7
3	ANALYTIC REDUNDANCY SPRT's	15	1/B9
	3.1 Introduction	15	1/B9
	3.2 Translational Kinematics	16	1/B10
	3.3 Translational Dynamics	21	1/C1
	3.4 Rotational Kinematics	24	1/C4
	3.5 Altitude Kinematics	28	1/C8
4	CALCULATION OF FDI SYSTEM PARAMETERS	33	1/C13
	4.1 Introduction	33	1/C13
	4.2 Rate Gyros	33	1/C13
	4.3 Attitude Gyros	37	1/D3
	4.4 Accelerometers	43	1/D9
	4.5 Altimeters	50	1/E2
	4.6 Alpha Vanes and Mach Meters	52	1/E4
	4.7 Additional Tests	55	1/E7
	4.8 Summary	60	1/E12
5	QUALITY SPRT's	63	1/F1
6	OUTER LOOP LOGIC	69	1/F7
	6.1 Introduction	69	1/F7
	6.2 Failure Identification - Redundancy Trigger ...	69	1/F7
	6.3 Failure Identification - Time Trigger	71	1/F9
	6.4 Additional Outer Loop Tasks	71	1/F9

<u>Section</u>		<u>Page</u>	
7	SIMULATION RESULTS	73	1/F11
	7.1 Introduction	73	1/F11
	7.2 Time Trigger Performance	73	1/F11
	7.3 Redundancy Trigger Performance	84	1/G8
	7.4 Hard Failure Identification	89	1/G13
8	APPLICATION TO FLIGHT TEST DATA	91	2/A6
	8.1 Introduction	91	2/A6
	8.2 Discussion of Flight Data	91	2/A6
	8.3 Calculation of FDI System Parameters	95	2/A10
	8.4 FDI Algorithm Modifications	102	2/B3
	8.5 Injected Failure Identification	105	2/B6
	8.6 Summary	114	2/C1
9	CONCLUSIONS AND RECOMMENDATIONS	159	2/F4
<u>Appendix</u>			
A	TURBULENCE ESTIMATOR	163	2/F8
B	AERODYNAMIC COEFFICIENT APPROXIMATION	167	2/F12
C	SCALE FACTOR FAILURES	171	2/G2
D	SIMULTANEOUS ϕ AND θ FAILURES	175	2/G6
E	DESIGN AND PERFORMANCE OF AN ALTITUDE KINEMATICS FILTER	179	2/G10
	E.1 Introduction	179	2/G10
	E.2 AK Filter Design	179	2/G10
	E.3 Acceleration Bias Estimation	182	2/G13
	E.4 Performance Results	184	3/A6
F	COMPENSATION OF TURN ERROR IN DIRECTIONAL GYROS	189	3/A11
	F.1 Introduction	189	3/A11
	F.2 Derivation of Turn Error Expression	190	3/A12
	F.3 Results of Turn Error Compensation of Flight Data	196	3/B4
	F.4 Summary and Conclusions	199	3/B7
	LIST OF REFERENCES	208	3/C2

LIST OF ILLUSTRATIONS

Figure		Page	
4-1	Low Turbulence Wind Profile	46	1/D12
7-1	Rate Gyro Time Trigger Performance	75	1/F13
7-2	Accelerometer Time Trigger Performance	80	1/G4
7-3	Mach Meter and Alpha Vane Time Trigger Performance .	82	1/G6
7-4	Rate Gyro Direct Redundancy Trigger Performance	85	1/G9
7-5	Accelerometer Direct Redundancy Trigger Performance	86	1/G10
7-6	Alpha Vane Direct Redundancy Trigger Performance ...	88	1/G12
8-1	Segment 1	117	2/C4
8-2	Segment 1 (cont.)	118	2/C5
8-3	Segment 2	119	2/C6
8-4	Segment 2 (cont.)	120	2/C7
8-5	Segment 3	121	2/C8
8-6	Segment 3 (cont.)	122	2/C9
8-7	Segment 4A	123	2/C10
8-8	Segment 4A (cont.)	124	2/C11
8-9	Segment 4B	125	2/C12
8-10	Segment 4B (cont.)	126	2/C13
8-11	Segment 4C	127	2/C14
8-12	Segment 4C (cont.)	128	2/D1
8-13	Segment 4D	129	2/D2
8-14	Segment 4D (cont.)	130	2/D3
8-15	Segment 5	131	2/D4
8-16	Segment 5 (cont.)	132	2/D5
8-17	Segment 6	133	2/D6
8-18	Segment 6 (cont.)	134	2/D7
8-19	Segment 4C, Roll Rate Gyro 1 +BFM Bias at T=29,RK ..	135	2/D8
8-20	Segment 4A, Roll Rate Gyro 2 +BFM Bias at T=0,RK ...	136	2/D9
8-21	Segment 3, Roll Rate Gyro 2 Fail to Zero at T=0,RK .	137	2/D10
8-22	Segment 4C, Pitch Rate Gyro 1 -BFM Bias at T=29,RK.	138	2/D11
8-23	Segment 4A, Pitch Rate Gyro 2 +BFM Bias at T=0,RK...	139	2/D12
8-24	Segment 3, Pitch Rate Gyro 2 Fail to Zero,RK.....	140	2/D13
8-25	Segment 4C, Yaw Rate Gyro 2 -BFM Bias at T=29,RK....	141	2/D14

List of Illustrations (cont.)

Figure		Page	
8-26	Segment 4A, Yaw Rate Gyro 1 +BFM Bias at T=0,RK.....	142	2/E1
8-27	Segment 3, Yaw Rate Gyro 1 Fail to Zero at T=0,RK....	143	2/E2
8-28	Segment 2, Roll Attitude Gyro 1 -BFM Bias at T=37,RK.	144	2/E3
8-29	Segment 2, Pitch Attitude Gyro 1 +BFM Bias at T=37,RK	145	2/E4
8-30	Segment 4B, Mach Meter 1 -BFM Bias at T=130,TK.....	146	2/E5
8-31	Segment 4B, Mach Meter 1 +BFM Bias at T=160,TK.....	147	2/E6
8-32	Segment 4A, Mach Meter 2 +BFM Bias at T=8,TK.....	148	2/E7
8-33	Segment 4B, Alpha Vane 1 +BFM Bias at T=130,TD.....	149	2/E8
8-34	Segment 4C, Alpha Vane 1 +BFM Bias at T=36,TD.....	150	2/E9
8-35	Segment 4B, Longitudinal Accelerometer 2 +BFM Bias at T=80,TK.....	151	2/E10
8-36	Segment 4A, Longitudinal Accelerometer 1 Fail to Zero at T=0,TK.....	152	2/E11
8-37	Segment 4A, Lateral Accelerometer 2 -BFM Bias at T=12,TD.....	153	2/E12
8-38	Segment 4C, Lateral Accelerometer 2 +BFM Bias at T=36,TD.....	154	2/E13
8-39	Segment 4B, Normal Accelerometer 2 -BFM Bias at T=90,AK.....	155	2/E14
8-40	Segment 4B, Normal Accelerometer 2 -BFM Bias at T=125,AK.....	156	2/F1
8-41	Segment 4B, Normal Accelerometer 2 -BFM Bias at T=140,AK.....	157	2/F2
8-42	Segment 4C, Normal Accelerometer 1 +BFM Bias at T=10,AK.....	158	2/F3
A-1	Continuous Velocity Estimator	163	2/F8
A-2	Residual Processing	164	2/F9
E-1	Segment 2, AK Filter Performance without Additive Acceleration Bias	186	3/A8
E-2	Segment 2, AK Filter Performance with and without Additive Acceleration Bias	187	3/A9
F-1	Elements of Error Geometry for a Directional Gyro...	191	3/A13
F-2	Turn Error Due to Non-horizontal Floor Plane	194	3/B2
F-3	Spherical Geometry for Non-horizontal Spin Axis ...	194	3/B2
F-4	Turn Error Due to Non-horizontal Spin Axis	196	3/B4
F-5	Attitude History for Segments 2, 3, 4A and 4C	201	3/B9
F-5	(cont.)	202	3/B10
F-6	Segment 4A, Turn Error Compensation Assuming Horizontal Spin Axes	203	3/B11
F-7	Segment 4A, Turn Error Compensation Assuming Non-horizontal Spin Axes	204	3/B12

List of Illustrations (cont.)

Figure		Page	
F-8	Segment 2, Turn Error Compensation Assuming Non-Horizontal Spin Axes	205	3/B13
F-9	Segment 3, Turn Error Compensation Assuming Non-horizontal Spin Axes	206	3/B14
F-10	Segment 4C, Turn Error Compensation Assuming Non-horizontal Spin Axes	207	3/C1

LIST OF TABLES

Table		Page	
I	Sensor Information	16	1/B10
II	Summary of FDI System Parameters	61	1/E13
III	Attitude Gyro and Altimeter Simulation Results	89	1/G13
IV	Hard Failure Simulation Results	90	1/G14
V	Flight Data Segment Times	91	2/A6
VI	Minimum BFM and Standard Deviation Data	97	2/A12
VII	New BFM Levels	101	2/B2
VIII	Self-Test Thresholds	104	2/B5
IX	AP-101 Execution Times	161	2/F6
B.1	Worst-Case Acceleration Error due to Polynomial Approximation	170	2/G1

SECTION 8

APPLICATION TO FLIGHT TEST DATA

8.1 Introduction

In this section we report the results of application of the FDI algorithm outlined in the previous sections to several segments of telemetry data from the flight of the F-8 DFBW aircraft. Differences between the assumed and observed instrument characteristics require some changes to the previously chosen FDI system parameters. However, the basic framework of the FDI algorithm is found sufficiently flexible that only minimal modifications are required to achieve good performance in finding failures superimposed on the flight data.

8.2 Discussion of Flight Data

Nine segments of flight data were provided by the NASA Dryden Flight Research Center for FDI algorithm analysis. The starting times and duration of these segments are given in Table V.

Table V Flight Data Segment Times

Segment	Starting Time (hr/min/sec)	Approximate Duration (sec)
1	9/47/27.064	53
2	9/54/ 7.124	66
3	9/57/ 9.24	51
4A	9/59/ 2.042	38
4B	10/01/ 0.042	180
4C	10/04/15.026	45
4D	10/05/16.065	14
5	10/08/36.002	24
6	10/21/ 0.004	70

For each segment, the outputs of two instruments are available for all redundant sensor types except altimeter, for which only one instrument output is provided for this study. In addition, nonredundant measurements of sideslip angle, elevator position, rudder position and aileron position are also available. Time histories of these variables are shown for the nine flight segments in Fig. 8-1 through 8-18. In all of these figures, the rate gyro output is in rad/sec, the attitude gyro output is in radians, the accelerometer output is in m/sec^2 , the alpha and beta vane outputs are in radians, the control surface positions are in degrees and the altimeter output is in meters. Numerical scaling of a dependent or independent variable is indicated by parentheses after the variable name enclosing the letter "E" followed by a signed integer. For example, a dependent variable name followed by "(E+2)" indicates that the ordinate value should be multiplied by 100 to obtain the value of the variable. We note that on this flight no automatic control loops are active and therefore the control surface positions reflect only pilot input.

Segment 1 includes the takeoff roll, liftoff and climbout to 600 m altitude. The engine afterburner is ignited at 2 sec and turned off at 39 sec. The F-8, which was an operational carrier-based Navy aircraft, was designed with a variable incidence wing. The wing is raised for takeoff and landing to decrease the required aircraft speed and pitch attitude angle. The transition from wing up to wing down, the standard flight position, may be seen by the dip in measured alpha* from 24 to 34 seconds into Segment 1.

For the first 36 seconds of Segment 1, the two Mach meters read appreciably different values. This is due to characteristics of the instruments which render them inoperative below Mach numbers of approximately 0.4. Also, there is a significant bias between the readings of the two yaw attitude gyros. This is to be expected, since the two instruments are independent and are not initialized to any reference azimuth. Additionally, for the first several seconds of segment 1, the alpha and beta vanes are erroneous due to insufficient dynamic pressure.

* The alpha and beta vanes are mounted on a boom extending from the nose of the aircraft, and measure the orientation of the aircraft air-relative velocity with respect to the aircraft body axes at that position.

It is important to note that the telemetry data shown in the figures are less accurate than the instrument outputs which are available to the aircraft computers. In particular, before telemetry the instrument outputs are first passed through analog signal conditioners, dedicated to each instrument, and then quantized. The instrument quantization levels for telemetry are at least four times the levels for the aircraft computers shown in Table I. By far the worst quantization degradation occurs in the altimeter output which is quantized at 30m for telemetry, compared to 3.4 m for the aircraft computer. In addition to the quantization increase in the telemetry data, comparison of the telemetry data with flight tape recordings of the instrument outputs used in the aircraft computers has revealed faulty signal conditioners for at least two of the instruments. Note that the negative peaks for yaw rate gyro 1 are less pronounced than the negative peaks for yaw rate gyro 2, resulting from a negative scale factor of less than unit magnitude for the signal conditioner of yaw rate gyro 1. Additionally, the signal conditioner for longitudinal accelerometer 1 has a higher damping coefficient than that for longitudinal accelerometer 2, resulting in less pronounced peaks and longer response times for instrument 1 relative to instrument 2.

Segment 2 is at 6.15 km altitude at Mach 0.42. During this segment there are elevator, aileron and rudder pulse and doublet commands, but the aircraft on the average is flying wings level. We mention here that a plot of a_y versus β for this segment indicates a value of $C_{y\beta}$ approximately 0.5 times the value used for this flight condition in the simulations available at the Langley Research Center

Segment 3 is similar to segment 2 but at a higher design flight condition at Mach 0.63 and 6.1 km altitude. Again there are several pulse and doublet control surface commands, with the aircraft very nearly trimmed for horizontal flight.

In segment 4A, the aircraft is at about the same airspeed and altitude as segment 3 but is in a turn with a roll angle of approximately -1.1 radians. Again several control surface pulses and doublets are present. Both the Mach number and altitude decrease as the aircraft changes heading. Note the time-varying difference between the two yaw attitude gyros. This is due to the time-varying difference in turn error for each of these directional gyros (DG's). A detailed explanation of turn error is given in Ref. 9 and

Appendix F. Here we simply note that the turn error for each DG, c , may be approximated by

$$c \approx \frac{1}{4}(\phi^2 - \theta^2) \sin 2\psi_g \quad (8.1)$$

where ψ_g is the azimuth angle between the aircraft roll axis and the angular momentum vector of the DG. Since the two DG's are not aligned, there is a difference between the turn errors for the two instruments, and in a banked turn this difference is time varying.

Segment 4B shows the aircraft at an average altitude of 6.4 km with increasing airspeed through Mach 1. At 115 seconds the ignition of the engine afterburner can be seen as a jump in the longitudinal accelerometer readings. At 130 seconds the aircraft breaks the speed of sound. At that time, large jumps occur in the outputs of the Mach meters, alpha vanes and in the barometric altimeter. These jumps are fictitious relative to the true aircraft state, and in fact these instrument types are in error from a time of about 100 seconds until after the speed of sound crossing. These errors are associated with shock induced local air flow variations which are present in the transonic flight regime. In addition, at supersonic speeds the alpha vane is biased by approximately +0.02 rad due to interaction with the shock wave formed at the tip of the air data boom. Clearly, the TK, TD and AK analytic redundancy tests will have test errors during the transonic region associated with the fictitious behavior of the air data sensors. In Section 8.4.2 we discuss the adaptation of the FDI algorithm to take these errors into account.

In segments 4C and 4D, the aircraft is oscillating in Mach number and altitude. Allowing for the sixteen second gap between the two segments, the time histories of Mach and altitude after the elevator spike at 11 seconds into segment 4C suggest excitation of the phugoid mode of the aircraft. The latter part of segment 4C contains the highest dynamic pressure encountered in the telemetry data.

For the first part of segment 5, the aircraft is at Mach 1.24 at an altitude of 12.2 km. After 16.2 seconds, the engine afterburner is turned off, and the airspeed begins decreasing. At 19.4 seconds the failure of one of the onboard computers results in loss of the altimeter data. Note that nearly twice the bias that existed in

earlier segments between the two roll angle measurements is present in segment 5. We also observe that between the end of segment 4D and the beginning of segment 5, a time of approximately 3 1/2 minutes, the yaw attitude has changed by about 2.7 radians. If we hypothesize that a long, shallow turn was carried out in this time interval, the increased bias between the roll attitude measurements may be explained by vertical gyro drift during erection cutout.

The vertical gyro (VG) is a two degree of freedom gyro with its spin axis slaved by a torque motor to a highly damped pendulum. In unaccelerated flight, the gimbal angles are therefore equal to the roll and pitch Euler angles. However, during long periods of longitudinal or lateral acceleration, the pendulum moves from alignment with the gravity vector to alignment with the specific force vector, and if the spin axis is slaved to the pendulum the gimbal angles will no longer correspond to roll and pitch angles. Thus it is desirable to remove the slaving of the gyro to the pendulum in the presence of acceleration. In most VG's, the question of longitudinal acceleration is ignored, but lateral acceleration is deduced by the presence of a sustained yaw rate. In the instruments aboard this aircraft, each vertical gyro has a self-contained yaw rate gyro whose output is fed through a first order low-pass filter with a time constant of 15 seconds. If the magnitude of this filtered output is greater than 0.0044 rad/sec, the roll slaving torque to the gyro is set to zero. When this erection cutout occurs, the roll angle measurements are degraded in time by the drift rates of the VG, which are specified to be no higher than 7.2×10^{-5} rad/sec per axis. During erection, the erection rate is required to be between 2.3×10^{-4} and 5.2×10^{-4} rad/sec. Later we will discuss possible incorporation of erection cutout logic into the FDI algorithm.

Segment 6 includes the aircraft touchdown at approximately 57 seconds. Altitude and Mach data are unavailable. The wing is raised throughout the entire segment, and moderate turbulence is present.

8.3 Calculation of FDI System Parameters

The groundrule for this study of flight data is that with the exception of the altimeter in segments 5 and 6, the telemetry data

should be considered as coming from unfailed instruments. Thus the FDI algorithm must be modified to give good performance when applied to the telemetry data; in particular there should be no direct redundancy triggers or false identifications on time triggers over the nine segments.

As a first step in the modification process, the differences in the outputs of the redundant instrument pairs are examined to determine the means and variances of the differences over one second windows. Recall from Section 4.3.1 that the direct redundancy threshold is set at 0.75 BFM. Thus the worst-case mean values establish minimum BFM sizes in that there will be no direct redundancy trigger on any instrument if the BFM for each instrument type is greater than four-thirds its worst case mean difference. Additionally, the variance of the instrument differences may be considered to be an estimate of twice the individual instrument variance. The calculated values for the minimum BFM's and estimated sensor noise standard deviations are given in Table VI. Note that there is no minimum BFM given for the DG's. In order to compensate the DG output for turn error it is necessary to know the angle between the spin vector of the instrument and the roll axis of the aircraft when the instrument reading is zero. With this information, it is possible to remove turn error from each of the instruments and run a direct redundancy trigger on the directional gyros. Unfortunately, this calibration information is not directly available and must be inferred from the noisy instrument outputs during maneuvers. Because of the preliminary nature of the DG turn error correction scheme and the present unavailability of sufficient telemetry data to verify the technique, we will not attempt to do FDI for the DG's here, and the rate gyro RK QSPRT's will assume nominal DG performance uncompensated for turn error. The question of DG FDI and turn error correction is discussed in Appendix F.

In the remainder of this subsection we will discuss the procedure by which the BFM's and ETL's for the various instrument types are chosen. Only the primary tests, those capable of identifying a BFM-sized failure, will be discussed. The calculation of B and ETL values for the secondary tests is straightforward.

8.3.1 Attitude Rate Gyros

In the case of the rate gyros, the BFM's are established by examination of time trigger RK residuals for the various segments.

Table VI Minimum BFM and Standard Deviation Data

Instrument Type	Minimum BFM	Standard Deviation
Mach	.01	.0023
α (rad)	.011	.005
a_x (m/sec ²)	2.0	.23
a_y (m/sec ²)	.08	.043
a_z (m/sec ²)	.88	.289
p (rad/sec)	.053	.005
q (rad/sec)	.032	.002
r (rad/sec)	.029	.002
ϕ (rad)	.08	.005
θ (rad)	.037	.0019
ψ (rad)	—	.005
δ (rad)	—	.005

The BFM values are chosen to be double the worst case bias present on the instruments implied by the RK residuals. In this way, BFM values of 0.062 rad/sec for p and 0.04 rad/sec for q and r are selected. In order to calculate the RK ETL's for the rate gyros, we assume attitude gyro noise standard deviations of 0.005 rad for ϕ and ψ and 0.002 rad for θ . The derivation follows the development of Section 4.2, except that the initialization now is done using raw angle measurements instead of the filtered estimates used before. Because of the increased unfailed rate gyro biases compared to the decreased attitude gyro noise, the bias in the filtered attitude estimate due to a BFM/2 bias on an unfailed rate gyro plus three times the standard deviation of the filtered estimate is now larger than three times the raw attitude measurement standard deviation. So we assume an initial attitude bias b of 0.015 rad for p and r and 0.006 rad for q . Since our sample period must be a multiple of the telemetry sample period of 20 msec, we choose a sample period T of 0.06 sec. Substituting these values and the BFM and σ^2 numbers mentioned above into Eq. (4.3) gives T_m values of 1.8 sec for p , 2.1 sec for q and 2.8 sec for r . In the past we have chosen the RK ETL's to be 1.5 times T_m . However, in the case

of the attitude rate gyros we note that substantial attitude error in the RK test may occur due to turn error in the directional gyros. In order to allow the signature of a BFM rate gyro bias, which is proportional to time, to exceed this test error, we set the RK ETL's for all three rate gyros to 40 sec. Additionally the turn error contribution to total test error is added to the rate gyro RK QSPRT's. This will be discussed in Section 8.4 together with other program modifications.

8.3.2 Vertical Gyros

The choice of BFM for the vertical gyros is made simple by the fact that there are no time triggers for these instruments. Thus we may choose the BFM's on the basis of Table VI only, and we choose the BFM to be 0.08 rad for ϕ and 0.037 rad for θ . Using Eq. (4.8) to find τ_m , the mean time to detect, we obtain values of 0.18 sec for ϕ and 0.12 sec for θ , where these numbers have been rounded to the next highest multiple of the sample period. Thus the $\tau_m/3$ term in Eq. (4.6) will be 0.06 for both ϕ and θ , since it must be an integral factor of the sample period T. We choose the initial attitude error to be the sum of the bias due to a BFM/2 bias in the corresponding rate measurement plus three times the standard deviation of the estimation error. These figures are:

$$M_{\phi} = 0.021 \text{ rad}$$

$$M_{\theta} = 0.012 \text{ rad}$$

Substituting these values into Eq. (4.8) results in ETL's of 0.29 sec for ϕ and 0.42 sec for θ .

The mechanism of vertical gyro erection cutout was described earlier. The minimum BFM level for ϕ in Table VI is required for segment 5, which follows a period of erection cutout. A value 29% lower could be used over the other flight segments. In order to attain maximum performance during erection, BFM logic for ϕ could be implemented using a filtered estimate of yaw rate from the yaw rate gyros analogous to the signal used by the vertical gyro. Two BFM levels for roll attitude would be used, with the calculated BFM value always lying between the two levels. The BFM calculation would proceed as follows: during erection the calculated BFM level would go toward (but not below) the lower

level at the erection rate, and during erection cutout the calculated BFM level would go toward (but not above) the higher level at the maximum specified drift rate. Unfortunately, this technique is impractical for use with the telemetry segments. Because the minimum BFM level for the yaw rate gyros is more than three times the level for erection cutout, the biased yaw rate instruments will tend to keep the ϕ BFM at its higher level. On the other hand, the poor yaw rate gyro behavior in the telemetry data appears to be due to a faulty analog signal conditioner and not to the instruments themselves. Thus the FDI algorithm for onboard tests might utilize a yaw rate gyro BFM which is low enough to make this vertical gyro variable BFM scheme workable.

8.3.3 Accelerometers

Recall that the primary test for the longitudinal accelerometers is TK. We will set the a_x BFM at 2m/sec^2 and assume a measurement noise standard deviation of 0.3m/sec^2 consistent with the corresponding figures in Table VI. Using the values for T_0 and σ^2 assumed in Section 4.4.2, the new TK ETL's are calculated to be 32 sec for low turbulence and 48 sec for high turbulence. We note that because throttle position and afterburner information are unavailable on the aircraft, TD is not available for the longitudinal accelerometer.

The primary test for the lateral accelerometer is TD. Although the fact that the dynamic effect of sideslip angle was observed to be approximately half the assumed value allows the worst-case table bias coefficients for the lateral channel in Table B.1 to be reduced from 0.65 to 0.3, we will retain the lateral accelerometer BFM at 2m/sec^2 since no lower level can be identified throughout the flight envelope. We also extend the TD ETL to 20 seconds to allow for the larger test error assumed from table error and beta vane bias at high Mach numbers. Because of the extremely large q and r BFM levels dictated by the telemetry data, TK is essentially useless for failure identification for the lateral and normal accelerometers.

The primary test for the normal accelerometers is AK. We again choose the BFM to be 1.5m/sec^2 . Because of the large altitude quantization, the values of e and M used in Section 4.7.6 are raised to 3 m/sec and 21 m respectively. Also σ^2 , the variance of the altitude measurements, is raised to 147 m^2 . Substitution of these values into Eq. (4.23) gives an AK ETL of 47 sec.

The BFM and ETL values for the accelerometers derived above produced no false failure identifications during time triggers run over the nine telemetry segments. However, in order to avoid false identifications in the transonic region, the QSPRT's for some of the tests must be modified to accommodate anomalous air data sensor behavior observed in segment 4B. These modifications will be discussed in Section 8.4.

8.3.4 Mach Meters and Alpha Vanes

The primary test for the Mach meters is TK, and we follow the development of Section 4.7.7. For practical considerations, the BFM and ETL derived for the high turbulence case are used in both the high and low turbulence situations. Because of the decreased Mach noise, we have

$$v = 9 \times 10^{-6}$$

$$M = 1.21 \text{ m/sec}$$

We assume a conservative high turbulence wind shear of

$$b = 5.0 \text{ m/sec}^2$$

and a test variance equal to the 99% Dryden wind level:

$$\sigma^2 = 30 \text{ m}^2/\text{sec}^2$$

We choose a Mach BFM of

$$B = 0.045 \mathcal{M}$$

which is essentially the minimum detectable value given these parameter choices. Solving Eq. (4.24) gives a Mach TK ETL of 0.6 sec.

The primary test for the alpha vanes is TD. The development of Section 4.6 is somewhat simplified by the fact that only the z-direction is available due to the lack of throttle information. We assume a z acceleration measurement error of 0.75 m/sec^2 , and from Appendix B a table error at the design flight condition of 0.53 m/sec^2 . We also assume two errors arising from a Mach bias of $\text{BFM}/\sqrt{2}$: the error in calculated dynamic pressure of 0.52

m/sec² and the table error due to Mach error of 0.69 m/sec². The RSS of these four errors gives a test error \bar{B} of 1.26 m/sec² at the design flight condition, which translates to a minimum alpha BFM of 0.0137 rad. Because of the rather tenuous behavior of the alpha vane TD in thunderstorm simulations, as discussed in Section 7, we have slowed the test by choosing an artificially high value of the test variance σ^2 of 40 m²/sec⁴. We choose the alpha vane BFM to be

$$B = 0.025 \text{ rad}$$

which is nearly 50% higher than before, and we calculate T_c to be 4.7 sec with a resulting TD ETL of 7 sec.

8.3.5 Summary

The BFM levels chosen for the dual redundant instruments available on the telemetry data are shown in Table VII. As mentioned earlier, on this flight insufficient data is available to allow low-level bias identification for the DG's and only a single altimeter output is provided.

Table VII New BFM Levels

Sensor Type	BFM
a_x, a_y	2.0 m/sec ²
a_z	1.5 m/sec ²
p	0.062 rad/sec
q, r	0.04 rad/sec
ϕ	0.08 rad
θ	0.037 rad
Mach	0.045
α	0.025 rad

8.4 FDI Algorithm Modifications

In this subsection we discuss some modifications to the FDI algorithm to incorporate previously unmodeled sensor behavior which is revealed in the telemetry data.

8.4.1 Mach Filter and Translational Test Delay

A 0.5 sec time constant Mach filter has been added to provide a clean estimate of Mach number at each sample time. Following a time trigger or direct redundancy trigger, the initiation of TK and TD tests is delayed until the estimated Mach exceeds a threshold value, currently 0.38. This delay in the initiation of translational tests is necessary to ensure the accuracy of Mach meter data. Additionally the QSPRT for a currently running TK or TD test is set to +9.2 when the estimated Mach drops below the threshold.

8.4.2 Modifications in Transonic Region

As mentioned in the discussion of telemetry segment 4B, the air data sensors behave badly in the transonic region. We define this region as the time that the filtered Mach estimate is between 0.91 and 1.04. Because the exact behavior of the Mach meters and altimeters in the transonic region is not known well enough for direct compensation, we assume some appropriate worst-case errors in the QSPRT's for those tests using these measurements. Additionally, the alpha vanes are biased by approximately 0.02 radians above Mach 1. This bias is removed from the alpha vanes for all TK and TD calculations at supersonic speeds, and to allow for some correction error the worst-case table errors given in Table B.1 are increased by 250 mg for TD QSPRT calculations.

The effect of the Mach meter transonic error is essentially limited to the TK test in the longitudinal direction. For this test the QSPRT includes an acceleration error of 0.77 m/sec^2 during the transonic region and a velocity error jump at Mach 1 of 18m/sec.

The effect of the erroneous altimeter behavior is limited to the AK test. The AK QSPRT contains an \dot{h} error of 12 m/sec during the transonic region and an altitude error jump at Mach 1 of 610 m in the opposite direction. To protect the altitude rate filter discussed in Section 3.5 from the jump in indicated altitude at Mach 1, the gains k_1 and k_2 are set to one and zero respectively in the transonic region.

8.4.3 Directional Gyro Turn Error Effects

The error in the rate gyro RK residuals arising from uncompensated directional gyro turn error are of the form

$$e(t) = \int_{t_0}^t \dot{c} \zeta dt = c \zeta \Big|_{t_0}^t - \int_{t_0}^t c \dot{\zeta} dt \quad (8.2)$$

where c is the directional gyro turn error and ζ is the function of ϕ and θ given by Eq. (3.16) for each of the rate gyros. We make an approximation to the absolute value of the error given in Eq. (8.2) by the following expression:

$$|e| \approx |c(t) \zeta(t)| + |c(t_0) \zeta(t_0)| \quad (8.3)$$

We note that Eq. (8.1) implies

$$|c| \leq \frac{(\phi^2 + \theta^2)}{4} \quad (8.4)$$

and we define the magnitude of the RK residual error arising from directional gyro turn error assumed for RK QSPRT calculations to be

$$E_\psi = \frac{1}{4} [(\phi^2(t_0) + \theta^2(t_0)) |\zeta(t_0)| + (\phi^2(t) + \theta^2(t)) |\zeta(t)|] \quad (8.5)$$

Although Eq. (8.5) is not strictly conservative for all hypothetical trajectories, we feel that the probability that Eq. (8.5) is optimistic in the constrained dynamic environment of an aircraft is exceedingly small. This belief is reinforced by the extremely conservative QSPRT's obtained including the term given by Eq. (8.5) when applied to the telemetry segments. We emphasize that future plans call for explicit DG turn error correction using the technique of Appendix F, obviating the need for the QSPRT term corresponding to Eq. (8.5).

8.4.4 Instrument Self-Test

One form of information which has been ignored up to this point is the fact that the change in the aircraft state between successive samples is limited by physical considerations. In order to exploit this fact, a self-test routine has been added to the FDI algorithm. A dual redundant instrument is declared failed if over a three sample interval

- 1) the magnitude of the difference between the sensor output and its output at the beginning of the interval

and

- 2) the magnitude of the difference between the sensor output and its neighbor instrument's output

both exceed a given threshold value at each sample. Of course only the test on the sensor's own output is required for a non-redundant sensor. Additionally, the sensor is provisionally failed the first time it fails the test. However, if it passes the test on one of the next two samples, the provisional failure status is removed. The threshold values currently employed for self-test are given in Table VIII. These threshold values have been chosen so that no false alarm is given by self-test for a single active instrument of any type throughout the nine telemetry segments. Because an instrument failing self-test is automatically removed from the active instrument complement, the thresholds should be chosen such that the probability of false alarm is essentially zero. Thus, if future flight data indicates that the performance of the aircraft exceeds any of these thresholds, that threshold should be raised.

Table VIII Self-Test Thresholds

Sensor Type	Threshold
a_x, a_y, a_z	.25 g
p	1.0 rad/sec
q, r	0.25 rad/sec
ϕ	0.6 rad
θ, ψ	0.15 rad
Mach	0.08
α, β	0.1 rad
h	300 m

The self-test routine is a suitable complement to the analytic redundancy FDI routines in the following way. Self-test removes an instrument with a large bias failure from all calculations in

as little as one sample period, while the analytic redundancy tests are of necessity slower in order to overcome possible unmodeled biases in other sensor types. On the other hand, the analytic redundancy tests can identify low level biases, and in many cases ramps and scale factor failures, which are totally undetectable via self-test.

8.5 Injected Failure Identification

In this subsection we review the performance of the modified FDI algorithm in identifying failures injected into the telemetry data. Although the results by no means represent an exhaustive combination of failure times, failure sizes, unfailed instrument noises etc., we feel the results are indicative of both the power of the algorithm and its limitations. The intent has been to inject failures at times of high potential test error. We have been careful to assure that the injected failures result in a failed instrument, e.g. we do not add a positive BFM bias to an instrument which already has a substantial negative bias.

For each injected failure discussed, a single figure will be presented containing four frames. The first frame indicates the time history of the direct redundancy (DR) SPRT for the failed instrument type. The remaining three frames show the time histories of quantities related to the primary form of analytic redundancy for the failed instrument type.* The second frame shows the QSPRT; the third frame shows the residuals for the two instruments, which are the inputs for their respective SPRT's; and the fourth frame shows the output of the two SPRT's. All variables are initialized to zero, and the time of failure detection by the direct redundancy trigger can best be seen as the time at which the DR SPRT first becomes nonzero. Periods during which the analytic redundancy test is not running, following false alarm indication or failure identification by the outer loop, are indicated by unchanging values of all of the plotted variables. The independent variable is time in seconds, and all of the dependent variables are dimensionless except the residuals, which have the dimensions of radians for RK, m/sec^2 for TD, m/sec for TK and meters for AK. In the third and fourth frames which contain two plots each, "x" denotes a variable associated with instrument 1 and "0" denotes a variable associated with instrument 2.

* Recall that these primary tests are RK for the attitude and attitude rate gyros, TD for the alpha vanes and lateral accelerometers, TK for the longitudinal accelerometers and AK for the normal accelerometers.

It is important to note that the SPRT's and QSPRT's plotted in the figures in this subsection have been normalized by the threshold magnitude of 9.2, and thus the failure and no-failure thresholds for the plotted variables are -1 and +1 respectively. Although we will refer to the plotted variables as QSPRT's and SPRT's, the word "normalized" should be tacitly assumed by the reader.

8.5.1 Roll Rate Gyros

Figure 8-19 indicates algorithm performance following the injection of a positive BFM bias on roll rate gyro 1 starting at 29.04 seconds of segment 4C. Reference to Fig. 8-12 indicates that at this time the aircraft is banked at 0.4 radians and is about to experience a roll rate pulse peaking at -0.6 rad/sec. The direct redundancy trigger occurs at 29.22 seconds initiating the RK tests. Following detection the DR SPRT grows progressively more negative, corroborating the trigger. Between 29.22 seconds and 30.96 seconds, the QSPRT is set at +1, indicating that $WCF > WCU$ as discussed in Section 5. At 30.96 seconds the QSPRT is set to WCF, which is negative but greater than -1. Because the SPRT for instrument 1 is less than -1 at this point, the outer loop provisionally fails roll rate gyro 1, removing it from all calculations unrelated to roll rate gyro FDI. One sample later at 31.02 seconds the QSPRT is below -1 and roll rate gyro 1 is identified as failed. Note that although the residuals for instrument 2 indicate a negative bias on that instrument with an average magnitude of approximately $BFM/3$, the SPRT for instrument 2 has no difficulty in determining that it is unfailed.

In Fig. 8-20, a positive BFM bias is added to roll rate gyro 2 from the beginning of segment 4A. In this segment the aircraft is at a bank angle of -1.1 radians. Therefore the QSPRT term due to turn error, Eq. (8.5), is generally larger in this segment than in segment 4C, and this is reflected in a longer identification time here than required for segment 4C. At $t=.18$ seconds the direct redundancy trigger is given, and the DR SPRT and the SPRT for instrument 2 both start growing negative. Until approximately 3 seconds, WCF is greater than WCU and the QSPRT is set to +1. From 3 seconds on, the QSPRT is set to WCF. At 4.68 seconds the QSPRT drops below -1, and since the SPRT for instrument 2 is below -1, instrument 2 is identified as failed. Again we note that in spite of the nonzero residuals for instrument 1, the SPRT has no difficulty in ascertaining that instrument 1 is unfailed.

In Fig. 8-21 roll rate gyro 2 is failed to zero at the beginning of segment 3. This segment contains a series of large roll rate doublets beginning at 17.7 seconds. However the roll rate gyro direct redundancy trigger is first given at 13.14 seconds due to a small negative roll rate indicated by instrument 1 compared to the zero output of instrument 1. The sign of the difference between instruments 1 and 2 is negative, and therefore the RK SPRT's are looking for the effects of a negative bias on instrument 1 and a positive bias on instrument 2. Because of the oscillatory nature of the actual roll rate, the sign of the error in instrument 2 soon changes from plus to minus, and this is reflected by the DR SPRT becoming positive. Thus at 14.64 seconds the outer loop declares a false alarm and all of the tests are terminated. We note that during the 1.5 seconds that the DR SPRT was negative, the SPRT for instrument 2 quickly crossed -1. However no identification was made because the QSPRT remained at +1, reflecting the small value of the error in instrument 1 compared to the possible test errors. At 17.7 seconds the direct redundancy trigger is again given, this time with the sign of the differences between instruments 1 and 2 being positive. Thus the RK SPRT's are initiated looking for the effects of a positive bias on instrument 1 and a negative bias on instrument 2. The DR SPRT immediately becomes negative as does the SPRT for instrument 2. In two samples, at 17.82 seconds, the QSPRT becomes negative and instrument 2 is provisionally failed. In two more samples the QSPRT crosses -1 and instrument 2 is identified as failed. The speed with which the QSPRT crosses -1 is directly related to the large difference between the two instrument outputs at this time, reflecting the large value of the true roll rate in this region.

8.5.2 Pitch Rate Gyros

Figures 8-22 through 8-24 present results for the pitch rate gyros analogous to the roll rate gyro results presented in Figs. 8-19 through 8-21. In Fig. 8-22 a negative BFM bias is added to the output of pitch rate gyro 1 at 29.04 seconds of segment 4C, and the direct redundancy trigger for the pitch rate gyros occurs at 29.16 seconds. At 30.66 seconds the QSPRT drops below -1, and since the RK SPRT for instrument 1 is also below -1 at this time instrument 1 is identified as failed. Note that the residuals for instrument 2 indicate a bias level of approximately BFM/4 on that sensor.

In Fig. 8-23 a positive BFM bias is added to the output of pitch rate gyro 2 from the beginning of segment 4A. Because of the large magnitude roll angle present during this segment, there is a large amount of turn error assumed in the pitch rate gyro RK QSPRT. This is reflected by the fact that the QSPRT remains at +1 until 33.96 seconds, at which point instrument 2 is identified as failed. Note that due to uncompensated DG turn error, the SPRT for instrument 1 is below -1 and less than the SPRT for instrument 2 for the first 16 seconds. However, no possibility for false identification exists because the RK QSPRT is +1 in that time interval.

In Fig. 8-24 the output of pitch rate gyro 2 is set to zero from the beginning of segment 3. With the onset of the negative pitch rate pulse at 5.64 seconds the pitch rate gyro direct redundancy trigger is given. Both the DR SPRT and the RK QSPRT and the RK SPRT for instrument 2 become negative immediately. After three samples the RK QSPRT becomes negative and instrument 2 is provisionally failed. At 6.3 seconds the QSPRT crosses below -1 and instrument 2 is identified as failed. The fact that the slope of the DR SPRT has just changed from negative to positive at failure identification indicates that the actual pitch rate measured by the unfailed sensor has just passed through zero.

8.5.2 Yaw Rate Gyros

Figures 8-25 through 8-27 present results for the yaw rate gyro analogous to the roll rate and pitch rate gyro results. In Fig. 8-25 a negative BFM bias is added to the output of yaw rate gyro 2 starting at 29.04 seconds of segment 4C. The direct redundancy trigger is given at 29.22 seconds, and the DR SPRT and RK SPRT for instrument 2 immediately grow negative. At 32.4 seconds WCF drops below WCU, the QSPRT is evaluated as WCF which is below -1, and instrument 2 is identified as failed. The initial ramp in the residuals for instrument 1 is due to the scale factor error in the signal conditioner for that sensor, the effect of which diminishes following the negative peak in yaw rate at 29.4 seconds.

In Fig. 8-26 a positive BFM bias is added to the output of yaw rate gyro 1 from the beginning of segment 4A. The direct redundancy trigger is given at .18 seconds. Due to the large turn error assumed by the RK QSPRT, the QSPRT is set to +1 until 20.32 seconds. In the mean time the DR SPRT and the RK SPRT for instrument 1 have both become large magnitude negative numbers. At 22.32 seconds the QSPRT

is calculated as WCF which is less than -1, and instrument 1 is identified as failed. As in Fig. 8-23 for the pitch rate gyros, there is some drift in the residuals due to DG turn error. Because the worst case turn error assumed by the yaw rate gyro RK QSPRT is proportional to $|\cos \phi|$ while the effect on the pitch rate gyros is proportional to $|\sin \phi|$, the roll angle of -1.1 radians present in this segment produces a larger effect of turn error on the pitch rate gyros than on the yaw rate gyros. This is reflected in the identification time of approximately 22 seconds in Fig. 8-26 compared to 34 seconds in Fig 8-23.

In Fig 8-27 the output of yaw rate gyro 1 is set to zero from the beginning of segment 3. The direct redundancy trigger is given eight times in the segment, but false alarm indicators are given in every case and the failure is not identified because of the low magnitudes of the actual yaw rate peaks and the fact that the yaw rate peaks appear at times of appreciable roll angle magnitude with corresponding large DG turn errors assumed by the RK QSPRT. The SPRT's for the two instruments, especially between 20 and 24 seconds, suggest that a clear decision is possible and the RK QSPRT is overly conservative in this particular run. Significantly better performance should be possible using DG outputs compensated for turn error as discussed in Appendix F. In that case little or no turn error need be assumed by the RK QSPRT's, and identification of yaw rate gyro failures to zero should be possible.

8.5.4 Vertical Gyros

Figures 8-28 and 8-29 illustrate the identification of simultaneous BFM magnitude biases on roll attitude gyro 1 and pitch attitude gyro 1, respectively, injected at 37.02 seconds into segment 2. The sign of the roll attitude gyro bias is negative and the sign of the pitch attitude gyro bias is negative. To investigate the worst-case conditions, roll rate gyro 1 and pitch rate gyro 1, which have small biases, are assumed disabled and only their larger biased companion instruments are used in the RK calculations. The sign of the injected bias on roll attitude gyro 2 is chosen to be opposite the sign of the bias in roll rate gyro 1, and the sign of the injected bias on pitch attitude gyro 1 is chosen to be opposite the sign of the bias in pitch rate gyro 2. This is the worst possible situation since the rate biases tend to cancel the effect of the bias on the

failed attitude gyro and tend to make the unfailed attitude gyro appear to be failed. Thus in the figures the sign of the residual for the unfailed attitude gyro is opposite that of the failed attitude gyro and the magnitude of the residual for the failed attitude gyro is smaller than the BFM size. It is important to remember that Figs 8-28 and 8-29 give only the values of the plotted variables after processing the stored window of residuals. Thus the sharp discontinuities should not be interpreted as actual time histories. The failure of roll attitude gyro 1 is detected by the direct redundancy trigger and identified at 37.14 seconds, while the failure of pitch attitude gyro 1 is detected and identified at 37.08 seconds. These results suggest that the more elaborate technique for VG FDI discussed in Appendix D is unnecessary.

8.5.5 Mach Meters

Recall that the primary test for the Mach meters is TK, and the bias failure signature is a jump in the $k=0$ residuals. To accommodate the jump behavior of an unfailed Mach meter in the transonic region and measurement noise, the TK QSPRT for the Mach meters assumes a worst case initialization error of 21 m/sec if detection occurs in the transonic region. This precludes identification of Mach BFM biases occurring in the transonic region. The need for this QSPRT provision is shown in Fig 8-30, in which a negative BFM bias is added to Mach meter 1 at 130 seconds of segment 4B. This is exactly the time at which the unfailed Mach meter jumps from .95 to 1.02. Note the high initial residual in unfailed instrument 2 and the low residual in instrument 1 due to cancellation of the actual jump and the injected bias. In this case the SPRT's indicate that instrument 2 would have been falsely identified as failed if the QSPRT had crossed -1. However the QSPRT remains positive and no identification is made. The DR SPRT remains negative indicating the persistence of the failure. After the TD ETL of 20 seconds, during which the secondary TD test is predictably unable to make an identification, the tests are started again. In this case there is no jump in the TK residuals, and although the QSPRT is initially below -1 no identification is possible following this or the subsequent restart. Note that following restart outside the transonic region the QSPRT quickly becomes positive to avoid false identification due to the ramps in the TK residuals arising from errors in the measured acceleration. We reiterate that although detected unidentifiable Mach BFM biases are possible in the transonic region, false identification is not.

In Fig. 8-31 a positive BFM bias is added to the output of Mach meter 1 at 160 seconds of segment 4B, and the failure is detected and identified at 160.2 seconds. In Fig. 8-32 a positive BFM bias is added to Mach meter 2 at 8.04 seconds into segment 4A, and the failure is detected and identified at 8.22 seconds.

8.5.6 Alpha Vanes

In Fig. 8-33 a positive BFM bias is added to alpha vane 1 at 130 seconds of segment 4B. The failure is detected at 130.8 seconds, and the DR and TD tests are initiated. The DR SPRT, TD QSPRT and TD SPRT for instrument 1 all grow negatively, and instrument 1 is identified as failed at 131.34 seconds. In Fig. 8-34 a positive BFM bias is added to alpha vane 1 at 36 seconds of segment 4C, a region of high dynamic pressure. Detection occurs at 36.84 seconds and identification at 37.32 seconds.

8.5.7 Longitudinal Accelerometers

Recall that the primary test for the longitudinal accelerometers is TK and that allowance for possible wind shear by the QSPRT makes detection times rather long. Additionally the QSPRT terms allowing for Mach meter behavior preclude BFM bias identification in the transonic region. However, because the effect of a longitudinal accelerometer bias persists as a ramp in the TK residuals, identification is only delayed and not prohibited as in the case of a Mach meter bias. This is illustrated in Fig 8-35 in which a positive BFM bias is added to longitudinal accelerometer 2 at 80 seconds into segment 4B. The failure is detected by the redundancy trigger at 80.82 seconds, and the DR SPRT and analytic redundancy tests are initiated. By our definition the transonic region is between 85 and 135 seconds of this segment. Thus at 85 seconds additional noise terms begin to be added to the TK QSPRT, and this prevents the QSPRT from becoming negative before the TK ETL of 32 seconds has elapsed. During this time the DR SPRT indicates there is no doubt that a failure is present. Thus at 113 seconds the DR SPRT and TK tests are restarted. Again the DR SPRT grows quite negative indicating the bias is still present, but the terms added to the TK QSPRT to accommodate Mach meter behavior in the transonic region do not allow WCF to drop below WCU before the TK ETL has elapsed. Thus a second restart is begun at 145 seconds, which is beyond the transonic region. Again the SPRT and the TK SPRT

for instrument 2 immediately grow negative. At 158 seconds the QSPRT becomes negative and instrument 2 is provisionally failed, and at 160.2 seconds the QSPRT crosses -1 and instrument 2 is identified as failed.

Although in most cases a failure to zero of a longitudinal accelerometer cannot be identified, it is possible in segment 4A, where the average longitudinal acceleration is .22 g. In Fig. 8-36 the output of longitudinal accelerometer 1 is set to zero from the beginning of segment 4A. Detection by the direct redundancy trigger occurs at .78 seconds. From that point on the DR SPRT and the TK SPRT for instrument 1 grow progressively more negative. At 20.7 seconds the TK QSPRT becomes negative and instrument 1 is provisionally failed, and when the QSPRT crosses -1 at 21.4 seconds instrument 1 is identified as failed.

8.5.8 Lateral Accelerometers

Figure 8-37 depicts the identification of a negative BFM bias on lateral accelerometer 2 injected at 12 seconds of segment 4A. In this segment there is a steady-state sideslip angle of -.02 radians, with a large aileron doublet and subsequent sideslip oscillation beginning at 14 seconds. The lateral accelerometer direct redundancy trigger is given at 12.48 seconds. As shown in the figure the DR SPRT, TD QSPRT and TD SPRT for instrument 2 all start growing negative. In these lateral accelerometer runs a factor of 0.3 was used to multiply the stored $C_{Y\beta}$ function, and the near zero residuals for unbiased instrument 1 before 14 seconds indicate that this correction is fairly accurate. The oscillatory behavior of the residuals starting at 14 seconds arises from the combined effects of neglecting the $C_{Y\delta a}$ term and $C_{Y\beta}$ error. The variance used in the lateral accelerometer TD SPRT's, currently $9.3 \text{ m}^2/\text{sec}^4$, is sufficiently large that these oscillations cannot lead to false identification. Returning to the figure, at 14.34 seconds the TD SPRT for instrument 2 reaches -1, at which time it is provisionally failed. When the TD QSPRT reaches -1 at 15.6 seconds, instrument 2 is identified as failed.

In Fig. 8-38 a positive BFM bias is added to the output of lateral accelerometer 2 at 36 seconds of segment 4C. Recall that this is a region of high dynamic pressure containing roll rate,

yaw rate and sideslip angle oscillations in response to a rudder doublet. The direct redundancy trigger is given at 36.48 seconds, and as before the DR SPRT, TD QSPRT and TD SPRT for instrument 2 start going negative. At 39.42 seconds the SPRT for instrument 2 reaches -1, and that instrument is provisionally failed. At 43.62 seconds, the TD QSPRT reaches -1 and instrument 2 is identified as failed.

8.5.9 Normal Accelerometers

The primary test for the normal accelerometers is AK, and neither TK nor TD is capable of identifying a normal accelerometer BFM bias because of possible test errors arising from BFM/2 biases in unfailed instruments. Because the vertical acceleration arising from a normal accelerometer bias is proportional to $\cos \phi$, the effect of a normal accelerometer failure is reduced by more than 50% in segment 4A, in which there is a sustained roll angle of -1.1 rad. Thus a BFM bias cannot be identified in segment 4A. This is a fundamental limitation of the AK test, and proper pilot response to the indication of an unidentifiable normal accelerometer failure would be leveling of the wings. We note that in all of the segments a 2 BFM or larger normal accelerometer bias jump is immediately identified by self-test.

The addition of error terms in the AK QSPRT in the transonic region does increase the identification time. The ability to identify the failure within the presently defined ETL depends upon where in the transonic region the failure occurs. This is illustrated in Fig. 8-39 and 8-40 in which negative BFM biases are added to normal accelerometer 2 at 90 seconds and 125 seconds respectively of segment 4B. In Fig. 8-39 the normal accelerometer direct redundancy trigger is given at 90.84 seconds, and from then on the DR SPRT and the AK SPRT for instrument 2 grow increasingly negative. Note that the fictitious behavior of the altimeter occurs long enough after failure detection that the SPRT's for the two instruments are not greatly affected. Reflecting this fact the QSPRT crosses the negative threshold at 137.1 seconds and instrument 2 is identified as failed. This identification occurs a fraction of a second before the AK ETL of 47 seconds has elapsed. In Fig. 8-40 the direct redundancy trigger occurs at 125.84 seconds, indicating the sign of instrument 1 minus instrument 2 is positive. The positive jump in the altimeter at 130 seconds results in positive residuals for both instruments,

and because of the sign of the instrument difference from the trigger instrument 1 appears to be failed. Thus the SPRT for instrument 1 begins growing very negative while the SPRT for instrument 2 grows quite positive. Not until a few seconds before ETL does the SPRT for instrument 1 start growing in the positive direction. After the ETL has elapsed at 172.8 the QSPRT is still at +1, and the tests are restarted. Insufficient time remains until the end of the segment for any decision to be made. The required identification time outside the transonic region is approximately twenty seconds. This is illustrated in Fig. 8-41, in which a negative BFM bias is added to normal accelerometer 2 at 140 seconds of segment 4B. The failure is detected at 140.9 seconds and identified at 160.9 seconds. The small error apparent in the residuals for instrument 1 verify the effectiveness of the algorithm modification to protect the altitude filters from the altimeter jump at Mach 1.

In Fig. 8-42 a positive BFM bias is added to normal accelerometer 1 at 10.02 seconds of segment 4C, and the direct redundancy trigger is given at 10.98 seconds. Recall that this segment contains some slow ramping in roll angle, which produces time-varying observability of the normal accelerometer bias in the AK residuals. However, because the maximum roll angle magnitude is only 0.4 radians, the effect on failure identification time is negligible with identification occurring at 30.54 seconds.

It is important to note that the relatively long normal accelerometer BFM bias failure identification times observed here are directly the result of the large altitude quantization size in the telemetry data, and therefore the identification times seen in Section 7 more closely reflect the performance of an onboard system.

8.6 Summary

In this section the analytic redundancy FDI algorithm has been modified to perform well on telemetry data from the F-8 DFBW aircraft. In essence the modification consists of two stages:

- 1) A choice of new BFM levels and ETL's using telemetry bias and noise characteristics and the techniques discussed in Section 4.
- 2) The addition of terms to appropriate QSPRT's to accommodate DG turn error and air data sensor behavior in the transonic region.

Additionally direct compensation is added for the alpha vane bias in supersonic flight*, and a technique for DG compensation for turn error has been developed in Appendix F which will be implemented in the future. We emphasize that the modification process is extremely simple and equally applicable to any set of instruments, and that the FDI framework of trigger, SPRT's and outer loop remains unchanged.

The FDI algorithm, although designed to identify instruments with bias jumps, has demonstrated its ability to identify failures to zero of the roll rate and pitch rate gyros in moderate level oscillatory maneuvers. In addition it is felt that this capability will be expanded to the yaw rate gyros with the addition of the DG turn error correction scheme. This demonstrated zero scale factor failure identification capability indicates that the explicit scale-factor FDI algorithm suggested in Appendix C is not necessary for this level of failure.

The addition of sensor self-test has allowed the accelerometer hard failure identification times obtained in Section 7 to be lowered. For a 1/2g bias failure the times in Table IV now are changed to zero detection time with provisional failure in one sample and failure identification in two additional samples. Because the rate gyro simulated hard failure level of 0.1 rad/sec used for Table IV is below our chosen rate gyro self-test thresholds, this level of bias must be identified by the RK tests in the present algorithm, and the detection and identification times for these rate gyro biases remain essentially unchanged.

The algorithm has proven its ability to detect and identify BFM biases throughout a range of flight conditions. Only three areas of significant performance degradation from previous simulation experience have been observed:

- 1) Inability to identify Mach BFM bias in the transonic region
- 2) Extended identification times for pitch rate gyro and yaw rate gyro BFM failures during long turns
- 3) Extended normal accelerometer BFM bias identification times.

Although problem 1) must remain in some region around Mach 1 due to the unfailed instrument characteristics, its effect may be minimized by decreasing the indicated Mach region within which the Mach meter TK QSPRT assumes a Mach jump may occur. Detailed examination of the

* In addition examination of the residuals in Fig. 8-35 and 8-39 suggest supersonic biases in the Mach meters and altimeters of approximately 0.04 Mach and 275 m respectively. The Mach bias will be compensated in future versions of the algorithm.

Mach meter output indicates that a sufficiently large region may be defined as the time that the filtered Mach estimate is between 0.94 and 1.03. On Segment 4B this region is only ten seconds long. It is anticipated that problem 2) will disappear with the addition of DG turn compensation, and problem 3) will not exist for the onboard system with available altimeter output quantized at 3.4 m.

Although no DG FDI was performed, the results of Appendix F indicate that the turn error compensated DG signals are quite well behaved, and that DG FDI is possible. However if it is determined that the dominant failure mode results in ramping RK residuals, the DG RK SPRT's should be modified to look for that effect.

Because the output of only one altimeter was provided, no altimeter FDI was performed. However, the only apparent limitation on altimeter FDI is the same as the restriction on Mach meter FDI, i.e., BFM bias jumps cannot be identified in a small region around Mach 1 due to nominal behavior of the instruments.

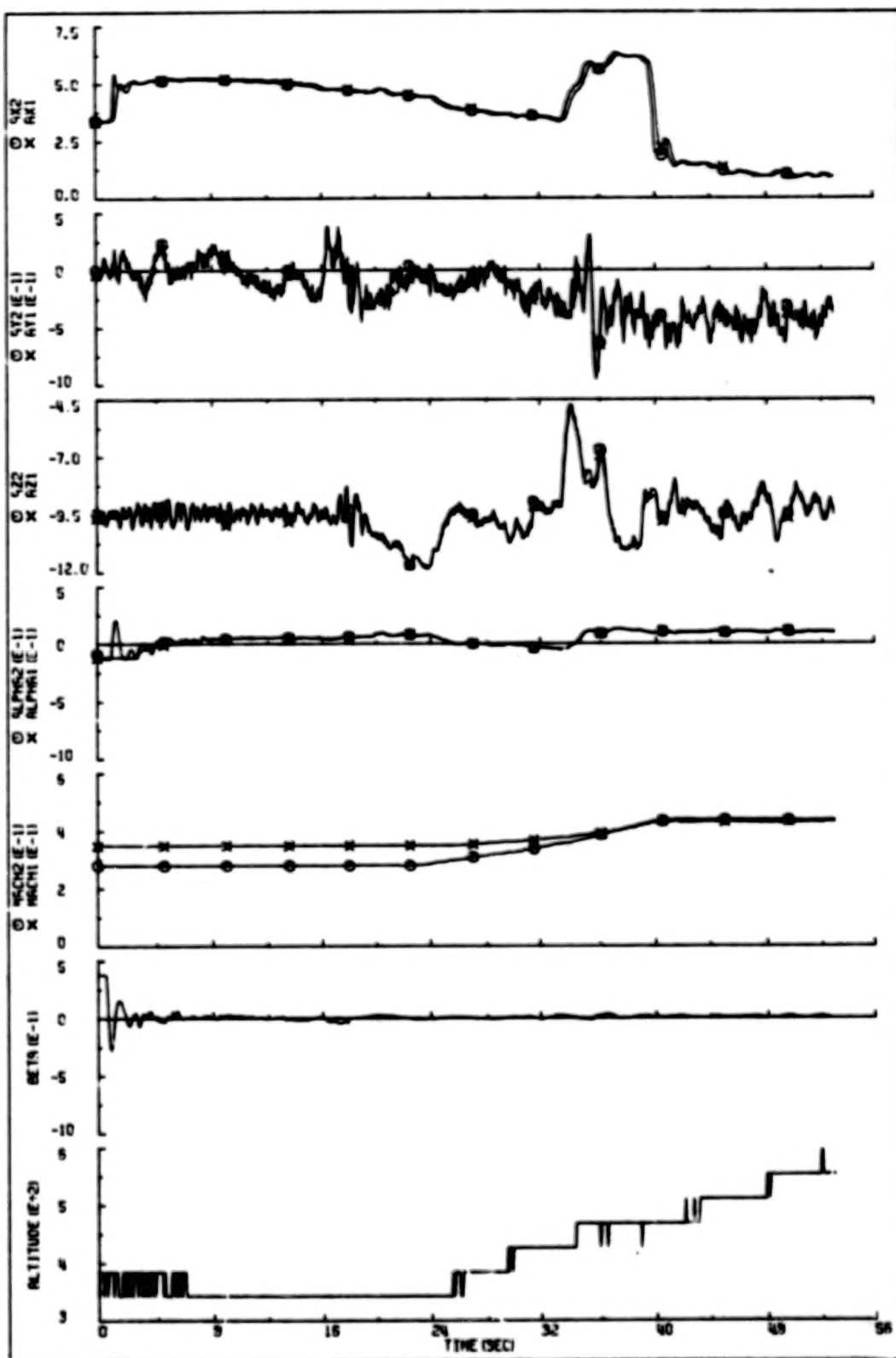


Figure 8-1 Segment 1

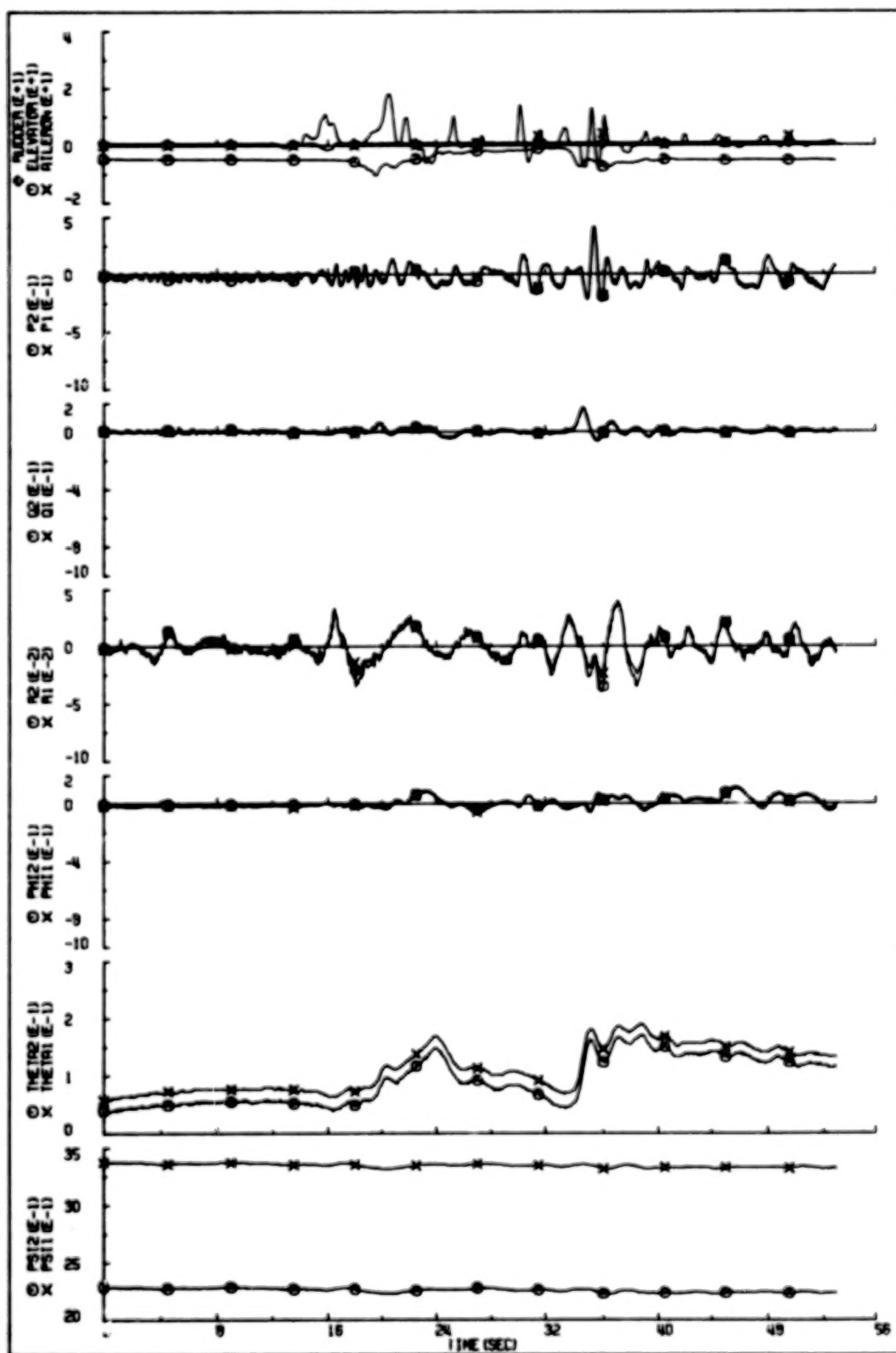


Figure 8-2 Segment 1 (cont.)

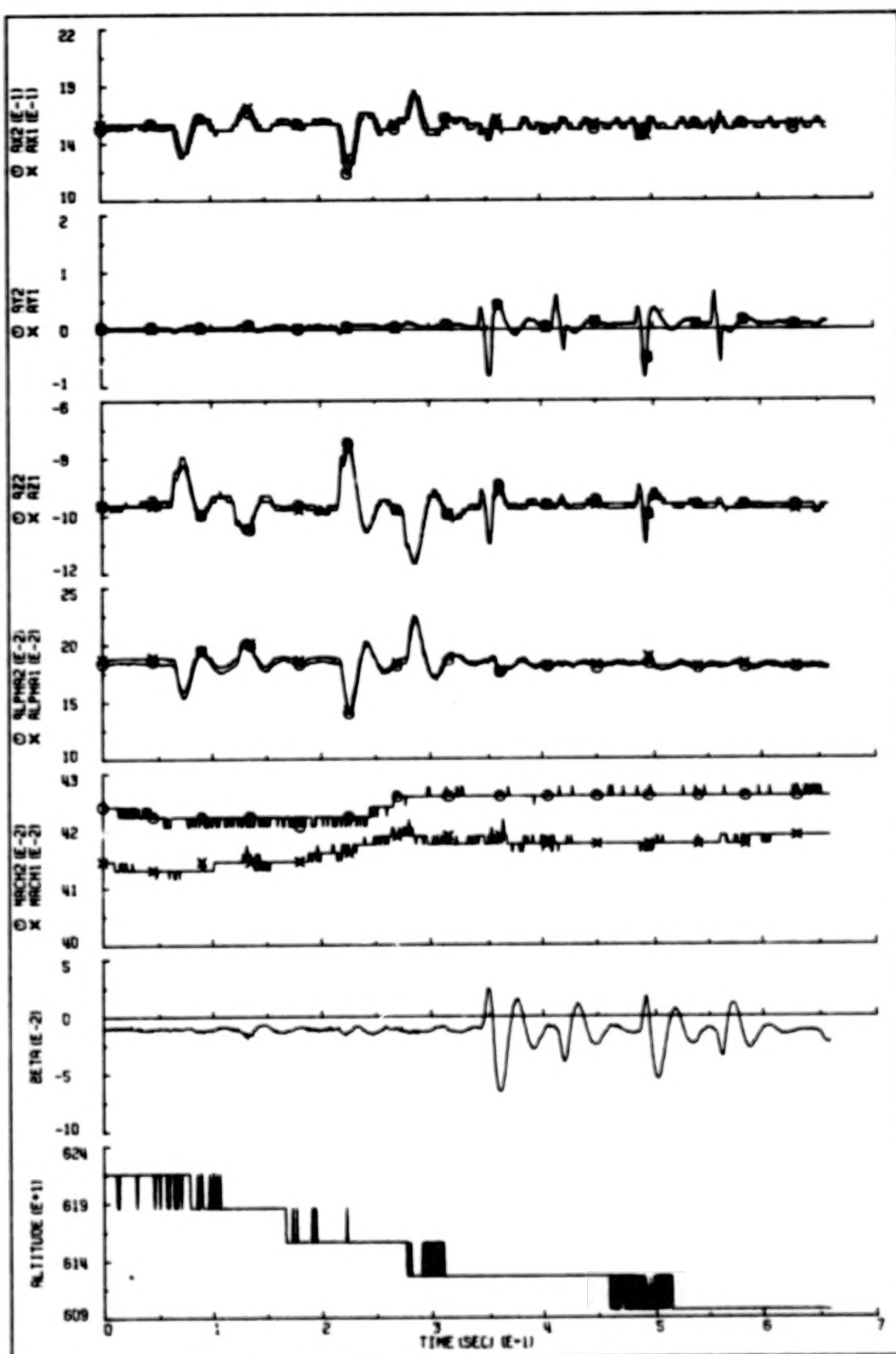


Figure 8-3 Segment 2

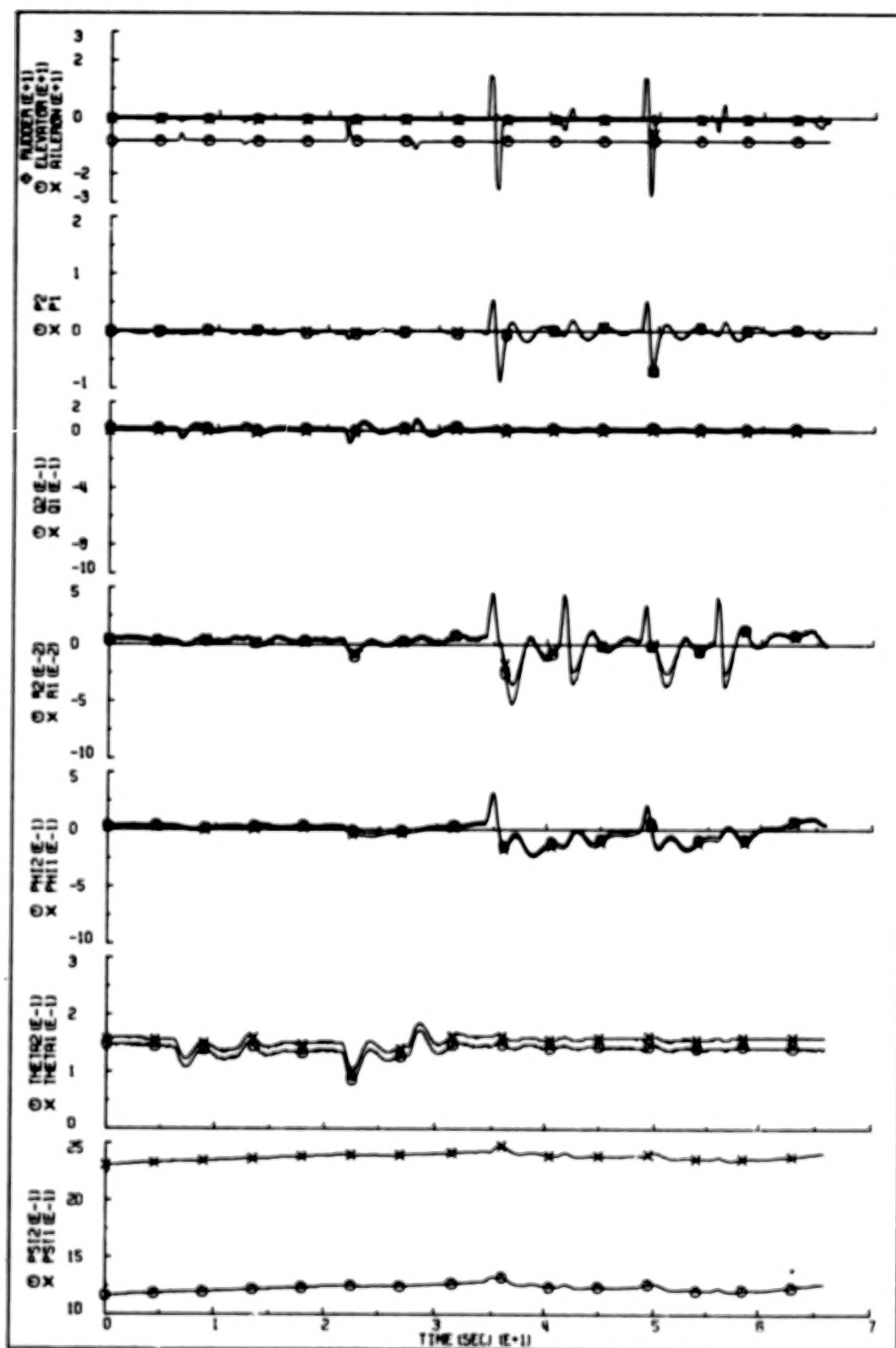


Figure 8-4 Segment 2 (cont.)

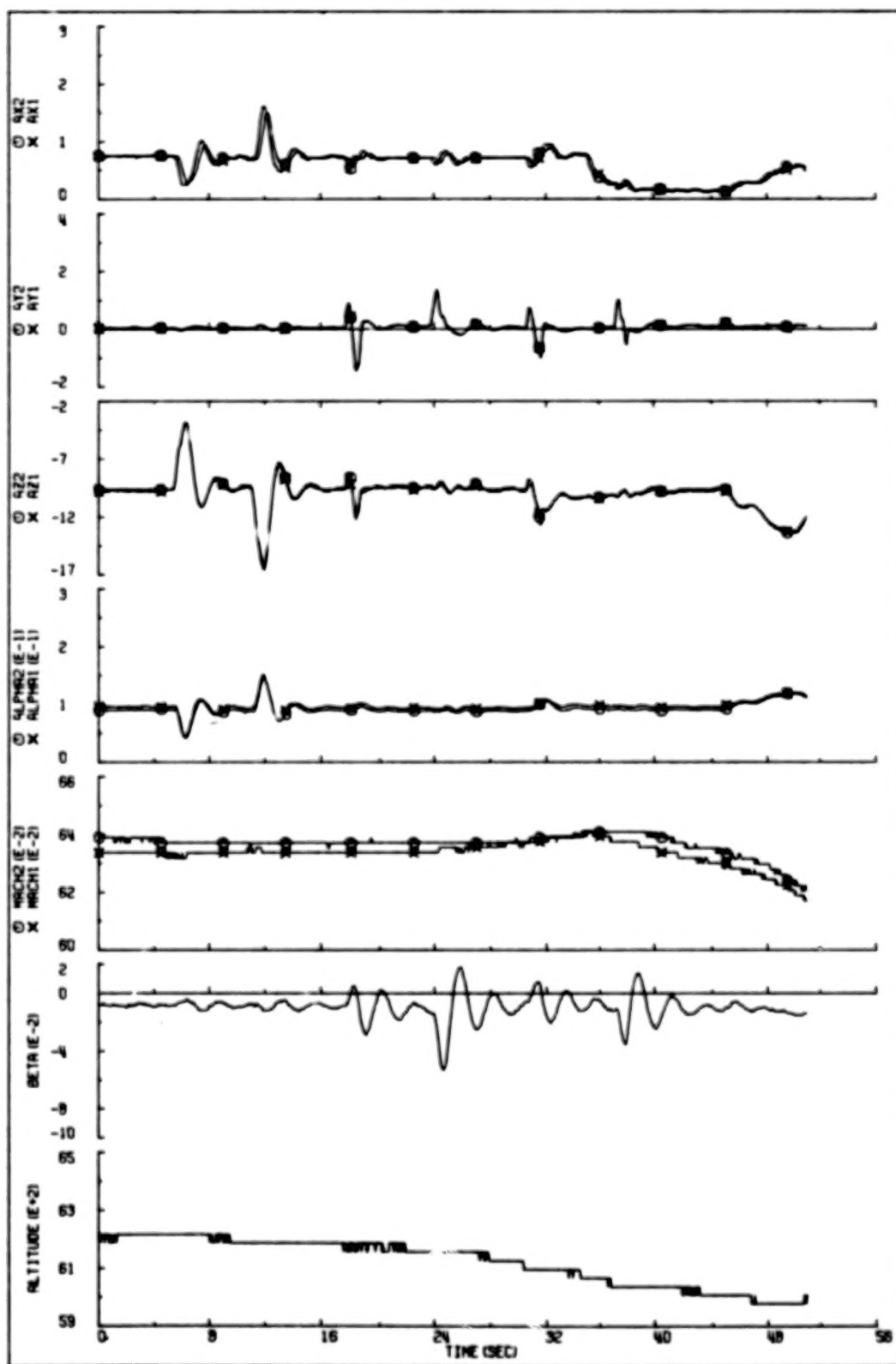


Figure 8-5 Segment 3

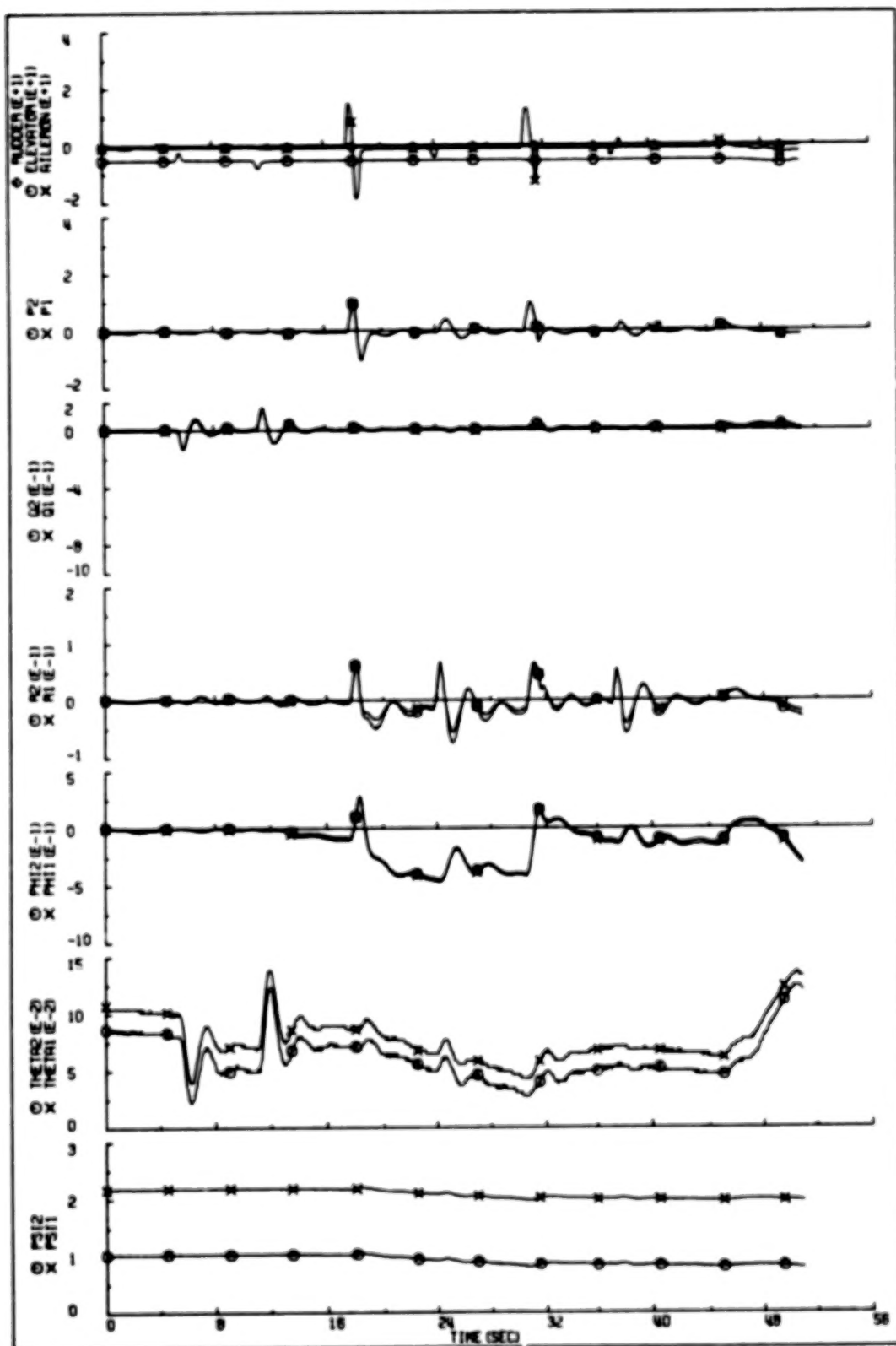


Figure 8-6 Segment 3 (cont.)

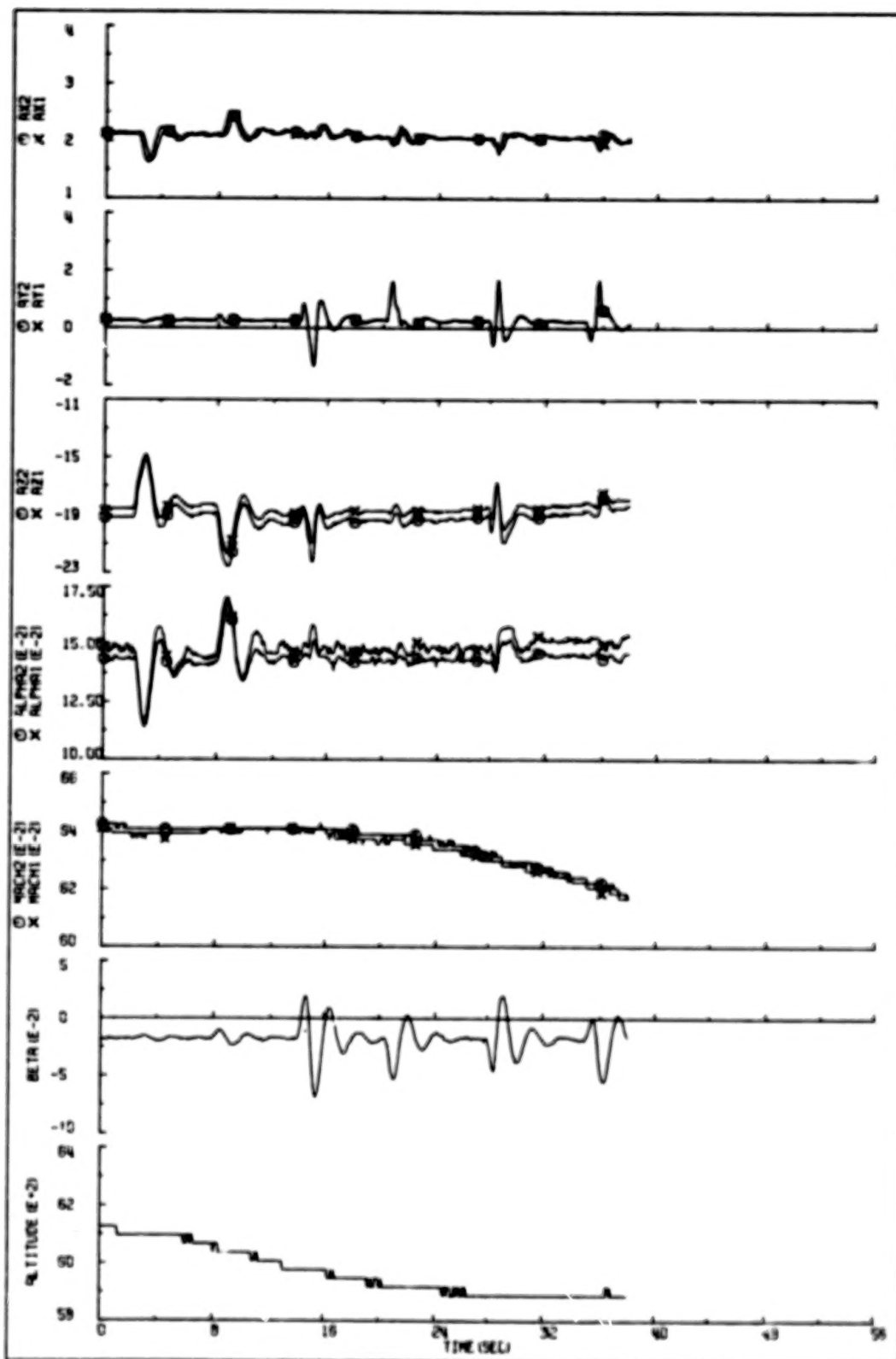


Figure 8-7 Segment 4A

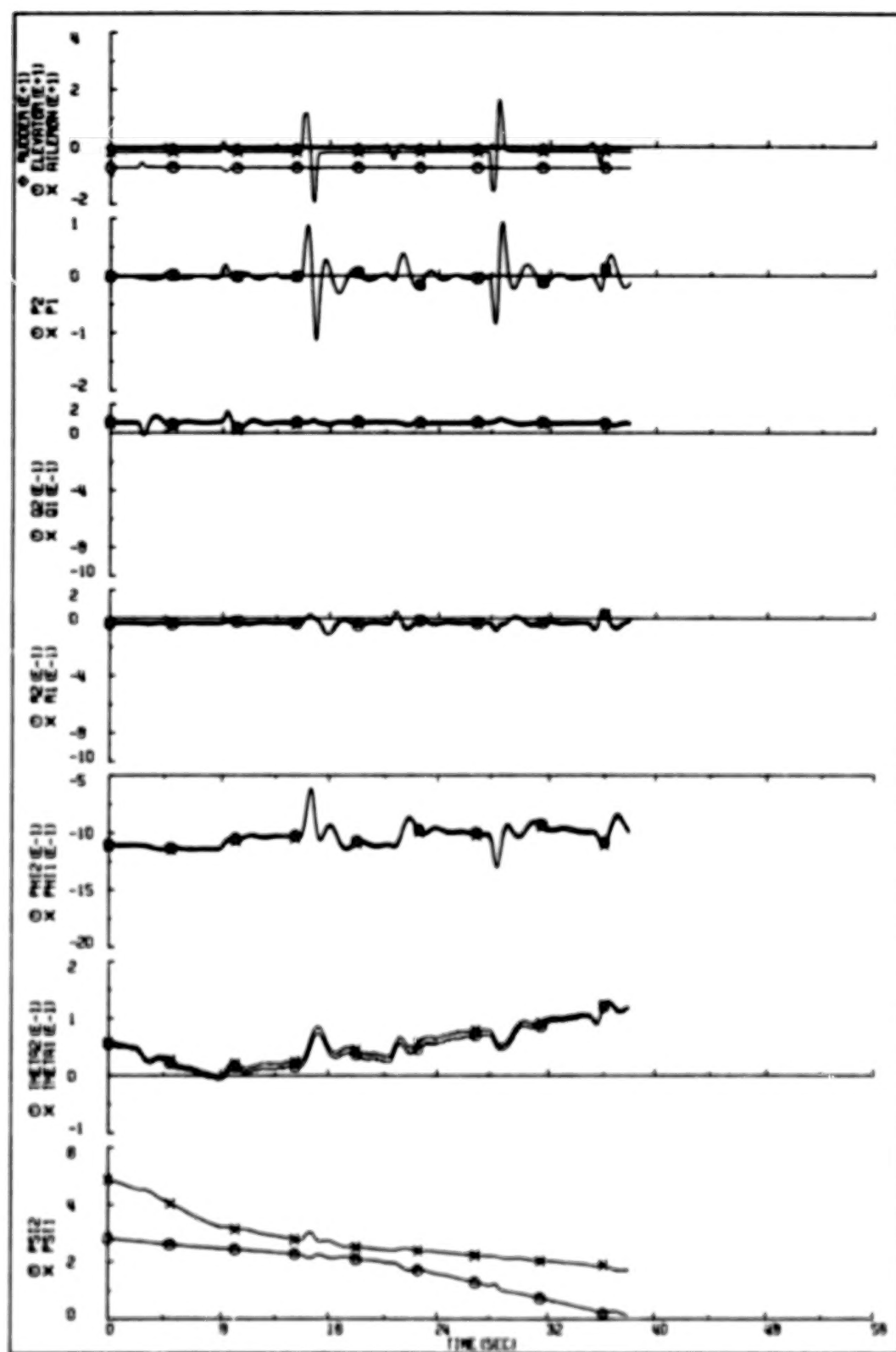


Figure 8-8 Segment 4A (cont.)

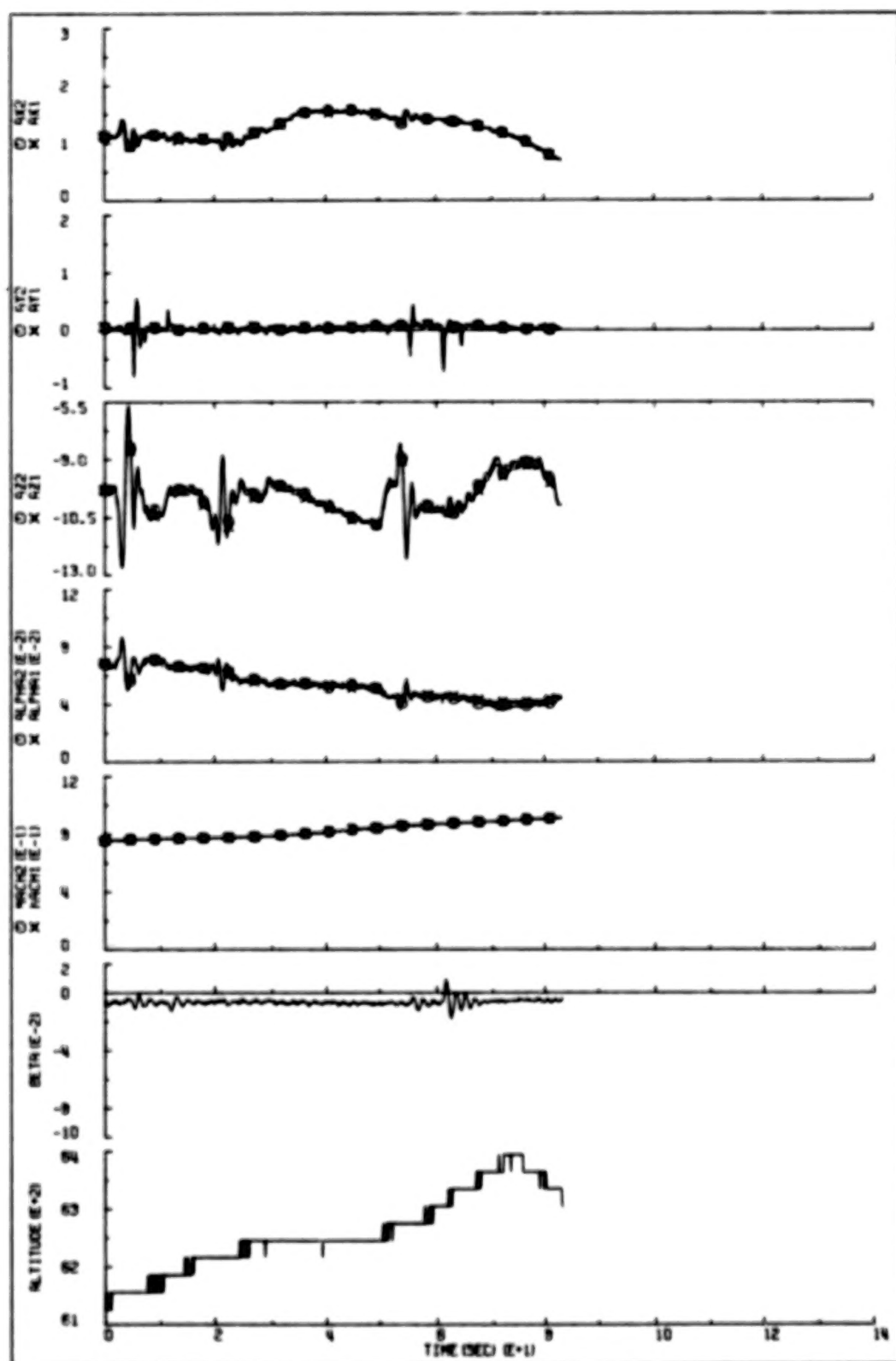


Figure 8-9 Segment 4B

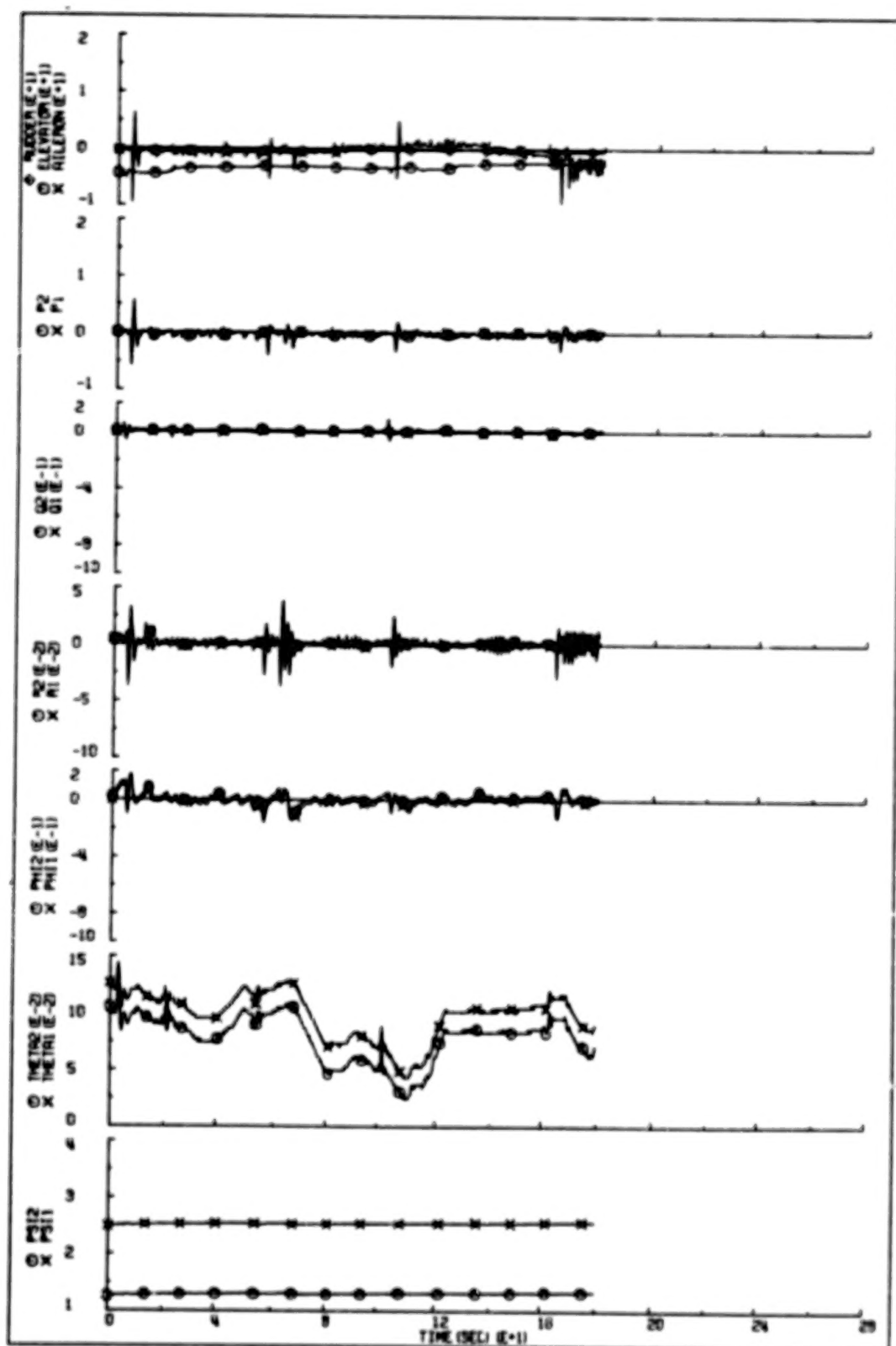


Figure 8-10 Segment 4B (cont.)

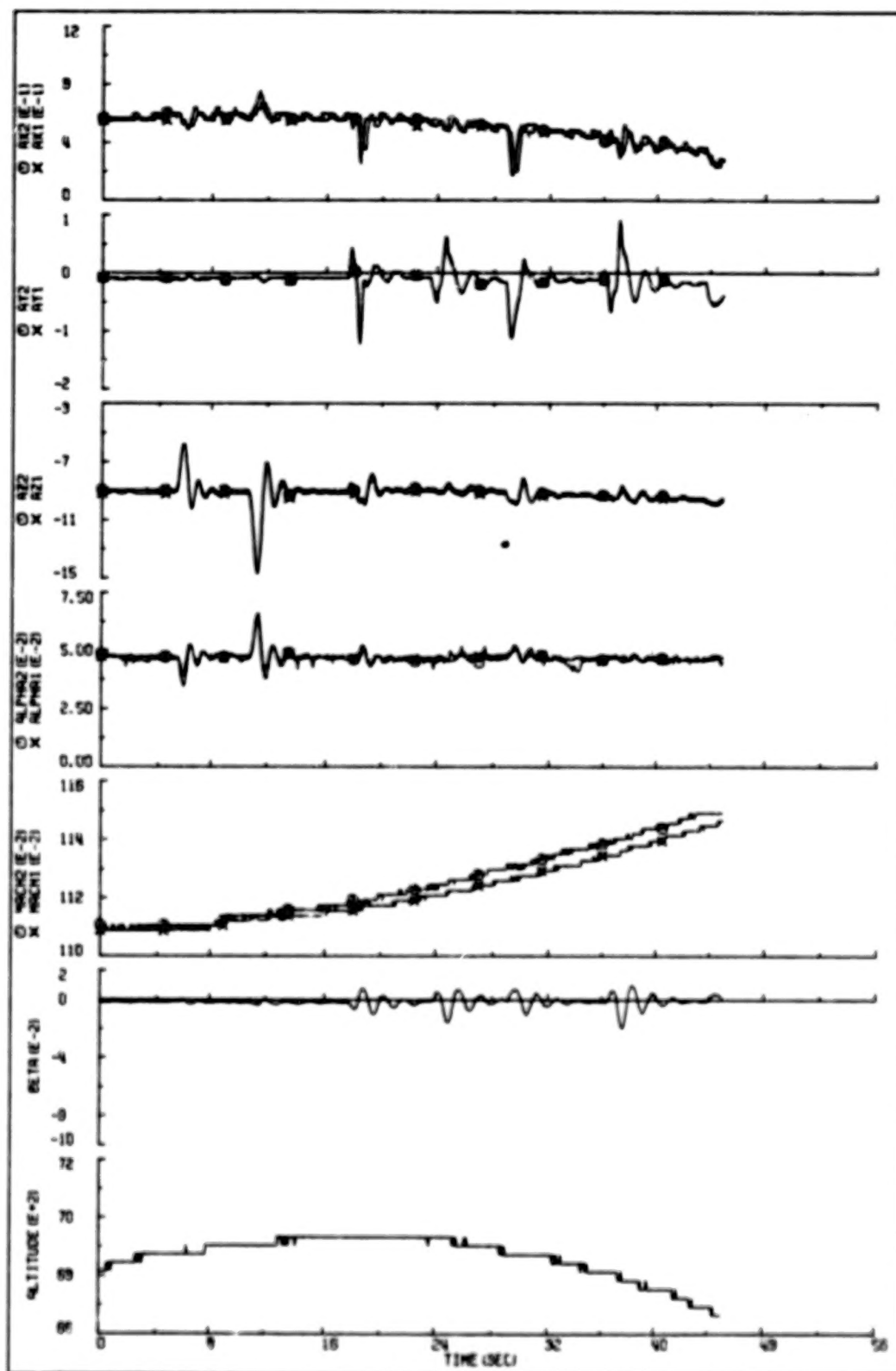


Figure 8-11 Segment 4C

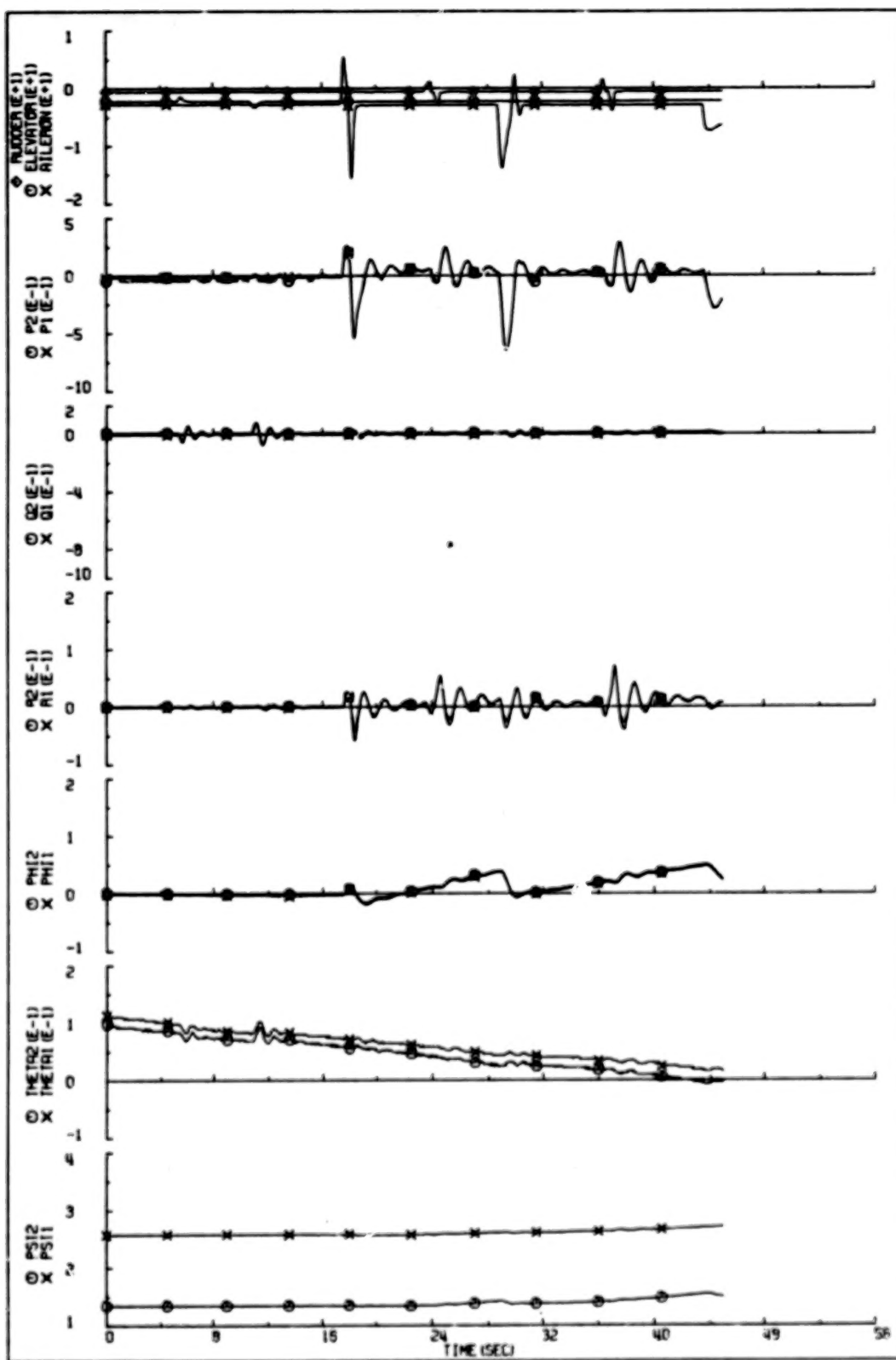


Figure 8-12 Segment 4C (cont.)

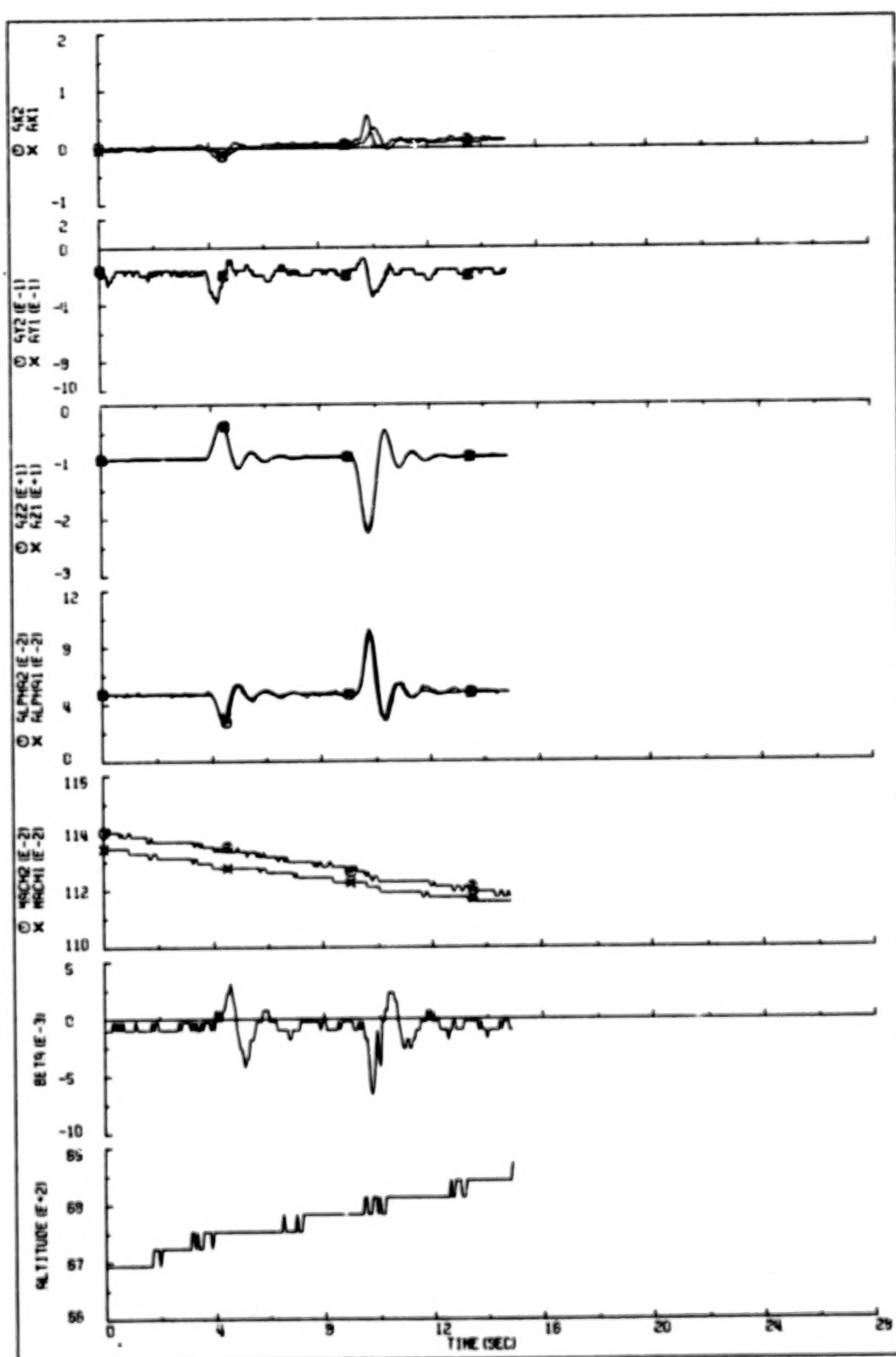


Figure 8-13 Segment 4D

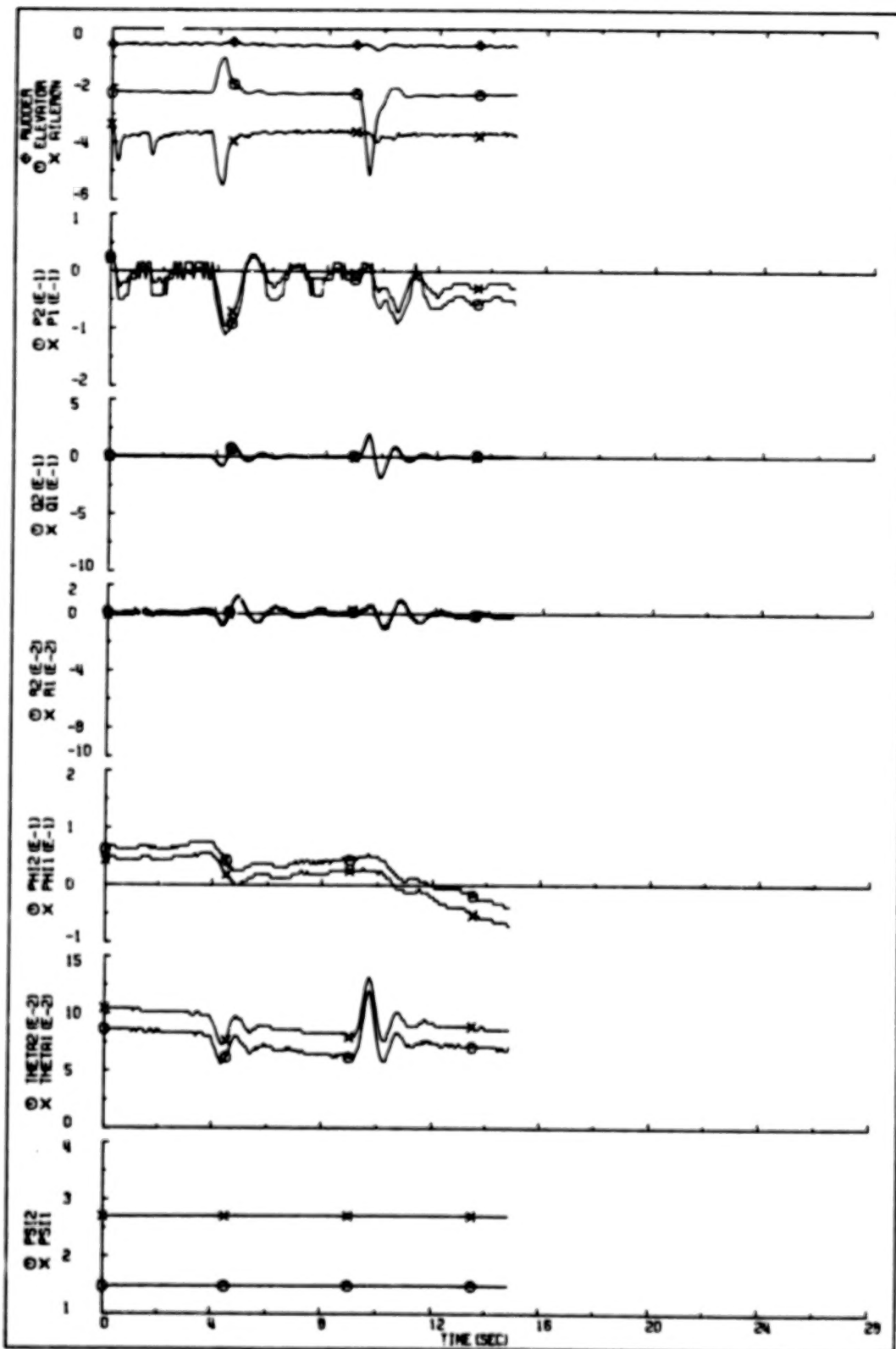


Figure 8-14 Segment 4D(cont.)

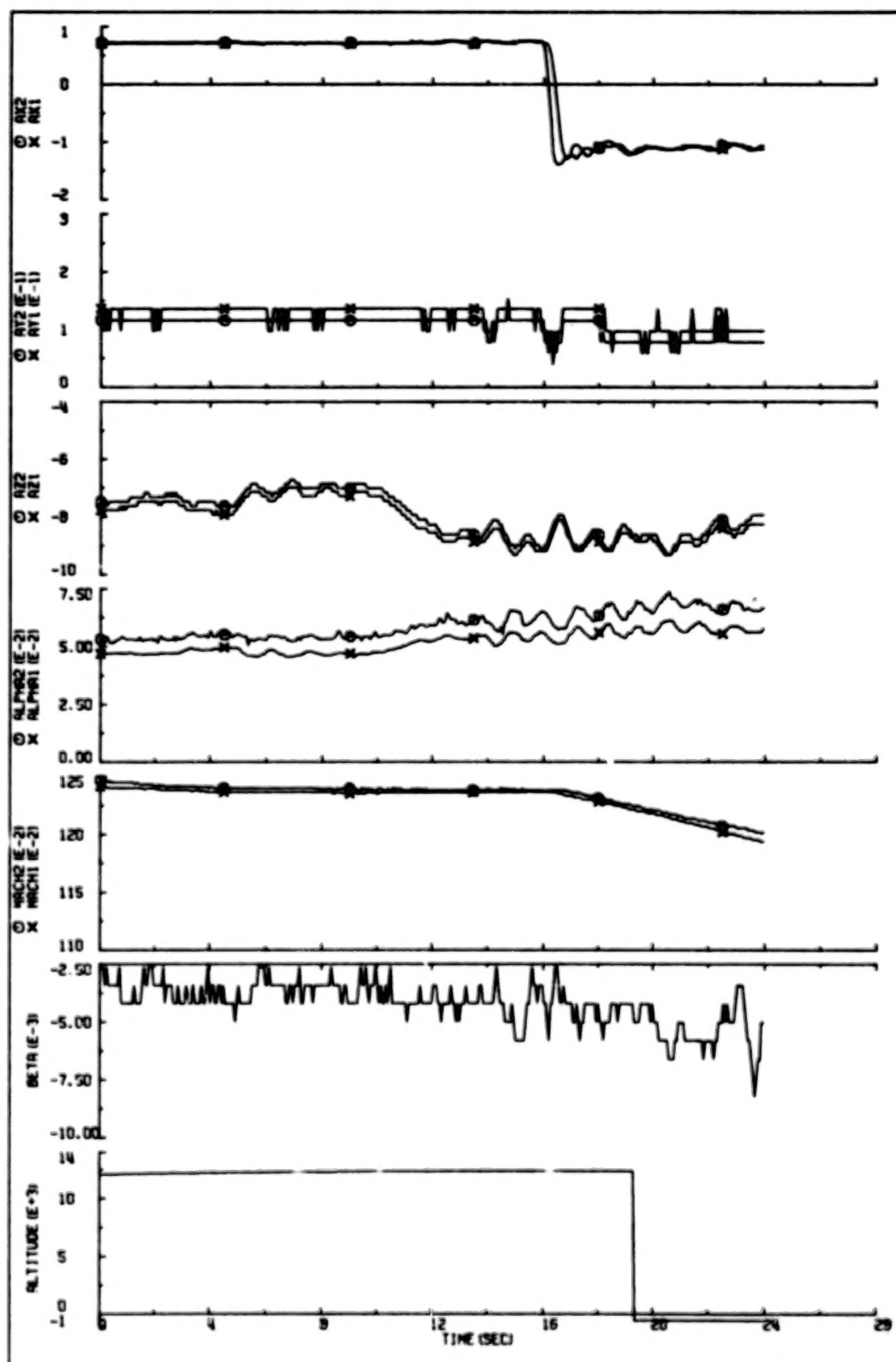


Figure 8-15 . Segment 5

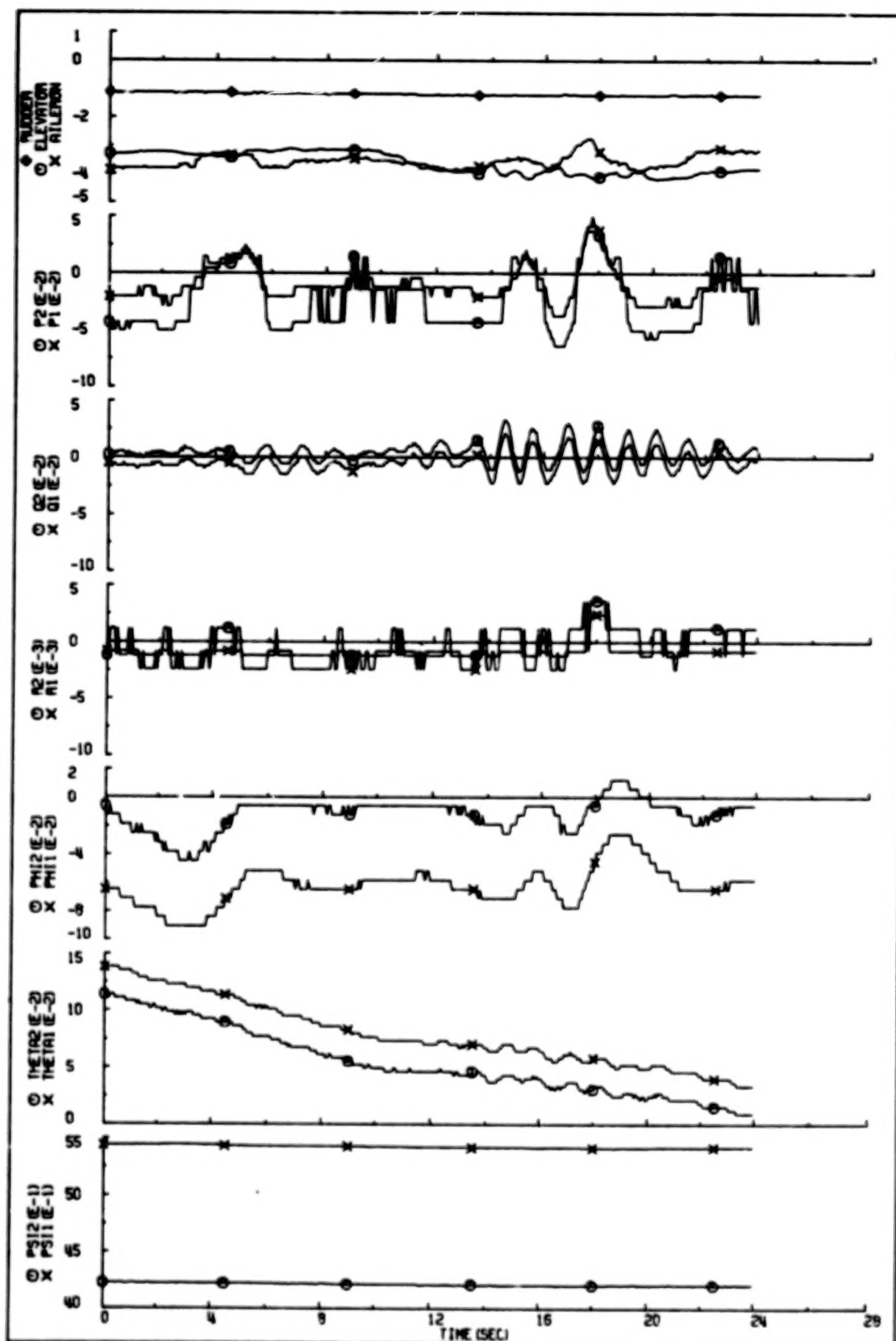


Figure 8-16 Segment 5 (cont.)

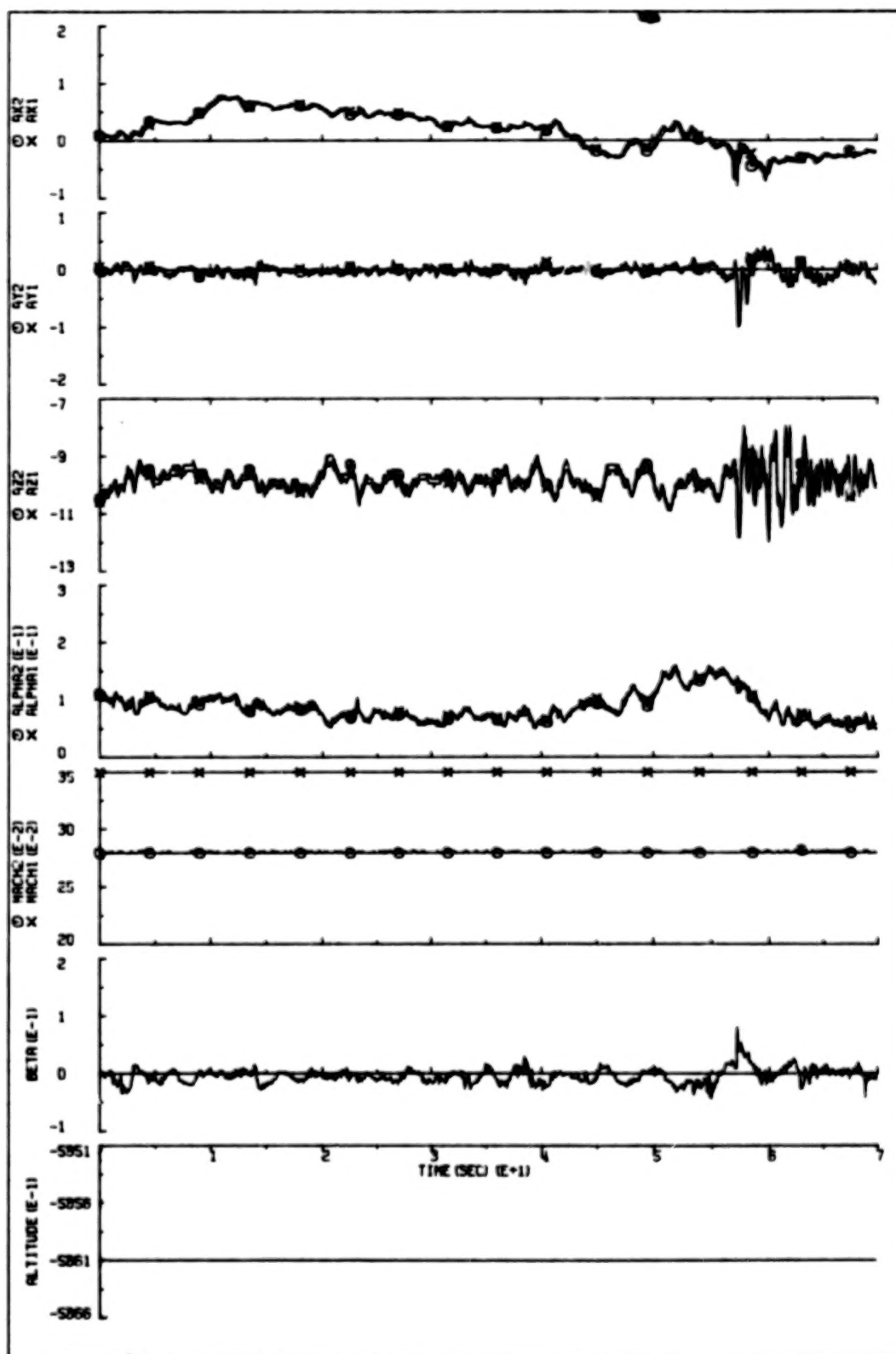


Figure 8-17 Segment 6

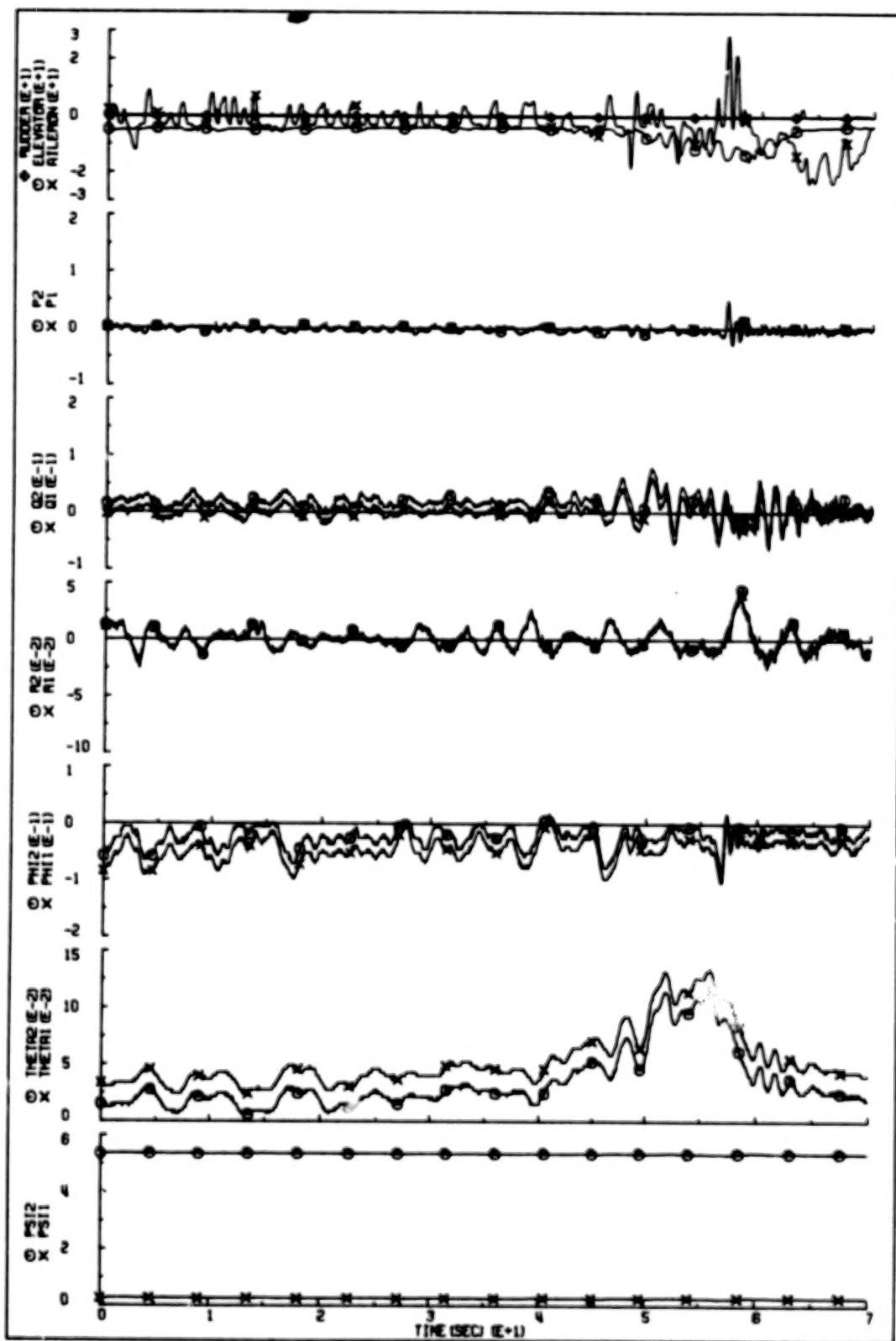


Figure 8-18 Segment 6 (cont.)

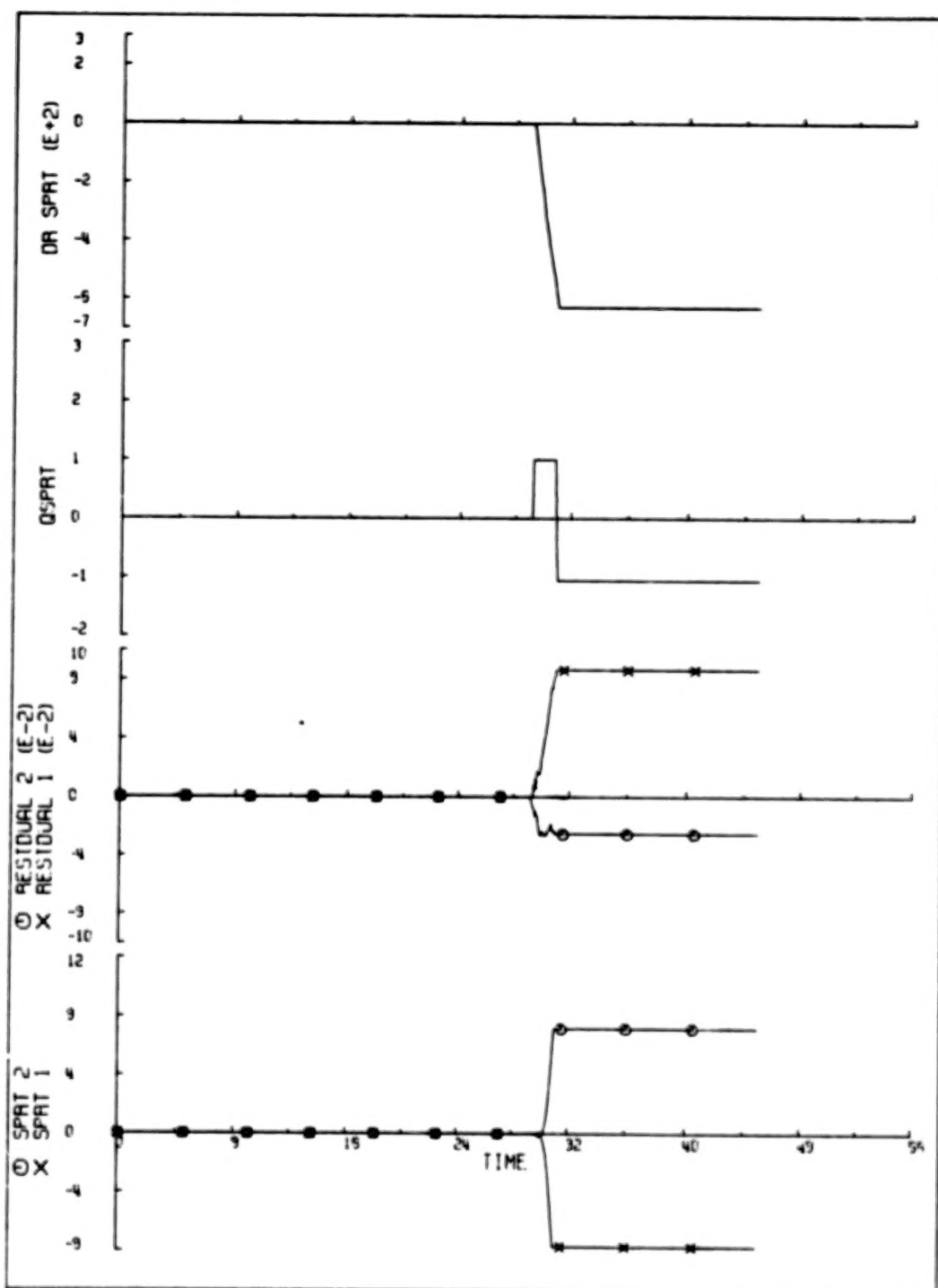


Figure 8-19 Segment 4C, Roll Rate Gyro 1 +BFM Bias at T=29, RK

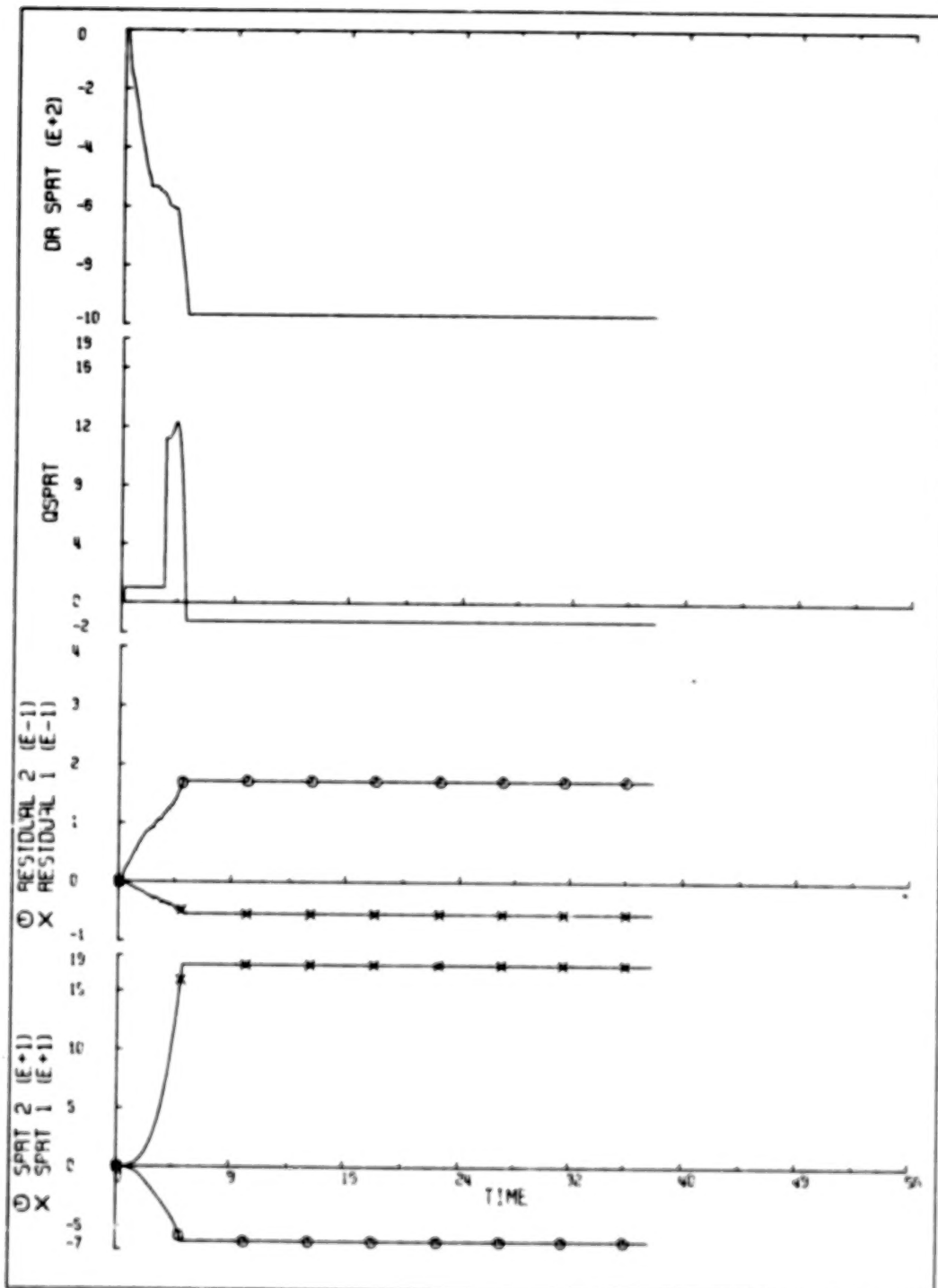


Figure 8-20 Segment 4A, Roll Rate Gyro 2 +BFM Bias at T=0, RK

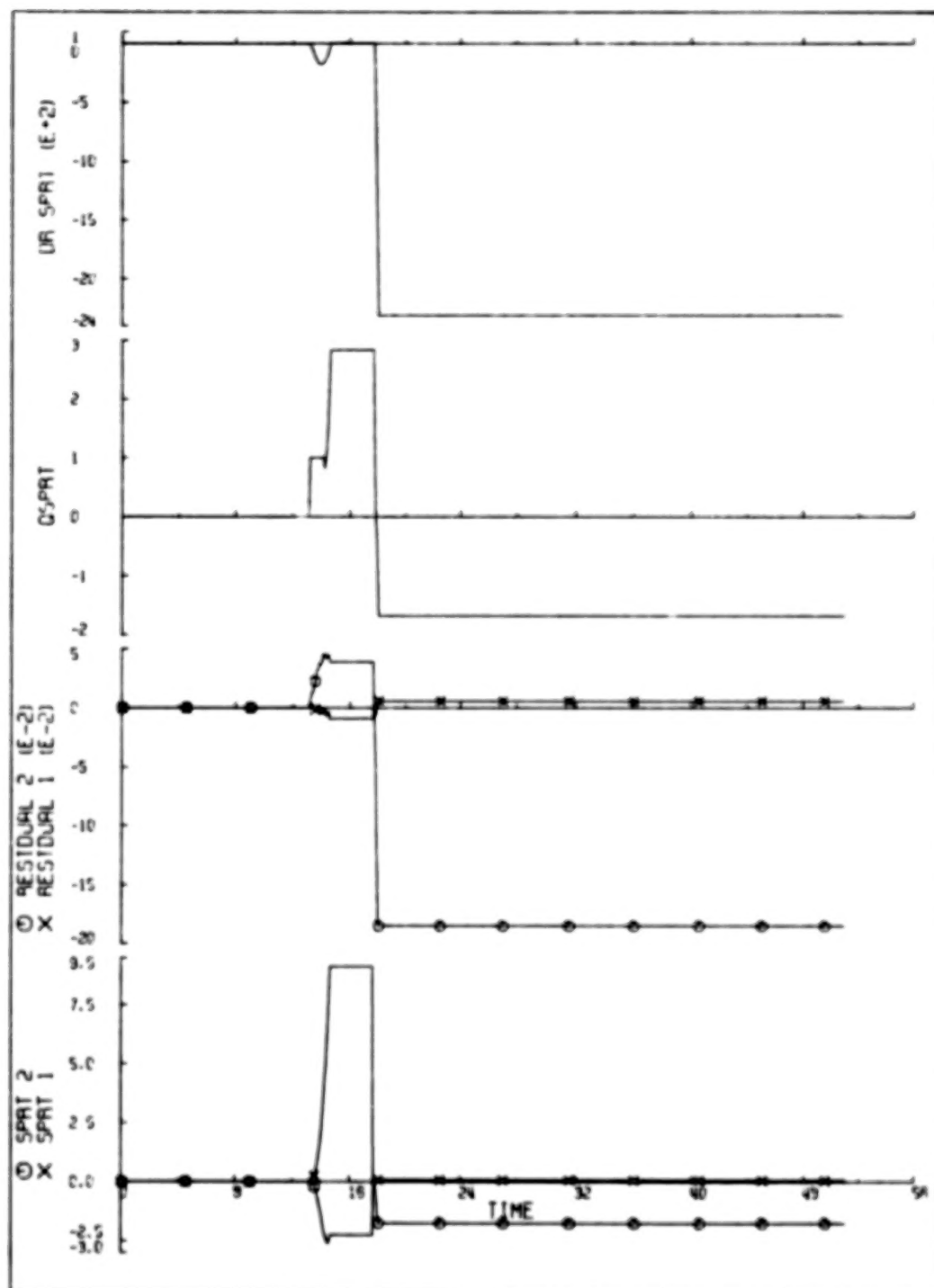


Figure 8-21 Segment 3, Roll Rate Gyro 2 Fail to Zero at $T=0$, RK

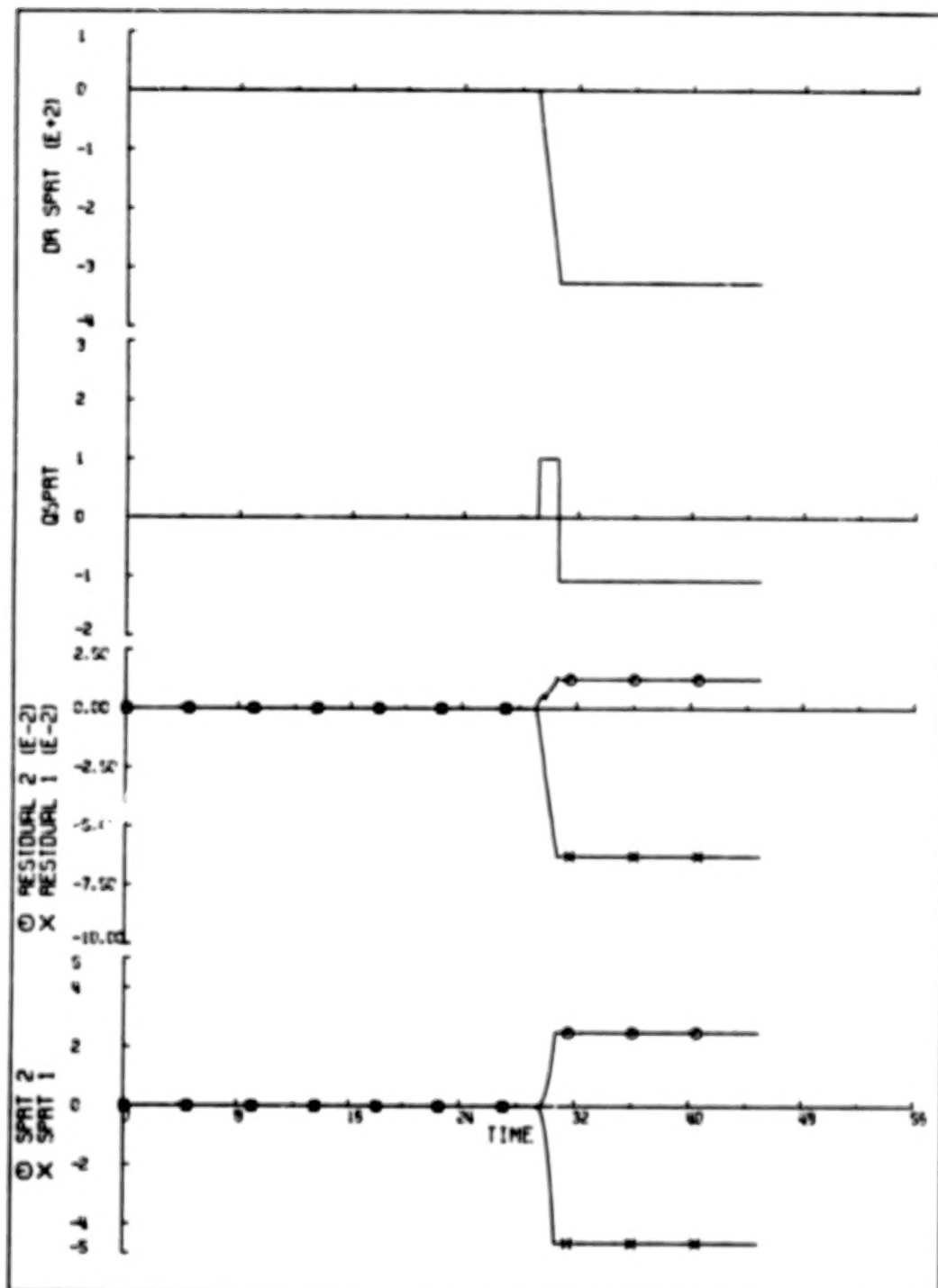


Figure 8-22 Segment 4C, Pitch Rate Gyro 1 -BPM Bias at T=29, RK

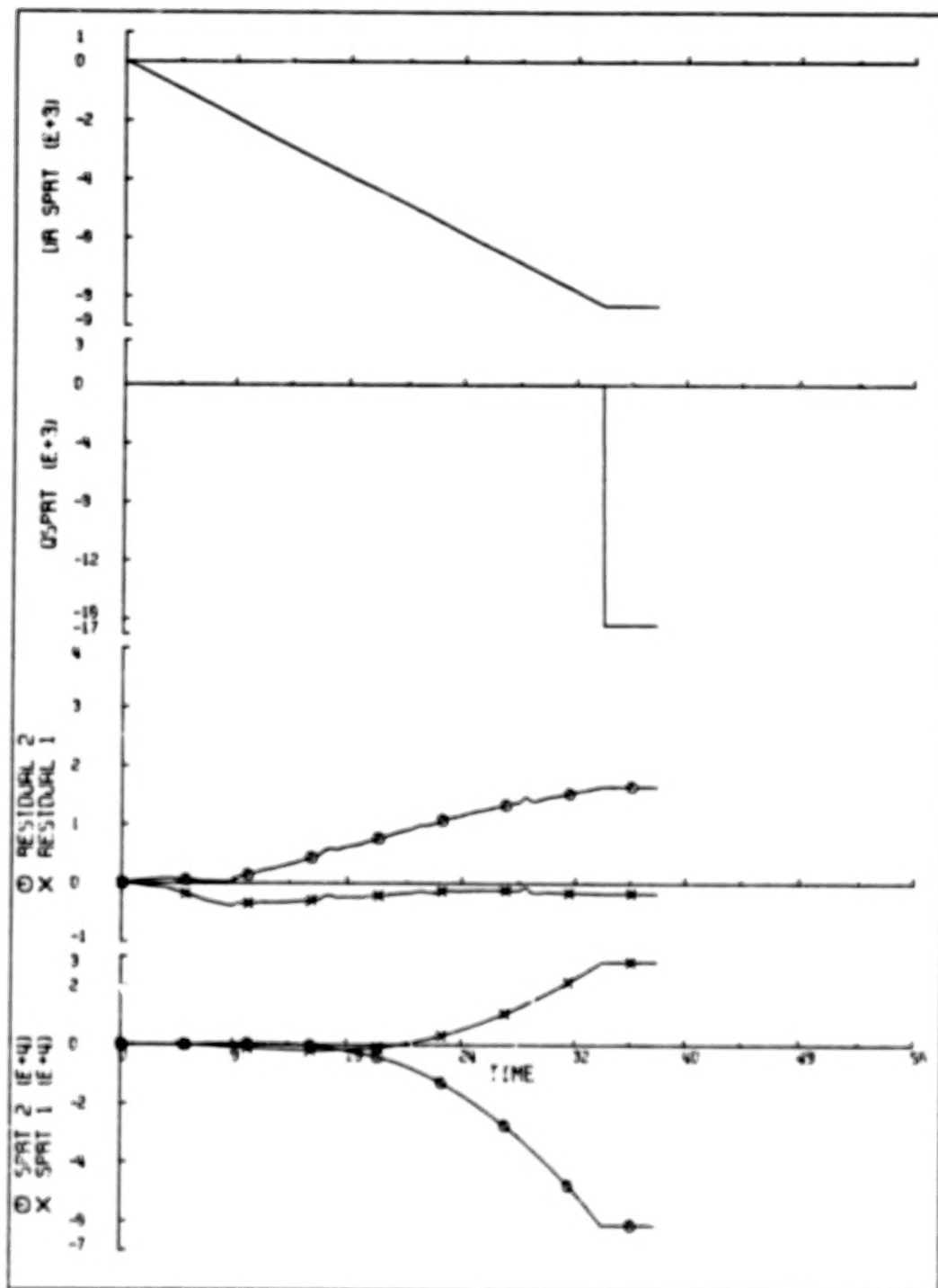


Figure 8-23 Segment 4A, Pitch Rate Gyro 2 +BPM Bias at T=0, RK

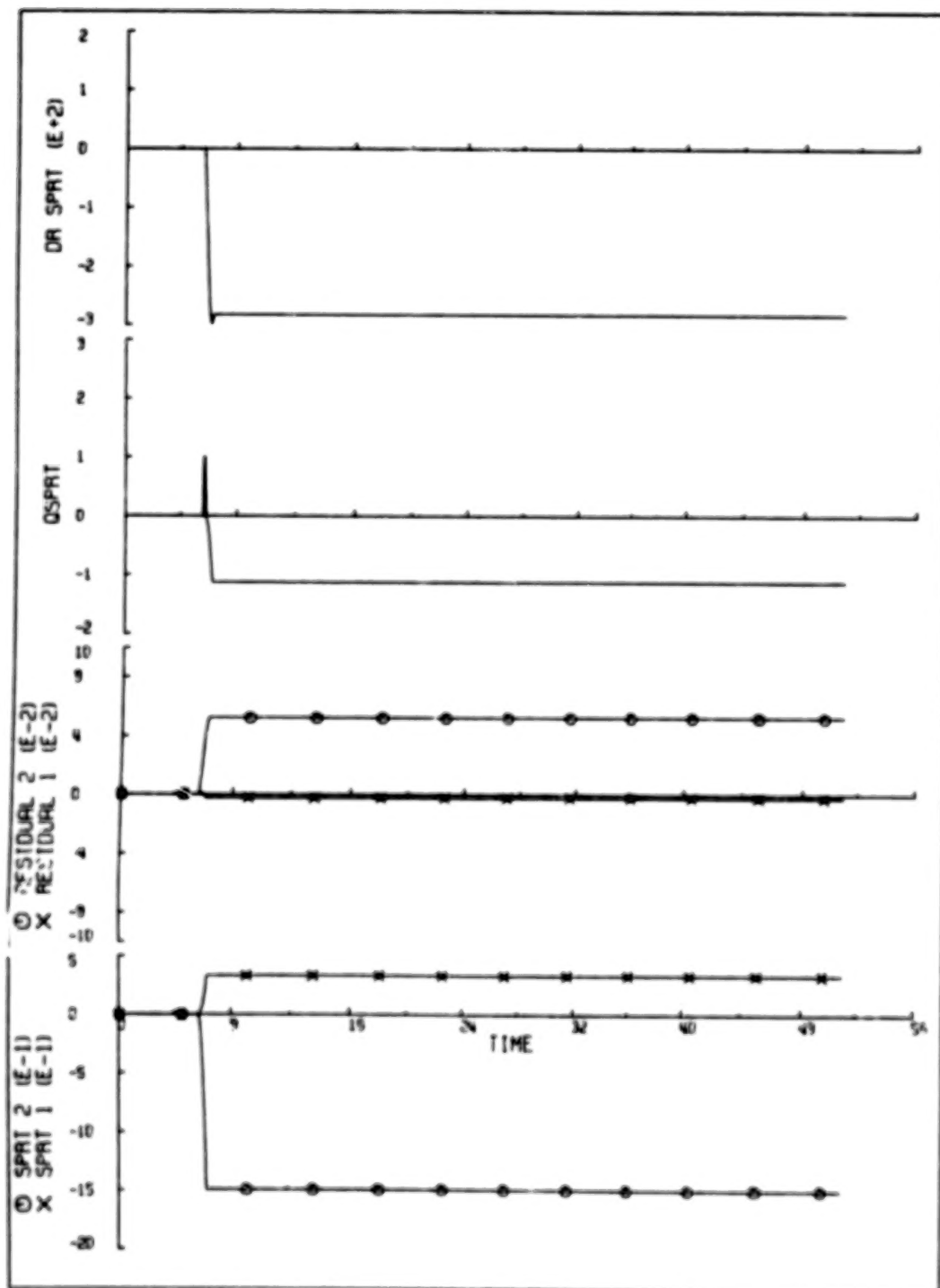


Figure 8-24 Segment 3, Pitch Rate Gyro 2 Fail to Zero at T=0, RK

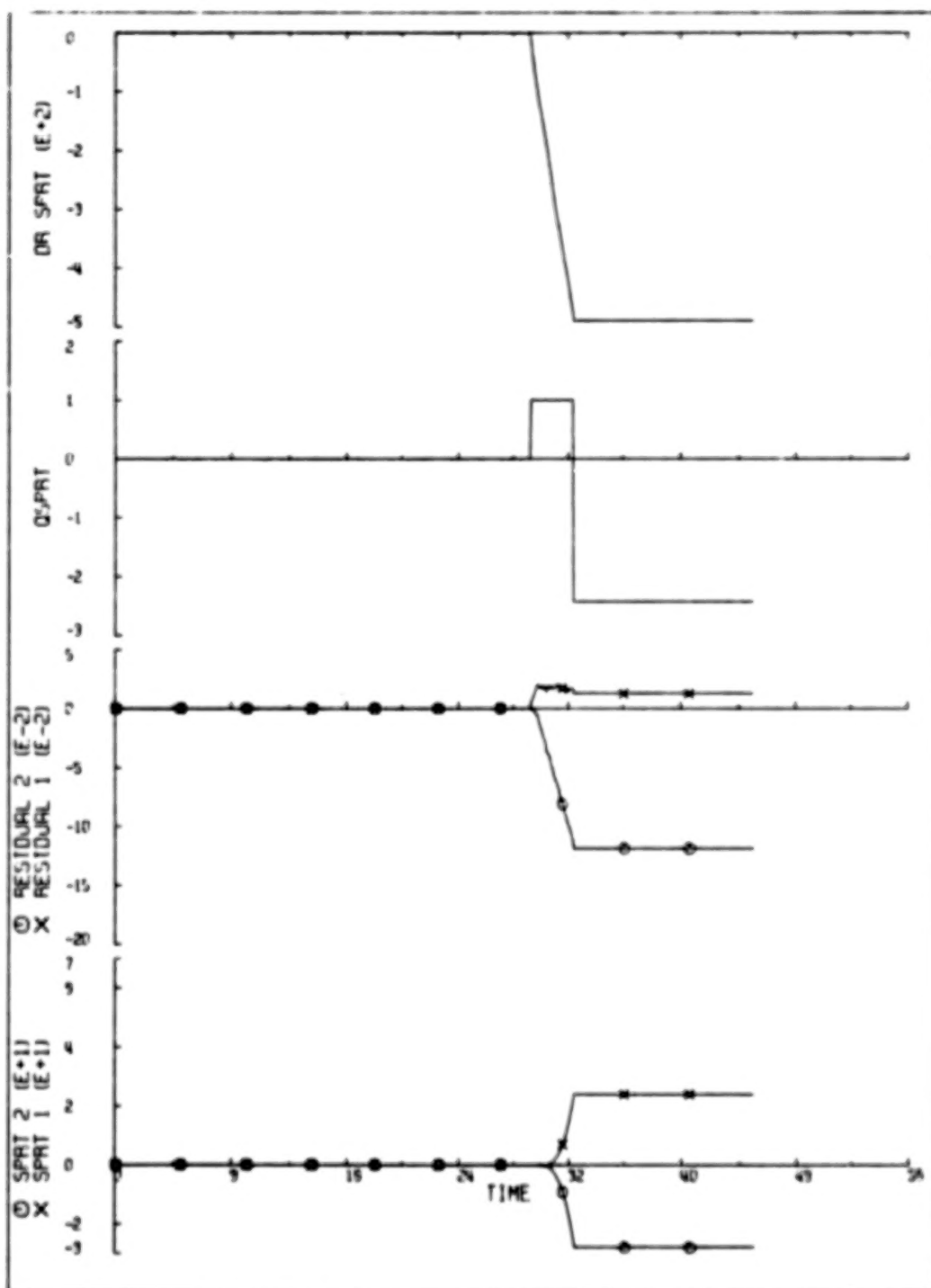


Figure 8-25 Segment 4C, Yaw Rate Gyro 2 -BFM Bias at T=29, RK

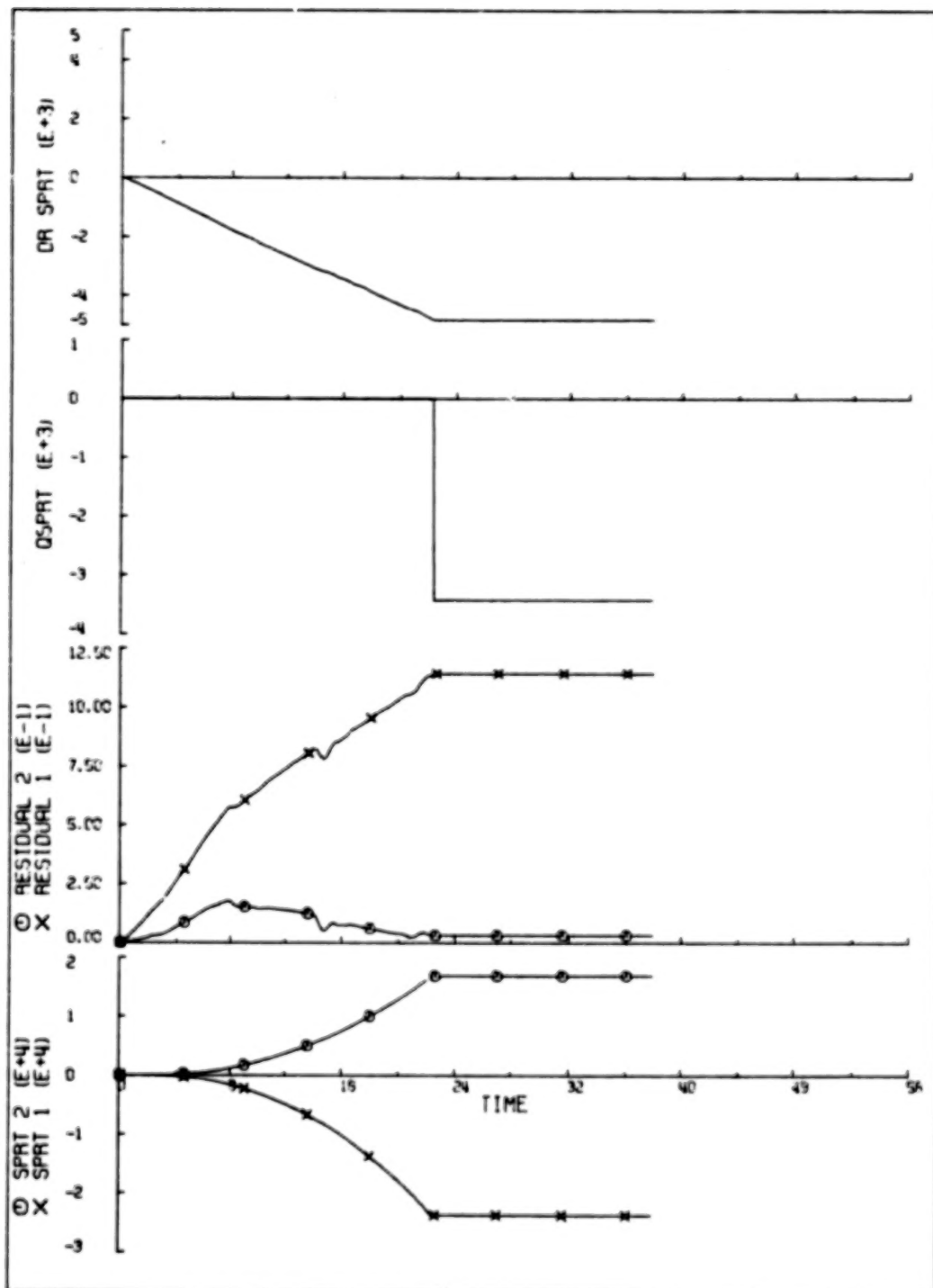


Figure 8-26 Segment 4A, Yaw Rate Gyro 1 +BFM Bias at T=0, RK

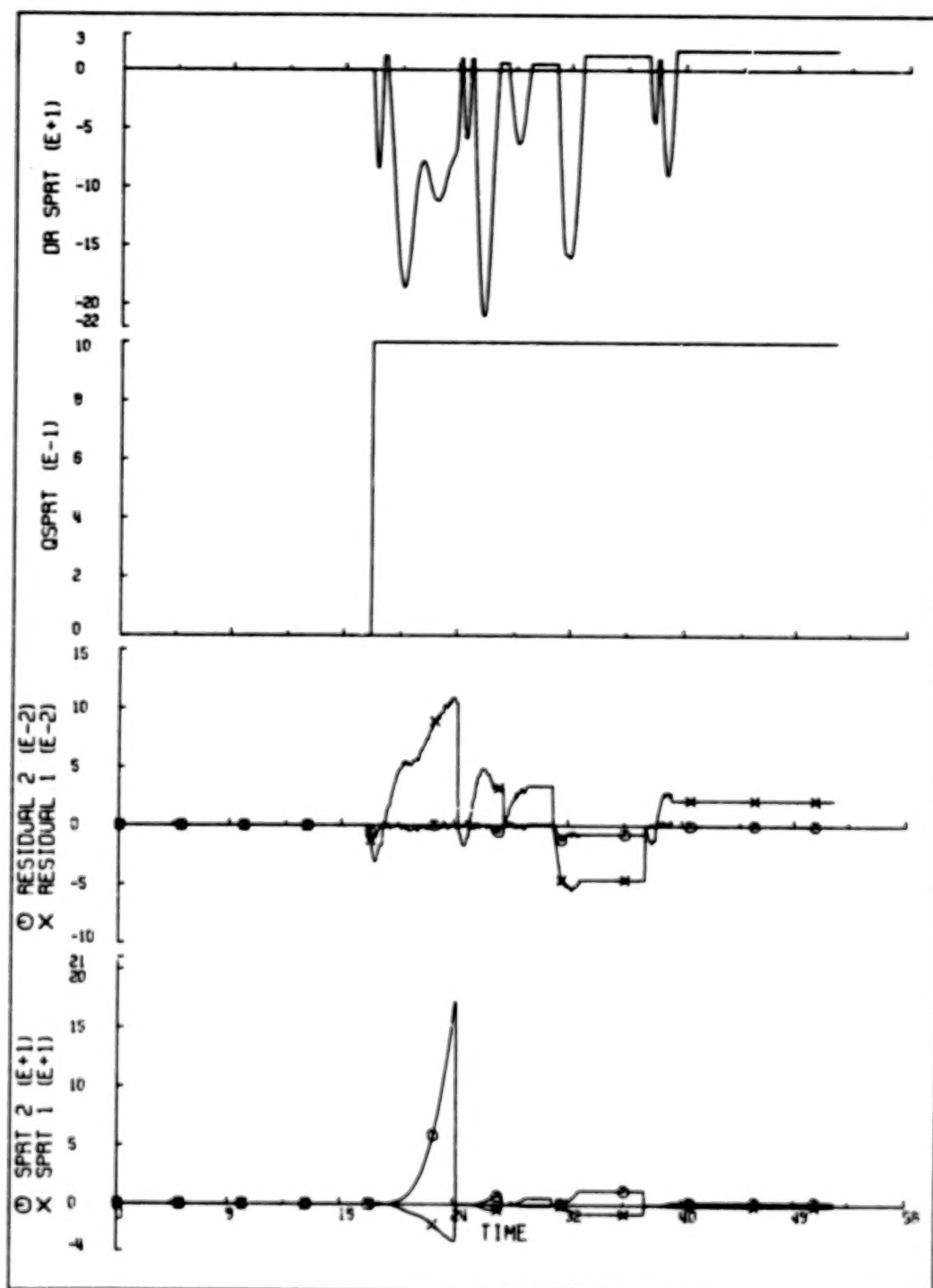


Figure 8-27 Segment 3, Yaw Rate Gyro 1 Fail to Zero at $T=0$, RK

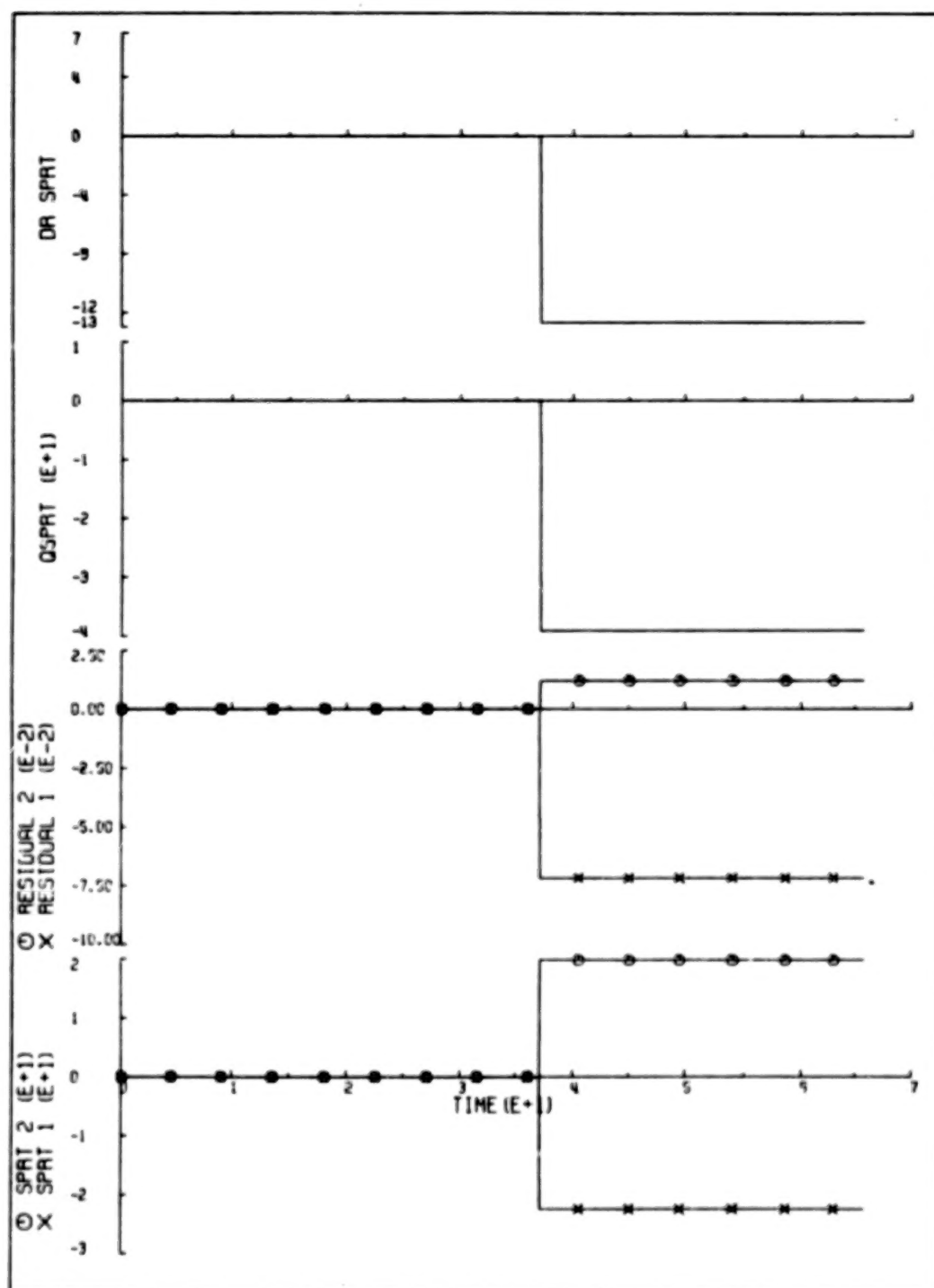


Figure 8-28 Segment 2, Roll Attitude Gyro 1 -BFM Bias at T=37, RK

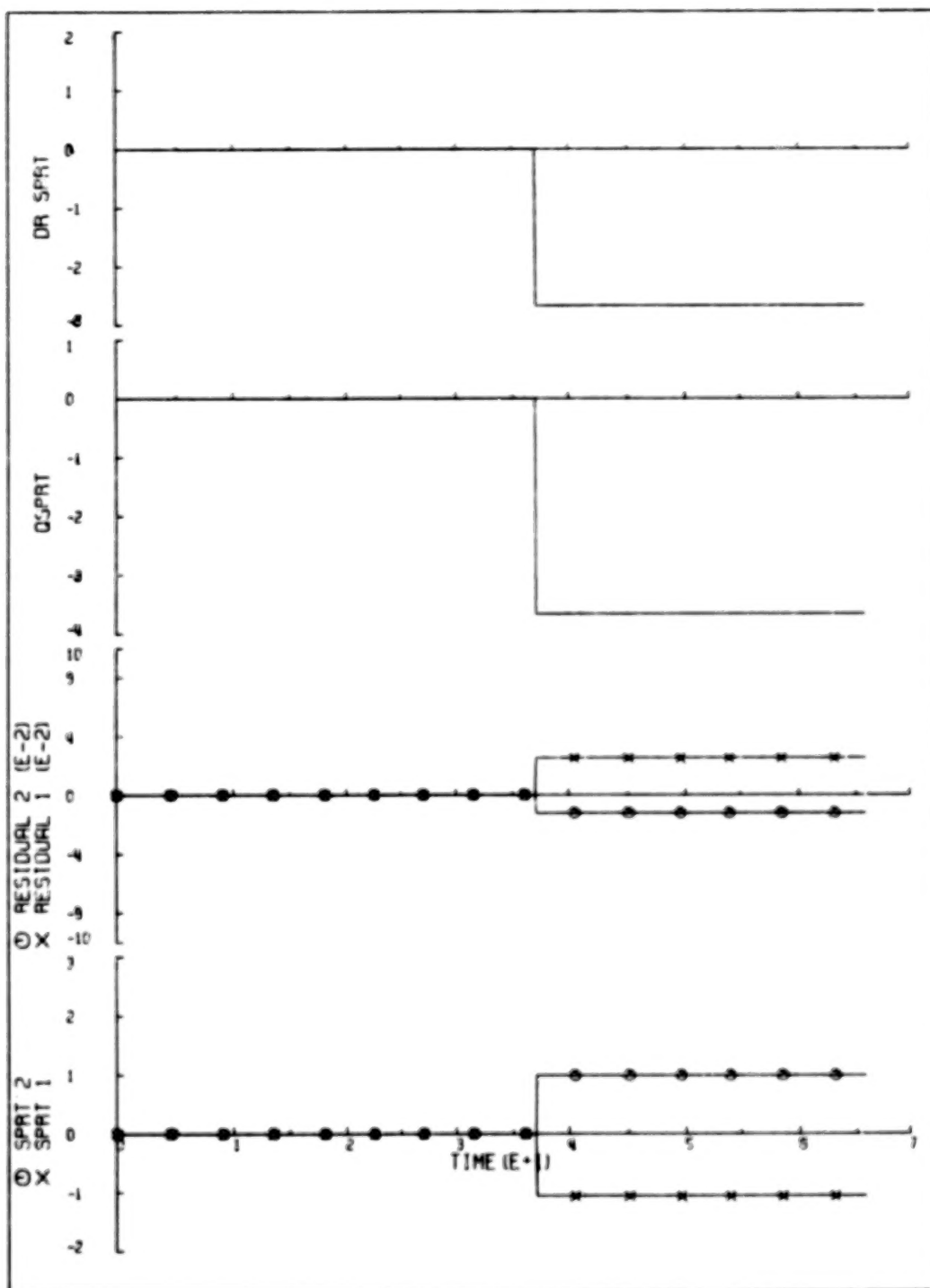


Figure 8-29 Segment 2, Pitch Attitude Gyro 1 +BPM Bias at T=37, RK

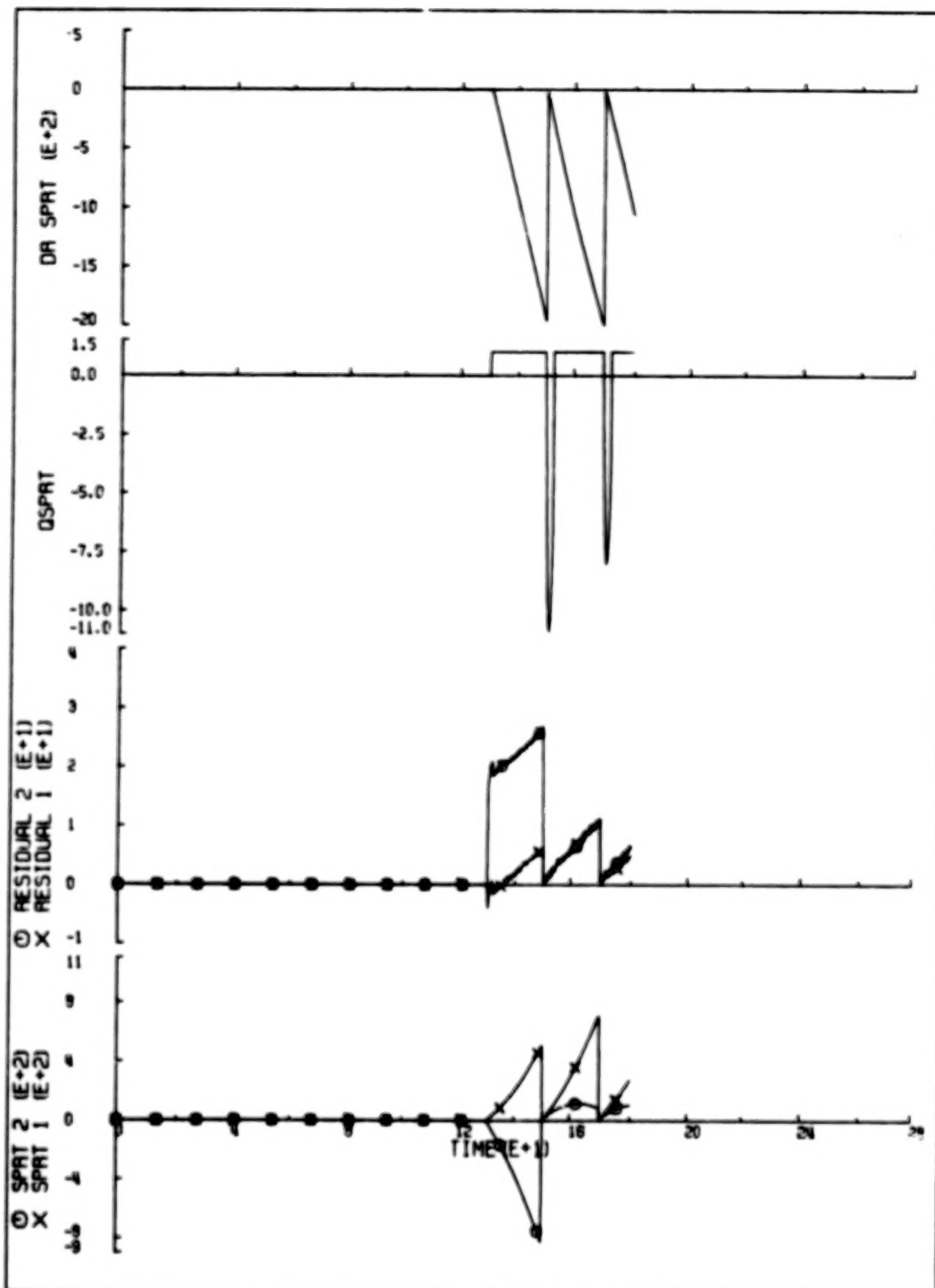


Figure 8-30 Segment 4B, Mach Meter 1 -BPM Bias at T=130, TK

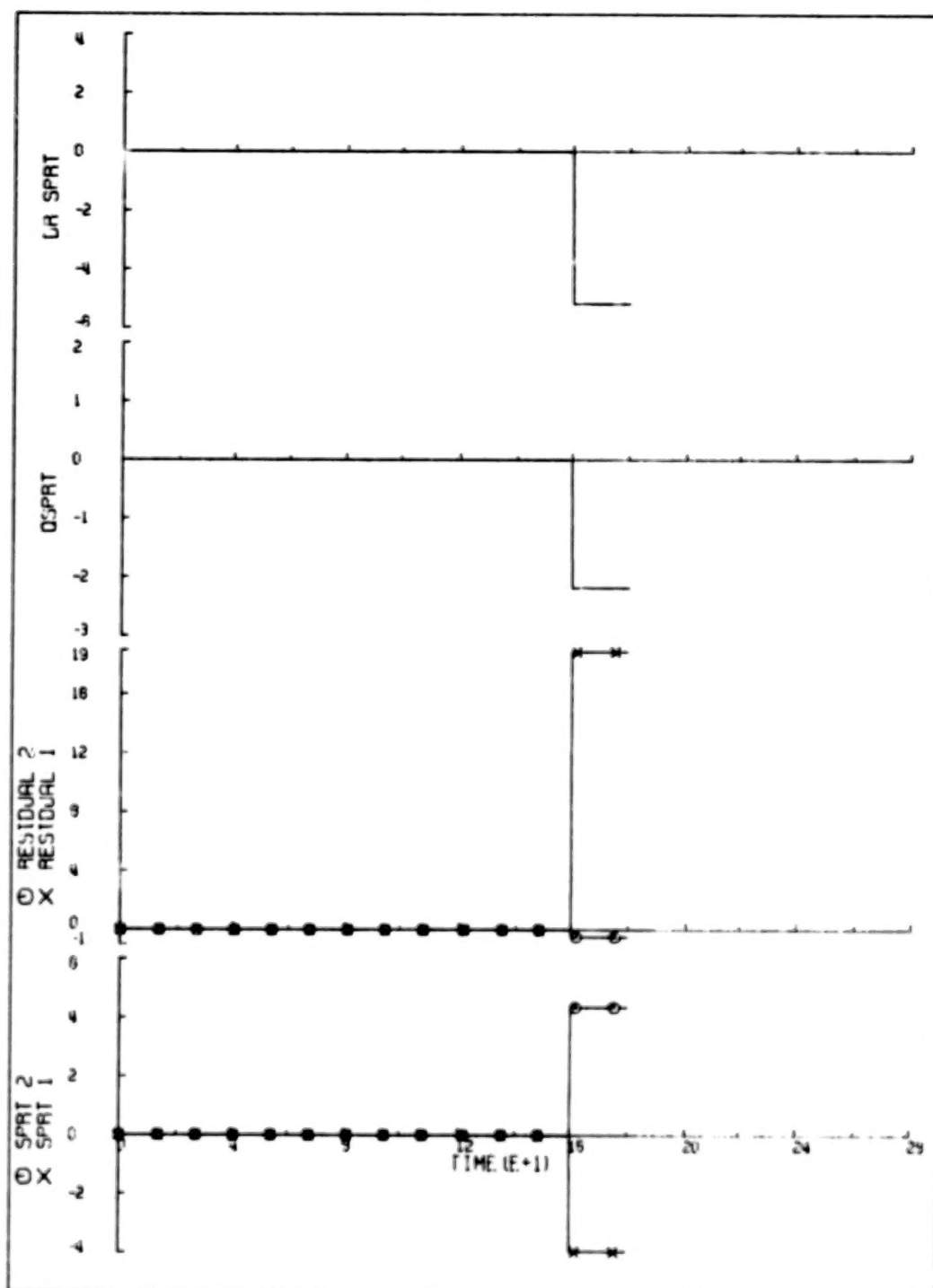


Figure 8-31 Segment 4B, Mach Meter 1 +BFM Bias at T=160, TK

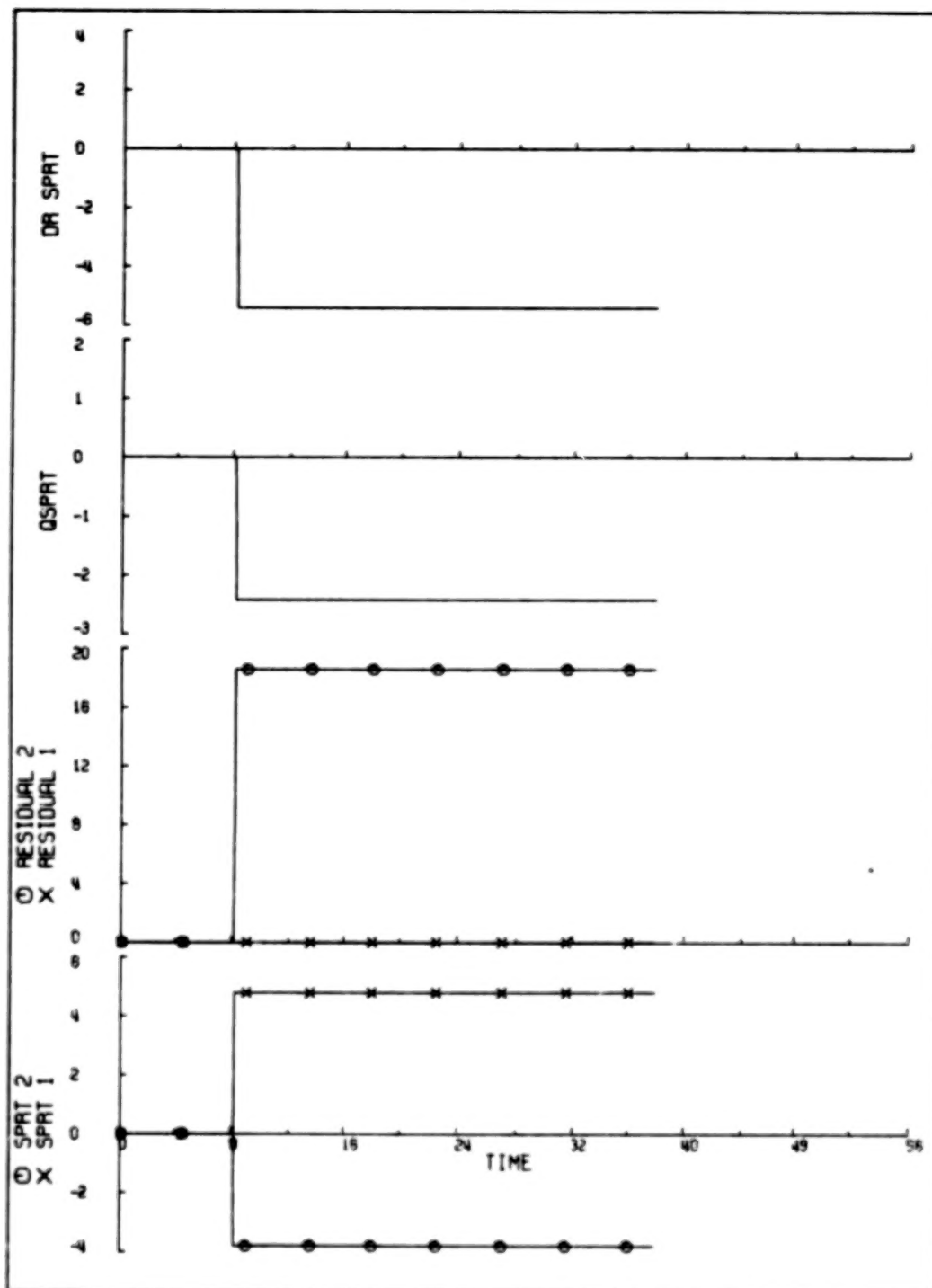


Figure 8-32 Segment 4A, Mach Meter 2 +BPM Bias at T=8, TK

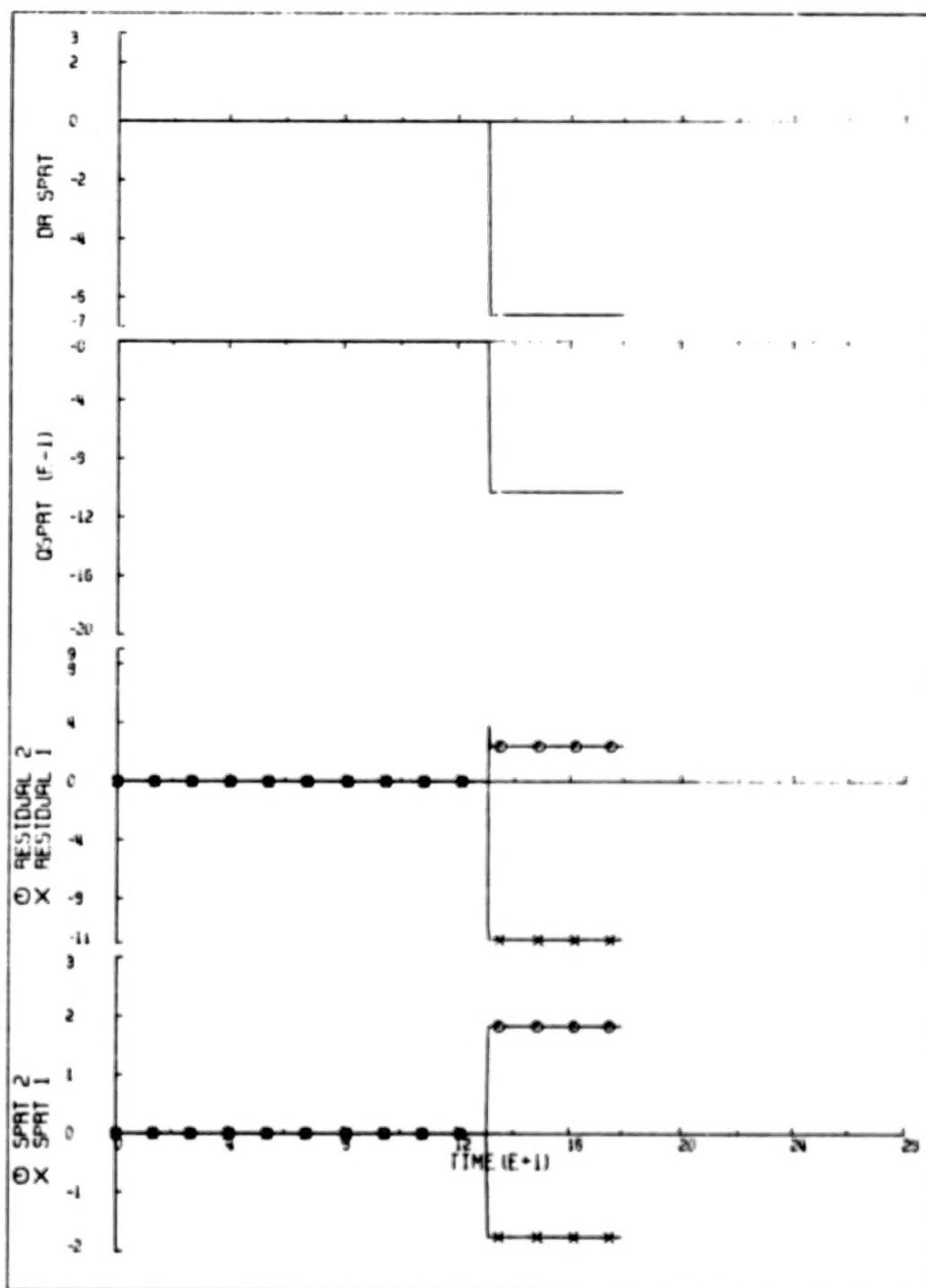


Figure 8-33 Segment 4B, Alpha Vane 1 +BFM Bias at T=130, TD

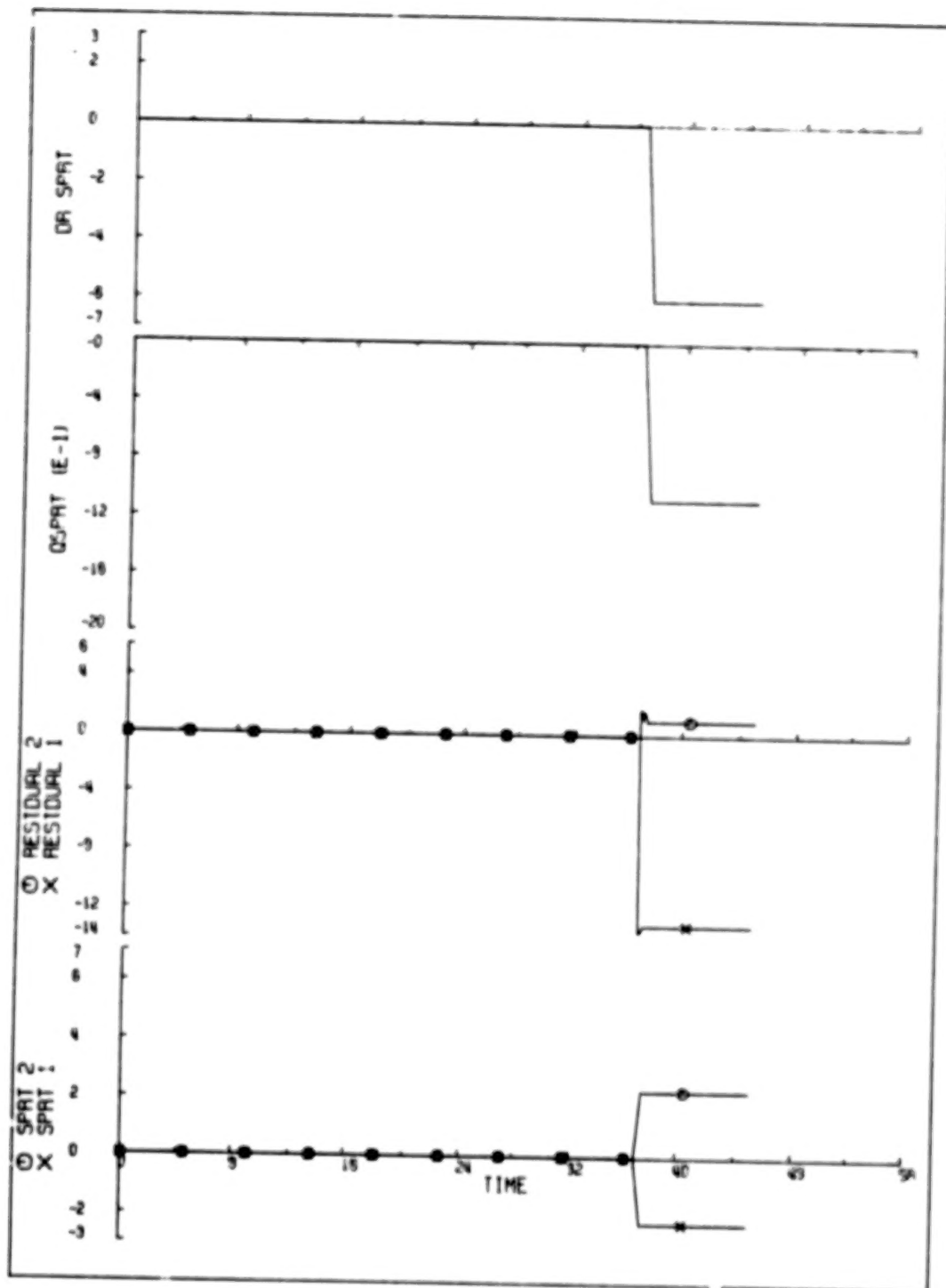


Figure 8-34 Segment 4C, Alpha Vane 1 +BFM Bias at T=36, TD

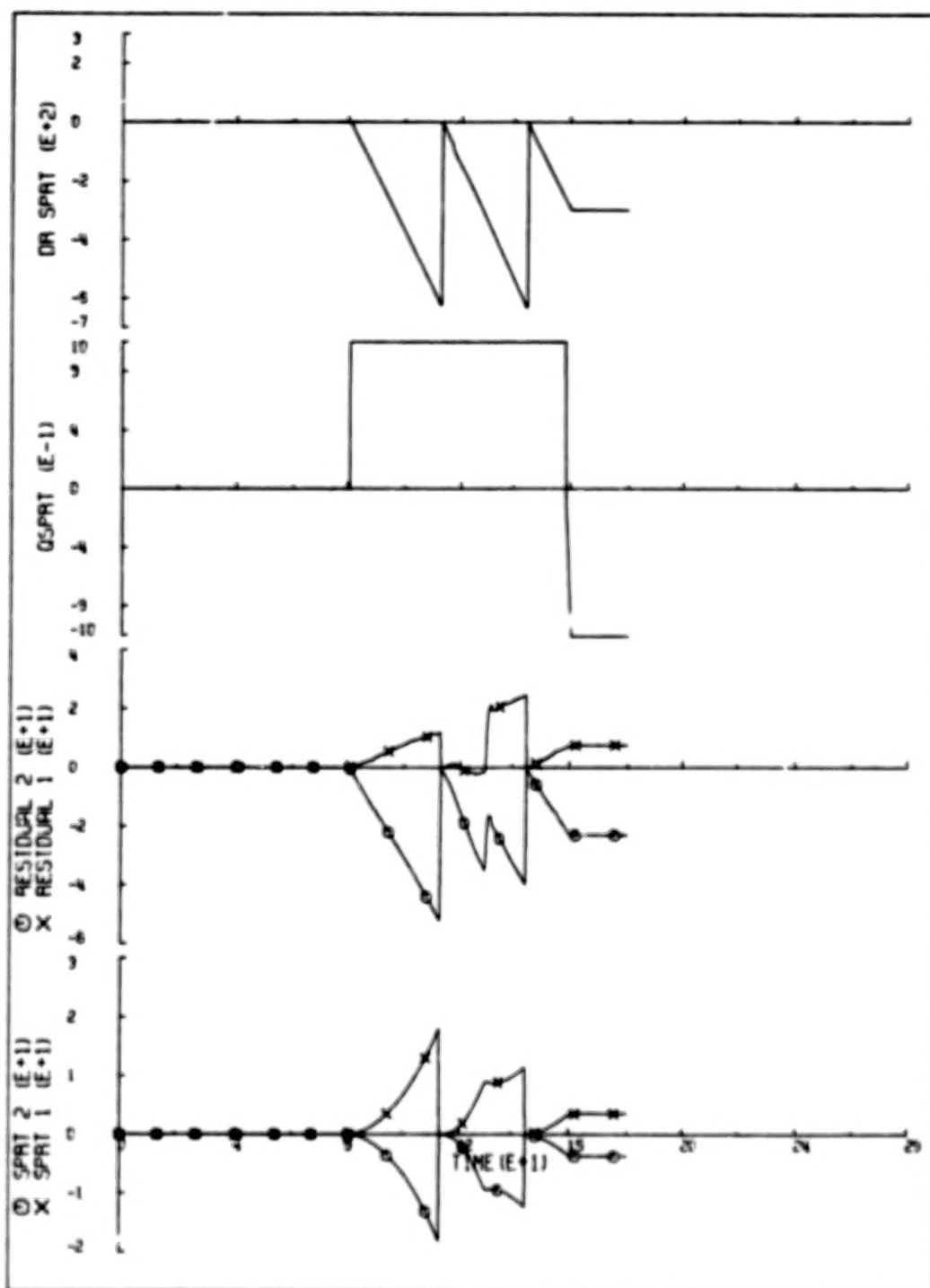


Figure 8-35 Segment 4B, Longitudinal Accelerometer 2 +BFM Bias at T=80, TX

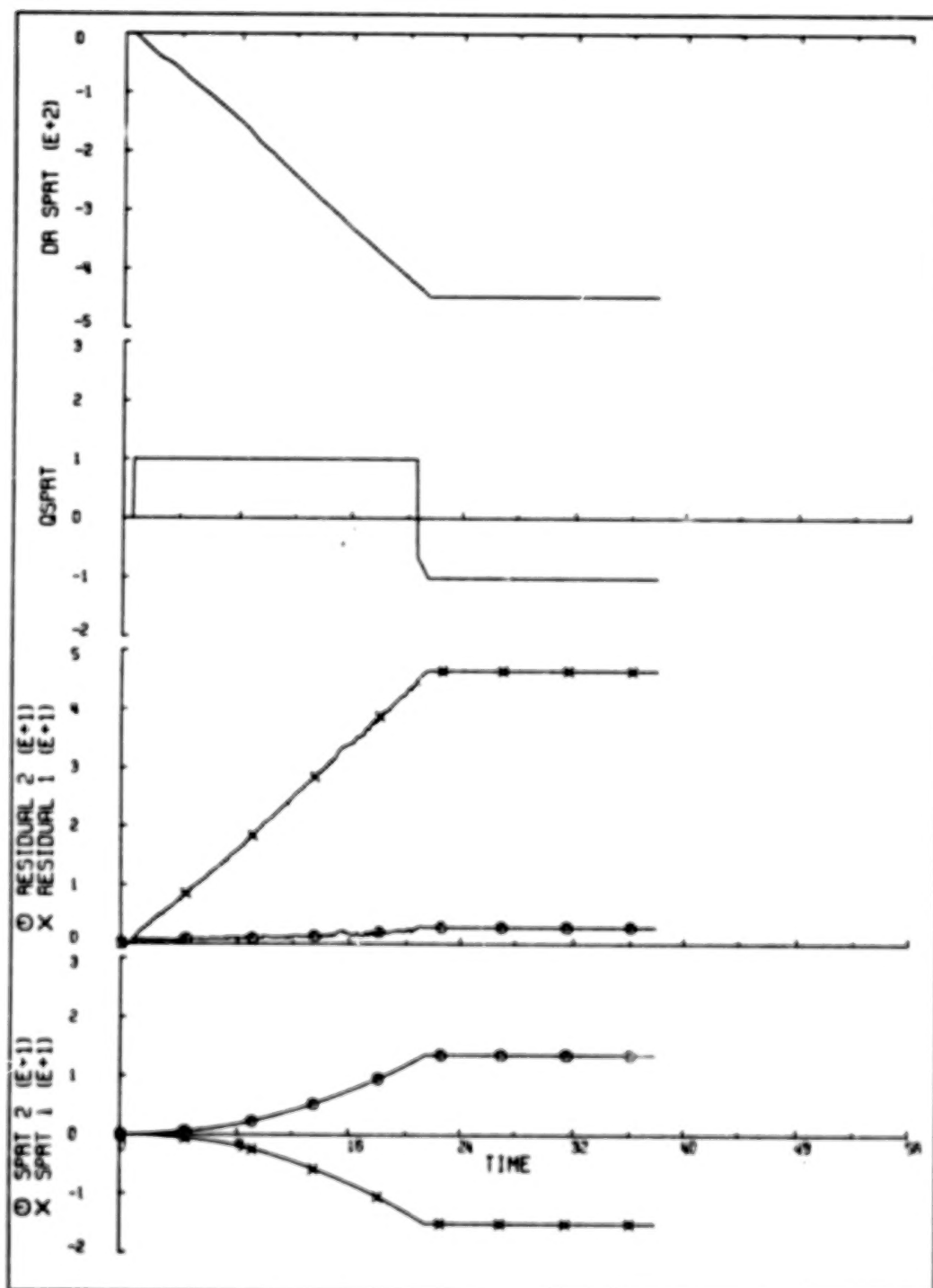


Figure 8-36 Segment 4A, Longitudinal Accelerometer 1 Fail to Zero at T=0, TK

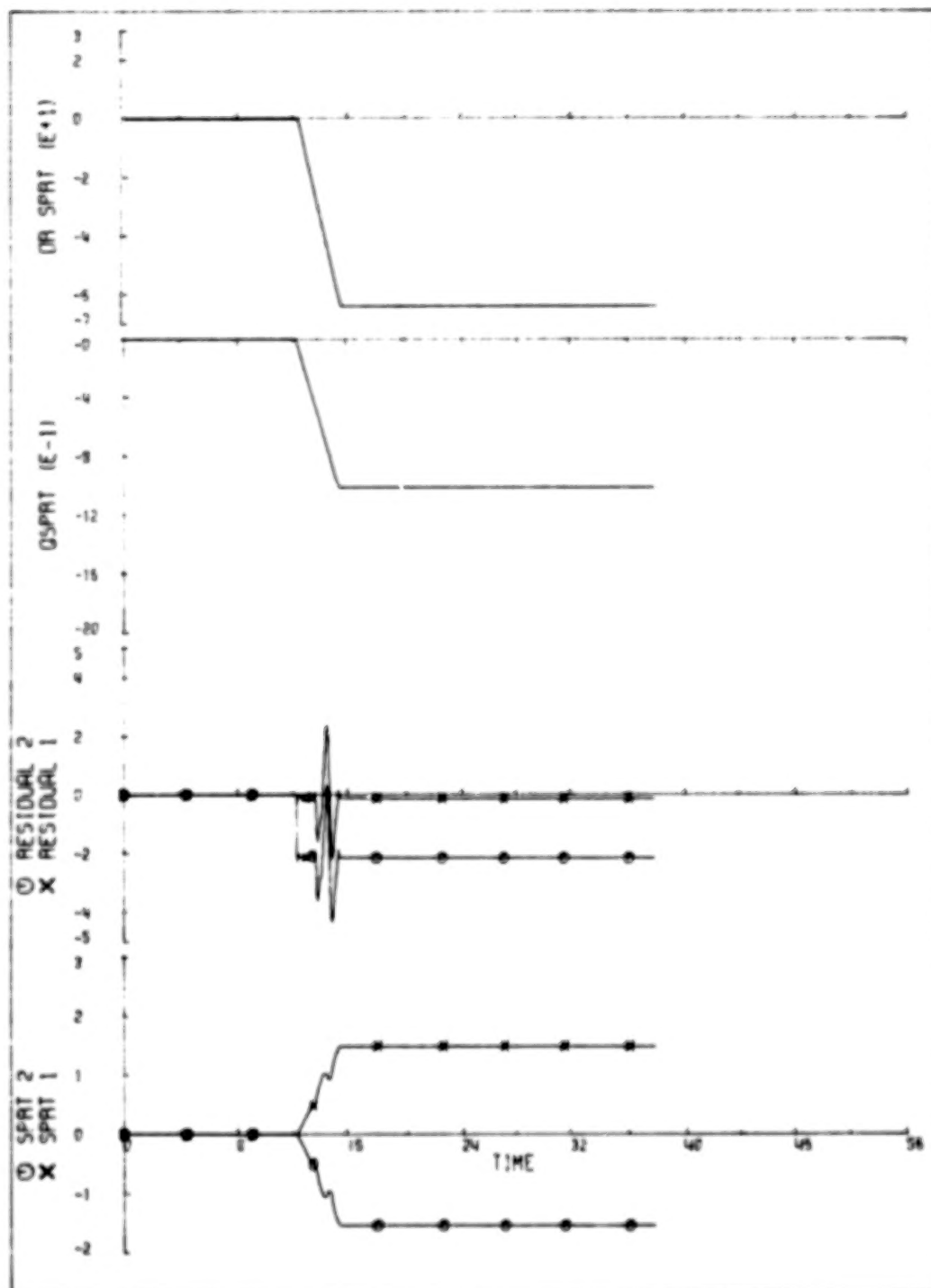


Figure 8-37 Segment 4A, Lateral Accelerometer 2 -BPM Bias at T=12, TD

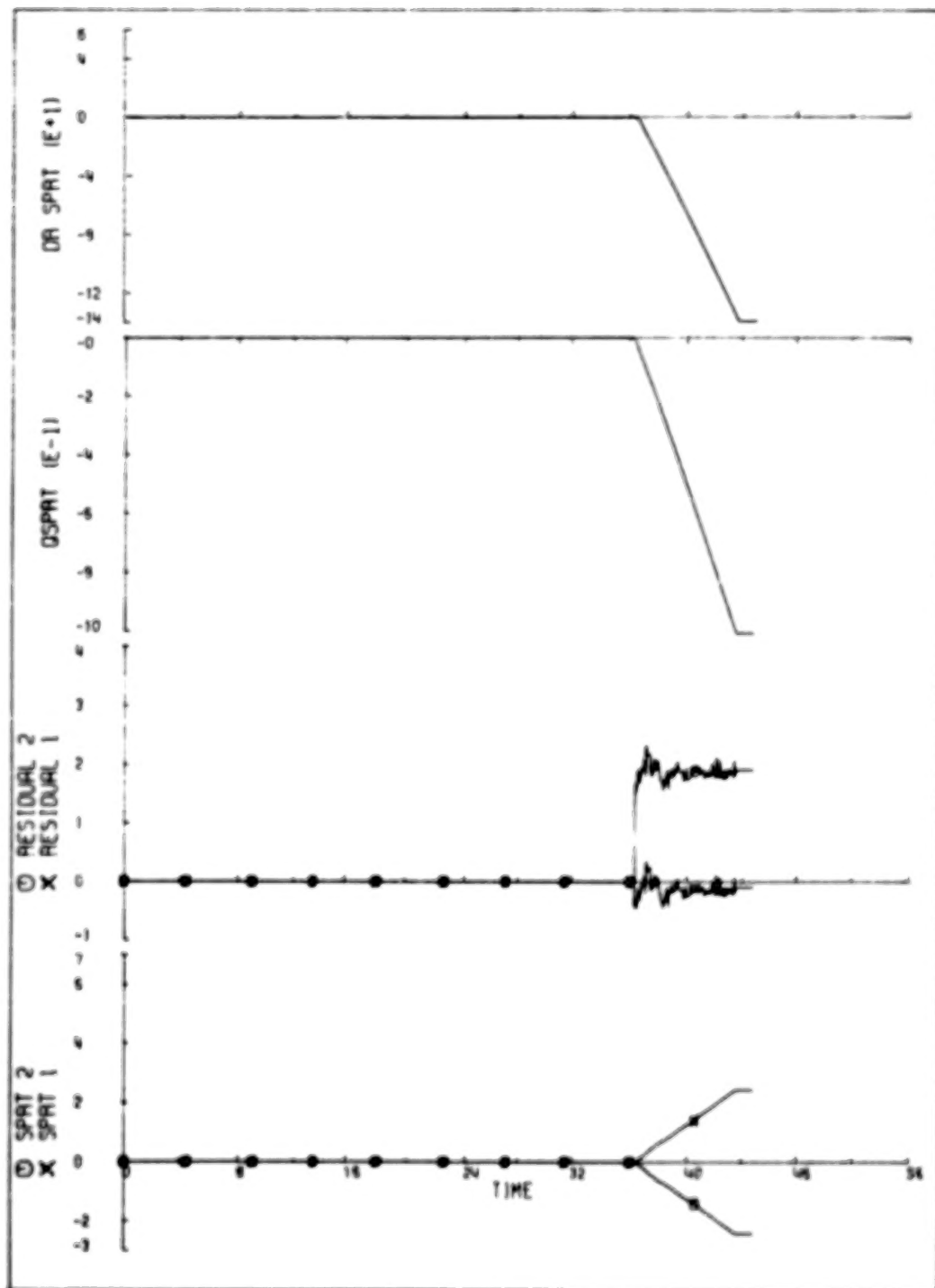


Figure 8-38 Segment 4C, Lateral Accelerometer 2 +BPM Bias at T=36, TD

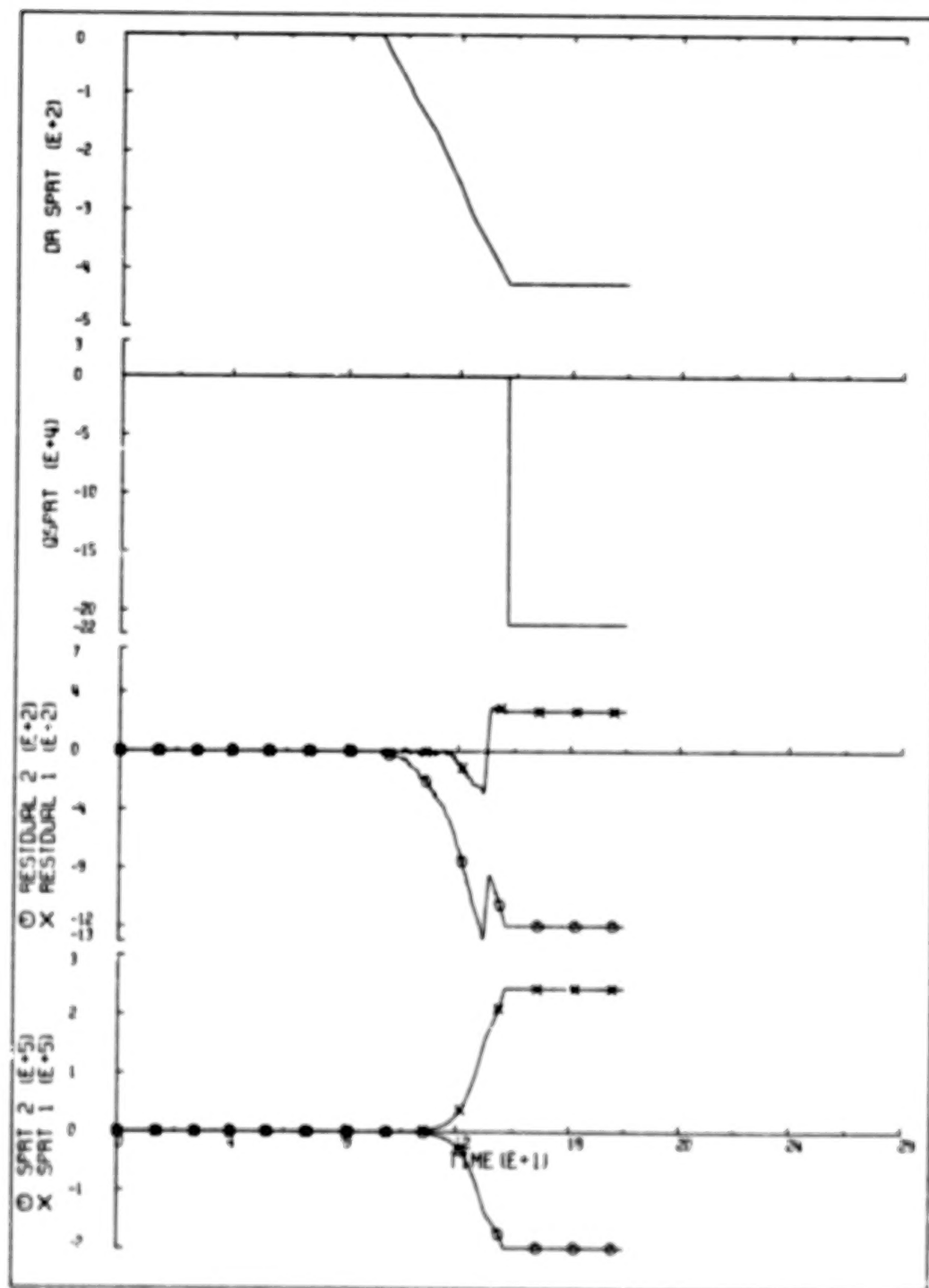


Figure 8-39 Segment 4B, Normal Accelerometer 2 -BFM Bias at T=90,AK

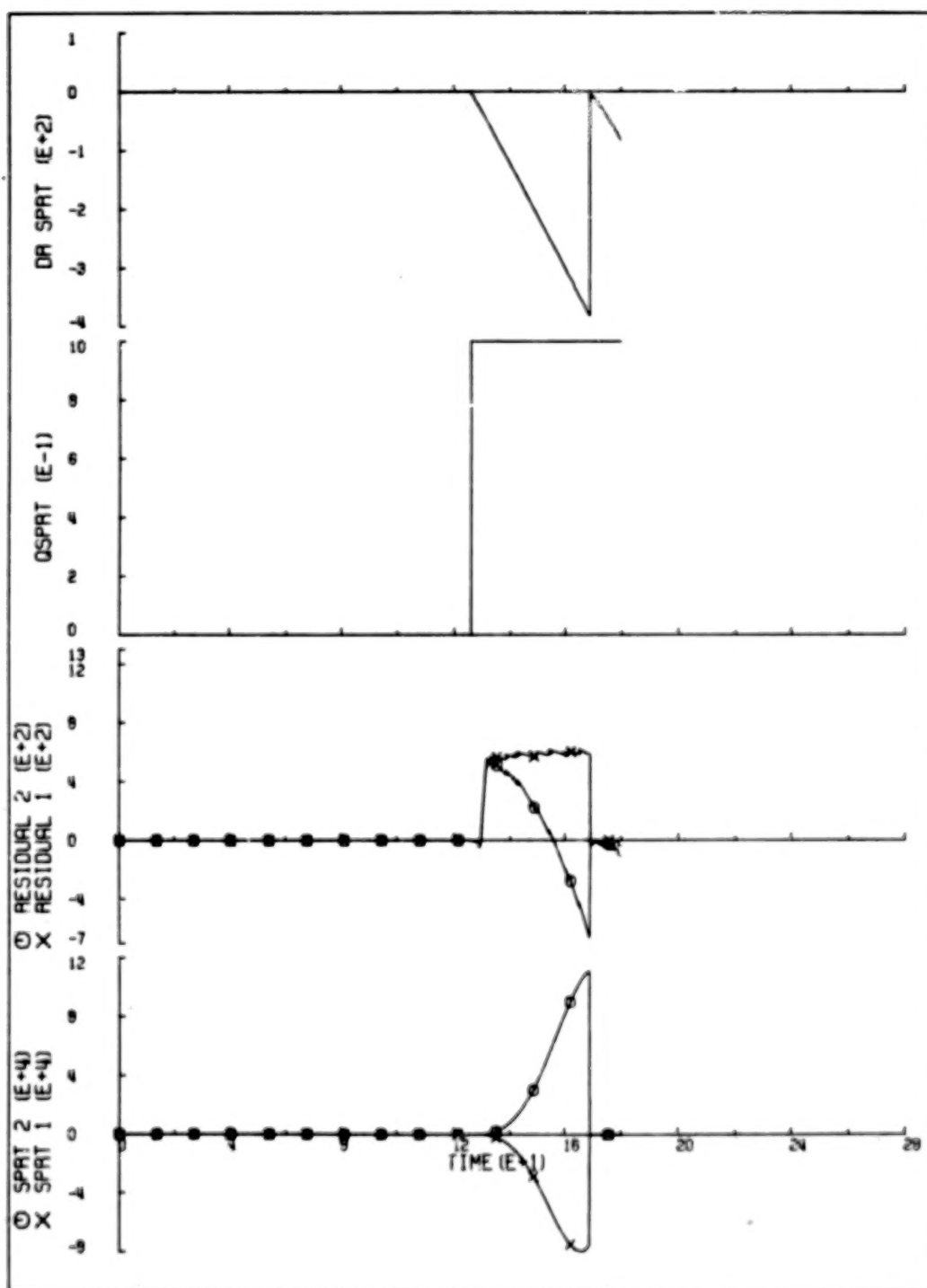


Figure 8-40 Segment 4B, Normal Accelerometer 2 -BFM Bias at T=125, AK

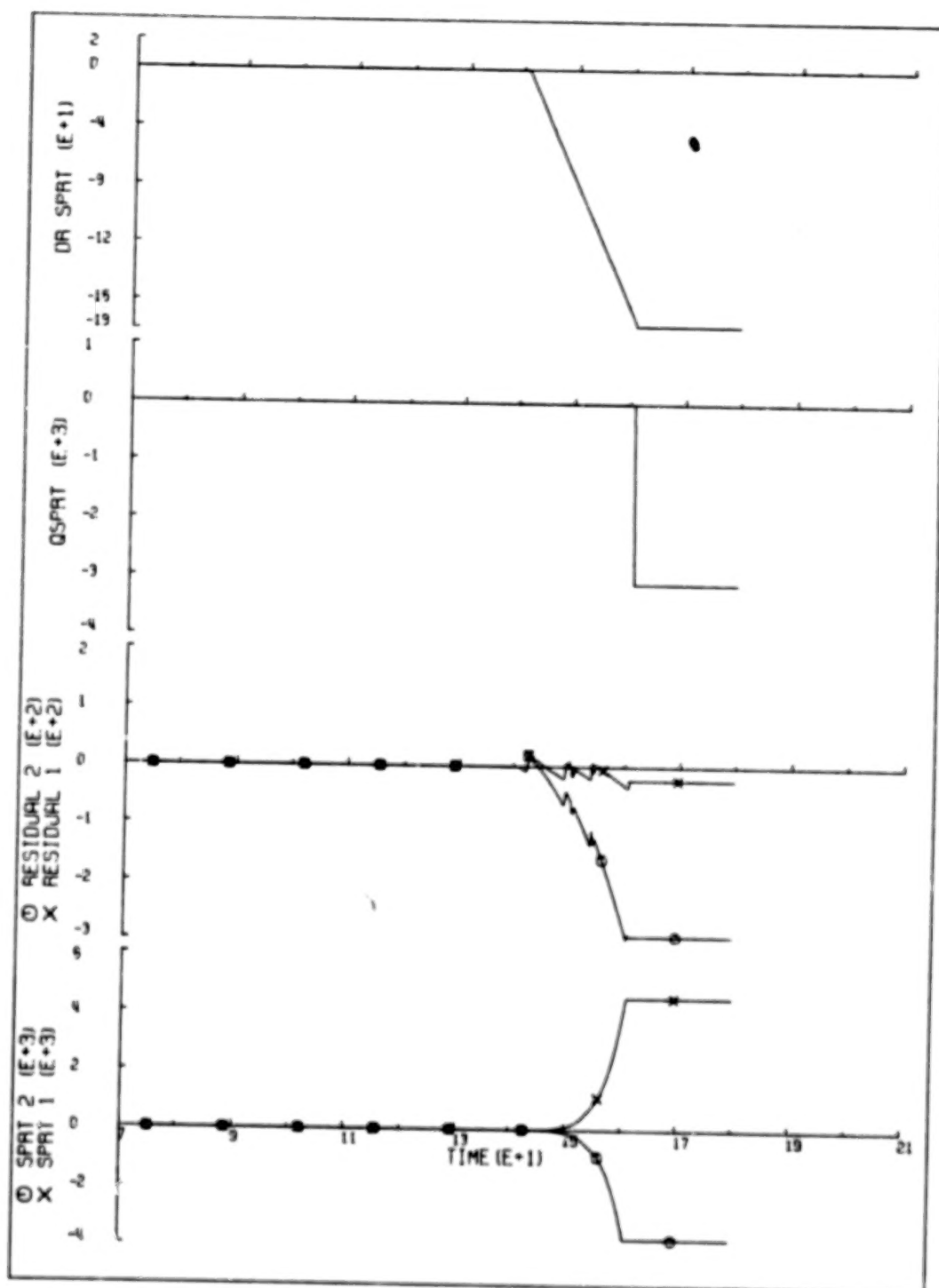


Figure 8-41 Segment 4B, Normal Accelerometer 2 -BFM Bias at T=140,AK

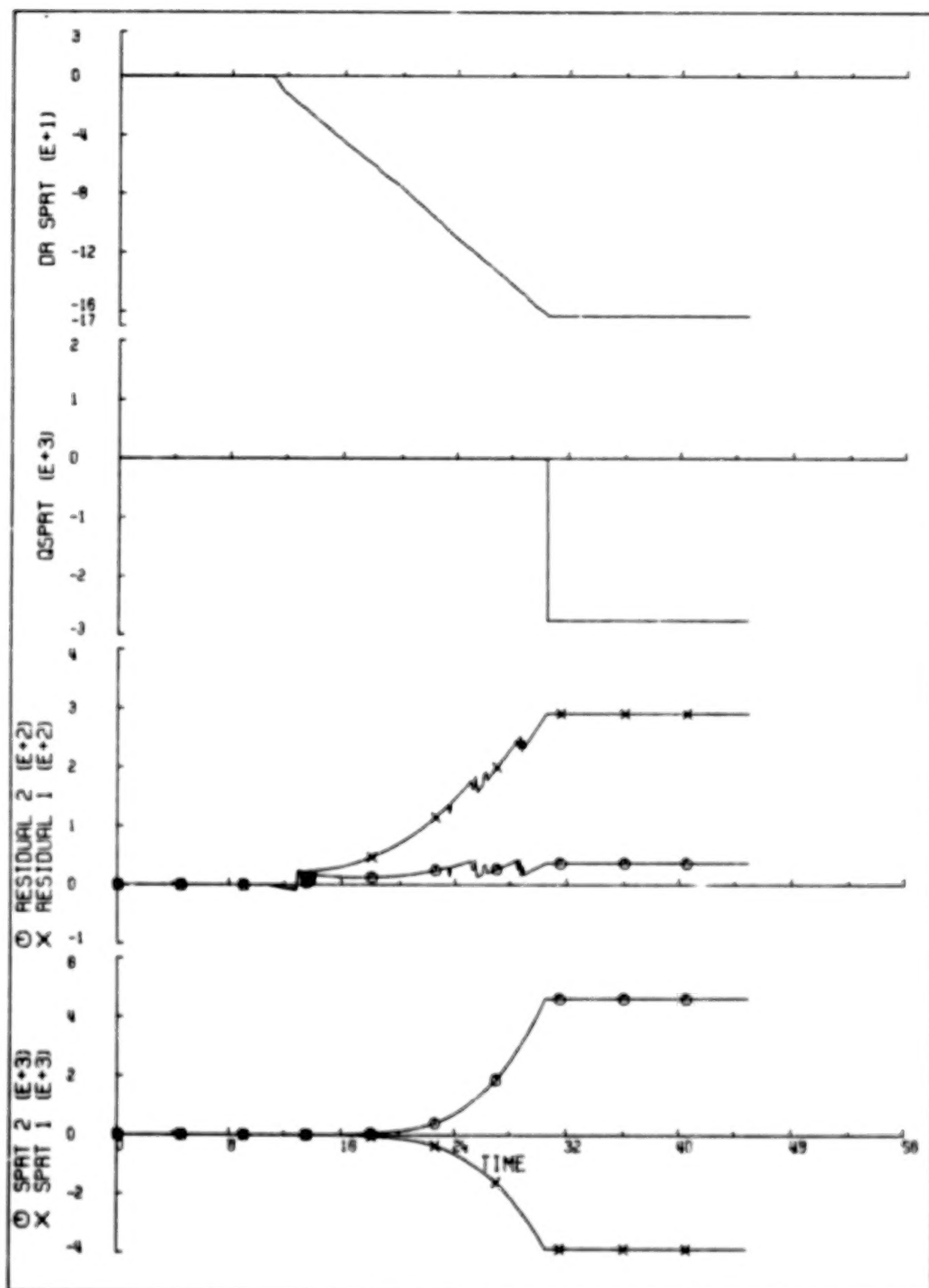


Figure 8-42 Segment 4C, Normal Accelerometer 1 +BFM Bias at T=10, AK

SECTION 9

CONCLUSIONS AND RECOMMENDATIONS

In this report we have presented the development of the analytic redundancy sensor FDI algorithm from its theoretical foundations through computer simulations to its successful application to telemetry data from the F-8 DFBW aircraft. The FDI framework of trigger, SPRT's, QSPRT's and outer loop has demonstrated its versatility through the ease by which it was modified to accommodate the instrument telemetry characteristics, which were significantly different in many cases from the idealized sensors of Table I. The modified FDI algorithm has given consistently reliable identification when applied to biases injected in the telemetry data and it has identified failure to zero in those situations where we feel the failure could critically impact the control system. Additionally no false detections or false identifications have been encountered in either the computer simulations described in Section 7 or the telemetry data applications discussed in Section 8. We also note that a technique has been developed to allow FDI for the DG's, whose raw outputs disagree drastically during maneuvers. This technique is essentially the same as that used for the VG's except that the DG outputs will be compensated for turn error before use and a low level drift between the compensated outputs of the two DG's will be allowed.

For completeness we mention here that as an alternative to time triggers a technique developed by Chien³ may be used to identify the failure of a single nonredundant sensor using the analytic redundancy tests we have developed. In Chien's procedure the SPRT output is reset to zero whenever it is computed to be positive, and the calculation of the negative (i.e. failure) threshold is somewhat different than for the standard SPRT, resulting in a slightly lower threshold for the same false alarm probability. Using either Chien's technique or a time trigger approach, we see that analytic redundancy allows nominal control system operation until such a time as no unfailed instrument of some type remains.

Recall that for nearly all of the instrument types for which secondary analytic redundancy tests exist, the secondary tests are unable to identify a BFM bias failure, and for those few secondary tests which can identify a BFM bias failure the identification time is significantly longer than for the primary test. Additionally, in none of the simulations performed to date has a failure remained unidentified by the primary test long enough to allow identification by the secondary test. Although this experience does not imply that there are no situations in which only the secondary test can identify the failure, it does suggest the low probability of such situations. And should such a situation ever arise, correct pilot response will enhance observability to allow identification by the primary test. For these reasons and in order to minimize computer timing and storage requirements, we suggest that for the flight test algorithm only the primary tests be retained for the Mach meters, alpha vanes, longitudinal accelerometers, rate gyros and attitude gyros. Thus secondary tests will be retained only for the lateral and normal accelerometers. We suggest retaining the secondary AK test for the lateral accelerometers to allow FDI on these instruments after the loss of the nonredundant beta vane, and we suggest retaining the secondary TD test for the normal accelerometers to allow some analytic redundancy coverage for these instruments during periods of sustained roll angle or transonic flight. We also propose retaining the self-test algorithm to minimize the impact of hard failures on the flight control system.

We feel that the BFM levels chosen in Section 8 should be retained for flight test except for the longitudinal accelerometers and yaw rate gyros which should be lowered to 1.5 m/sec^2 and $.01 \text{ rad/sec}$ respectively. These changes are justified because the BFM's chosen in Section 8 for these instruments reflected faulty signal conditioner behavior and not the actual instrument characteristics. The lowered yaw rate gyro BFM should also facilitate DG FDI

In an effort to trim inefficient calculations, the $k \neq 0$ attitude estimators should be eliminated entirely, with the differences between the measured and propagated attitude changes over each interval of the window saved for the attitude gyro RK SPRT's. Similarly the $k \neq 0$ air-relative velocity estimators should be eliminated, with differences between the measured and propagated longitudinal velocity changes over each interval of the window saved for the Mach meter TK SPRT's. This new procedure also reduces the construction of the $k = 0$ residuals

to a simple sum. The wind turbulence estimator will still follow the technique of Appendix A, but the input will be the difference between measured and propagated lateral velocity change over each successive sample interval.

Preliminary estimates have been made on the computer timing and core requirements for the proposed FDI algorithm. The timing estimate is obtained by adding the times required for all overhead arithmetic calculations such as self-test, DR triggers, failure injection and filter management to the time required for analytic redundancy tests for the sensor types with the most processing - the lateral and normal accelerometers. The execution times for various arithmetic operations on the IBM AP-101 computer which were used in this estimate are shown in Table IX.

Table IX AP-101 Execution Times

OPERATION	TIME (μ sec)
+	2
-	2
x	5.8
.	9.6

The combined time for arithmetic operations is then multiplied by 1.3 to allow for the non-arithmetic calculations, and a figure of 3 msec is obtained. Assuming a cycle time of 60 msec, this represents a 5% computer timing requirement.

In order to estimate the computer core requirements for the proposed onboard FDI algorithm, a FORTRAN IV System 360 version of the proposed algorithm has been written and compiled using the H option with the optimization parameter OPT set to 2. This FORTRAN program occupies 6800 32-bit words. It is very difficult to accurately translate this figure into equivalent AP-101 code for two reasons: First, direct translation efficiency is extremely dependent upon the actual FORTRAN code and second, direct coding in machine language to accomplish a particular job step is almost always more efficient than translating code generated by a high order language such as FORTRAN. Despite these difficulties, a worst case conversion factor from FORTRAN/360 to AP-101 core requirements of .67 is often used,

and this figure arises from the large number of half-word instructions in the AP-101 instruction set compared with FORTRAN. Using this factor the maximum core required by the proposed analytic redundancy sensor FDI algorithm is 4600 words, which represents approximately 14% of the total computer space. However we feel that through direct machine language coding this core requirement figure can be lowered to the neighborhood of 3000 words.

APPENDIX A*

TURBULENCE ESTIMATOR

As indicated in Section 3.2, it is necessary for us to be aware of the presence of turbulence in order to slow down the translational kinematics SPRT's, thus eliminating false identification due to wind shear. Our philosophy, outlined in Section 4.4.2, is to assume one of two levels of turbulence, either low or high, and to assume corresponding low or high worst-case shears for the SPRT calculations. In this appendix we outline the technique for detecting the presence of high turbulence.

We utilize the residuals γ from the translational filter, each channel of which has the following form in continuous time:

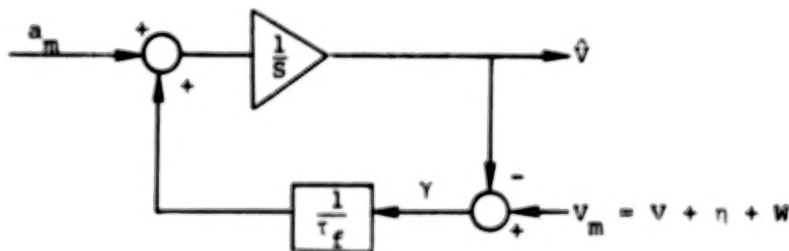


Figure A-1 Continuous Velocity Estimator

In Figure A-1, a_m is the measured acceleration from the compensated accelerometer outputs, V_m is the measured velocity from the air-data sensors, η is the velocity measurement noise (assumed white), V is the velocity of the aircraft with respect to inertial space and W is the inertial velocity of the wind.

Now, our objective is to determine whether the variance of the wind velocity W is "high". Assuming V is of low frequency, we see that the residual γ consists essentially of the high frequency components of W and η and the low frequency noise in a_m . Because

*The work summarized in Appendices A and B was performed by E. Y. Chow.

the high frequency component of W is the turbulence we are looking for, we high-pass filter the residual γ to eliminate the accelerometer noise, leaving only the high frequency components of η and W . To obtain a measure of the size of these components, and thus a measure of the turbulence, we square the high-passed residual and then low-pass the squared signal. Thus we have

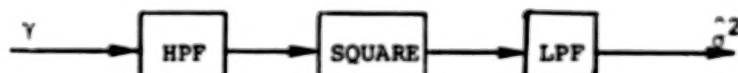


Figure A-2 Residual Processing

In Figure A-2, HPF and LPF denote first order high- and low-pass filters respectively. The time constants for these two filters are parameters chosen to give good performance in determining the presence of high turbulence. The time constant of LPF indicates the speed of response to changes in the wind turbulence, and we have chosen it to be 5 seconds. Because most of the energy of W is at low frequencies, we would like a large time constant for HPF. On the other hand, too large a choice will result in corruption of the variance estimate $\hat{\sigma}^2$ with the low frequency error of a_m . With a wind turbulence variance of $30 \text{ m}^2/\text{sec}^2$ (the 99% Dryden level) and a variance in η of $3.3 \text{ m}^2/\text{sec}^2$, the performance of the variance estimator in Figure A-2 is essentially unchanged for HPF time constants from 5 sec to 50 sec. However, for time constants lower than 0.5 sec, the estimator performance becomes degraded in the presence of a large mean wind velocity, which is clearly undesirable. Thus we have also chosen the HPF time constant to be 5 sec.

With the assumption that the wind is isotropic, the effective measurement noise in the y channel of the decoupled translational estimator is the minimum of the three channels over all angles of attack, and therefore we have chosen to monitor the residual from this channel only for the wind variance estimator.

Because we have chosen from practical considerations to make only a high/low turbulence decision, we must choose thresholds on the wind variance estimator $\hat{\sigma}^2$ for this purpose. In simulations without

turbulence, the wind variance estimate remains near $3.7 \text{ m}^2/\text{sec}^2$. With the onset of the 99% turbulence level, the wind variance estimate quickly grows to at least $7.4 \text{ m}^2/\text{sec}^2$ with peaks of $17 \text{ m}^2/\text{sec}^2$. Thus we have chosen the high turbulence threshold to be $6.5 \text{ m}^2/\text{sec}^2$. Following the indication of high turbulence, we demand that the variance drop below $5.6 \text{ m}^2/\text{sec}^2$ before making a low turbulence decision. This hysteresis has given satisfactory performance in all simulations to date.

1087 XHQJQ

BLANK PAGE

BLANK PAGE

APPENDIX B

AERODYNAMIC COEFFICIENT APPROXIMATION

Assuming that the aircraft is in the "clean" configuration, seven coefficients are required to perform FDI using the translational dynamics tests. These parameters, listed as functions of flight condition, are*:

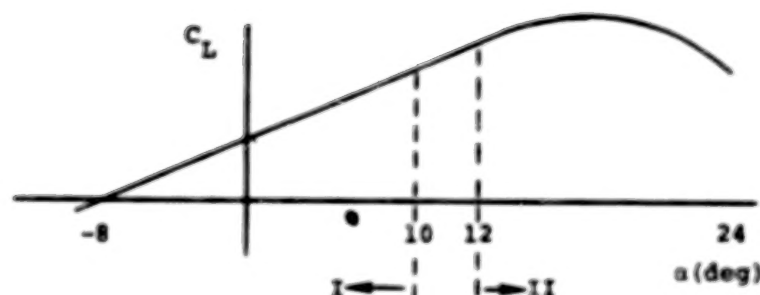
$$\begin{aligned} C_L(\alpha, \delta e, M) & , \quad C_{Y\beta}(\alpha, M) & , \quad T_{MIL}(h, v) \\ C_D(\alpha, M) & , \quad C_{Y\delta r}(\alpha, M) & , \quad T_{AB}(h, v) \\ C_{D\delta e}(\alpha, \delta e) & , \end{aligned}$$

For digital simulation purposes at CSDL and at NASA LRC, multidimensional table interpolation is used to determine these coefficients as functions of time. However, since the total number of table entries for these seven coefficients is approximately 1300, the storage overhead for this approach was felt to be too large for onboard implementation. This motivated an effort to obtain polynomial approximations to these coefficients, and resulted in a reduction in data storage locations by a factor of 8 with only a modest overhead in program storage and execution time. Some details of the approximations and the resulting vehicle acceleration errors follow.

As a function of Mach, C_L is rather ragged, but it is much smoother as a function of α and δe . We note that

1. C_L is almost linear in δe
2. C_L as a function of α for fixed δe and Mach is shaped roughly as follows:

*The coefficients $C_{Y\delta a}$, C_{Yp} and C_{Yr} are of negligible effect and have been ignored in this study. T_{MIL} and T_{AB} are used to compute F_e .



With these ideas in mind, the approximating polynomial for C_L is chosen to be first order in δe . For each Mach breakpoint we have the following: for $\alpha \leq 10^\circ$, defined as region I, the polynomial is first order in α while for $\alpha \geq 12^\circ$, defined as region II, the polynomial is second order in α . Thus at each Mach breakpoint we have:

Region I

$$C_L = A_1 + A_2 \delta e + A_3 \delta e \alpha + A_4 \alpha$$

Region II

$$C_L = B_1 + B_2 \delta e + B_3 \delta e \alpha + B_4 \alpha + B_5 \alpha^2 + B_6 \alpha^2 \delta e$$

For the region $10^\circ < \alpha < 12^\circ$, C_L is obtained by linear interpolation between regions I and II. As the polynomial coefficient A's and B's are stored at 12 Mach breakpoints, C_L is obtained at a particular Mach number by linear interpolation between the values of C_L obtained at the bracketing breakpoints. The choice of the A's and B's for C_L were obtained with the objective of keeping the fits good around the trim flight condition for two reasons. First, the majority of flight time will be spent in that region. Second, the actual error which degrades the translational dynamics SPRT's is the acceleration error, which is proportional to the table error times the square of Mach. Thus, even "better" polynomial fits in the high Mach region will not appreciably improve the error in the translational dynamics tests in that region.

The coefficients C_D and $C_{y\delta}$ are functions of Mach and α , and as with C_L are ragged as functions of Mach. Thus, noting that the

accuracy of transonic data is questionable, we have defined three Mach regions and the polynomial approximation within the regions as follows:

Region I: $.18 \leq M \leq .9$

$$C_D[C_{y\beta}] = D_1 + D_2 \alpha + D_3 M + D_4 \alpha M$$

Region II: $1.2 \leq M \leq 1.9$

$$C_D[C_{y\beta}] = E_1 + E_2 \alpha + E_3 M + E_4 \alpha M$$

Region III: Wing up, without ground effect

$$C_D[C_{y\beta}] = F_1 + F_2 \alpha + F_3 \alpha^2$$

For values of Mach between .9 and 1.2, linear interpolation is employed.

The other coefficients are fitted across the entire tabulated region as the resulting acceleration errors are much smaller than those due to C_L and C_D :

$$T_{MIL}[T_{AB}] = G_1 + G_2 h + G_3 v + G_4 hv$$

$$\begin{aligned} C_{D\delta e} = & H_1 + H_2 \alpha + H_3 \delta e + H_4 \alpha \delta e + H_5 \alpha^2 + H_6 \alpha^2 \delta e \\ & + H_7 \alpha^2 \delta e^2 + H_8 \alpha \delta e^2 + H_9 \delta e^2 \end{aligned}$$

$$C_{y\delta r} = L_1 + L_2 M + L_3 M^2 + L_4 M^3$$

The Q/PRT's for the translational dynamics tests for the accelerometers and air-data sensors require knowledge of the worst-case acceleration biases in the test due to errors in the coefficients. For this purpose, extensive evaluations were performed of the acceleration errors in body axes due to the polynomial approximations to the seven parameters discussed above. As a result of these tests two regions were defined: a region of "good" fit and a region of "bad" fit. The region of good fit is within the bounds:

$$-10^\circ \leq \delta e \leq 5^\circ$$

$$-4^\circ \leq \alpha \leq (20 - 13.3M)^\circ$$

while the region of bad fit is everywhere outside the good region. The worst-case accelerations along body axes, due to the polynomial approximations, are given as functions of Mach in Table B.1 for the good and bad fit regions:

Table B.1 Worst-Case Acceleration Error due to Polynomial Approximation

Body Axis	Good Region (m/sec ²)	Bad Region (m/sec ²)
x	$1.96M^2 + .0063/M^2$	$.29e^{2M} + .00064e^{10M}$
y	$.65M^2$	$.65M^2$
z	$.98M^2 + .29M$	$.016e^{8M} + .04/M$

At trim at Mach = 0.6, the acceleration errors are .73 m/sec² in x, .24 m/sec² in y and .53 m/sec² in z.

APPENDIX C

SCALE FACTOR FAILURES

We have developed a methodology for adapting the analytic redundancy SPRT's for the various instrument types to the detection of scale factor failures. In this section we derive the form of the SPRT for the roll rate gyro. The analysis for the other instruments is similar. Recall that the rotational kinematics residual for p is of the form

$$\gamma(t) = \int_0^t p_m(\tau) d\tau - \phi_m(t) + \phi_m(0) + \int_0^t \dot{\psi}_m(\tau) \sin \theta_m(t) dt$$

Suppose now that we have a scale factor failure, i.e., that

$$p_m(t) = v p(t) + \text{noise}$$

where v is the scale factor. Let us define

$$\xi(t) \equiv \int_0^t p(\tau) d\tau \quad (C.1)$$

and

$$\rho(t) \equiv \phi_m(t) - \phi_m(0) - \int_0^t \dot{\psi}_m(t) \sin \theta_m(t) dt = \xi(t) + \text{noise} \quad (C.2)$$

Then

$$\gamma(t) = (v-1) \rho(t) + \text{noise}$$

and we can define an SPRT of the form

$$u_n = \sum_{k=1}^n \frac{(v-1) \rho(t_k)}{\sigma^2} \left[\frac{(v-1) \rho(t_k)}{2} - \gamma(t_k) \right]$$

Note that in this case the residual $\rho(t)$ is dependent on the data and must be computed on-line, i.e., the effect of a scale factor failure is modulated by the flight trajectory. For example, if $p(t) \equiv 0$, then except for the noise $\rho(t) \equiv 0$. Also note that v is the "failure extent parameter" which must be chosen, replacing the bias size B . Finally, it is clear that the time until detection depends upon the time history of the variable p . Thus in order to calculate ETL we must postulate a nominal trajectory for p . Given the time history of p , we can compute the expectation of the SPRT output when there is no failure (H_2) as

$$E[u_n | H_2] = \sum_{j=1}^n \frac{(v-1)^2 \xi^2(t_j)}{2\sigma^2} + \frac{(v^2-1)n}{2} \quad (C.3)$$

and when there is a failure (H_1) as

$$E[u_n | H_1] = - \sum_{j=1}^n \frac{(v-1)^2 \xi^2(t_j)}{2\sigma^2} + \frac{(v^2-1)n}{2} \quad (C.4)$$

In Eq. (C.3) and (C.4) the second term is due to the fact that $\rho(t)$, the measurement of $\xi(t)$, contains noise of variance σ^2 . Note that for $v < 1$, this test bias tends to drive the SPRT toward the negative (failure) threshold. Hence, one may want to remove this bias from the SPRT before making failure decisions.

We now illustrate how one might evaluate the parameters for a failure identification system based on this SPRT. To do this we must postulate a trajectory for p . We will exclude the case of constant p from consideration since the failure will effectively appear as a bias and will be identified by the SPRT's enumerated in Sections 3 and 4. Because oscillatory trajectories for p are those which most require a scale factor test, we consider trajectories of the form

$$p(t) = A \sin \omega t \quad (C.5)$$

Making the usual integral approximation to Eq. (C.4) and substituting Eq. (C.1) gives the following equation for the time T_c at which the failure threshold is crossed:

$$\frac{(v-1)^2}{2\sigma^2 T} \int_0^{T_c} \left[\int_0^{\tau} p(s) ds \right]^2 d\tau = 9.2 + \frac{(v^2-1) T_c}{2T}$$

Evaluating the integral using (C.5) gives

$$\frac{A^2(v-1)^2}{2\sigma^2 \omega^2 T} \left[\frac{3T_c}{2} - \frac{2}{\omega} \sin \omega T_c + \frac{1}{4\omega} \sin 2\omega T_c \right] = 9.2 + \frac{(v^2-1) T_c}{2T} \quad (C.6)$$

We assume the following parameters:

$$\begin{aligned} v &= 0.5 \\ A &= 0.026 \text{ rad/sec} \\ \omega &= \pi/4 \text{ rad/sec} \\ \sigma^2 &= 0.0002 \text{ rad}^2 \\ T &= 0.0625 \text{ sec} \end{aligned}$$

Substituting those values into Eq. (C.6) and solving gives the time for the SPRT to reach the threshold as

$$T_c = 2.55 \text{ sec}$$

Using similar analysis, a QSPRT can be developed for this scale factor test incorporating the effects of unidentified instrument biases as enumerated in Section 5.

2000 10/10

BLANK PAGE

BLANK PAGE

APPENDIX D

SIMULTANEOUS ϕ AND θ FAILURES

Since ϕ and θ are both measured by the vertical gyro, one possible failure mode would involve the simultaneous development of biases in both ϕ and θ . Suppose then that we have simultaneous redundancy triggers for both ϕ and θ . The basic philosophy of the proposed identification scheme is as follows: we use the rotational kinematics SPRT for ϕ to look for a bias in the ϕ measurement using only θ_1 data in the ϕ_1 test and θ_2 data in the ϕ_2 test; however, possible θ biases may corrupt one of these tests. We then show that a realistic size for this θ bias is such that it can easily be picked up by translational kinematics. Combining these pieces, we obtain an overall identification scheme.

Let us go through the details. Recall the basic equation

$$\dot{\phi} = p + \dot{\psi} \sin \theta$$

In this case the ϕ bias manifests itself as a bias in the residual, and we also have the worst-case effects considered in Section 4: an initialization bias and a ramp due to a possible p bias. We also now have the possibility in the failed instrument only of a ramp bias of the form

$$\dot{\psi}_{\max} |\sin \theta - \sin \theta_m| t \quad (D.1)$$

where the $[\sin \theta - \sin \theta_m]$ term reflects the possible simultaneous θ bias failure. The maximum value of $\dot{\psi}$ is calculated assuming a sustained 6g turn at Mach 0.6. This yields

$$\dot{\psi}_{\max} = 0.312 \text{ rad/sec}$$

We observe that the SPRT for the unfailed ϕ instrument should work precisely as we have developed it. The only possible difficulty arises with the failed instrument. In this case the expectation of the probability ratio is given by Eq. (4.6), where the value of b must now reflect the term given in Eq. (D.1). For the sake of this development, let us set the other parameters in Eq. (4.6) as before

$$M = 0.012 \text{ rad}, B = 0.08 \text{ rad}, \sigma^2 = 0.0001 \text{ rad}^2$$

Substituting into Eq. (4.8) we obtain the following equation for the time T_c at which $E(u_n)$ crosses the failure threshold

$$6400 b T_c^2 + [575 b - 358.4] T_c + 9.2 = 0 \quad (D.2)$$

We also have

$$b = [.01 + .312 |\sin \theta - \sin \theta_m|] \quad (D.3)$$

where the .01 rad/sec contribution comes from possible p biases.

Note now from Eq. (3.10) that in translational kinematics the error $(\sin \theta - \sin \theta_m)$ causes a bias in \dot{V}_x of magnitude

$$9.81 |\sin \theta - \sin \theta_m| \text{ m/sec}^2 \quad (D.4)$$

We have already seen that we can detect a 1.5 m/sec^2 acceleration bias in the longitudinal direction. Hence, we can detect a $|\sin \theta - \sin \theta_m|$ error of size

$$|\sin \theta - \sin \theta_m| \geq \frac{1.5}{9.81} = .153 \quad (D.5)$$

Using this bound in Eq. (D.3) we have

$$b = .0565 \text{ rad/sec}$$

and in this case

$$T_c = .03 \text{ sec}, .87 \text{ sec}$$

Thus we can put together the following detection system: we implement the ϕ rotational kinematics and the a_x translational kinematics SPRT's. In both cases the SPRT for the unfailed instrument will work correctly, thereby eliminating the problem of declaring the unfailed instrument to be failed. If the θ bias is substantial (as defined by Eq. (D.5)), the translational kinematics will isolate the failed instrument. If the θ bias is not large enough to be detected, it is also not large enough to corrupt the rotational kinematics test, which then can identify the failed vertical gyro.

SCAT-000000

BLANK PAGE

BLANK PAGE

APPENDIX E

DESIGN AND PERFORMANCE OF AN ALTITUDE KINEMATICS FILTER

E.1 Introduction

Altitude kinematics (AK) is the most reliable form of analytical redundancy available for the FDI of a normal accelerometer. However, the FDI process is inherently slow due to the second order differential relationship of AK, and is slowed down further by the QSPRT to enable a reliable determination of the presence or absence of the accelerometer failure signature in the AK residuals in the presence of initialization errors.

The initialization errors arise due to errors in the estimates of altitude and altitude rate. These estimates are used to start the AK residual formation process, which essentially involves a straightforward double integration of the relationship

$$\ddot{h} = a_v \quad (E.1)$$
$$a_v = a_x \sin \theta - (a_y \sin \phi + a_z \cos \phi) \cos \theta - g$$

The effects of errors in the estimates of h and \dot{h} are a bias and ramp respectively in the AK residuals, thus necessitating the aforementioned slowdown until the effect of the expected failure becomes comparable to the effect of the initialization errors.

E.2 AK Filter Design

We discuss here some of the considerations involved in the design of the AK filter to help reduce the effect of initialization errors on the FDI process.

The basic structure of the filter follows from Kalman filter considerations for the double integrator system of Eq. (E.1) and is given by:

$$\begin{aligned}\dot{\hat{h}} &= \hat{v} + k_1(h_m - \hat{h}) \\ \dot{\hat{v}} &= a_{v,m} + k_2(h_m - \hat{h}),\end{aligned}\quad (E.2)$$

$$a_{v,m} = a_{x,m} \sin\theta_m - (a_{y,m} \sin\phi_m + a_{z,m} \cos\phi_m) \cos\theta_m - g$$

where $a_{v,m}$ represents the derived vertical acceleration with the subscript m denoting the measurements of various quantities. Based on the steady state Kalman gains, k_2 is selected to be equal to $k_1^2/2$ to yield a filter with a damping coefficient of 0.707 and a natural frequency of $\omega = k_1/2$ rad/sec. The gain k_1 is chosen based on the trade-off consideration of keeping small the combined effect on the filter estimates of errors in the altimeter data and the derived vertical acceleration.*

From Eqs. (E.1) and (E.2) we get the following Laplace transform equations for e_h and e_v , the errors in the estimates of altitude and altitude rate respectively:

$$e_h(s) = \frac{[-a_e - (sk_1 + k_2)h_e] + [se_{ho} + e_{vo}]}{s^2 + k_1s + k_2} \quad (E.3)$$

$$e_v(s) = \frac{[-(s+k_1)a_e - sk_2h_e] + [(s+k_1)e_{vo} - k_2e_{ho}]}{s^2 + k_1s + k_2} \quad (E.4)$$

In the above equations, h_e and a_e represent errors in h_m and $a_{v,m}$ respectively, with e_{ho} and e_{vo} representing initial conditions on e_h and e_v .

Of main concern in the initialization errors is the effect of slowly varying sensor errors on the estimate of the altitude rate. These errors may arise due to allowable or undetectable biases in the accelerometers and due to the relatively high level of quantization in the altimeter data.

A min-max approach is adopted (consistent with the FDI approach for maximum reliability) to select the gain k_1 so as to minimize

* Only the continuous time filter is discussed here. The discrete time filter gains are obtained by multiplying the continuous time gains by the sample period T .

the worst case error that may occur in the presence of allowable biases in both h_m and $a_{v,m}$. Since the effect of a bias in h_m on the estimate of \hat{h} is transient in nature, the worst case error is calculated as follows: The steady state bias values of $e_{ho} = 2a_b/k_1^2$ and $e_{vo} = 2a_b/k_1$, attained in the presence of a bias a_b in $a_{v,m}$, are assumed as the initial estimation errors existing at the onset of a bias change of h_b in the altimeter data, and the worst case error in the transient is calculated using Eq. (E.4). It can be shown that the worst case error in the estimate of velocity occurs \tilde{t} seconds after the bias change in h_m , with \tilde{t} and the error given by,

$$\tilde{t} = \frac{2}{k_1} \tan^{-1} \left(\frac{k_1^2 - 2\zeta}{k_1^2 + 2\zeta} \right), \quad (E.5)$$

$$e_{v_{\max}}(\tilde{t}) = \frac{h_b}{\sqrt{2}} \left(k_1^2 + \frac{4\zeta^2}{k_1^2} \right)^{1/2} \cdot \exp \left(-\frac{k_1 \tilde{t}}{2} \right), \quad (E.6)$$

where $\zeta = a_b/t_b$. It can be shown from Eqs. (E.5) and (E.6) that the minimum worst case error of

$$e_{v_{\max}}^* = 1.13 \sqrt{h_b \cdot a_b} \quad (E.7)$$

is achieved with the selection of the gain

$$k_1^* = \sqrt{4.828 a_b/h_b} \quad (E.8)$$

with * signifying the optimal values. Further the time of occurrence of $e_{v_{\max}}^*$ with respect to the time of the bias change h_b is given by

$$\tilde{t} = \frac{\pi}{8\omega}, \quad (E.9)$$

where $\omega = k_1/2$ represents the natural frequency of the filter.

Now, the quantization level Q in the altimeter data is substantially high with $Q=30$ meters in the telemetered data and $Q=3.4$ meters in the data available for onboard FDI. Further the process of quantization introduces a substantial nonlinearity into the problem, which leaves no easy way of modeling the error in the quantized output. However, the worst case effect of a quantum level change can be obtained by treating a change in the level equivalently as an onset

of a bias of $Q/2$ (half the quantization level magnitude), corresponding to a situation that would arise for a flight with slowly changing altitude. Moreover the initial error value of $e_{ho} = -2a_b/k_1^2$ used in the above analysis also needs to be increased by half the quantization level as well. It can be shown that the above considerations are equivalent to assuming a bias change of Q in h_m with no change required in the value of e_{ho} as referenced above.

Using in Eqs. (E.8) and (E.9) the values of $a_b = 0.75 \text{ m/sec}^2$ and $h_b = 30 \text{ m}$ to correspond to half the BFM for the normal accelerometer and the level of quantization in the telemetered data respectively, the optimum gain and the min-max error in the velocity estimate are given by:

$$\begin{aligned} k_1^* &= 0.347, \\ e_{v_{\max}}^* &= 5.38 \text{ m/s.} \end{aligned} \quad (\text{E.10})$$

For the low quantization of 3.4 meters in the altimeter data available for onboard FDI, the above values modify to

$$\begin{aligned} k_1^* &= 1.03 \\ e_{v_{\max}}^* &= 1.81 \text{ m/s.} \end{aligned} \quad (\text{E.11})$$

Thus to be strictly conservative, the worst-case errors in the initialization estimates assumed by the AK QSPRT should be

$$\begin{aligned} e_h &= Q \\ e_v &= e_{v_{\max}}^* \end{aligned} \quad (\text{E.12})$$

E.3 Acceleration Bias Estimation

A steady bias in $a_{v,m}$ can be estimated, and its effect on the estimates of h and \dot{h} duly compensated, by employing an appropriate low bandwidth estimator which looks for a steady bias effect in the AK filter residuals, $\gamma = h_m - \hat{h}$.

Based on the optimal estimator for process noise bias¹¹, the structure of the filter is given by

$$\dot{\hat{a}}_b = \frac{1}{\tau} \left(-\hat{a}_b - \frac{k_1^2}{2} \gamma \right) \quad (E.13)$$

where

\hat{a}_b = estimate of the bias in $a_{v,m}$,

τ = time constant of the estimator, to be chosen appropriately.

Further, the estimates of h and \dot{h} provided by the AK filter can be corrected for the effect of the bias in $a_{v,m}$ to yield,

$$\begin{aligned} \hat{h}_c &= \hat{h} - \frac{2\hat{a}_b}{k_1^2} \\ \hat{v}_c &= \hat{v} - \frac{2\hat{a}_b}{k_1} \end{aligned} \quad (E.14)$$

where the subscript c denotes "corrected" estimates.

Some of the factors which deserve further consideration in the implementation of such an estimator are as follows:

(1) The bias estimator primarily tracks the bias in the normal accelerometers except during the times of large attitude maneuvers when the effect of biases in the other sensors (involved in the estimate of $a_{v,m}$) becomes significant. A measure such as temporary disabling of the estimator (by setting τ to a very large value) during times of large and sustained attitude maneuvers would help prevent the bias estimate from being affected by biases in sensors other than the normal accelerometers.

(2) The effect on the bias estimator of transients in the AK filter residuals arising from altitude quantization level changes can be decreased by choosing the bandwidth of the bias estimator to be smaller than the bandwidth of the AK filter. The actual bandwidth chosen must be a tradeoff between sensitivity to bias changes and sensitivity to quantization errors in h_m .

TABLE OF CONTENTS

<u>Section</u>		<u>Page</u>	
1	SUMMARY AND INTRODUCTION	1	1/A9
2	FDI STRUCTURE	9	1/B3
	2.1 Introduction	9	1/B3
	2.2 Redundancy Trigger	9	1/B3
	2.3 The Sequential Probability Ratio Test	10	1/B4
	2.4 Time Trigger	12	1/B6
	2.5 Failure Identification by the Outer Loop	13	1/B7
3	ANALYTIC REDUNDANCY SPRT's	15	1/B9
	3.1 Introduction	15	1/B9
	3.2 Translational Kinematics	16	1/B10
	3.3 Translational Dynamics	21	1/C1
	3.4 Rotational Kinematics	24	1/C4
	3.5 Altitude Kinematics	28	1/C8
4	CALCULATION OF FDI SYSTEM PARAMETERS	33	1/C13
	4.1 Introduction	33	1/C13
	4.2 Rate Gyros	33	1/C13
	4.3 Attitude Gyros	37	1/D3
	4.4 Accelerometers	43	1/D9
	4.5 Altimeters	50	1/E2
	4.6 Alpha Vanes and Mach Meters	52	1/E4
	4.7 Additional Tests	55	1/E7
	4.8 Summary	60	1/E12
5	QUALITY SPRT's	63	1/F1
6	OUTER LOOP LOGIC	69	1/F7
	6.1 Introduction	69	1/F7
	6.2 Failure Identification - Redundancy Trigger ...	69	1/F7
	6.3 Failure Identification - Time Trigger	71	1/F9
	6.4 Additional Outer Loop Tasks	71	1/F9

<u>Section</u>		<u>Page</u>	
7	SIMULATION RESULTS	73	1/F11
7.1	Introduction	73	1/F11
7.2	Time Trigger Performance	73	1/F11
7.3	Redundancy Trigger Performance	84	1/G8
7.4	Hard Failure Identification	89	1/G13
8	APPLICATION TO FLIGHT TEST DATA	91	2/A6
8.1	Introduction	91	2/A6
8.2	Discussion of Flight Data	91	2/A6
8.3	Calculation of FDI System Parameters	95	2/A10
8.4	FDI Algorithm Modifications	102	2/B3
8.5	Injected Failure Identification	105	2/B6
8.6	Summary	114	2/C1
9	CONCLUSIONS AND RECOMMENDATIONS	159	2/F4
 <u>Appendix</u>			
A	TURBULENCE ESTIMATOR	163	2/F8
B	AERODYNAMIC COEFFICIENT APPROXIMATION	167	2/F12
C	SCALE FACTOR FAILURES	171	2/G2
D	SIMULTANEOUS ϕ AND θ FAILURES	175	2/G5
E	DESIGN AND PERFORMANCE OF AN ALTITUDE KINEMATICS FILTER	179	2/G10
E.1	Introduction	179	2/G10
E.2	KX Filter Design	179	2/U10
E.3	Acceleration Bias Estimation	182	2/G13
E.4	Performance Results	184	3/A6
F	COMPENSATION OF TURN ERROR IN DIRECTIONAL GYROS	189	3/A11
F.1	Introduction	189	3/A11
F.2	Derivation of Turn Error Expression	190	3/A12
F.3	Results of Turn Error Compensation of Flight Data	196	3/B4
F.4	Summary and Conclusions	199	3/B7
LIST OF REFERENCES		208	3/C2

LIST OF ILLUSTRATIONS

Figure		Page	
4-1	Low Turbulence Wind Profile	46	1/D12
7-1	Rate Gyro Time Trigger Performance	75	1/F13
7-2	Accelerometer Time Trigger Performance	80	1/G4
7-3	Mach Meter and Alpha Vane Time Trigger Performance .	82	1/G6
7-4	Rate Gyro Direct Redundancy Trigger Performance	85	1/G9
7-5	Accelerometer Direct Redundancy Trigger Performance	86	1/G10
7-6	Alpha Vane Direct Redundancy Trigger Performance ...	88	1/G12
8-1	Segment 1	117	2/C4
8-2	Segment 1 (cont.)	118	2/C5
8-3	Segment 2	119	2/C6
8-4	Segment 2 (cont.)	120	2/C7
8-5	Segment 3	121	2/C8
8-6	Segment 3 (cont.)	122	2/C9
8-7	Segment 4A	123	2/C10
8-8	Segment 4A (cont.)	124	2/C11
8-9	Segment 4B	125	2/C12
8-10	Segment 4B (cont.)	126	2/C13
8-11	Segment 4C	127	2/C14
8-12	Segment 4C (cont.)	128	2/D1
8-13	Segment 4D	129	2/D2
8-14	Segment 4D (cont.)	130	2/D3
8-15	Segment 5	131	2/D4
8-16	Segment 5 (cont.)	132	2/D5
8-17	Segment 6	133	2/D6
8-18	Segment 6 (cont.)	134	2/D7
8-19	Segment 4C, Roll Rate Gyro 1 +BFM Bias at T=29,RK ..	135	2/D8
8-20	Segment 4A, Roll Rate Gyro 2 +BFM Bias at T=0,RK ...	136	2/D9
8-21	Segment 3, Roll Rate Gryo 2 Fail to Zero at T=0,RK .	137	2/D10
8-22	Segment 4C, Pitch Rate Gryo 1 -BFM Bias at T=29,RK.	138	2/D11
8-23	Segment 4A, Pitch Rate Gyro 2 +BFM Bias at T=0,RK...	139	2/D12
8-24	Segment 3, Pitch Rate Gyro 2 Fail to Zero,RK.....	140	2/D13
8-25	Segment 4C, Yaw Rate Gyro 2 -BFM Bias at T=29,RK....	141	2/D14

List of Illustrations (cont.)

Figure		Page	
8-26	Segment 4A, Yaw Rate Gyro 1 +BFM Bias at T=0,RK.....	142	2/E1
8-27	Segment 3, Yaw Rate Gyro 1 Fail to Zero at T=0,RK....	143	2/E2
8-28	Segment 2, Roll Attitude Gyro 1 -BFM Bias at T=37,RK.	144	2/E3
8-29	Segment 2, Pitch Attitude Gyro 1 +BFM Bias at T=37,RK	145	2/E4
8-30	Segment 4B, Mach Meter 1 -BFM Bias at T=130,TK.....	146	2/E5
8-31	Segment 4B, Mach Meter 1 +BFM Bias at T=160,TK.....	147	2/E6
8-32	Segment 4A, Mach Meter 2 +BFM Bias at T=8,TK.....	148	2/E7
8-33	Segment 4B, Alpha Vane 1 +BFM Bias at T=130,TD.....	149	2/E8
8-34	Segment 4C, Alpha Vane 1 +BFM Bias at T=36,TD.....	150	2/E9
8-35	Segment 4B, Longitudinal Accelerometer 2 +BFM Bias at T=80,TK.....	151	2/E10
8-36	Segment 4A, Longitudinal Accelerometer 1 Fail to Zero at T=0,TK.....	152	2/E11
8-37	Segment 4A, Lateral Accelerometer 2 -BFM Bias at T=12,TD.....	153	2/E12
8-38	Segment 4C, Lateral Accelerometer 2 +BFM Bias at T=36,TD.....	154	2/E13
8-39	Segment 4B, Normal Accelerometer 2 -BFM Bias at T=90,AK.....	155	2/E14
8-40	Segment 4B, Normal Accelerometer 2 -BFM Bias at T=125,AK.....	156	2/F1
8-41	Segment 4B, Normal Accelerometer 2 -BFM Bias at T=140,AK.....	157	2/F2
8-42	Segment 4C, Normal Accelerometer 1 +BFM Bias at T=10,AK.....	158	2/F3
A-1	Continuous Velocity Estimator	163	2/F8
A-2	Residual Processing	164	2/F9
E-1	Segment 2, AK Filter Performance without Additive Acceleration Bias	186	3/A8
E-2	Segment 2, AK Filter Performance with and without Additive Acceleration Bias	187	3/A9
F-1	Elements of Error Geometry for a Directional Gyro...	191	3/A13
F-2	Turn Error Due to Non-horizontal Floor Plane	194	3/B2
F-3	Spherical Geometry for Non-horizontal Spin Axis	194	3/B2
F-4	Turn Error Due to Non-horizontal Spin Axis	196	3/B4
F-5	Attitude History for Segments 2, 3, 4A and 4C	201	3/B8
F-5	(cont.)	202	3/B10
F-6	Segment 4A, Turn Error Compensation Assuming Horizontal Spin Axes	203	3/B11
F-7	Segment 4A, Turn Error Compensation Assuming Non-horizontal Spin Axes	204	3/B12

List of Illustrations (cont.)

Figure		Page	
F-8	Segment 2, Turn Error Compensation Assuming Non-Horizontal Spin Axes	205	3/B13
F-9	Segment 3, Turn Error Compensation Assuming Non-horizontal Spin Axes	206	3/B14
F-10	Segment 4C, Turn Error Compensation Assuming Non-horizontal Spin Axes	207	3/C1

LIST OF TABLES

Table		Page	
I	Sensor Information	16	1/B10
II	Summary of FDI System Parameters	61	1/E13
III	Attitude Gyro and Altimeter Simulation Results	89	1/G13
IV	Hard Failure Simulation Results	90	1/G14
V	Flight Data Segment Times	91	2/A6
VI	Minimum BFM and Standard Deviation Data	97	2/A12
VII	New BFM Levels	101	2/B2
VIII	Self-Test Thresholds	104	2/B5
IX	AP-101 Execution Times	161	2/F6
D.1	Worst-Case Acceleration Error due to Polynomial Approximation	170	2/G1

(3) Reinitialization of the bias estimate to zero should be made following any change in the complement of sensors used by the AK filters.

(4) In addition to improving the estimates of h and \dot{h} and thus increasing the speed and performance of the AK FDI tests, the bias estimate may be employed for other tasks such as initiating FDI tests or on-line calibration of the normal accelerometers.

E.4 Performance Results

Here, we examine the performance of the filter and the estimator using the F-8 telemetry data from flight segment 2. Figures E-1 and E-2 show the performance of the filter-estimator with and without bias in the derived vertical acceleration $a_{v,m}$, with the bias values added to $a_{v,m}$ being explicitly identified in the labels of the plots. It may be noted that the units of position, velocity and acceleration in these figures are meters, m/sec and m/sec^2 respectively.

As regards the structure of the filter-estimator, the gain k_1 is selected to be 0.347 (according to Eq. (E.10)), and the time constant of the estimator is chosen to be equal to 74 seconds to correspond to $2 \tau_f$ where $\tau_f = 2\pi/\omega$ and ω is the natural frequency of the filter. The filter is initialized at the start of the segment with $\hat{h}(t=0) = h_m(t=0)$ and $\dot{\hat{h}}(t=0) = -2.1$ m/sec, with the value for \dot{h} chosen to correspond to the average altitude rate during the segment.

The first two plots of Fig. E-1 show the time histories of the altimeter data, $h_m(t) - h_m(t=0)$, and the vertical acceleration $a_{v,m}(t)$ derived from the #1 sensors, with the rest of the plots showing the performance of the filter with no additive bias in $a_{v,m}$ (i.e. $a_b = 0$). The third plot shows the estimate of the altitude, $\hat{h}(t) - \hat{h}(t=0)$, with the altimeter data repeated for comparison; the fourth plot shows the altitude measurement residual history which exhibits a typical second order system response; and the fifth plot shows for comparison the velocity estimate and the predicted velocity

$$v_p = -2.1 + \int_0^t a_{v,m} dt.$$

The predicted velocity gives a good measure of the actual velocity of the aircraft except at low frequencies, where errors may arise due to errors in the initial velocity estimate and in the derived vertical acceleration $a_{v,m}$. Thus the comparison of the time histories

of the two velocity plots gives a measure, though not a very accurate one, of the error in the velocity estimate arising due to quantization in the altimeter data.

The effects of an acceleration bias of -0.75 m/sec^2 on the performance of the filter-estimator are shown in the plots of Fig. E-2 which also show for comparison the performance of the filter-estimator with no bias. The acceleration bias is seen to introduce steady bias errors in the estimates of h , \dot{h} and the h_m residual. Further, the additional error introduced in the estimate of velocity is seen to be of the order of 4 m/sec leading to a maximum total error of 5 m/sec (with respect to the predicted velocity) at about 54 seconds.

The last three plots in Fig. E-2 show the performance of the bias estimator and the resulting corrected estimates of h and \dot{h} . In the case of zero additive bias it may be seen that the estimate of the bias, \hat{a}_b , and hence the corrections in \hat{h} and $\dot{\hat{h}}$ are very small. With the acceleration bias, the estimator is seen to steadily improve its estimate of bias with time, with the bias estimate reaching a value of -0.4 m/sec^2 which is approximately half the actual bias value. The bias estimate can be expected to improve in time since the time constant of the estimator is large and the estimator has not reached steady state. The comparison of the corrected time histories of the estimates with and without bias also gives an indication of the residual error left uncorrected in the estimates of h and \dot{h} when acceleration bias is present in $a_{v,m}$.

The above results demonstrate the potential of the bias estimator to help reduce the errors in the estimates of h and \dot{h} and consequently enhance the speed and reliability of the AK FDI tests. The results also demonstrate the desirability of investigating the filter-estimator performance using data from a flight segment which is of significantly longer duration and includes large and sustained attitude maneuvers as well.

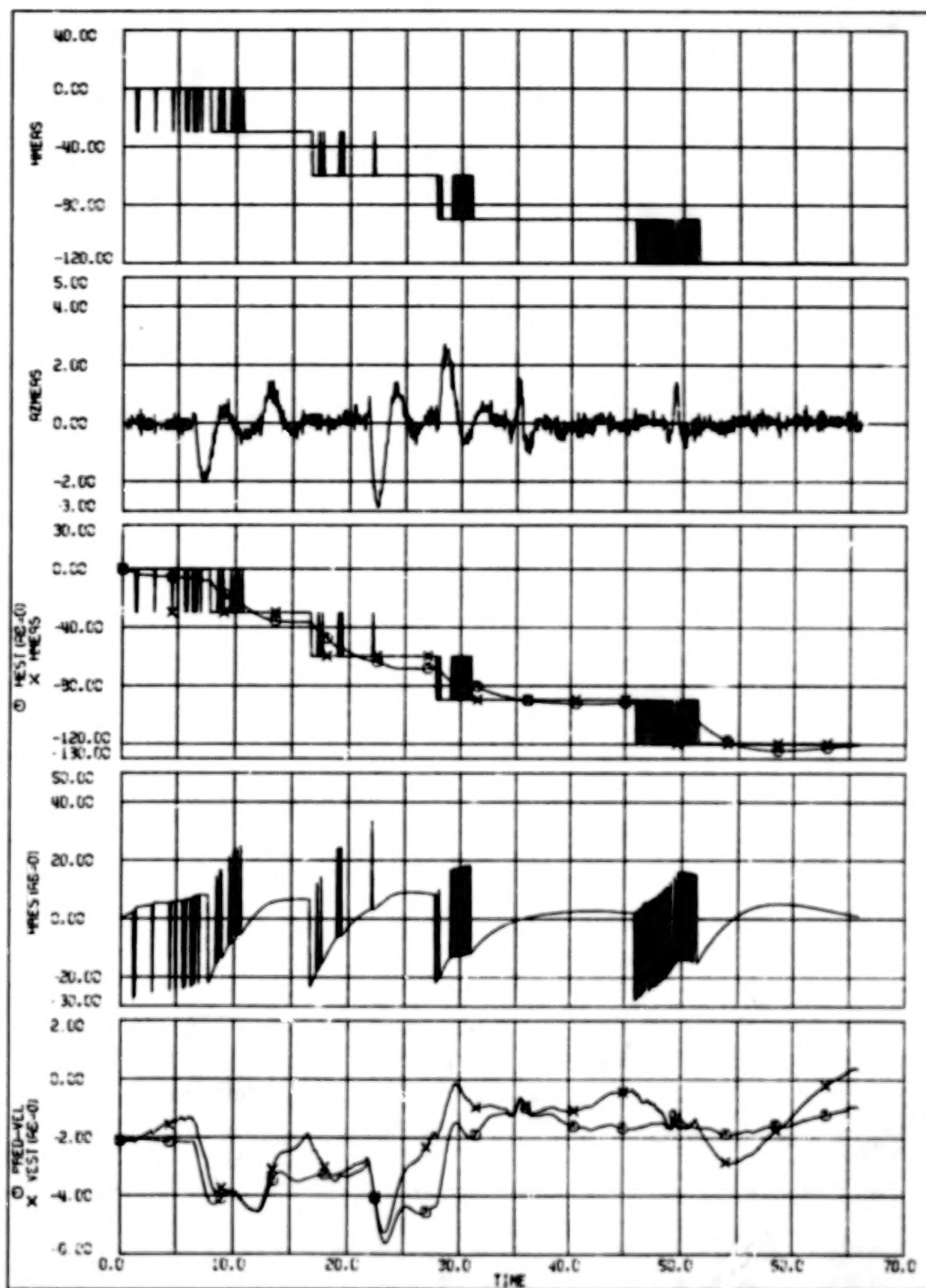


Figure E-1 Segment 2, AK Filter Performance Without Additive Acceleration Bias

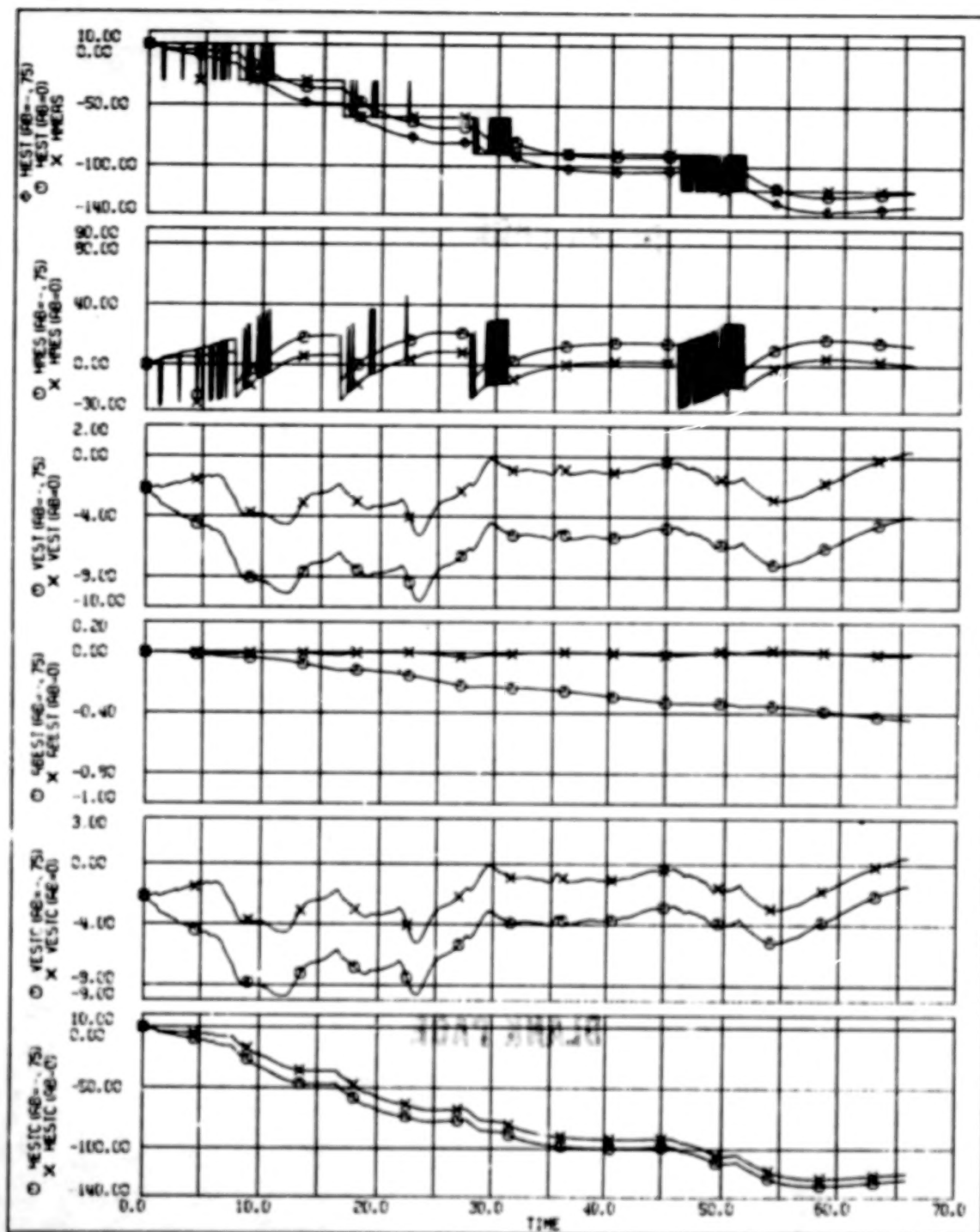


Figure E-2 Segment 2. AK Filter Performance with and without additive Acceleration Bias

BLANK PAGE

BLANK PAGE

APPENDIX F

COMPENSATION OF TURN ERROR IN DIRECTIONAL GYROS

2.1 Introduction

The directional gyros are known to develop a systemic or predictable type of error when the aircraft floor plane is not horizontal. Unless accounted for either in the QSPRT or by direct compensation of the indicated azimuth, the SPRT output using the rotational kinematics relations may provide erroneous FDI information, especially during maneuvers involving large and/or sustained attitude excursions.

Here we derive an analytical expression for this systemic type of error, called turn error, for the general case when an aircraft is pitched as well as banked and the spin axis of the directional gyro is non-horizontal. Further, the flight data from four segments involving significant attitude excursions and noticeable DG drifts are examined in an attempt to understand the behavior of the two DG's. The examination of the azimuth data reveals that the observed drift in the two DG's can be appropriately explained by the turn error calculated from the derived analytic expression. The turn error expression involves the zero offset in the azimuth reading for each DG and the tilt angle of the spin axis with aspect to the horizontal in the case of DG 1. The estimation of these quantities is based on matching the observed drift in the data from segment 4A, which involves a steady turn of 165 degrees over a period of 38 seconds. The estimated quantities are used to predict the turn error for the other three flight segments: 4C, 2 and 3. A close match between the observed and the predicted error for the four flight segments indicates that the spin axes of the two DG's maintain their inertial position within expected bounds over the time of the flight spanning the four segments considered here. The results also indicate that unlike the case of DG 2, the spin axis of DG 1 is tilted by about 7° with respect to the horizontal. This could be due to faulty spin vector erection at the start of the flight or subsequent development of the tilt prior to the start of segment 2.

The zero offset of a DG is its reading when its spin axis and the aircraft roll axis are collinear. Thus, the value determined from one flight should remain unchanged as long as the spatial orientation of the DG case with respect to the aircraft remains unchanged. With the knowledge of zero offset values the turn error in the azimuth data, except for the error due to a tilt of the spin axis from the horizontal plane, can be compensated for on-line, improving considerably the FDI performance in the case of rate gyro and/or attitude gyro failures.

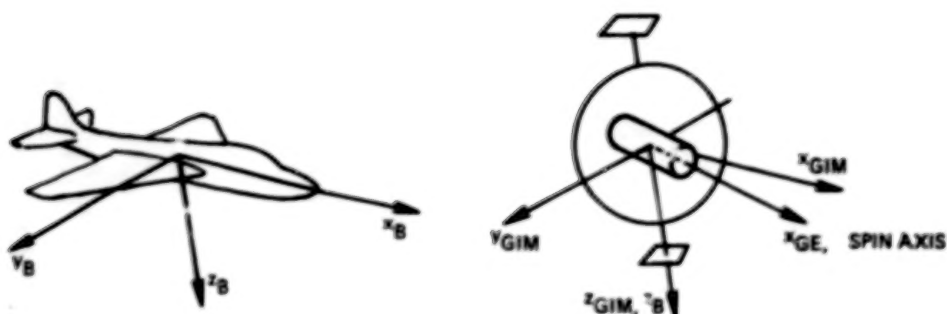
F.2 Derivation of Turn Error Expression

We derive here the expression for the true azimuth of the aircraft in terms of the azimuth indicated by the DG when the aircraft floor plane is tilted with respect to the horizontal plane. We shall consider first the case of a horizontal spin axis followed by the case of a non-horizontal spin axis.

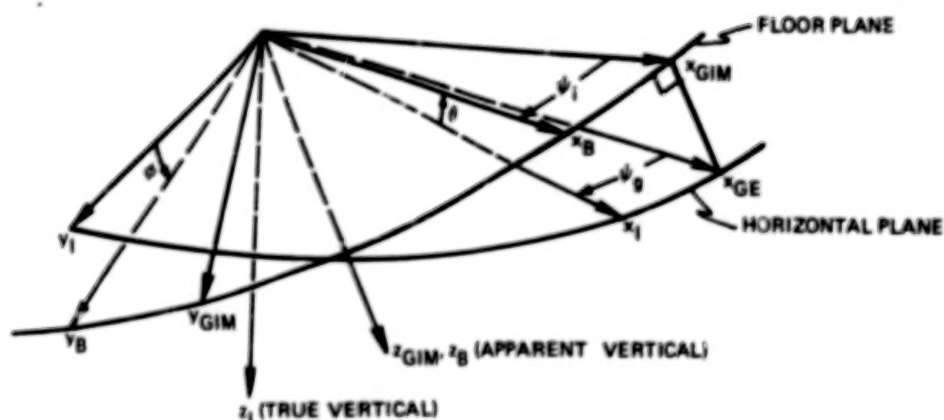
F.2.1 Horizontal Spin Axis

Figure F-1 shows the various elements of the geometry that enter into the determination of the turn error at any given instant of time. Figure F-1b shows the relative orientation of the aircraft and the gimbal axes with respect to the horizontal plane, with the two axis systems defined in Figure F-1a. The angle between the aircraft roll axis x_B and the x gimbal axis in the floor plane of the aircraft represents the indicated azimuth which is read about the outer gimbal axis. The determination of this angle for a given azimuth orientation of the aircraft proceeds as follows. The spin axis is assumed to maintain its inertial position along x_{GE} in the horizontal plane. The orientation of the x_B axis with respect to the spin axis is determined by the true azimuth ψ_g and the pitch and roll angles θ and ϕ respectively. With the outer gimbal axis mounted normal to the floor plane along z_B , the x, y gimbal axes lie in the floor plane (i.e. $x_B y_B$ plane) of the aircraft, and the orientation of the x gimbal axis is determined from the requirement imposed by the DG mounting that the spin axis lie in a plane perpendicular to the floor plane.

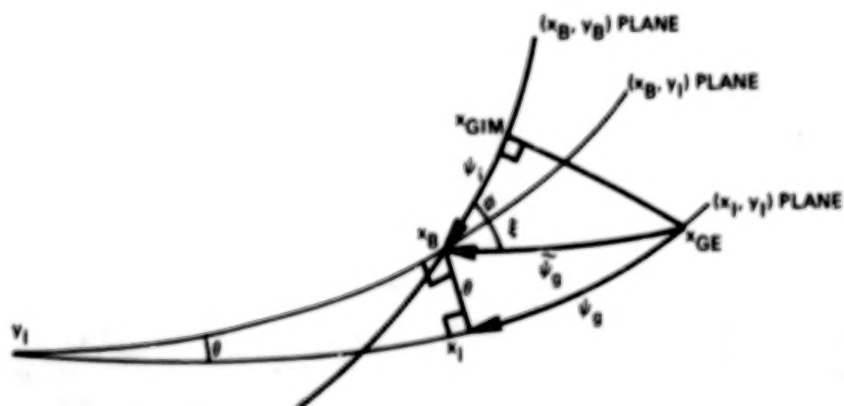
The analytical relationship between the true and indicated azimuth follows from the consideration of the spherical geometry shown in



a) Definition of Aircraft and DG Gimbal Axes



b) Geometry of Aircraft and Gimbal Axes wrt Horizontal Plane



c) Spherical Geometry of an Attitude Change

Figure F-1 Elements of Error Geometry for a Directional Gyro

Fig. F-1c formed by the tips of unit vectors associated with the aircraft and the gimbal axes during an attitude change of the aircraft. The attitude change is assumed to take place in two stages: a pitch rotation about y_I which changes the (x_I, y_I) orientation to the (x_B, y_I) orientation, followed by a roll rotation about x_B to obtain the present (x_B, y_B) orientation. The application of Napier's Law to the two spherical triangles formed by the tips of unit vector triads (x_B, x_I, x_{GE}) and (x_B, x_{GE}, x_{GIM}) yields the following relations:

$$\sin \tilde{\psi}_g \cos \xi = \sin \psi_g \quad (F.1)$$

$$\cos \tilde{\psi}_g = \cos \psi_g \cos \theta \quad (F.2)$$

$$\tan \xi = \frac{\sin \theta}{\tan \psi_g} \quad (F.3)$$

$$\tan \psi_i = \tan \tilde{\psi}_g \cos (\phi + \xi) \quad (F.4)$$

Using Eqs (F.1), (F.2) and (F.3) in (F.4) yields after some algebra:

$$\tan \psi_i = \frac{\cos \phi}{\cos \theta} \tan \psi_g - \sin \phi \tan \theta \quad (F.5)$$

or

$$\tan \psi_g = \frac{\cos \theta}{\cos \phi} \tan \psi_i + \sin \theta \tan \phi \quad (F.6)$$

With the knowledge of θ and ϕ from the vertical gyro, the true azimuth of the aircraft can be calculated using Eq. (F.6).

The degree of severity of the turn error problem with attitude excursions can be seen from Fig. F-2 which shows the variation of turn error, $c = \psi_g - \psi_i$, with respect to the true azimuth calculated from Eq. (F.6) for a pitch attitude of 4 degrees and five roll attitude values of 15, 30, 45, 60 and 75 degrees. Thus, for example, in a 60 degree bank angle turn, the turn error can be as large as 22 degrees with error changing at the rate of 0.8 degrees per degree turn. The turn error is seen to vary at twice the frequency of ψ_g ,

with the error going to zero at four headings during a 360 degree turn. At two of these headings, the roll axis is orthogonal to the spin axis with $\psi_g = 90^\circ$ and 270° . At the other two headings the roll axis is nearly collinear with the spin axis (i.e., $\psi_g \approx 0^\circ, 180^\circ$). It can be shown from Eq. (F.5) that the extrema of the turn error occur at ψ_g^* given by

$$\tan \psi_g^* = \frac{-\sin\theta\sin\phi + (1-\cos\theta\cos\phi) \sqrt{\cos\theta/\cos\phi}}{\cos\theta - \cos\phi} \quad (\text{F.7})$$

and the errors at the extrema are given by

$$\tan c = \frac{1}{2} \frac{(\cos\phi - \cos\theta)}{\sqrt{\cos\theta \cos\phi}} \cdot \frac{1}{\zeta}, \quad (\text{F.8})$$

$$\text{where } \zeta = \frac{1-\cos\theta\cos\phi}{\cos\theta-\cos\phi} + \frac{\sin\theta\sin\phi}{\sqrt{\cos\theta\cos\phi}} \cdot \frac{(\cos\theta + \cos\phi)}{(\cos\theta - \cos\phi)}$$

For small θ and ϕ , the turn error is approximately given by

$$c \approx \frac{1}{4} (\phi^2 - \theta^2) \sin 2\psi_g + \theta\phi \cos^2 \psi_g \quad (\text{F.9})$$

F.1.2 Non-horizontal Spin Axis

In the case of a non-horizontal spin axis, it can be shown that the turn error component \bar{c} due to the non-horizontal component of the momentum vector is given by

$$\sin \bar{c} = \frac{\tan \delta}{\cos \theta} (\cos \bar{\psi}_g \tan \phi - \sin \bar{\psi}_g \sin \theta) \quad (\text{F.10})$$

where

$$\bar{c} \equiv \psi_g - \bar{\psi}_g$$

$\bar{\psi}_g$ = the corrected azimuth obtained using Eq. (F.6), i.e. compensation assuming the spin axis to be horizontal

and δ = the tilt angle of the spin axis from the horizontal plane, with positive denoting a spin axis below the horizontal.

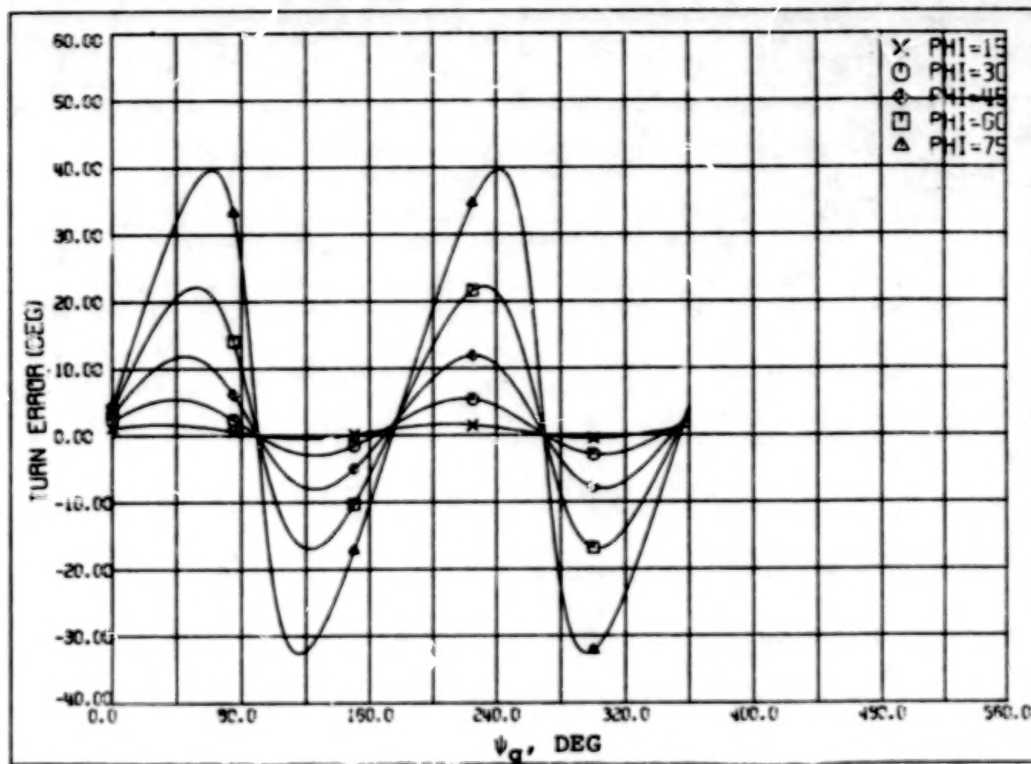


Figure F-2 Turn Error Due to Non-horizontal Floor Plane

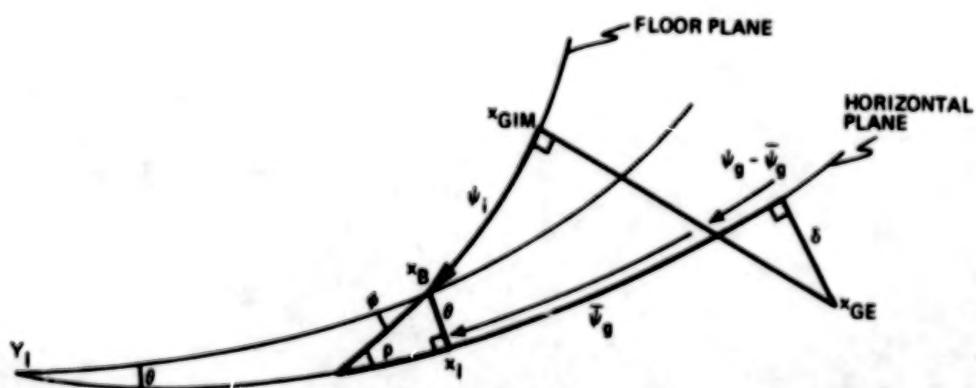


Figure F-3 Spherical Geometry for Non-horizontal Spin Axis

The derivation of Eq. (F.10) follows from the application of Napier's rule to the three spherical triangles shown in heavy outline on Fig. F-3. The definition of δ , ψ_g and \bar{c} also becomes clear in the context of Fig. F-3.

It may be remarked that with no apriori knowledge of the tilt angle, \bar{c} represents the component of turn error that cannot be compensated. Figure F-4 shows the amount of this irreducible component that could be expected at different azimuths for tilt angle values of 0, 5, 7.5, 10 and 15 degrees, with pitch and roll attitude values of 4 and 60 degrees respectively. Unlike the turn error variation for a horizontal spin axis seen earlier, the residual error \bar{c} is seen to vary with the same frequency as ψ_g . It can be shown that the peak error results when the x gimbal axis is horizontal and lies along the intersection of the floor plane of the aircraft and the horizontal plane. The peak error magnitude \bar{c}_{peak} is given by

$$\sin \bar{c}_{\text{peak}} = \pm \tan \delta \tan \rho \quad (\text{F.11})$$

where

$$\cos \rho = \cos \theta \cos \phi$$

and ρ represents the tilt angle of the floor plane (see Fig. F-3).

For small δ and θ , the residual turn error can be approximated by

$$\bar{c} = \delta \tan \phi \cos \bar{\psi}_g. \quad (\text{F.12})$$

Further, for small θ, ϕ and δ , an approximate expression for the total turn error $c = \psi_g - \psi_i$ is obtained by combining Eq. (F.9) and (F.12) to yield:

$$c \approx \phi [\theta \cos \psi_g + \delta] \cos \psi_g + \frac{1}{4}(\phi^2 - \theta^2) \sin 2\psi_g \quad (\text{F.13})$$

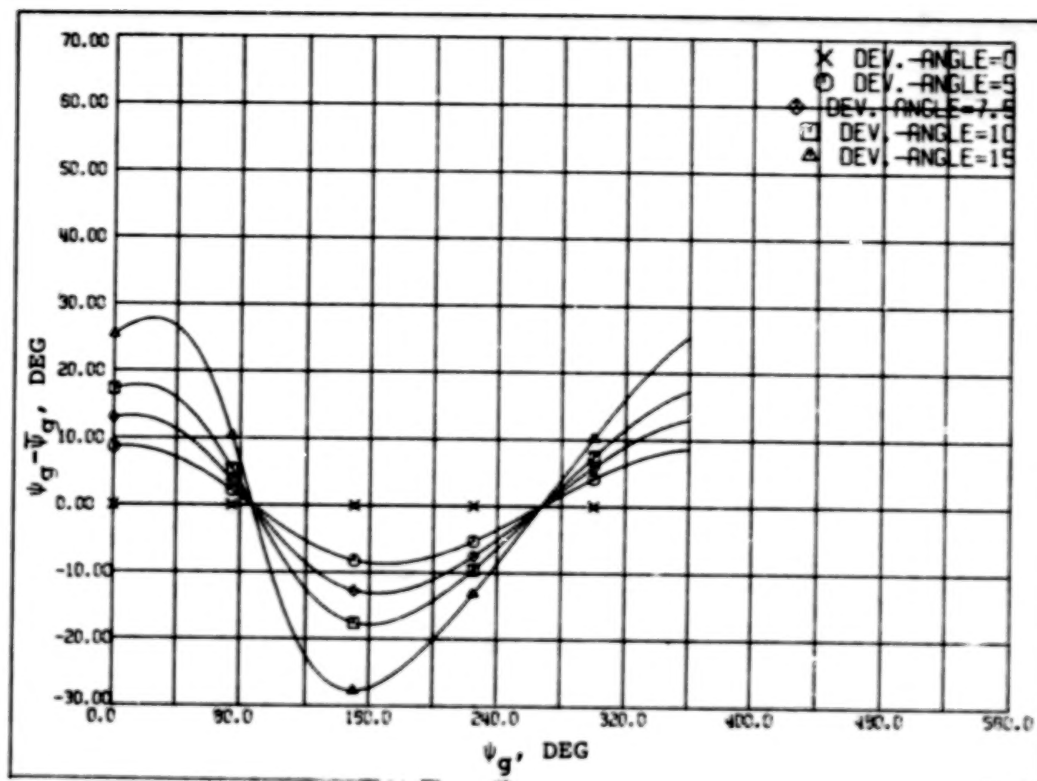


Figure F-4 Turn Error Due to Non-horizontal Spin Axis

F.3 Results of Turn Error Compensation of Flight Data

Here, we examine the results of an effort to apply the turn error correction to the DG data from four F-8 telemetry segments: 2, 3, 4A and 4C. A measure of the degree of success of this effort and also of the performance of the gyros is provided by examining the direct redundancy (DR) and the rotational kinematics (RK) residuals that result from the direct comparison of the compensated data for the two DG's and from the comparison against the rate gyros and vertical gyros using the rotational kinematic relations.

For the four flight segments, the time histories of the pitch and roll attitude data from VG 1 and the indicated azimuth from two DG's are shown in Fig. F-5*. The indicated azimuth is obtained

* In Figs. F-5 thru F-10, the units of the ordinate variables are radians.

by subtracting from the DG data the zero offset of the particular DG under consideration, where the determination of the zero offset will be discussed shortly. Also shown in the figure is the difference in the indicated azimuth of the DG's. In the absence of any attitude excursions, the difference is seen to remain constant providing a measure of the relative orientation of the spin axes of the two instruments. Any deviation of the difference from this mean provides an indication of possible turn error in one or both of the DG's. Among the four segments, segment 4A involves a steady banked turn and is the only segment exhibiting significant turn error throughout. The other three segments involve essentially no-turn straight line flights exhibiting turn error only during large transient roll attitude excursions. The rest of the flight segments not considered here do not exhibit any noticeable DG drift in the DR or RK residuals.

With no a priori knowledge of the zero offset for each DG, the turn error compensation first involves the estimation of these zero offset values. A rough estimate of the zero offset for each DG can be formed from the RK residuals obtained by using the relation (see Section 3.4)

$$r = -\dot{\theta} \sin \phi + \dot{\psi} \cos \theta \cos \phi.$$

The change in the RK residual over a given time period (t, t_0) due to turn error $c = \psi_g - \psi_i$ is given by

$$\gamma_r(t) - \gamma_r(t_0) = \int_{t_0}^t \dot{c} \cos \theta \cos \phi \, dt \quad (F.14)$$

A judicious choice of a time interval and the use of simplified Eq. (F.9) for turn error c in Eq. (F.14) readily yields a rough estimate of the zero offset for each DG that could explain the observed change in the RK residuals. This estimate of the offset can be iteratively refined by using the exact turn error compensation given by Eq. (F.6).

The final results of such an effort for Segment 4A are shown in Fig. F-6. The figure shows the time histories of azimuth and DR and RK residuals for the two DG's using both the corrected and the uncorrected azimuth histories signified by suffixes C and NC respectively. The zero offsets used in the correction are $-.85$ and $-.75$ radians for DG 1 and DG 2 respectively, and the RK residuals are

obtained using yaw rate gyro 2. Comparison of the corrected and uncorrected versions of the RK residuals shows that the effect of turn error compensation is remarkable for DG 2, reducing the peak error from 0.3 radians to 0.02 radians. In the case of DG 1, the reduction in the peak error is not as great, although a factor of two reduction in the peak error is achieved. We note that in Fig. F-6, the nature of the variation of the RK residual for DG 1 after compensation over the 165 degree turn is similar to the variation of the residual error seen in Fig. F-4 due to a non-horizontal spin axis. This suggests that the residual error after compensation for DG 1 is due not so much to an error in the estimate of zero offset as to a violation of the assumption of a horizontal spin axis.

Fig. F-7 shows the result of compensation for segment 4A using the values of 7.5 and 0 degrees for the spin vector tilt angles for DG 1 and DG 2 respectively. In the case of the RK residuals for DG 1, residuals resulting from compensation using 0 for the spin vector tilt angle are shown again for comparison and marked with diamonds. From the RK residual plots, the degree of compensation is seen to be excellent for both DGs, signifying that the spin vectors maintain their inertial orientation during the segment with the spin vector dipped below the horizontal plane by approximately 7.5 degrees for DG 1.

As remarked earlier, the zero offset value of a DG should remain unaltered unless the relative orientation of the DG case with respect to the aircraft is changed. On the other hand the spin vector orientation depends upon the mode of spin vector erection, the mode (if any) employed to maintain its orientation and disturbance torques such as friction. However for a normal DG, the effects on the RK residuals of drifts due to disturbance torques and torquing employed to maintain the spin vector orientation should be very small.

The same values of zero offsets and spin vector tilt angles as used in Fig. F-7 for segment 4A are used for turn error compensation for segments 2, 3 and 4C, and the results are shown in Figs. F-8 through F-10. Unlike segment 4A, the observability of the turn error is limited to those times when roll attitude excursion is significant, with the effects of turn error and compensation most noticeable around the times of rapid roll attitude change. It may be remarked that during other times the RK residuals for both DG's show a noticeable contribution from the error in yaw rate gyro 2.

Among these three segments the most noticeable turn error is in DG 2 during segment 4C as seen from its uncorrected RK residuals in Fig. F-10, the size of the error itself being much smaller than the peak error observed in segment 4A. At approximately 29 seconds there is a snap wing leveling maneuver, and the effectiveness of the turn error compensation can be judged with respect to the time when the wings are level and the turn error is thus very small. Although the effect of turn error compensation is not as dramatic as in segment 4A, nonetheless a factor of four reduction in turn error is achieved by compensation, and the magnitude of the remaining error on the RK residuals is sufficiently small that rate gyro FDI should not be affected. For the other segments where the uncorrected RK residuals for each DG do not show significant changes, the effectiveness of compensation can be judged by the absence of change in the corrected RK residuals around times of rapid roll attitude change. In the case of DG 2, there seems to be little if any change in the corrected RK residuals at the times of rapid attitude change in segments 2 and 3. Such is also the case for DG 1 assuming a tilt angle value of 7.5 degrees. However, using a zero value for the tilt angle, the change in the residuals (marked by diamonds) during times of significant roll attitude change is seen to be quite pronounced, again demonstrating the tilt of the spin vector for DG 1 from the horizontal plane.

It is important to note that further refinement is undoubtedly possible on the zero offset estimates for the two DG's, and future examination of additional flight segments containing significant sustained attitude maneuvers would be of great help in this effort.

F.4 Summary and Conclusions

In conclusion we make the following observations based on the results discussed above:

- (1) The spin vectors of the two DG's maintain their inertial orientation within acceptable bounds during the flight time spanned by the segments considered here, with the spin axis non-horizontal for DG 1 and horizontal for DG 2. This conclusion derives from the observation that the drift in the RK and DR residuals can be explained by the systemic turn error derived above.

(2) With the knowledge of the zero offset values, which may be assumed invariant, the effect of turn error for a nominal DG with horizontal spin axis can be compensated on-line.

(3) With turn error compensation, a rational basis now exists to identify faulty operation of the DG's due to causes such as a non-horizontal spin axis or excessive drift. The observability of a failure mode such as non-horizontal spin axis depends upon the tilt angle of the spin vector and the pitch, roll and azimuth attitude of the aircraft. As in the case of segment 3, the failure can lead to a sudden bias-type change in the RK residual due to a rapid attitude maneuver of the aircraft. Or it may manifest itself as a slowly varying change in the RK residuals as in the case of segment 4A, a change that can be identified by an SPRT looking for a ramp in the residuals. The SPRT's looking for biases or ramps in the RK residuals can be initiated upon detection of a ramp or bias change in the direct redundancy residuals over a time window.

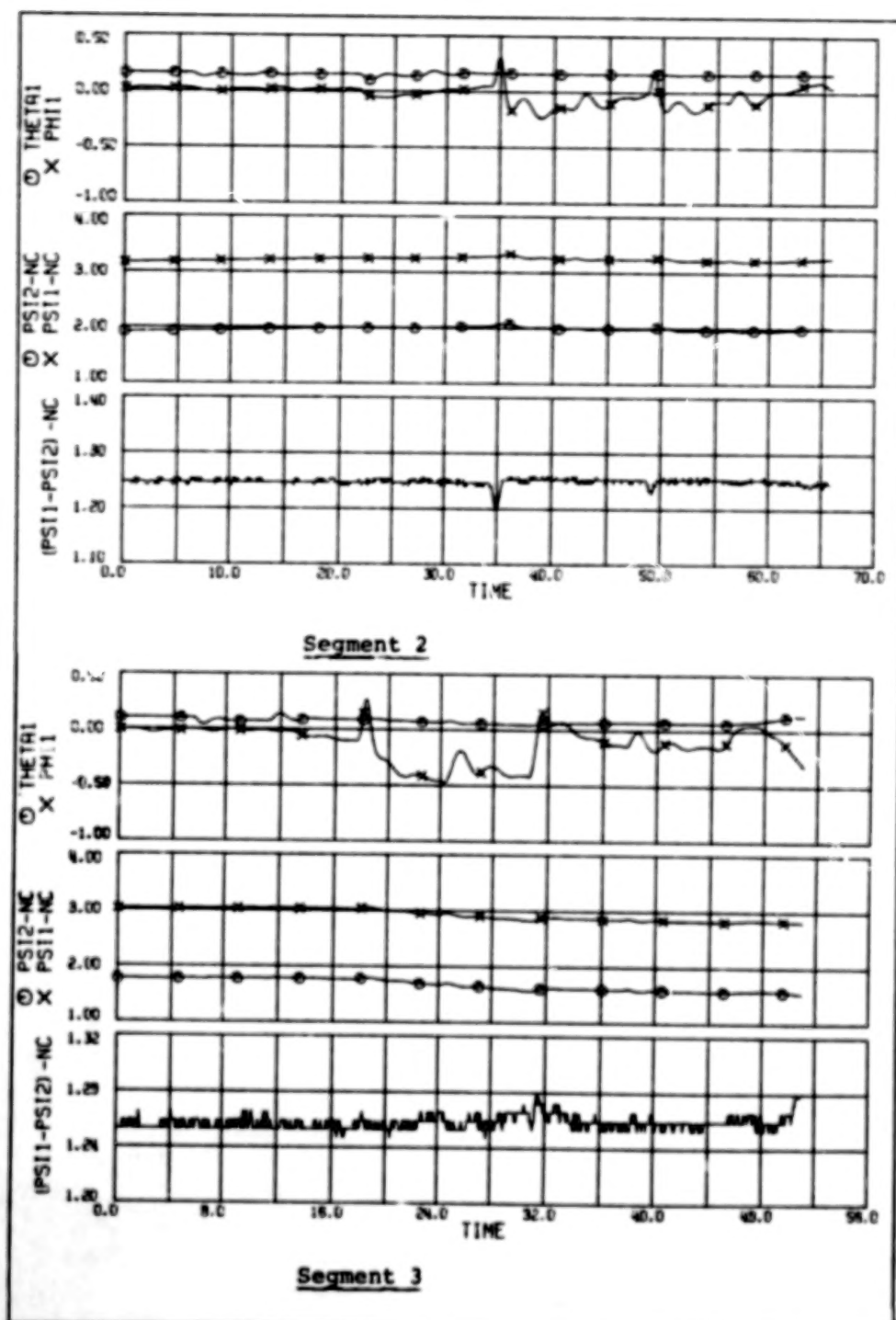


Figure F-5 Attitude History for Segments 2, 3, 4A and 4C

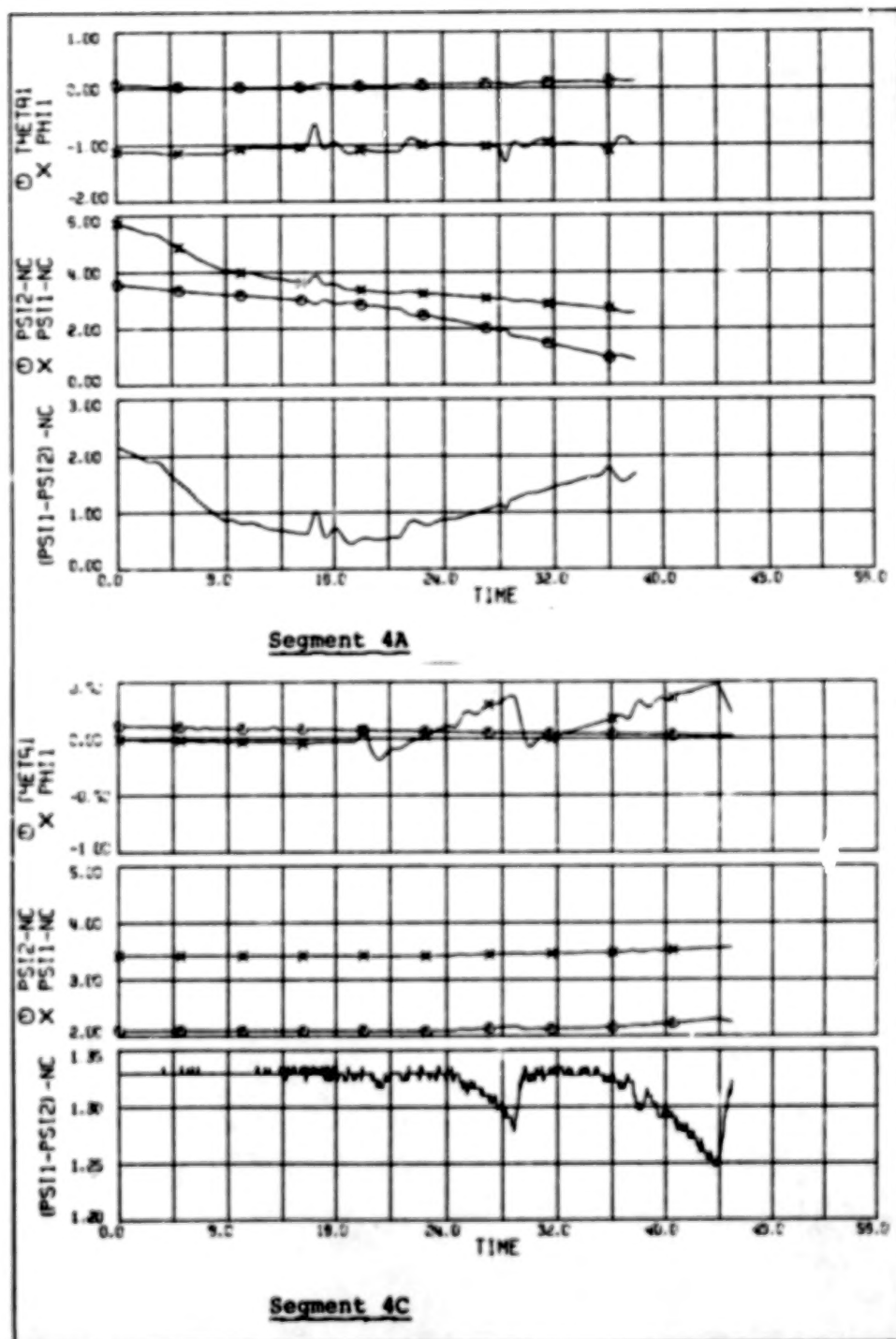


Figure F-5 Attitude History for Segments 2, 3, 4A and 4C (cont.)

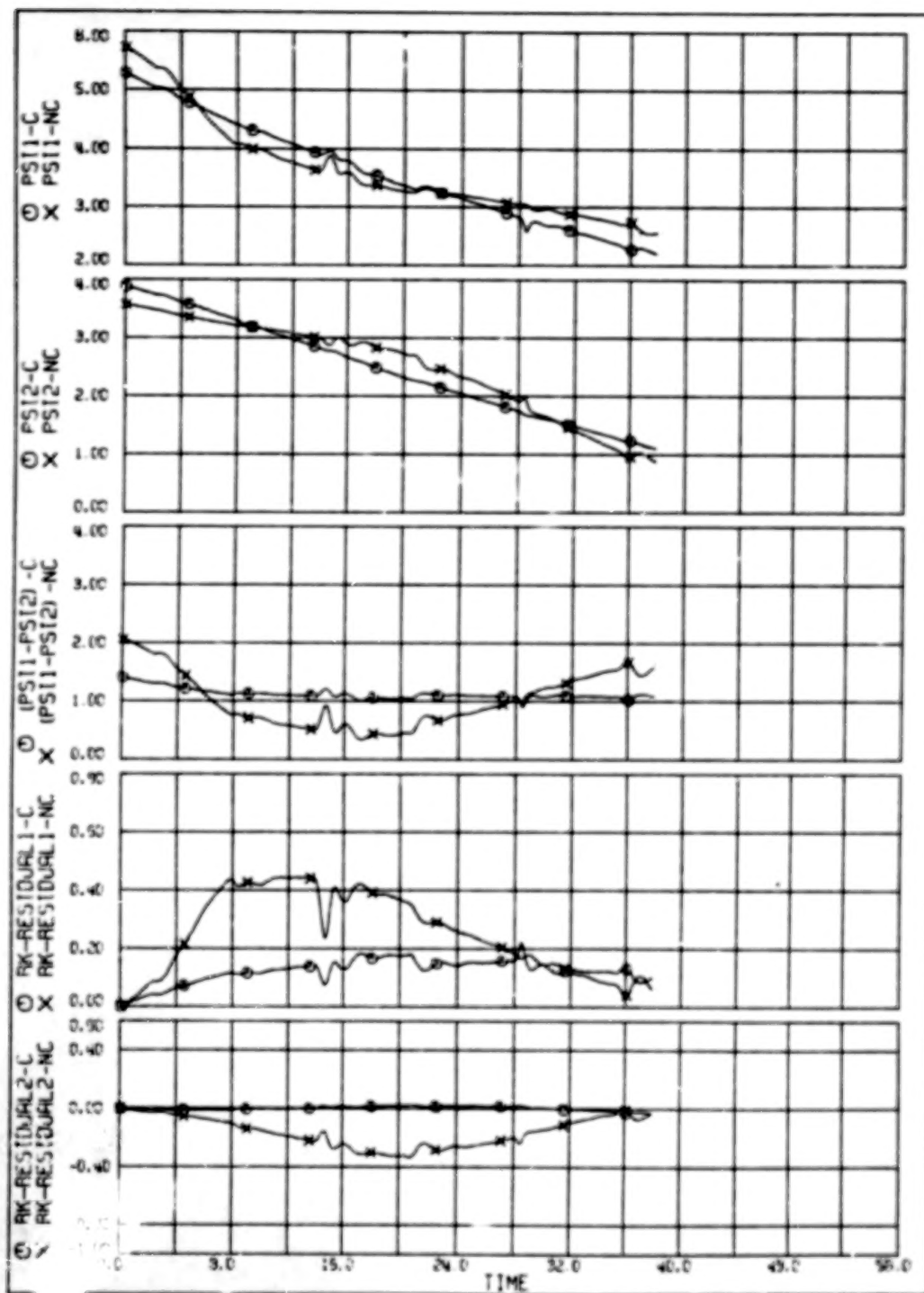


Figure F-6 Segment 4A, Turn Error Compensation Assuming Horizontal Spin Axes

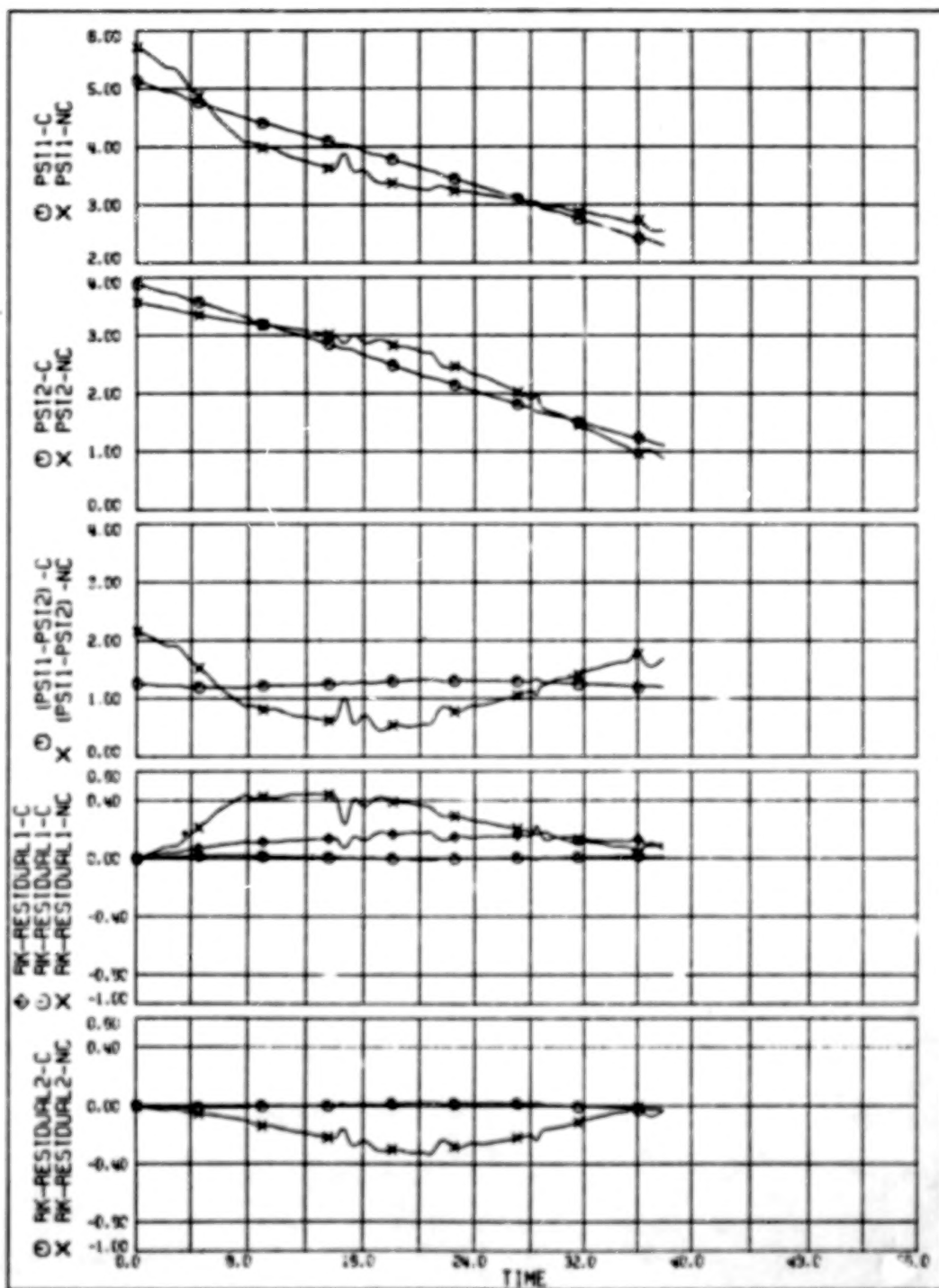


Figure P-7 Segment 4A, Turn Error Compensation Assuming Non-horizontal Spin Axes

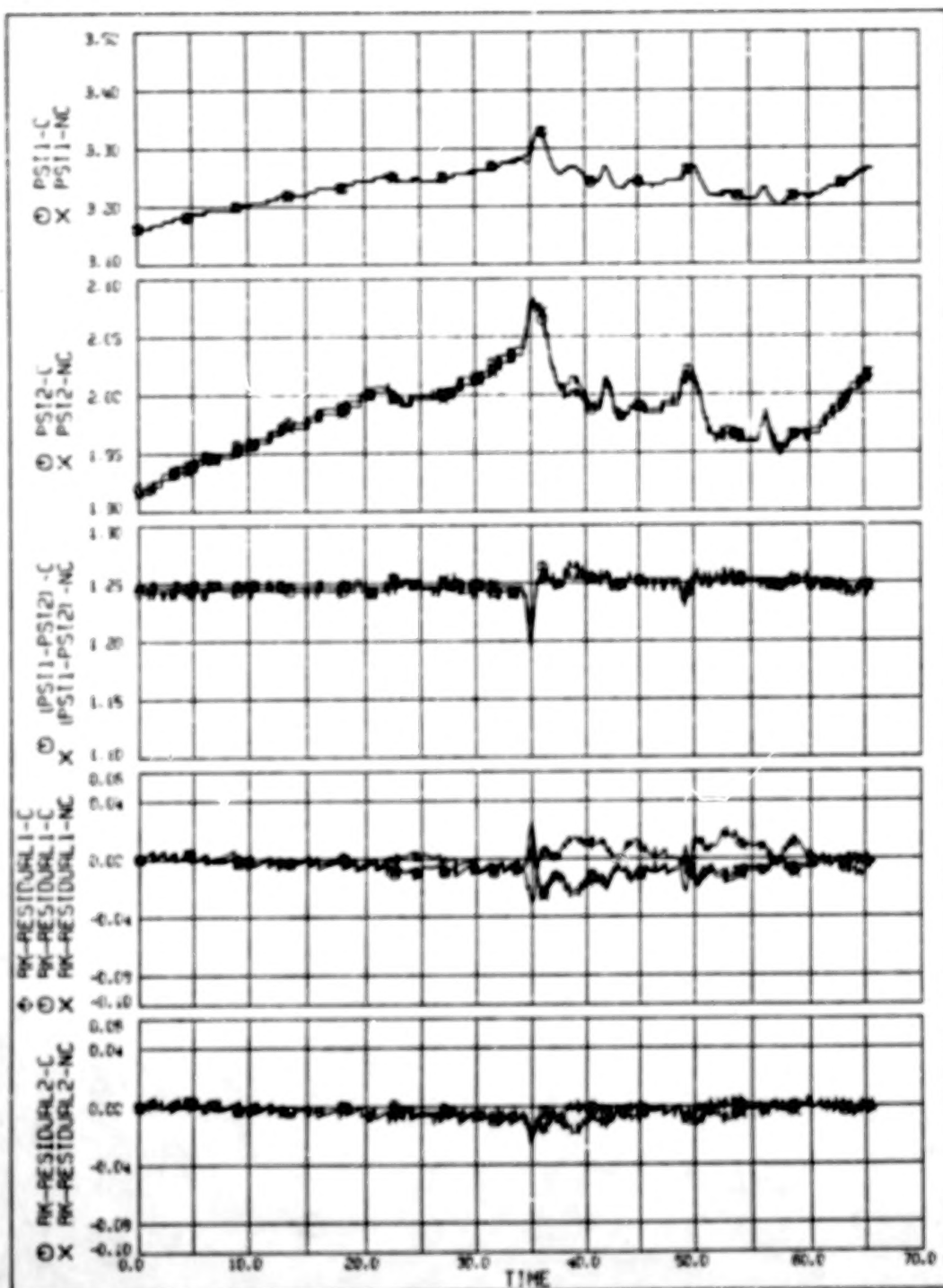


Figure F-8 Segment 2, Turn Error Compensation Assuming Non-horizontal Spin Axes

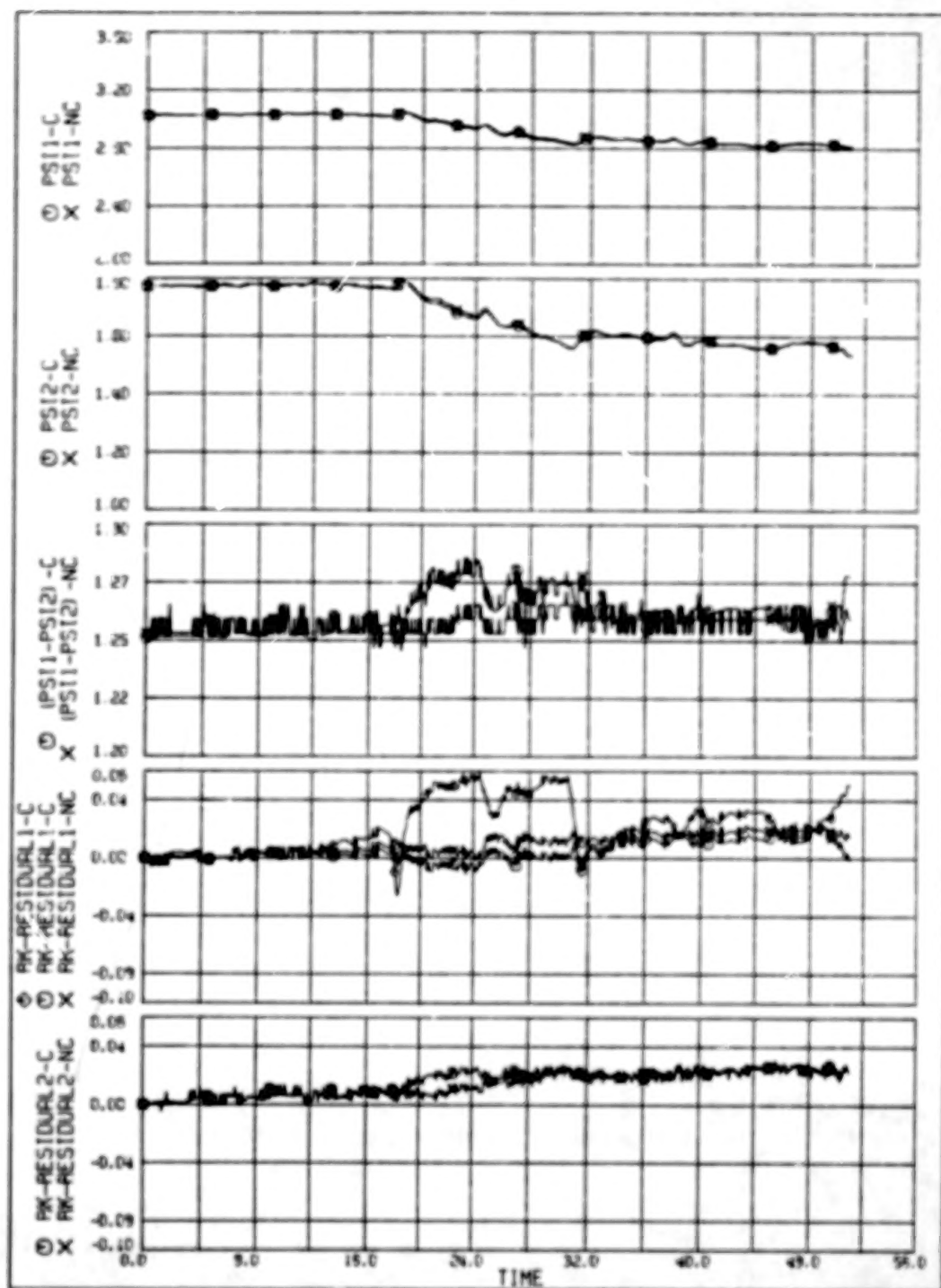


Figure F-9 Segment 3, Turn Error Compensation Assuming Non-horizontal Spin Axes

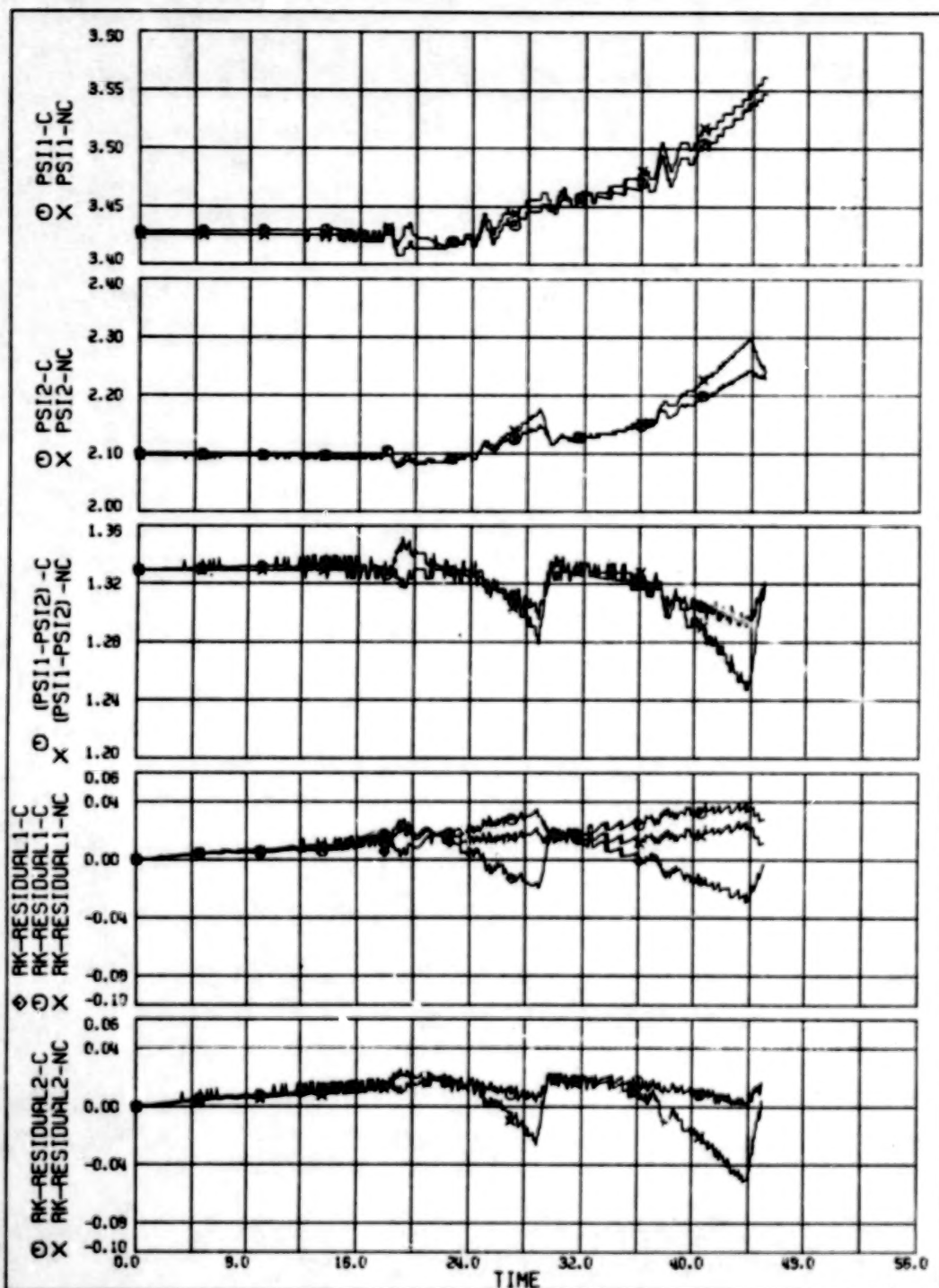


Figure F-10 Segment 4C, Turn Error Compensation Assuming Non-horizontal Spin Axes

LIST OF REFERENCES

1. Beard, R. V., Failure Accommodation in Linear Systems through Self-Reorganization, CR-118314, NASA, Washington, D.C., 1971.
2. Jones, H. L., Failure Detection in Linear Systems, Ph.D. Thesis, Dept. of Aeronautics and Astronautics, M.I.T., Cambridge, Mass., September, 1973.
3. Chien, T. T., An Adaptive Technique for a Redundant-Sensor Navigation System, CR-140313, NASA, Washington, D.C., 1972.
4. Wald, A., Sequential Analysis, Wiley, New York, 1947, Chapter 3.
5. Fukunaga, K., Introduction to Statistical Pattern Recognition, Academic Press, New York, 1972, pp. 77-84.
6. Jazwinski, A. H., Stochastic Processes and Filtering Theory, Academic Press, New York, 1970, Chapter 8.3.
7. Halfman, R. L., Dynamics, Vol. I. Addison-Wesley Publishing Co., Inc., Reading, Mass., 1962, p. 200.
8. Houbolt, J. C., R. Steiner and K. G. Pratt, "Dynamic Response of Airplanes in Atmospheric Turbulence Including Flight Data on Input and Response," NASA TR R-199, 1964.
9. Wrigley, W., Hollister, W. and Denhard, W., Gyroscopic Theory, Design and Instrumentation, M.I.T. Press, Cambridge, Mass., 1969, pp. 142-145.
10. Willsky, A. S., "A Survey of Design Methods for Failure Detection in Dynamic Systems," Automatica, Vol. 12, 1976, pp. 601-611.
11. Friedland, B., "Treatment of Bias in Recursive Filtering", IEEE Trans. Automat. Contr., Vol. AC-14, pp 359-367, Aug. 1969.

1. Report No. NASA CR-2944	2. Government Accession No.	3. Recipient's Catalog No.	
4. Title and Subtitle RELIABLE DUAL-REDUNDANT SENSOR FAILURE DETECTION AND IDENTIFICATION FOR THE NASA F-8 DFBW AIRCRAFT		5. Report Date February 1978	
		6. Performing Organization Code	
7. Author(s) James C. Deckert, Mukund N. Desai, John J. Devst, Jr., Alan S. Willsky		8. Performing Organization Report No. R-1077	
9. Performing Organization Name and Address The Charles Stark Draper Laboratory, Inc. 555 Technology Square Cambridge, Massachusetts 02139		10. Work Unit No.	
		11. Contract or Grant No. NAS1-13914	
12. Sponsoring Agency Name and Address National Aeronautics and Space Administration Langley Research Center Hampton, Virginia 23665		13. Type of Report and Period Covered Contractor Report 6/75 - 5/77	
		14. Sponsoring Agency Code	
15. Supplementary Notes Langley technical monitor: Raymond C. Montgomery Final report.			
16. Abstract A technique is developed which provides reliable failure detection and identification (FDI) for a dual-redundant subset of the flight control sensors onboard the NASA F-8 digital fly-by-wire (DFBW) aircraft. The technique is successfully applied to simulated sensor failures on the NASA Langley Research Center real-time F-8 digital simulator and to sensor failures injected on telemetry data from a test flight of the F-8 DFBW aircraft. For failure identification the technique utilizes the analytic redundancy which exists as functional and kinematic relationships among the various quantities being measured by the different control sensor types. The technique may be used not only in a dual-redundant sensor system, but also in a more highly redundant system after FDI by conventional voting techniques has reduced to two the number of unfailed sensors of a particular type. In addition the technique may be easily extended to the case in which only one sensor of a particular type is available.			
17. Key Words Suggested by Author Analytic Redundancy, Reliability, Digital fly-by-wire, Failure Detection and Identification, Redundancy Management		18. Distribution Statement Unclassified - Unlimited Subject Category 08	
19. Security Classif. (of this report) Unclassified	20. Security Classif. (of this page) Unclassified	21. No. of Pages 214	22. Price \$9.25

END

8-18-78